

REAL-SPACE SIMULATION OF TWO-DIMENSIONAL
INTERACTING QUANTUM CONDENSED MATTER SYSTEMS

Francisco Monteiro de Oliveira Brito

PhD

University of York

Physics, Engineering and Technology

December 2023

Abstract

The proliferation of quantum fluctuations and long-range entanglement presents an outstanding challenge for the numerical simulation of quantum condensed matter systems with exotic ground states. In this thesis, I tackle two classes of two-dimensional interacting models on the honeycomb lattice: multi-orbital Hubbard models on zig zag transition metal dichalcogenide nanoribbons and generalised Kitaev models on periodic clusters.

In the first part of the thesis, I discuss novel results obtained in a comparative study of mean field theory (MFT) and determinant quantum Monte Carlo (DetQMC). MFT reveals the influence of the edge filling on the ground state of the ribbons. The unbiased, numerically exact DetQMC confirms the stability of one of the possible ground states, albeit with quantitative differences, such as the critical Hubbard interaction for the onset of magnetic order. Unfortunately, DetQMC is severely plagued by the sign problem for this model. The variance of its estimators grows exponentially as most of the relevant edge fillings are reached and simulations are rendered unfeasibly expensive from the computational standpoint.

Motivated by the difficulties posed by the sign problem, I carry out a survey of general purpose numerical methods. The second part of the thesis addresses quantum spin liquids — which have attracted increasing attention — presenting a toolset of Chebyshev spectral methods developed here, namely: the finite temperature Chebyshev polynomial and the hybrid Lanczos-Chebyshev methods. The first one enables studies of temperature dependence for quantities of experimental interest, such as the specific heat, with a two-fold speed-up with respect to state-of-the-art methods. The second one gives access to spectral functions efficiently and with unparalleled flexibility. I use it to obtain novel results for the spin susceptibility of the Kitaev-Ising model, unravelling dynamical signatures of a liquid-to-liquid transition.

Finally, I briefly discuss the integration of the novel Chebyshev toolset with existing open-source software.

Contents

Abstract	iii
Contents	v
Acknowledgements	xv
Author's declaration	xvii
1 Introduction	1
1.1 Transition metal dichalcogenides	4
1.1.1 Nanoribbons	4
1.1.2 Minimal intra-orbital Hubbard model	6
1.2 Kitaev magnets	7
1.2.1 Spin-orbit entangled Mott insulators	8
1.2.2 Quantum spin liquids	12
1.2.3 Honeycomb Kitaev model	13
1.2.4 Generalised Kitaev models	18
2 Methods	21
2.1 Classical Monte Carlo method	22
2.2 Determinant quantum Monte Carlo	25
2.3 Chebyshev spectral methods: rationale	29
2.4 Vector recursions and bit representation of the Hamiltonian	31
2.5 Lanczos exact diagonalisation	36
2.6 Kernel polynomial method	39
2.6.1 Chebyshev expansions	39
2.6.2 Kernels and Gibbs oscillations	43
2.6.3 Delta function and density of states	48
2.7 Microcanonical ensemble	50
2.7.1 Microcanonical Lanczos	51
2.7.2 Thermal pure quantum states	52
2.7.3 Chebyshev polynomial Green's function	53
2.8 Canonical ensemble	58
2.8.1 Finite temperature Lanczos method	59
2.8.2 Canonical thermal pure quantum states	60
2.8.3 A novel finite temperature Chebyshev polynomial approach	61
2.9 Dynamical properties	64
2.9.1 Dynamical autocorrelation response functions with Lanczos	65
2.9.2 Original hybrid Lanczos-Chebyshev method for spectral functions	66

PART 1 — MEAN FIELD THEORY AND DETERMINANT QUANTUM MONTE CARLO: A COMPARATIVE STUDY FOR A TWO-DIMENSIONAL NANOSTRUCTURE	71
3 Edge magnetism in transition metal dichalcogenide nanoribbons	73
3.1 Overview	73
3.1.1 Mean field theory	75
3.1.2 Determinant quantum Monte Carlo	76
3.2 Results	78
3.2.1 Mean field theory: intraorbital interaction	79
3.2.2 Mean field theory: multiorbital interaction	83
3.2.3 Determinant quantum Monte Carlo simulations	84
3.2.4 Comparison between mean field theory and quantum Monte Carlo	88
3.3 Discussion and conclusion	89
 PART 2 — REAL-SPACE SPECTRAL SIMULATION OF GENERALISED KITAEV MODELS	 91
4 Kitaev-Heisenberg Model	93
4.1 Numerical implementation of the model	95
4.2 Zero-temperature consistency and microcanonical approaches	99
4.3 Canonical approaches: finite temperature	108
4.4 Bench-marking the hybrid Lanczos-Chebyshev method against the continued fraction Lanczos approach	113
5 Kitaev-Ising Model	115
5.1 Model Hamiltonian	116
5.2 Lanczos bench-mark	117
5.3 Finite temperature: Comparing Thermal Pure Quantum States and Chebyshev	118
5.4 Dynamics: Hybrid Lanczos-Chebyshev approach	119
5.5 Dynamics: Chebyshev approximation of the time evolution operator	120
6 Concluding remarks	125
 FUTURE WORK AND CONCLUSION	 129
7 Integration with the open-source software KITE	131
8 Conclusion	135
 APPENDICES	 137
A Appendix to Chapter 2	139
A.1 Coefficients of the Fejér kernel	139
A.2 Coefficients of the Jackson kernel	140
A.3 A prescription to generate a sequence of microcanonical pure quantum states	142
A.4 Estimating temperature with microcanonical pure quantum states	143

B Appendix to Chapter 3	147
B.1 Effect of edge bandwidth on edge magnetic order of zig zag transition metal dichalco- genide nanoribbons	147
C Appendix to Chapter 7	149
C.1 Setting up the honeycomb Kitaev model with PyBinding: a minimal example . . .	149
Glossary	153
Bibliography	155
Alphabetical Index	173

List of Tables

4.1	Phase boundaries of the Kitaev-Heisenberg model on a periodic 24-spin hexagonal cluster obtained with Lanczos.	101
4.2	Number of iterations (or Chebyshev polynomials) required for convergence for each method and CPU time per core per iteration.	108
5.1	Average CPU times for calculations with microcanonical thermal pure quantum states and the finite temperature Chebyshev polynomial method for the Kitaev-Ising model on a 24-spin hexagonal cluster.	118

List of Figures

1.1	Schematic for the structure coordination in the trigonal prismatic phase of a transition metal dichalcogenide.	6
1.2	Projection of the trigonal prismatic structure onto a honeycomb lattice.	6
1.3	Generic phase diagram for a system with electronic correlations and spin-orbit coupling.	9
1.4	Formation of spin-orbit entangled local moments.	10
1.5	Edge-sharing octahedra.	11
1.6	Honeycomb plane and iridate unit cell.	11
1.7	Resonating valence bond state.	12
1.8	Kitaev interaction.	13
1.9	Phase diagram of the Kitaev model.	13
1.10	Coulomb phase of the classical Kitaev model.	14
1.11	Representation of the flux for a plaquette.	14
1.12	Thermal fractionalisation. Temperature dependence of the specific heat and entropy density.	16
1.13	Decorated triangle-honeycomb structure.	16
1.14	Thermal fractionalisation for the triangle-honeycomb Kitaev model.	17
1.15	Phase diagram of the generic model Hamiltonian for spin-orbit assisted Mott insulators.	19
1.16	Schematic phase diagram of candidate quantum spin liquid materials with ferromagnetic Kitaev interactions.	20
2.1	In the spectral approach, the energy spectrum is probed using a coarse-grained average of energy states within the required energy resolution.	29
2.2	First six Chebyshev polynomials of the first kind.	41
2.3	Eigenvalues of a 14-spin Heisenberg chain.	48
2.4	Density of states of a 14-spin Heisenberg chain obtained with the kernel polynomial method using the Lorentz kernel.	50

2.5	Density of states of a 14-spin Heisenberg chain obtained with the Chebyshev polynomial Green's function method.	58
2.6	Modified Bessel functions up to order five.	62
3.1	Band structures of the three-band tight-binding model for various infinitely long zig zag transition metal dichalcogenide nanoribbons with a width of 64 transition metal atoms.	74
3.2	Folded band structure of the three-band tight-binding model for a molybdenum disulfide nanoribbon with a width of 20 transition metal atoms and a doubled unit cell in the longitudinal direction.	75
3.3	Mean field magnetic ordering at zero temperature for varying edge filling. The phases depicted include: ferromagnetic phases on both edges or only on the transition metal-terminated edge and two edge-antiferromagnetic phases.	79
3.4	Mean field phase diagrams in the Hubbard interaction-temperature plane at: half edge filling and three-quarter edge filling for a ribbon with 5 transition metal atoms of width.	80
3.5	Mean field band structure for various edge fillings corresponding to the different types of magnetic ordering on the edges.	81
3.6	Comparison between ribbons of increasing width (5, 10 and 20 transition metal atoms) at zero temperature. Staggered magnetisation and electron density profiles as the row position varies, while keeping the Hubbard interaction fixed; results for 10 and 20 transition metal atoms of width are indistinguishable. Staggered magnetisation versus Hubbard interaction at the transition metal and chalcogen-terminated edges.	82
3.7	Zero temperature phase diagrams in the intraorbital-interorbital Hubbard interactions plane for the case of the multiorbital model, obtained for a ribbon width of 16 transition metal atoms for edge fillings 62.5%, 65% and 75%. For three-quarter edge filling, I first contemplate the possibility of simultaneous edge polarisation, without Hund or pair-hopping interactions. Then, I consider the effect of these interactions in a separate panel of the figure. For the other edge fillings, I consider all interactions. I find a wealth of phases depending on the relative strengths of these competing interactions: ferromagnetism solely on the transition metal or chalcogen-terminated edges, or on both edges, and similarly for edge-antiferromagnetism.	83
3.8	Average sign obtained in the Monte Carlo sampling for varying longitudinal length and Hubbard interaction at fixed temperature, for molybdenum disulfide nanoribbons of 5 transition metal atoms of width approximately at three-quarter edge filling. Chemical potential used in the determinant quantum Monte Carlo algorithm to obtain the required edge filling for each system size.	84
3.9	Evidence for the edge-antiferromagnetic phase at three-quarter edge filling, obtained with determinant quantum Monte Carlo for molybdenum disulfide nanoribbons, for fixed Hubbard interaction and temperature. Spin-spin correlations for a 10×5 ribbon. Magnetic structure factor per row. Here, I consider a 22×5 molybdenum disulfide ribbon at three-quarter edge filling.	85
3.10	Spin-spin correlators between even and odd sites, along the chalcogen-terminated edge of molybdenum disulfide nanoribbons measured with determinant quantum Monte Carlo for three-quarter edge filling. On separate panels, I vary the Hubbard interaction and keep the temperature fixed and vice-versa.	86

3.11	Antiferromagnetic structure factor for nanoribbons with a width of 5 transition metal atoms and fixed Hubbard interaction and temperature for three-quarter edge filling. The peak signaling magnetic order sharpens as the longitudinal length increases. Spin-spin correlations corresponding to the structure factor curves with additional data shown for longitudinal lengths between 10 and 26. I also show fits to the determinant quantum Monte Carlo data using decreasing power laws.	87
3.12	Determinant quantum Monte Carlo results for the antiferromagnetic structure factor at the chalcogen-terminated edge as a function of the inverse longitudinal length, for nanoribbons with a width of 5 transition metal atoms at fixed temperature and three-quarter edge filling. Also shown are fits to the data using a scaling hypothesis and an extrapolation to the thermodynamic limit. Comparison between the staggered magnetisations on the chalcogen-terminated edge obtained with mean field theory and determinant quantum Monte Carlo as a function of the Hubbard interaction. Mean field theory results are for a width of 5 transition metal atoms at zero temperature.	88
4.1	24-spin hexagonal cluster with periodic boundary conditions on the honeycomb lattice.	95
4.2	Conversion between the two widely used parameterisations of the Kitaev-Heisenberg model in the literature.	96
4.3	Periodic boundary conditions for a 24-spin hexagonal cluster.	98
4.4	Minimum and maximum eigenvalues of the Kitaev-Heisenberg Hamiltonian on a 24-spin periodic hexagonal cluster on the honeycomb lattice, computed with Lanczos exact diagonalisation. Target energies used later to compare microcanonical Lanczos method and Chebyshev polynomial Green's function method.	99
4.5	Ground state energy density and spin-spin correlation obtained with Lanczos exact diagonalisation and thermal pure quantum states. The peaks of the negative second derivative of the Lanczos exact diagonalisation curve (obtained via finite differences) allow one to identify the quantum critical points.	100
4.6	Convergence in computations of ground state nearest neighbour spin-spin correlations. Dependence of the optimal number of iterations on the model parameter with Lanczos and thermal pure quantum states. In-depth convergence study around the Kitaev limits.	102
4.7	Comparative study between the Chebyshev polynomial Green's function method and the microcanonical Lanczos method: Ground state energy density and nearest neighbour spin-spin correlation (Chebyshev results are presented with varying resolution to illustrate spectral convergence) as a function of the model parameter.	103
4.8	Behaviour of the standard deviation of the nearest neighbour spin-spin correlation with the number of realisations of the initial random state for the Chebyshev polynomial Green's function method. The expected inverse square root dependence is recovered. .	104
4.9	Number of iterations required for convergence with the Chebyshev polynomial Green's function method times the required resolution, and spectrum width. The optimal number of polynomials for convergence is approximately proportional to the spectrum width and inversely proportional to the required resolution. Thus, the number of iterations required for convergence can be estimated in advance, unlike in other approaches. Computer time required for convergence using the microcanonical Lanczos method and the Chebyshev polynomial Green's function method.	105

4.10	Convergence of the ground state nearest neighbour spin–spin correlation computed with the microcanonical Lanczos and Chebyshev polynomial Green’s function methods around the Kitaev limits.	107
4.11	Finite temperature nearest neighbour spin correlator computed with the microcanonical thermal pure quantum states, finite temperature Chebyshev polynomial, canonical thermal pure quantum states, and finite temperature Lanczos methods for the 24-site cluster at the Kitaev limit. I used 50 random vector realisations in all cases. Error bars are negligibly small, except for the finite temperature Lanczos method. Inset: Standard deviation of the nearest neighbour spin correlator. Results of the canonical thermal pure quantum states method are not shown because the fluctuations are comparable to its microcanonical counterpart.	109
4.12	Specific heat (entropy density on the inset) computed with microcanonical thermal pure quantum states, finite temperature Chebyshev polynomial, canonical thermal pure quantum states, and finite temperature Lanczos methods. I use 50 realisations of the initial random state for all methods. The error bars are negligibly small in most of the temperature range, except for temperatures below that of the low-temperature peak, where they are comparable for every method. Model parameters as in Figure 4.11. . . .	110
4.13	Three-peak structure of the specific heat near the ferromagnetic quantum spin liquid-stripy transition of the Kitaev-Heisenberg model.	112
4.14	Three-stage release of the entropy density near the ferromagnetic quantum spin liquid-stripy transition of the Kitaev-Heisenberg model.	112
4.15	Dynamical spin susceptibility obtained with the hybrid Lanczos-Chebyshev method for the Kitaev-Heisenberg model on the hexagonal 24-spin cluster in the interval of model parameters containing the ferromagnetic, quantum spin liquid and stripy antiferromagnetic phases.	113
5.1	Negative first and second derivatives of the Lanczos ground state energy density and mean square of the magnetisation. These results match those of an earlier work and illustrate quantum phase transitions between ferromagnetic, nematic and quantum spin liquid phases. Here, a single realisation of the initial random state was found to be sufficient due to negligible statistical fluctuations.	116
5.2	Thermal pure quantum states and finite temperature Chebyshev polynomial results for the Kitaev-Ising model on a periodic hexagonal 24-spin cluster with fixed Kitaev anisotropy and two Ising coupling strengths, corresponding to the nematic and quantum spin liquid phases, respectively. Specific heat and entropy density, displaying signs of thermal fractionalisation. Also shown is the finite temperature expectation of the kinetic energy of the Majorana fermions.	117
5.3	Dynamical spin susceptibility of the Kitaev-Ising model for varying Ising coupling strength and fixed Kitaev anisotropy. The results obtained with the continued fraction Lanczos and hybrid Lanczos-Chebyshev methods are identical.	120
5.4	Staggered magnetisation after the quench for varying anisotropy. In the isotropic case, the magnetisation dies out quicker than in the anisotropic case, persisting for longer as the anisotropy becomes more pronounced.	122
5.5	Timescale for the loss of 99.9% of the staggered magnetisation for varying anisotropy. .	122

7.1	Periodic 4×3 cluster on the honeycomb lattice, generated with PyBinding.	132
7.2	24-spin hexagonal cluster on the honeycomb lattice, generated with PyBinding.	132
7.3	36-spin hexagonal cluster on the honeycomb lattice, generated with PyBinding.	133
7.4	42-spin hexagonal cluster on the honeycomb lattice, generated with PyBinding.	133
7.5	54-spin hexagonal cluster on the honeycomb lattice, generated with PyBinding.	134
B.1	Variation of the mean field staggered magnetisations at the transition metal and chalcogen-terminated edges for the three-quarter filling edge-antiferromagnetic phase for different zig zag transition metal dichalcogenide nanoribbons, all of them with a width of 5 transition metal atoms and fixed Hubbard interaction. Example of the gapped edge-antiferromagnetic phases obtained with mean field theory for a tungsten diselenide nanoribbon.	147

Acknowledgements

This thesis is dedicated to the memory of my grandad, Amadeu, who sadly passed away during my PhD. I would like to thank my friends and family (both in Portugal and in the UK) for the unconditional support they have given me over the last few years. In particular, I would like to thank my partner, Megan, for her infinite patience and love. I am indebted to my parents, Laura and João, for giving me the conditions to reach this point of my life.

I am also indebted to my supervisor, Professor Aires Ferreira, for believing in me and giving me the opportunity to work with him, for all the fruitful discussions we have had, and for his support during my stay at York.

I am thankful for having had great colleagues, with whom I shared countless lunch breaks, cups of coffee and with one of them even a house!

This project was undertaken on the Viking Cluster, which is a high performance computing facility provided by the University of York. I am grateful for computational support from the University of York High Performance Computing service (Viking) and the Research Computing team. Lastly, I am also grateful for the support of a Doctoral Training Partnerships studentship funded by the Engineering and Physical Sciences Research Council.

Author's declaration

I declare that this thesis is a presentation of original work and I am the sole author. This work has not previously been presented for an award at this University or elsewhere. All sources are acknowledged as References.

This work contains adaptations of articles that are either published in peer-reviewed scientific journals, in the process of being submitted for publication or going through the refereeing process. In particular, work from Chapter 1, Chapter 2 and Chapter 3 elaborates on the work published in:

- ▶ "Edge magnetism in transition metal dichalcogenide nanoribbons: Mean field theory and determinant quantum Monte Carlo", Francisco M. O. Brito, Linhu Li, João M. V. P. Lopes, and Eduardo V. Castro, *Physical Review B* **105**, 195130 (20 May 2022)

Work from Chapter 1, Chapter 2, Chapter 4 and Chapter 5 expands on

- ▶ "Real-space spectral simulation of quantum spin models: Application to generalized Kitaev models", Francisco M. O. Brito and Aires Ferreira, *SciPost Physics Core* **7**, 006 (21 February 2024)

I declare that I am the main contributor to the research presented here. In particular, I was responsible for:

- ▶ Creating software with original implementations of both existing and novel numerical methods created by me, which are described in this work;
- ▶ Performing analytical calculations, running simulations on a High Performance Computing facility and processing output data from those simulations;
- ▶ Interpreting results and drafting the papers mentioned above. Editing and final revisions to those papers were carried out in collaboration with my supervisor.

Francisco Brito

In strongly correlated materials, the interplay between different types of interactions can engender rich zero temperature phase diagrams. In particular, for interacting quantum spins, these are characterised by a series of transitions between paramagnetic, magnetically ordered and quantum spin liquid (QSL) phases. These quantum phase transitions are driven by one or more parameters in the Hamiltonian, such as an external magnetic field or a spin exchange coupling constant. When a drastic change in the ground state occurs as one of these parameters is varied, there is an accompanying change in the thermodynamic properties. This change manifests itself in the form of critical behaviour of quantities such as the structure factor and the susceptibility, which scale with the parameter that drives the transition [1, 2].

The study of the competition between quantum fluctuations and interactions at the heart of quantum phase transitions often calls for a numerical approach [3–11]. Exact solutions are only known for a handful of cases (a well-known example is the isotropic Heisenberg chain [12]). Moreover, in low dimensions, the presence of strong quantum fluctuations limits the applicability of mean field theory (MFT). Exact diagonalisation (ED) methods, such as those based on the Lanczos algorithm [13], are the next step beyond exact analytical solutions. There are several examples of the application of this method to interacting spin systems, for example References [5, 11, 14]. Unfortunately, these are limited to relatively small system sizes, even when algorithms are optimised to reflect symmetries of the model. The culprit is the exponential scaling of the computational cost with the system size, which is particularly severe in dimensions greater than one. Beyond the Lanczos algorithm and its more recent variants [15–17], several attempts to go beyond the limitations of full exact diagonalisation have been made. Powerful numerical techniques have been deployed with varying degrees of success, including series expansions [18–24], quantum Monte Carlo (QMC) [7, 8, 25, 26], density matrix renormalisation group (DMRG) [27–30], tensor-network approaches (such as infinite Projected Entangled Pair States (iPEPS)) [10, 31–33] and thermal pure quantum states (TPQ) [32, 34–36]. Efficient numerical schemes amenable to large-scale computations share a key feature: they aim at reconstructing expectation values of quantum observables without having to fully diagonalise the Hamiltonian. The resulting computational cost depends crucially on how the expectation values of the observables are evaluated. Here, two relevant aspects are at play. The first has

1.1	Transition metal dichalcogenides	4
1.2	Kitaev magnets	7

[1]: Carr (2010), *Understanding Quantum Phase Transitions*

[2]: Sachdev (2011), *Quantum Phase Transitions*

[12]: Bethe (1931), ‘Zur Theorie der Metalle’

[13]: Lanczos (1950), ‘An iteration method for the solution of the eigenvalue problem of linear differential and integral operators’

[5]: Gotfryd et al. (2017), ‘Phase diagram and spin correlations of the Kitaev-Heisenberg model’

[11]: Hickey et al. (2020), ‘Field-driven gapless spin liquid in the spin-1 Kitaev honeycomb model’

[14]: Winter et al. (2018), ‘Probing α -RuCl₃ Beyond Magnetic Order’

[15]: Jaklič et al. (1994), ‘Lanczos method for the calculation of finite-temperature quantities in correlated systems’

[16]: Aichhorn et al. (2003), ‘Low-temperature Lanczos method for strongly correlated systems’

[17]: Prelovšek et al. (2013), ‘Ground State and Finite Temperature Lanczos Methods’

- [7]: Nasu et al. (2014), ‘Vaporization of Kitaev Spin Liquids’
- [8]: Nasu et al. (2015), ‘Thermal fractionalization of quantum spins in a Kitaev model’
- [26]: Sato et al. (2021), ‘Quantum Monte Carlo simulation of generalized Kitaev models’
- [39]: Troyer et al. (2005), ‘Computational Complexity and Fundamental Limitations to Fermionic Quantum Monte Carlo Simulations’
- [40]: Nakamura (1998), ‘Vanishing of the negative-sign problem of quantum Monte Carlo simulations in one-dimensional frustrated spin systems’
- [41]: Honecker et al. (2016), ‘Thermodynamic properties of highly frustrated quantum spin ladders’
- [42]: Alet et al. (2016), ‘Sign-Problem-Free Monte Carlo Simulation of Certain Frustrated Quantum Magnets’
- [43]: Li et al. (2019), ‘Sign-Problem-Free Fermionic Quantum Monte Carlo’
- [44]: Levy et al. (2021), ‘Mitigating the Sign Problem through Basis Rotations’
- [45]: Huang et al. (2022), ‘Sign-free determinant quantum Monte Carlo study of excitonic density orders in a two-orbital Hubbard-Kanamori model’
- [46]: Weber et al. (2022), ‘Quantum Monte Carlo simulations in the trimer basis’

to do with how the corresponding operators are reconstructed. The second relates to the process by which one obtains the expectation value. Usually this process is a stochastic one, unless there is prior knowledge about some of the system’s features, in which case a variational approach can be viable [25, 37, 38].

In principle, QMC methods can be used to probe large systems in any number of dimensions, while remaining numerically exact [7, 8]. However, they often encounter the so-called sign problem [26, 39]. This is a situation where the variance of the estimators of quantities of interest increases exponentially due to quantum statistics. The severity of the problem depends on the computational basis used to tackle the specific model [40–46]. Generally, the sign problem tends to be more acute in frustrated systems [47, 48], hampering the use of QMC to extract quantities of interest, such as correlation functions. The sign problem and the limited range of models that QMC is able to access emphasise the need for a general purpose method that can be used more broadly as an alternative to Lanczos ED and QMC.

The study of quantum many-body systems requires numerical methods that strike an elusive balance between two attributes that rarely go hand in hand: simplicity and reliability. The goal of this thesis is two-fold. On the one hand, I wish to illustrate the need for unbiased numerical methods with rigorous control over accuracy with practical examples of timely models. On the other hand, I seek to devise general purpose, unbiased numerical methods that are efficient, thus taking full advantage of the available computational resources.

The first part of this thesis illustrates both the virtues and the shortcomings of the simplicity of the MFT approach. I assess its validity in the context of a model of interacting fermions with emergent magnetism. Despite qualitatively agreeing with the more reliable determinant quantum Monte Carlo (DetQMC) method, MFT misses a number of crucial quantitative aspects. Namely, MFT is shown to be biased towards magnetic ordering, exaggerating the tendency for long-range order and underestimating the critical parameter for a quantum phase transition to occur. QMC clarifies the nature of a particular phase of the model, which is shown to harbour *quasi* long range order, *i.e.* algebraic decay of spin correlations. Additionally, one of the quantum critical points of the model is rigorously estimated with a finite-size scaling study of QMC results. The study also yields a critical parameter that is about 68% larger than the MFT estimate, with the latter clearly displaying a bias towards long-range order. MFT suggests a strong dependence of the ground state on the occupation of localised electronic edge states — dubbed edge filling — which drives

quantum phase transitions. Unfortunately, computational effort becomes a limiting factor with QMC, as I find the relevant model of interacting fermions to be severely sign-problematic for most fillings of interest, except the one corresponding to the phase mentioned above, which was rigorously studied. As a consequence of the sign problem, the wealth of phases predicted by MFT is deemed inaccessible to DetQMC due to excessive computational cost.

Motivated by the unbiased and numerically exact nature of the QMC approach, but also conscious of the limitations imposed by the sign problem, in the second part of the thesis, I embark on a quest to develop a framework of numerical methods based on Chebyshev polynomial expansions. Remaining on the topic of two-dimensional quantum many-body systems, this time I focus on models of interacting spins hosting QSL ground states. These have seen an explosion of the interest [49–55] since an exactly solvable model was put forward by Kitaev [56]. Generalised Kitaev models with no known analytical solution demand a numerical approach, with the exactly solvable limit anchoring one’s physical intuition. In these models, competing interactions tend to drive quantum phase transitions between magnetically ordered, paramagnetic and QSL phases [3, 4, 57]. The identification of the latter is challenging because, even though QSLs display no magnetic ordering down to zero temperature [58], they have specific properties, such as spin fractionalisation and long-range entanglement, which warrant their classification as a separate phase of matter.

Probing the quantum observables that describe QSL behaviour requires efficient numerical methods that are unbiased and bypass the need to introduce approximations. These are often applied to the study of quantum criticality, temperature dependence of experimentally relevant quantities, such as the specific heat and the entropy, or dynamical signatures of QSLs, *e.g.* in the spin susceptibility [5, 7–9, 59–61]. The second part of this thesis is devoted to a general purpose framework of efficient Chebyshev-based methods developed in this work that are used to study models with QSL ground states. The Chebyshev approach successfully identifies thermal and dynamical signatures of QSL behaviour, with advantageous convergence properties and increased flexibility with respect to comparable state-of-the-art methods.

The remainder of this chapter aims to motivate recent interest in the quantum many-body systems tackled in this work. In Section 1.1, I summarise the key properties of transition metal dichalcogenides (TMDs) and explain why I consider them a rich platform for the study of edge physics. In particular, I discuss nanoribbons, which have previously been shown to host emergent edge-magnetism in

[56]: Kitaev (2006), ‘Anyons in an exactly solved model and beyond’

[3]: Chaloupka et al. (2010), ‘Kitaev-Heisenberg Model on a Honeycomb Lattice’

[4]: Chaloupka et al. (2013), ‘Zigzag Magnetic Order in the Iridium Oxide Na_2IrO_3 ’

[57]: Rau et al. (2014), ‘Generic Spin Model for the Honeycomb Iridates beyond the Kitaev Limit’

[58]: Kitagawa et al. (2018), ‘A spin-orbital-entangled quantum liquid on a honeycomb lattice’

[62]: Fujita et al. (1996), ‘Peculiar Localized State at Zigzag Graphite Edge’

[63]: Feldner et al. (2010), ‘Magnetism of finite graphene samples’

[64]: Feldner et al. (2011), ‘Dynamical Signatures of Edge-State Magnetism on Graphene Nanoribbons’

[65]: Manzeli et al. (2017), ‘2D transition metal dichalcogenides’

[66]: Radisavljevic et al. (2011), ‘Single-layer MoS₂ transistors’

[67]: Koppens et al. (2014), ‘Photodetectors based on graphene, other two-dimensional materials and hybrid systems’

[68]: Mak et al. (2016), ‘Photonics and optoelectronics of 2D semiconductor transition metal dichalcogenides’

[70]: Mak et al. (2010), ‘Atomically Thin MoS₂: A New Direct-Gap Semiconductor’

[62]: Fujita et al. (1996), ‘Peculiar Localized State at Zigzag Graphite Edge’

graphene [62–64], inspiring my search for analogous phenomena in TMDs. I also discuss the generalised Hubbard Hamiltonian used to model zig zag transition metal dichalcogenide nanoribbons (zTMDNRs). In Section 1.2, I give an overview of the history of the field of Kitaev magnets over the last 15 years. I start with a general discussion about the conjugation of competing interactions that leads to the appearance of bond-directional spin interactions in spin-orbit assisted Mott insulators. Then, I present a motivated definition of a QSL in terms of its exotic properties. Lastly, I discuss the honeycomb Kitaev model and its generalisations, which are regularly used to model QSL candidate materials, including the ones studied in this work.

1.1 Transition metal dichalcogenides

TMDs are prominent members of the two-dimensional materials family [65] with numerous prospective technological applications [66–68]. While monolayer graphene is gapless and its bilayer counterpart has a tunable, but small gap of the order of 10^{-1} eV [69], TMD monolayers are semiconductors, with intrinsic band gaps exceeding 1 eV [70]. Since the direct band gap lies in the visible frequency range, these semiconducting analogues of graphene are promising for optoelectronic applications [71–73]. TMDs are also promising in the rapidly growing fields of spin- and valleytronics [74–78], where it is particularly important to manipulate the electronic spin and valley degrees of freedom [79].

1.1.1 Nanoribbons

The presence of one-dimensional edges is a distinctive feature of any two-dimensional material. The reduced dimensionality gives rise to unique properties which are not present in the bulk. Zig zag graphene nanoribbons (zGNRs) are known examples where low energy edge states appear. In the tight-binding picture, the latter correspond to bands close to the Fermi energy that become flatter and flatter as the width of the ribbon is increased. In Reference [62], MFT was used to study electron-electron interactions in zGNRs, revealing the possibility of spontaneous magnetic order at the edges. Subsequent studies unraveled the rich physics of these edge-states, supporting the existence of the magnetic phase predicted using MFT, and unveiling electronic properties such as half-metallicity [80–86]. Despite the successful fabrication of graphene nanoribbons [87, 88], the observation of magnetised zigzag edges is limited to the detection of spin-split edge bands using scanning tunneling microscopy [89]. Long-range magnetic

order remains elusive [90], and zGNR fabrication alternatives [91] as well as new strategies to enhance edge magnetism are currently being explored [92].

Similarly to graphene, TMDs can also be synthesised in the form of nanoribbons, as recently demonstrated through a variety of methods [93–98]. However, contrary to graphene, there is ample experimental evidence of edge-magnetic ordering on few-layer TMD nanostructures [99–106]. In ultrathin MoS₂ and WS₂ nanosheets, ferromagnetic order sets in even at room temperature [99–103]. The onset of magnetic order has been attributed to the presence of zigzag edges and/or structural defects such as grain boundaries or vacancies related to the synthesis process. The ferromagnetic behaviour found in few-layer MoS₂ nanomeshes [104] supports the idea of a dominant zigzag edge contribution: on the one hand, the dependence on interpore distance mimics the dependence on the zigzag nanoribbon width; on the other hand, ferromagnetism is absent in samples without annealing, where the proportion of as-grown defects compared to zigzag edges is higher. Contrasting with exfoliated nanosheets, for which clear signs of ferromagnetism are observed, pristine TMDs, such as MoS₂ in its three-dimensional form, are diamagnetic [104]. Moreover, mono-/bi-layer MoS₂ nanosheets show enhanced room temperature ferromagnetism attributed to an increased density of zigzag edges and/or defects [106], while bulk monolayers are only spin-valley polarised upon doping [107].

On the theory side, extensive work based on density functional theory (DFT) calculations have predicted both metallic behaviour and ferromagnetism at the edges of zig zag transition metal dichalcogenide nanoribbons (zTMDNRs) [108–117]. These calculations indicate that the energy difference between ferromagnetic and antiferromagnetic spin ordering at the edges is around tens of meV [115, 117]. Such a small energy difference casts some doubt on what is the thermodynamically stable phase and also indicates that magnetic ordering in zTMDNRs may be sensitive to external perturbations, such as a back gate voltage, which in turn changes the edge filling. A realistic tight-binding parametrisation with a mean field decoupling of the Hubbard interaction was recently used to test the stability of edge magnetism against disorder in zigzag MoS₂ nanoribbons [117]. However, the sensitivity to the filling of the edge was not considered. In zGNRs and also phosphorene nanoribbons, edge magnetism has been studied using DetQMC [63, 64, 118–120]. The results for zGNRs further support the emergence of edge-magnetic order from electron-electron interactions and it is possible to make a direct comparison between DetQMC and MFT results. DetQMC overcomes the limitations of the approximate local or semi-local functionals used in DFT calculations [121], and

[99]: Mao et al. (2013), ‘Ferromagnetism in exfoliated tungsten disulfide nanosheets’

[100]: Gao et al. (2013), ‘Ferromagnetism in freestanding MoS₂ nanosheets’

[101]: Yang et al. (2015), ‘Realization of high Curie temperature ferromagnetism in atomically thin MoS₂ and WS₂ nanosheets with uniform and flower-like morphology’

[102]: Zhang et al. (2014), ‘Ferromagnetism in ultrathin MoS₂ nanosheets: from amorphous to crystalline’

[103]: Huo et al. (2014), ‘Edge-states ferromagnetism of WS₂ nanosheets’

[104]: Kondo et al. (2017), ‘Edge-spin-derived magnetism in few-layer MoS₂ nanomeshes’

[115]: López-Urías et al. (2015), ‘Electronic, magnetic, optical, and edge-reactivity properties of semiconducting and metallic WS₂ nanoribbons’

[117]: Vancsó et al. (2019), ‘Stability of edge magnetism against disorder in zigzag MoS₂ nanoribbons’

[63]: Feldner et al. (2010), ‘Magnetism of finite graphene samples’

[64]: Feldner et al. (2011), ‘Dynamical Signatures of Edge-State Magnetism on Graphene Nanoribbons’

[118]: Yang et al. (2016), ‘Room-temperature magnetism on the zigzag edges of phosphorene nanoribbons’

[119]: Raczkowski et al. (2017), ‘Interplay between the edge-state magnetism and long-range Coulomb interaction in zigzag graphene nanoribbons’

[120]: Yang et al. (2017), ‘Strain-tuning of edge magnetism in zigzag graphene nanoribbons’

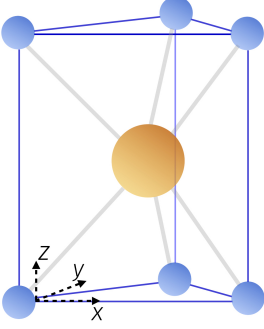
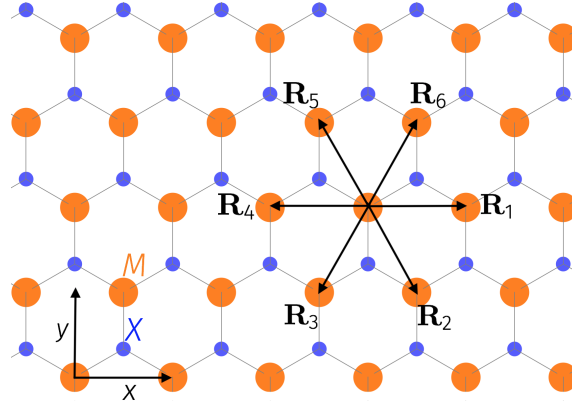


Figure 1.1: Schematic for the structure coordination in the trigonal prismatic phase of a TMD.

Figure 1.2: Projection of the trigonal prismatic structure onto the xy plane, yielding a honeycomb lattice. Hopping terms directly involving the X atoms are neglected in the model used here. Thus I identify only the relevant nearest M neighbours by the vectors $\mathbf{R}_{i=1,2,\dots,6}$. This lattice represents part of the nanoribbon with a width of 5 M atoms I shall consider later. Each row of the ribbon is defined as a set of M atoms for which y is constant.



also the typical overestimation of long-range order in MFT [63]. Until this work, unbiased, numerically exact approaches had not yet been applied to study the magnetism of z TMDNRs.

1.1.2 Minimal intra-orbital Hubbard model

Group 6 TMDs contain transition metals $M = \text{Mo}, \text{W}$, and chalcogens $X = \text{S}, \text{Se}, \text{Te}$, in a 1:2 proportion, and thus have the chemical formula MX_2 . In the monolayer form, M atoms are arranged in a triangular lattice, sandwiched between two layers of X atoms. The most common stacking structure — shown in Figure 1.1 — is denoted trigonal prismatic. In this work, I consider the planar honeycomb lattice corresponding to the trigonal prismatic unit cell depicted in the top-down view of Figure 1.2.

I mainly consider a minimal intraorbital Hubbard model based on the three-band tight-binding model (3BTB) of Reference [122]:

$$\hat{H} = \sum_{\langle i,j \rangle, \sigma, \alpha, \beta} c_{i,\alpha,\sigma}^\dagger K_{\alpha\beta}(\mathbf{R}_{ij}) c_{j,\beta,\sigma} + U \sum_{i,\alpha} n_{i,\alpha,\uparrow} n_{i,\alpha,\downarrow}, \quad (1.1)$$

where $\langle i, j \rangle$ are nearest-neighbour sites on the triangular (M atom) lattice, $c_{i,\alpha,\sigma}^\dagger, c_{j,\beta,\sigma}^\dagger$ are electron creation operators on lattice sites i, j , M atom orbitals

$$\alpha, \beta = d_{z^2}, d_{xy}, d_{x^2-y^2}$$

and spin $\sigma = \uparrow, \downarrow$, $n = c^\dagger c$ is the number operator and U is the on-site Hubbard repulsion. I use the hopping parameters $K_{\alpha\beta}(\mathbf{R}_{ij})$ obtained with the generalised-gradient approximation in Reference [122].

To mimic the geometry of the nanoribbon, I consider periodic boundary conditions (PBCs) along the longitudinal (x) direction and open boundary conditions (OBCs) along the transverse (y)

[122]: Liu et al. (2013), ‘Three-band tight-binding model for monolayers of group-VIB transition metal dichalcogenides’

direction (see Figure 1.2). In order to capture potential multiorbital effects, one needs to go beyond the minimal Hubbard model by adding the following terms to the Hamiltonian of Equation 1.1: an interorbital on-site interaction term (U'), a Hund term (J) and a pair-hopping term (J'):

$$\hat{H}_{\text{inter-orb.}} = \frac{U'}{2} \sum_{\substack{i,\alpha \neq \beta \\ \sigma, \sigma'}} n_{i,\alpha,\sigma} n_{i,\beta,\sigma'}, \quad (1.2)$$

$$\hat{H}_{\text{Hund}} = \frac{J}{2} \sum_{\substack{i,\alpha \neq \beta \\ \sigma, \sigma'}} c_{i,\alpha,\sigma}^\dagger c_{i,\beta,\sigma'}^\dagger c_{i,\alpha,\sigma'} c_{i,\beta,\sigma}, \quad (1.3)$$

$$\hat{H}_{\text{pair hopp.}} = \frac{J'}{2} \sum_{\substack{i,\alpha \neq \beta \\ \sigma \neq \sigma'}} c_{i,\alpha,\sigma}^\dagger c_{i,\alpha,\sigma'}^\dagger c_{i,\beta,\sigma'} c_{i,\beta,\sigma}. \quad (1.4)$$

Assuming rotational invariance, out of the four parameters characterising the on-site interaction, only two are independent. For d -orbitals, the following relation holds: $J' = J = (U - U')/2$ [123]. Despite the lack of full rotational symmetry in TMDs, deviations from this relation are not severe [124], and I still use it here.

1.2 Kitaev magnets

I have already mentioned the honeycomb Kitaev model as a rare example of an exactly solvable model of interacting quantum spins in two dimensions [56]. Exact solvability endows the model with great theoretical interest, not least because the solution allows for both gapped and gapless QSL phases, including a chiral QSL, for which nonabelian Ising anyons¹ appear. The unconventional exchange behaviour of the non-Abelian anyons harboured by the Kitaev model has recently been observed for the first time by Google Quantum AI and collaborators [126]. This is thought to be an alternate route to topological quantum computation, enjoying robustness against environmental noise².

Regardless of its importance in quantum computation, in condensed matter physics, the importance of the hunt for a solid-state realisation of the Kitaev model is of fundamental nature. Several important questions may be posed regarding the synthesis of spin liquid materials and their use as experimental probes for the properties of Majorana fermions and gauge physics. At first sight, the quantum spin interaction proposed by Kitaev seemed artificial and perhaps solely of theoretical interest. It was not until the seminal work of Jackeli and Khaliullin [127] that the community realised that the Kitaev interaction could be the dominant spin interaction in a family of spin-orbit entangled Mott insulators, later referred to

[124]: Ribic et al. (2014), ‘Cubic interaction parameters for t_{2g} Wannier orbitals’

1: Anyons are quasiparticles occurring only in two dimensions, which are neither bosons nor fermions. Under exchange of two particles, a bosonic wave function is symmetric, while a fermionic one is antisymmetric, *i.e.* the wavefunction is multiplied by $e^{i\theta}$, with $\theta = 0, \pi$. For anyons, the restriction on the angle θ is relaxed and the wavefunction is therefore multiplied by an arbitrary phase. θ is referred to as the statistical angle, corresponding to an anyon with statistics θ . For a review, see Reference [125].

[126]: Andersen et al. (2023), ‘Non-Abelian braiding of graph vertices in a superconducting processor’

2: See recent [blog post](#) by researchers from the Google Quantum AI Team who co-authored the paper (Accessed: 1 December 2023).

[127]: Jackeli et al. (2009), ‘Mott Insulators in the Strong Spin-Orbit Coupling Limit’

- [137]: Zare et al. (2021), ‘Spin liquid in twisted homobilayers of group-VI dichalcogenides’
- [138]: Kiese et al. (2022), ‘TMDs as a platform for spin liquid physics’
- [49]: Witczak-Krempa et al. (2014), ‘Correlated Quantum Phenomena in the Strong Spin-Orbit Regime’
- [50]: Rau et al. (2016), ‘Spin-Orbit Physics Giving Rise to Novel Phases in Correlated Systems’
- [51]: Savary et al. (2016), ‘Quantum spin liquids’
- [52]: Winter et al. (2017), ‘Models and materials for generalized Kitaev magnetism’
- [53]: Hermanns et al. (2018), ‘Physics of the Kitaev Model’
- [54]: Motome et al. (2020), ‘Hunting Majorana Fermions in Kitaev Magnets’
- [55]: Trebst et al. (2022), ‘Kitaev materials’

3: The intensity of SOC scales with Z^4 , where Z is the atomic number.

as Kitaev magnets. These are among the candidates for a physical realisation of the Kitaev model. Following the initial proposal of Kitaev magnets, several other materials have been proposed [128–136] as potential physical realisations of the Kitaev interaction, including TMDs [137, 138], in particular WSe_2 .

This section is based on the following reviews [49–55]. I shall summarise the evolution of the field documented in these reviews as I cite them roughly in chronological order.

1.2.1 Spin-orbit entangled Mott insulators

A common thread between this section and the previous one, devoted to zTMDNR, is the modelling of transition metal compounds. In the previous section, I discussed a model where the local Hubbard repulsion, U , between electrons occupying the same d -orbital could lead to emerging magnetism. In this section, I focus on transition metal oxides, where strong spin-orbit coupling (SOC) is also a key ingredient, following Reference [49]. Here, I am particularly interested in cases where magnetism does not emerge, but the system acquires additional structure nonetheless, when compared to a paramagnet. As far as the Hamiltonian is concerned, SOC corresponds to the addition of a term of the type

$$\hat{H}_{\text{SOC}} = \lambda \sum_i \mathbf{L}_i \cdot \mathbf{S}_i \quad (1.5)$$

to the Hamiltonian given by adding up the contributions of Equations 1.1-1.4, where λ is the strength of the atomic SOC between spin, \mathbf{S}_i , and angular momentum, \mathbf{L}_i . For heavy transition metal compounds taken from the $5d$ and, occasionally the $4d$ series of the periodic table, the d -orbitals are more extended than for lighter compounds, *e.g.* in the $3d$ series. Consequently, electronic repulsion is reduced. At the same time, SOC increases dramatically³, which splits degenerate bands of the original tight-binding model and tends to decrease the kinetic energy. Correlation physics then comes into play as U becomes dominant relative to the other energy scales, despite its relative attenuation for extended d -orbitals.

The general form of the phase diagram of a model combining SOC and electron-electron interactions is outlined in Figure 1.3. The strengths of the Hubbard and SOC interactions are given relative to the dominant electron hopping integral, t . The diagram does not represent any specific physical system as the phase boundaries vary considerably with the choice of orbitals, lattice and band structure encoded in the hoppings, *e.g.* $K_{\alpha\beta}(\mathbf{R}_{ij})$ in Equation 1.1.

The left hand side of Figure 1.3 represents conventional transition metal compounds, *i.e.* the limit $\lambda \ll t$. These undergo a metal/band insulator-Mott insulator transition as U approaches the bandwidth, which is typically a few times t . As SOC increases in the $U \ll t$ regime, the metallic/semiconducting state becomes either a topological insulator [139, 140] or a Weyl semimetal [141], as depicted in the lower right region of the diagram. When $U \sim \lambda$, the two interactions have a cooperative net effect.

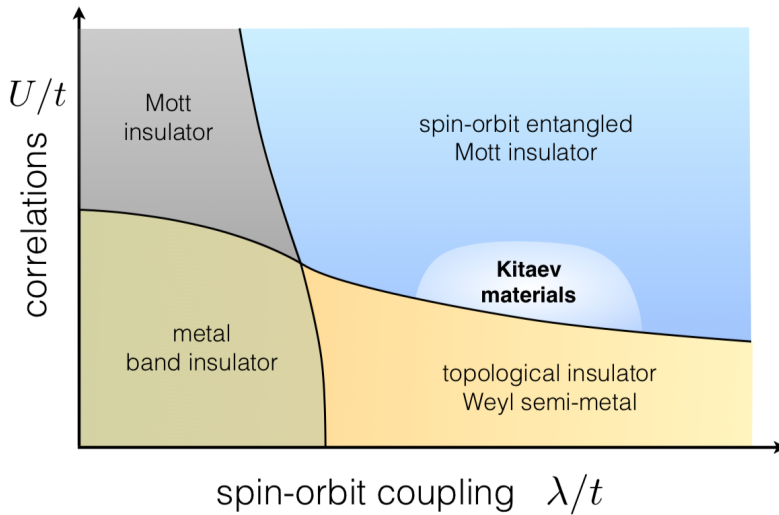


Figure 1.3: Generic phase diagram for a system with electronic correlations and spin-orbit coupling. Source: This figure is an adaptation from [55] of a figure originally appearing in [49].

Suppose that one approaches the intermediate regime for which U and λ are comparable from the strong Mott limit ($U \gg t$) on the upper left region. The Hubbard term tends to localise electrons, in turn decreasing their kinetic energy. The on-site SOC term is comparatively less sensitive to localisation, so it is enhanced with respect to the kinetic energy, which explains the shift of the vertical phase boundary to the left as U increases. The horizontal phase boundary shifts downward as λ increases because SOC favours the splitting of degenerate bands, resulting in a larger set of narrow bands, where Hubbard-induced localisation prevails.

I shall focus on cases where Mott insulating phases are only made possible by strong SOC. Since these systems would be either metals or band insulators in the low SOC regime, they are referred to as spin-orbit assisted Mott insulators. Consider the regime on the lower right region of the diagram. As U increases, electron band topology ceases to play a leading role as electronic states become more localised. Then, SOC contributes to the physics mainly by lifting the orbital degeneracy of partially filled d -shells. The orbital and spin degrees of freedom become entangled — hence the alternative designation spin-orbit *entangled* Mott insulators — and the Jahn-Teller effect, which favours orbital ordering, can be avoided. In some transition metal oxides, the degeneracy is fully lifted, resulting in strongly anisotropic exchange interactions that

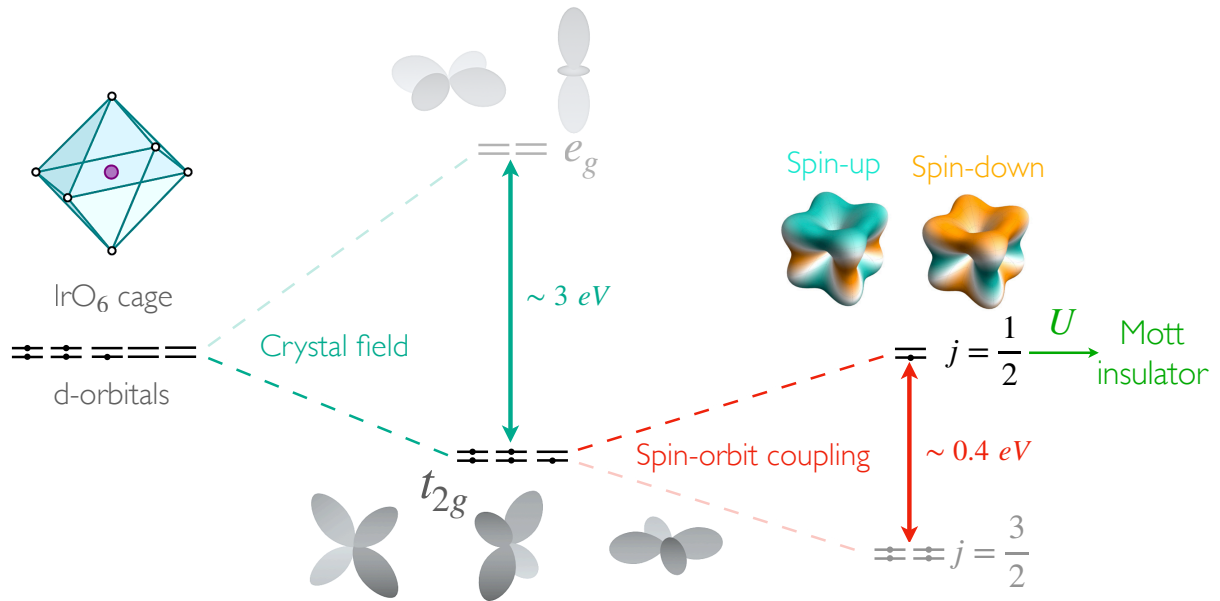


Figure 1.4: Formation of spin-orbit entangled local moments. Adapted from [50], [54] and [55].

promote large quantum fluctuations. This mechanism [127] was proposed to design spin models hosting QSL phases in honeycomb iridates, such as Na_2IrO_3 and $\alpha\text{-Li}_2\text{IrO}_3$, but also other compounds, *e.g.* $\text{H}_3\text{LiIr}_2\text{O}_6$, $\text{Cu}_3\text{LiIr}_2\text{O}_6$, $\text{H}_3\text{NaIr}_2\text{O}_6$ and $\alpha\text{-RuCl}_3$ [55].

The peculiar bond-directional spin interaction in the Kitaev model appears as a result of an accidental conjugation of electronic correlations and spin-orbit coupling along with crystal field effects [50]. In honeycomb iridates, for each IrO_6 cage (see left hand side of Figure 1.4), an octahedral crystal field splits the atomic states of partially filled $4d$ or $5d$ ions into a triplet, t_{2g} , and a doublet, e_g . The crystal field splitting is large compared with other energy scales, so the doublet is neglected, provided that the electron filling is less than six. I shall consider electronic configurations of the type d^5 , so that there is a single hole in t_{2g} .

By projecting the angular momentum of the d electrons onto the manifold of t_{2g} states, one obtains a set of $l = 1$ angular momentum operators. SOC acting upon the t_{2g} states splits them once again. Adding the orbital angular momentum to the electronic spin, one obtains a $j = 3/2$ quartet and a $j = 1/2$ doublet (see right hand side of Figure 1.4). For strong electron correlations ($U \gg t$), holes (unoccupied levels) are approximately localised on each lattice site

and the local spin-orbit entangled moments are pseudo-spin-1/2 variables, S_i [52, 142]. This is because the general multi-orbital model — gathering terms of the type of Equations 1.1-1.5 — reduces to a pseudo-spin model in the strongly correlated regime, similarly to the strong coupling limit of the Hubbard model, which is known to be a Heisenberg model.

In fact, there are no symmetry constraints that prohibit non-Kitaev interactions, *e.g.* Heisenberg exchange. The mechanism proposed by Jackeli and Khaliullin [127] puts forward a 90° bonding geometry — where neighbouring IrO_6 octahedra share an edge (see Figure 1.5) — as a pathway to achieve dominance of the Kitaev term over other possible interactions. The two possible $\text{Ir} - \text{O} - \text{Ir}$ exchange paths interfere destructively and the symmetric Heisenberg exchange that they favour for $j = 1/2$ is suppressed. A more careful analysis of the multi-orbital model reveals that virtual exchange processes involving the $j = 3/2$ bands enable the preservation of a residual Heisenberg exchange. The main contribution to the effective spin model comes from a bond-directional coupling arising from a Hund term similar to Equation 1.3, coupling via the multiplet structure of the excited levels. This is the so called Kitaev interaction, which couples the pseudo-spin degrees of freedom via a bond-dependent Ising interaction

$$-\frac{8t_O^2 J}{3U^2} S_1^\gamma S_2^\gamma, \quad (1.6)$$

with varying magnetic easy-axis, $\gamma = x, y, z$, perpendicular to the plane spanned by the two exchange paths (represented by dashed lines in Figure 1.5). Here, t_O is the hopping term mediated by the oxygen ions and $S_{1,2}$ are the pseudo-spin operators on two neighbouring sites of the honeycomb lattice (see left panel of Figure 1.6). Sites on the lattice are occupied by localised pseudo-spins corresponding to the neighbouring octahedra and generated via the aforementioned mechanism (see right panel of Figure 1.6).

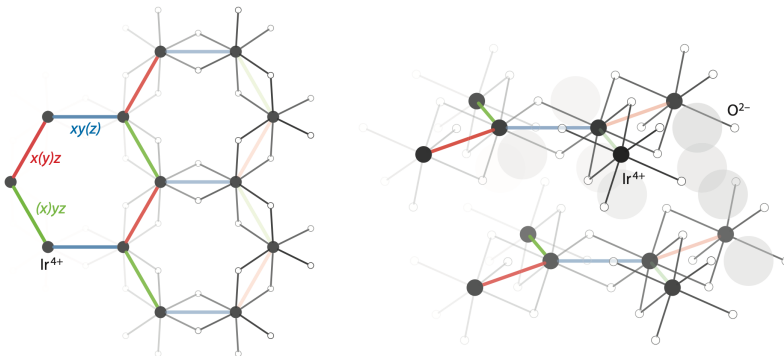


Figure 1.6: Honeycomb plane (left) and iridate unit cell (right). In the left panel, the bond-directional character of the Kitaev interaction is represented by the colours red, green and blue, with the parenthesis singling out the relevant component of the spin operator. The right panel illustrates how this two-dimensional honeycomb lattice arises within the structure of iridates. Take A_2IrO_3 , with $\text{A} = \text{Na}, \text{Li}$. Then, the shaded grey circles represent either sodium or lithium ions, A^+ . Source: [50].

Most materials thought to realise Kitaev interactions order mag-

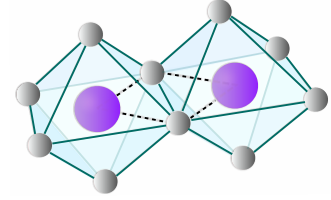


Figure 1.5: Edge-sharing octahedra.

[58]: Kitagawa et al. (2018), ‘A spin–orbital-entangled quantum liquid on a honeycomb lattice’

[8]: Nasu et al. (2015), ‘Thermal fractionalization of quantum spins in a Kitaev model’

[143]: Nasu et al. (2016), ‘Fermionic response from fractionalization in an insulating two-dimensional magnet’

[144]: Anderson (1973), ‘Resonating valence bonds’

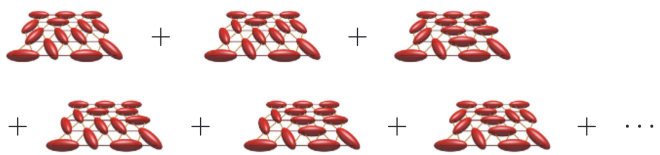
4: A noncollinear 120° ordered phase is a prominent candidate for the ground state, but this controversial matter is still under discussion (see *e.g.* [145]).

Figure 1.7: Resonating valence bond state. Each ellipsoid represents the state $(|\uparrow\downarrow\rangle - |\downarrow\uparrow\rangle)/\sqrt{2}$. Each state comprising the sum is constructed using a tensor product of these singlets.

netically at low temperature. Despite the relative strength of these bond-directional interactions, QSL phases are elusive and rarely stabilised [58]. Thus, normally the signs of the phase are detected indirectly, *e.g.* by looking for evidence of spin fractionalisation at finite temperature [8], or proximate spin liquid behaviour [143].

1.2.2 Quantum spin liquids

Anderson coined the term ‘quantum liquid’ in a quest to shed light on the ground state of the frustrated spin-1/2 Heisenberg antiferromagnet on the triangular lattice [144]. Anderson put forward a ‘resonating valence bond’ (RVB) state, comprised of a quantum superposition of different pairings of spins into singlets, as a lower energy alternative ground state compared to the Néel state. The RVB state, illustrated in Figure 1.7, turned out not to be the correct description of the system⁴. Instead, it sowed the seed for the search of a new class of quantum disordered ground states of spin systems; for a survey of the properties defining quantum spin liquids in the modern sense, candidate materials and technical details, see Reference [51].

$$|\text{RVB}\rangle = \begin{array}{ccccccc} \text{[Diagram 1]} & + & \text{[Diagram 2]} & + & \text{[Diagram 3]} & + & \dots \\ \text{[Diagram 4]} & + & \text{[Diagram 5]} & + & \text{[Diagram 6]} & + & \dots \end{array}$$


Broadly speaking, QSLs are a unique phase of matter with exotic properties, such as long-range entanglement and spin fractionalisation. They are magnetic insulators, where spins fluctuate strongly even at zero temperature. Despite the absence of conventional symmetry breaking preventing magnetic order from setting in, the ground state is nontrivial [53] due to high correlations stemming from quantum spin interactions. In QSLs, the description of the ground state of the quantum magnet emerges as the decomposition of the basic degrees of freedom, *e.g.* the local moments of the previous section, into fractionalised quantum particles, or partons, coupled to a gauge field. QSLs can then be classified in terms of the symmetry of the gauge field. For example, in the next section, I will discuss a \mathbb{Z}_2 QSL.

Before I move on, I briefly discuss the experimental realisation and characterisation of QSLs. Highly-entangled quantum matter is scarce and lacking in unambiguous experimental signatures due to the difficulty in probing nonlocal features and measuring degree of entanglement. Still, traditional procedures, such as neutron scattering [146–149], nuclear magnetic resonance [150, 151] and x-ray scattering [152, 153] have had some degree of success in probing

Kitaev magnets, despite being optimised to detect order and local — rather than nonlocal — excitations. Measurements of specific heat and magnetic susceptibility could also provide support for the existence of QSLs [58], but they do not give smoking-gun evidence. To complicate matters further, many materials that are thought to realise — or nearly realise — QSLs actually show signs of magnetic ordering at very low temperatures. Thus, the definition of a ‘candidate’ material encompasses proximate liquids, which are thought to be described by a Hamiltonian that includes Kitaev interactions. The relative strength of the other interactions can be estimated in order to quantify the degree of proximity to the QSL phase, and even potentially be tuned to bring one closer to the QSL phase. As a rule of thumb, the main ingredients for a potential QSL are frustration, small spin (I only consider spin-1/2 here) and proximity to a Mott transition [51], all of which are present in the spin-orbit entangled Mott insulators, on which I focus from now on.

1.2.3 Honeycomb Kitaev model

The honeycomb Kitaev model is the paradigmatic example of a quantum spin model hosting a \mathbb{Z}_2 QSL. The Hamiltonian consists of nearest neighbouring spin-1/2 moments interacting via a strongly anisotropic Ising exchange (represented in Figure 1.8):

$$\hat{H}_{\text{Kitaev}} = - \sum_{\langle i,j \rangle^\gamma} K_\gamma \hat{\sigma}_i^\gamma \hat{\sigma}_j^\gamma, \quad (1.7)$$

where $\gamma = x, y, z$ refers to both the magnetic easy axes and the type of bond on the honeycomb lattice⁵. K_γ are potentially non-uniform exchange couplings, and $\hat{\sigma}_i^\gamma$ are the Pauli operators on the lattice sites, i . Kitaev interactions between neighbouring spins cannot be minimised simultaneously, leading to *exchange frustration*, and driving the system into a QSL phase with no magnetic order and residual ground-state entropy. Shortly, I will show that when a particular coupling constant dominates, one obtains a gapped QSL. Around the isotropic point, there is an extended QSL gapless phase, with itinerant fermions forming a Majorana metal.

Interestingly, in the classical Kitaev model, exchange frustration produces a large number of degenerate ground states, which grows exponentially with the number of spins [154]. There is no finite temperature phase transition; instead, there is a thermal crossover to a macroscopically degenerate Coulomb phase [155], which is depicted in Figure 1.10. This phase differentiates itself from the high-temperature paramagnet through an emergent magnetostatic description of its excitations. The extensive degeneracy is lifted for

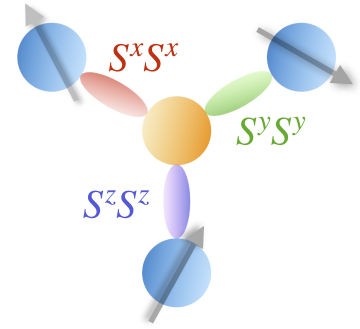


Figure 1.8: Kitaev interaction. Nearest neighbour bonds coloured in red, green and purple (respectively $\gamma = x, y, z$ in the cartoon). The bond-directional character of the Kitaev interaction implies that to each bond corresponds a different type of interaction. Similarly to the case of the Ising model on the triangular lattice, where one has geometrical frustration, here one has exchange frustration due to the nature of the interaction and it is not possible to find a spin configuration that simultaneously minimises the energy on all bonds.

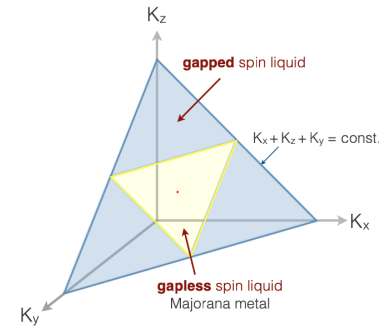


Figure 1.9: Phase diagram of the Kitaev model. Considering a fixed energy scale $K_x + K_y + K_z = 1$ corresponds to the plane shown on the figure. Three gapped phases appear, with a gapless phase around the isotropic point. Source: [55].

5: The Kitaev model can be extended to any tricoordinate lattice. In fact, the lattice need not even be two-dimensional.

[154]: Baskaran et al. (2008), ‘Spin-S Kitaev model’

[155]: Henley (2010), ‘The “Coulomb Phase” in Frustrated Systems’

[54]: Motome et al. (2020), ‘Hunting Majorana Fermions in Kitaev Magnets’

[156]: Pavarini et al. (2023), *Orbital Physics in Correlated Matter*

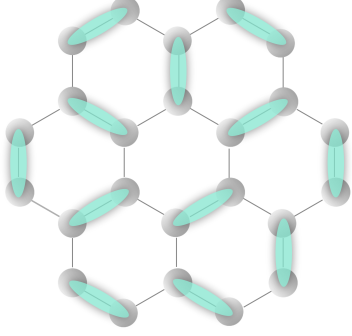


Figure 1.10: Depiction of the Coulomb phase: a dimer covering of the honeycomb lattice representing one of the possible ground states of the classical Kitaev model. Each dimer corresponds to a pairing of two spins pointing along one of the three principal axes. This configuration satisfies only one of the three interaction terms for every spin.

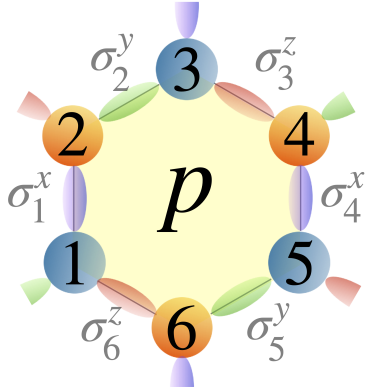


Figure 1.11: Representation of the flux, W_p for plaquette p .

quantum spins, and a QSL is stabilised, whose highly entangled nature endows it with additional structure compared with the high-temperature paramagnet [54, 156].

Define plaquette operators

$$\hat{W}_p = \sigma_1^x \sigma_2^y \sigma_3^z \sigma_4^x \sigma_5^y \sigma_6^z, \quad (1.8)$$

which commute with the Hamiltonian, thus representing constants of motion. The product of exchange terms is taken over a plaquette, p , which is shown in Figure 1.11. Each site on the plaquette is labeled with a number from 1 to 6. By performing the product of these operators over all plaquettes, one recovers the identity operator

$$\prod_p \hat{W}_p = I. \quad (1.9)$$

Since the lattice is bipartite, there is always an even number of bonds. Thus, the plaquette operator has eigenvalues ± 1 . The eigenvalue $w_p = 1$ corresponds to a state of zero flux, while the eigenvalue $w_p = -1$ corresponds to a π -flux state.

There is a macroscopically large number of conserved quantities. In fact, all plaquette operators commute with each other and with the Hamiltonian. This implies that the problem may be simplified by restricting it to a given flux sector. In general, the ground state flux sector is not known analytically. However, a theorem due to Lieb gives a widely applicable condition for the flux of the ground state, implying that the flux-free sector contains the ground state. The solution of the Kitaev model on the honeycomb lattice is based on representing the spin degrees of freedom

$$\hat{d}_j^\alpha = i b_j^\alpha c_j, \quad (1.10)$$

using four Majorana operators obeying the anticommutation relations

$$\begin{aligned} \{b_j^\alpha, b_k^\beta\} &= 2\delta_{j,k}\delta_{\alpha,\beta} \\ \{c_j, c_k\} &= 2\delta_{j,k} \\ \{b_j^\alpha, c_k\} &= 0, \end{aligned} \quad (1.11)$$

where j, k are site indices and α, β are spin components.

For each spin, the extended Hilbert space is now four-dimensional instead of two-dimensional. Still, the physical Hilbert space may be recovered by requiring that the spin algebra remains valid and using the projection operator $\hat{P}_i = \frac{1}{2}(1 + b_i^x b_i^y b_i^z c_i)$, which projects generic states onto the local physical Hilbert space.

In terms of the Majorana operators, the interaction term becomes quartic:

$$\sigma_i^\gamma \sigma_j^\gamma = -(ib_i^\gamma b_j^\gamma) ic_i c_j \equiv -i\hat{u}_{i,j} c_i c_j. \quad (1.12)$$

Luckily, the bilinear operators $\hat{u}_{i,j}$ commute with each other as well as with any bilinear operator containing the c -operators, so they can be replaced by their eigenvalues ± 1 . I will now prove that the Kitaev model of Equation 1.7 may be reduced to non-interacting itinerant Majorana fermions in a static background \mathbb{Z}_2 gauge field, which is the emerging structure I sought.

The operators \hat{u}_{ij} satisfy the following relations: $\hat{u}_{ij} = -\hat{u}_{ji}$, $\hat{u}_{ij}^2 = 1$, $\hat{u}_{ij}^\dagger = \hat{u}_{ji}$. In terms of them, the Kitaev interaction becomes $\sigma_i^\gamma \sigma_j^\gamma = -i\hat{u}_{ij} c_i c_j$. Consequently, the Hamiltonian reads

$$\hat{H} = \frac{i}{4} \sum_{\langle i,j \rangle} \hat{A}_{ij} c_i c_j, \text{ where } \hat{A}_{ij} = 2K_{ij} \hat{u}_{ij}, \quad (1.13)$$

and the couplings $K_{ij} = K_x, K_y, K_z$ depend on whether the link is a x -, y - or z -bond. Notice that the plaquette operators can be written in terms of the \hat{u} operators:

$$\hat{W}_p = \prod_{i,j \in \text{plaquette}} \hat{u}_{ij}. \quad (1.14)$$

It is possible to show that $[\hat{H}, \hat{u}_{ij}] = 0$, which implies that after fermionisation of the spins, the vortex configuration can be fixed by specifying the eigenvalues $u_{ij} = \pm 1$ for every link i, j . When $u_{ij} = -1$, the link i, j either connects two vortices or is contained within a loop. A vortex is said to be located at plaquette p if the eigenvalue of the plaquette operator is $w_p = -1$.

The flux-free ground state admits two distinct types of excitations: those of the itinerant Majorana fermions and those of the \mathbb{Z}_2 fluxes. These quasiparticle excitations are a consequence of spin fractionalisation. The dispersion relation of the itinerant Majorana fermions is familiar from graphene-like systems with a Dirac cone:

$$E(\mathbf{k}) = \pm 2 \left| K_x \exp(i\mathbf{k} \cdot \mathbf{a}_1) + K_y \exp(i\mathbf{k} \cdot \mathbf{a}_2) + K_z \right|, \quad (1.15)$$

with $\mathbf{a}_1 = (1/2, \sqrt{3}/2)$ and $\mathbf{a}_2 = (-1/2, \sqrt{3}/2)$, *i.e.* the primitive translation vectors of the honeycomb lattice.

The flux excitations are generated by flipping W_p , driving the system away from the flux-free ground state. The localised nature of the plaquette operator is associated with gapped flux excitations.

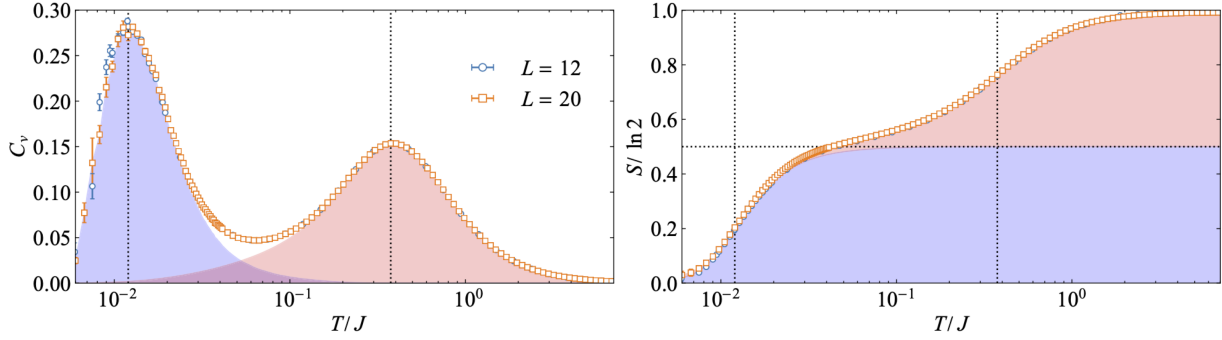


Figure 1.12: Thermal fractionalisation in the pure Kitaev model. Temperature dependence of the specific heat (left panel) and entropy density (right panel), obtained by Majorana-based Monte Carlo simulation of clusters with size $N = 2L^2$. The shaded red area represents a fermionic contribution, while the blue area represents a gauge field contribution. Source: [54].

[8]: Nasu et al. (2015), ‘Thermal fractionalization of quantum spins in a Kitaev model’

The first excited state is obtained by flipping the flux of two neighbouring plaquettes. The difference between the energy scales of the two excitations — dispersive modes of itinerant Majorana fermions that can be either gapped or gapless, and dispersionless, gapped flux excitations — is more than one order of magnitude [54], and it affects the thermodynamics and spin dynamics. Thus, signatures of spin fractionalisation can be found, for example in the specific heat [8].

The two energy scales of the excitations appear as two characteristic temperatures. The higher one, T_H , is associated with the itinerant Majorana fermions and is set by the center of mass of the fermionic density of states. As T_H is approached, there is a crossover that does not depend strongly on dimensionality or details of the model [54]. In contrast, the lower temperature, T_L , can mark either a crossover or a phase transition, depending on the nature of the flux excitations that it is associated with. In the interval $T_L \lesssim T \lesssim T_H$, the system is said to be in an unconventional state called fractional paramagnet. Below T_L , the state asymptotically approaches a QSL. For the Kitaev model, this behaviour is accompanied by a two-peak structure of the specific heat (with peaks at T_H and T_L) and a two-stage release of the entropy density. From the latter, one infers that the original spin carrying an entropy of $k_B \ln 2$ fractionalises into two types of quasiparticles, each carrying half of that entropy. In Reference [8], the authors track spin fractionalisation carefully, tracing the contributions to each peak/step back to either the Majorana fermions or the localised fluxes. Their results are shown in Figure 1.12. The Fermi degeneracy of the itinerant Majorana fermions sets in as the temperature is decreased past T_H , with the fluxes remaining disordered. The resulting fractionalised paramagnet eventually reaches T_L , at which point the flux-free configuration is approached asymptotically.

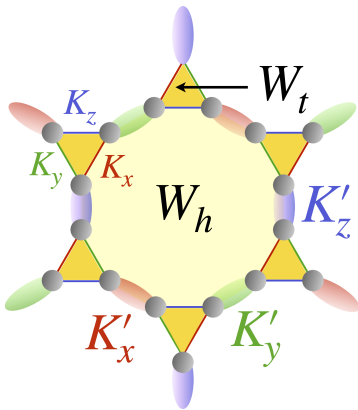


Figure 1.13: Decorated triangle-honeycomb structure.

To close this section, I remark that in Reference [157], the authors

have reported a multi-stage release of entropy, corresponding to multiple peaks of the specific heat in a generalisation of the Kitaev model for the triangle-honeycomb lattice depicted in Figure 1.13. The latter is a decorated version of the honeycomb lattice, where each site is extended to a triangle, and Kitaev interactions occur both within the triangles and between vertices neighbouring other triangles. The interpretation for the peculiar thermodynamical behaviour is given in terms of the flux excitations, which align coherently, or freeze, for the different polygons appearing in the lattice at different temperatures (a dodecagon, or 12-gon, and a triangle). Unfortunately, not all peaks/steps can be resolved as they appear at an extremely low temperature, which is inaccessible to the Monte Carlo approach followed by the authors. The results for the specific heat and entropy are shown in Figure 1.14.

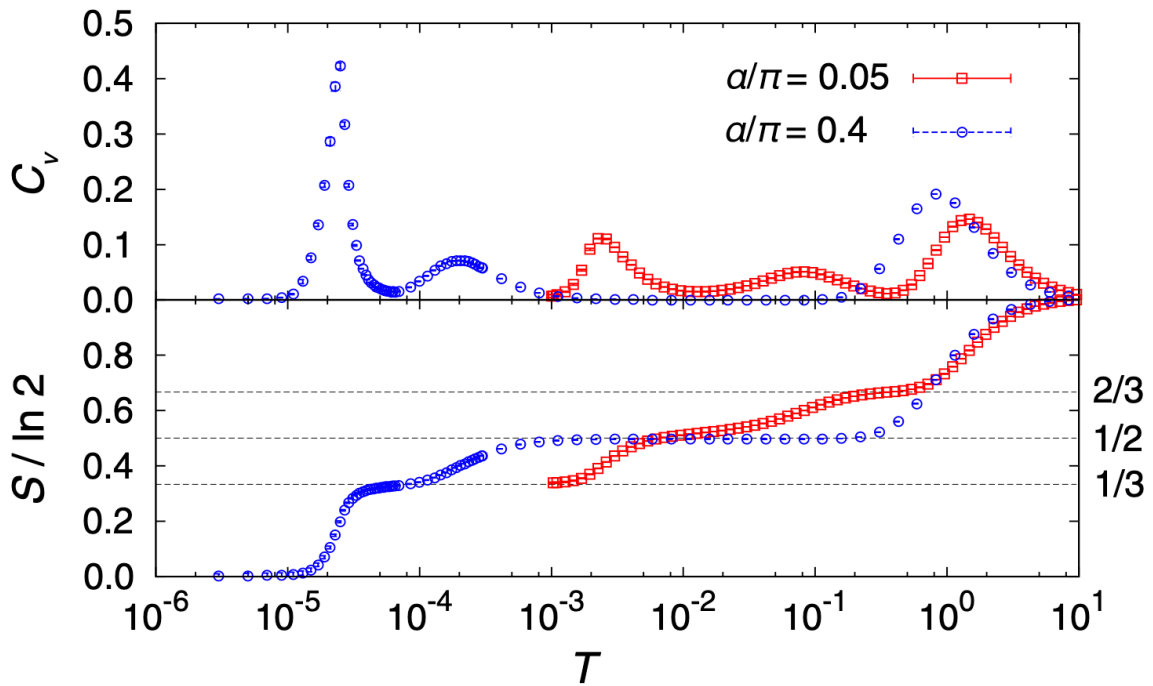


Figure 1.14: Thermal fractionalisation for the triangle-honeycomb Kitaev model. Temperature dependence of the specific heat (top panel) and entropy density (bottom panel). The Kitaev interactions $K_\gamma = K$ and $K'_\gamma = K'$, $\forall \gamma \in \{x, y, z\}$ are parametrised as follows: $K = \cos \alpha$, $K' = \sin \alpha$. Source: [157].

The Chebyshev-based methods I introduce in the next chapter can be used more broadly in the sense that they can access very low temperatures and also other models beyond the Kitaev model, for which a Monte Carlo approach is not feasible. The next section gives an overview of the physics beyond the Kitaev model.

[50]: Rau et al. (2016), ‘Spin-Orbit Physics Giving Rise to Novel Phases in Correlated Systems’

[54]: Motome et al. (2020), ‘Hunting Majorana Fermions in Kitaev Magnets’

[142]: Winter et al. (2016), ‘Challenges in design of Kitaev materials’

[158]: Yamaji et al. (2016), ‘Clues and criteria for designing a Kitaev spin liquid revealed by thermal and spin excitations of the honeycomb iridate Na_2IrO_3 ’

[50]: Rau et al. (2016), ‘Spin-Orbit Physics Giving Rise to Novel Phases in Correlated Systems’

[52]: Winter et al. (2017), ‘Models and materials for generalized Kitaev magnetism’

[57]: Rau et al. (2014), ‘Generic Spin Model for the Honeycomb Iridates beyond the Kitaev Limit’

1.2.4 Generalised Kitaev models

A very general model with nearest neighbour interactions attempting a realistic description of spin-orbit assisted Mott insulators, sometimes called $JK\Gamma$ -model, is given below [50, 54, 142, 158]:

$$\hat{H} = \sum_{\langle i,j \rangle'} \left[J \mathbf{S}_i \cdot \mathbf{S}_j + K S_i^\gamma S_j^\gamma + \Gamma (S_i^\alpha S_j^\beta + S_i^\beta S_j^\alpha) \right], \quad (1.16)$$

where J is the Heisenberg exchange coupling and Γ is the strength of a symmetric off-diagonal bond-directional exchange, coupling the two orthogonal spin components $\alpha, \beta \perp \gamma$ for each bond. These are all the microscopic interactions allowed by symmetry [50, 52]. Yet, in materials with trigonal distortion, *i.e.* nonideal octahedra, there is an additional interaction with strength Γ' , which couples the γ -component of the spin with each of the orthogonal ones α, β . Anisotropies and suppression of these terms can also occur. For example, the Heisenberg term may be reduced to an Ising term in certain cases by suppression of interactions involving two of the spin components.

Even though the relative strengths of the different coupling constants may vary from material to material, for Kitaev magnets, the Kitaev term remains dominant, *i.e.* $|K| > |J|, |\Gamma|$. In this thesis, I shall consider two variations of this Hamiltonian, both with $\Gamma = \Gamma' = 0$: the Kitaev-Heisenberg (K-H) model, for which an isotropic Heisenberg interaction is considered, and the Kitaev-Ising (K-I) model, for which only an Ising interaction between a single component of the spins, say S^z , is considered.

The phase diagram of the generic spin model with $\Gamma' = 0$ is studied using ED for a 24-site cluster in Reference [57]. An energy scale is fixed, $\sqrt{J^2 + K^2 + \Gamma^2} = 1$, and the exchanges are parametrised so as to sweep the all possible combinations of parameters: $J = \sin \theta \cos \phi$, $K = \sin \theta \sin \phi$, $\Gamma = \cos \theta$. The cases $\Gamma > 0$ and $\Gamma < 0$ are treated separately and the respective phase diagrams are shown in panels a) and b) of Figure 1.15.

The phase boundaries are determined by computing the second derivatives of the ground state energy with respect to the model parameters, $-\partial^2 E / \partial \phi^2$ and $-\partial^2 E / \partial \theta^2$. Singular features in these functions indicate quantum phase transitions. The nature of the phases is identified via the static structure factor

$$S_{\mathbf{q}} = \frac{1}{N} \sum_{i,j} e^{i\mathbf{q} \cdot (\mathbf{R}_i - \mathbf{R}_j)} \langle \hat{S}_i \cdot \hat{S}_j \rangle, \quad (1.17)$$

where the sum is over all sites i, j on the lattice, \mathbf{q} determines the periodicity of the magnetic ordering and $\mathbf{R}_{i,j}$ are the positions of

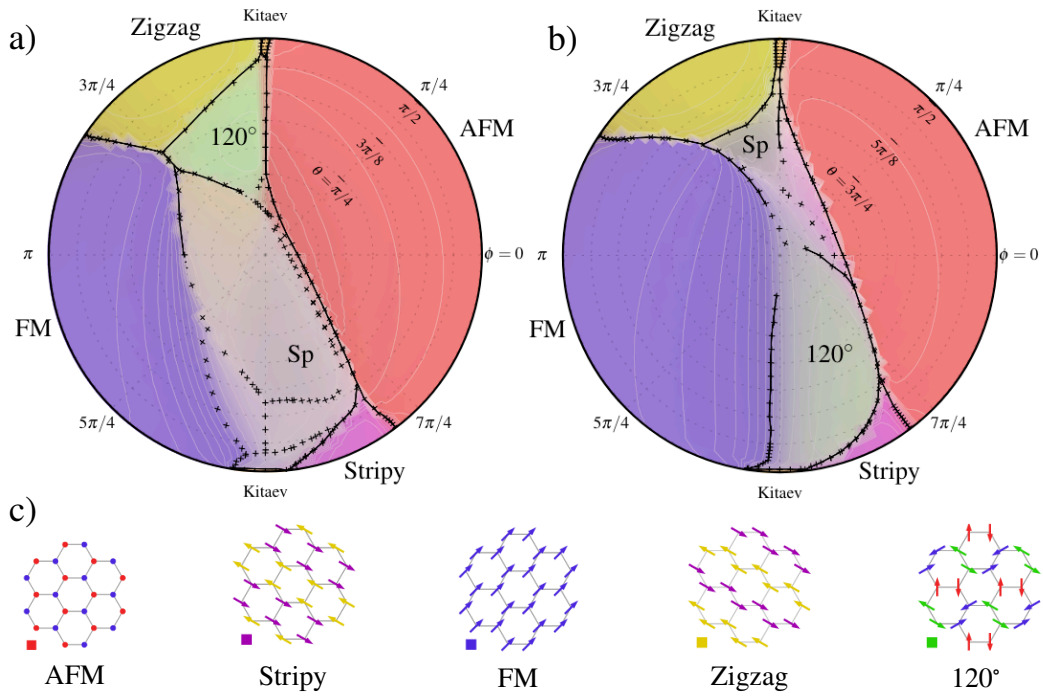


Figure 1.15: Phase diagram of the generic JKT Hamiltonian for spin-orbit assisted Mott insulators. ‘SP’ stands for spiral order. Here, the periodicity of spiral order is the longest allowed by the cluster size. The other phases are illustrated schematically. a) $\Gamma > 0$. b) $\Gamma < 0$. c) Ground state spin configuration in each phase. Source: [57]

the sites on the lattice. The types of magnetic ordering in the phase diagram are summarised in panel c) of Figure 1.15.

The K-H model that is studied in this thesis corresponds to the boundary of the two circles shown in panels a) and b) of Figure 1.15. QSL phases appear both on the top and on the bottom of the diagram, corresponding to antiferromagnetic and ferromagnetic Kitaev couplings, respectively. Other than the Kitaev spin liquids, the model hosts four types of magnetic order: ferro- and antiferromagnetic ordering around the purely Heisenberg points and two other ordered phases, originating from the so called Klein duality [159]. The latter maps the ferromagnet to the stripy phase and the antiferromagnet to the zigzag phase, via a four-sublattice rotation of the spins [3, 4].

Notice that the Kitaev spin liquid phases are restricted to narrow regions of the phase diagram around the exactly solvable points. Fortunately, signatures of spin liquid physics survive thermal fluctuations. The terminology *proximate spin liquid* has been introduced to refer to materials that order magnetically at some low temperature. Above this temperature, they display evidence of a QSL near their position on the phase diagram and are said to be in an

[159]: Kimchi et al. (2014), ‘Kitaev-Heisenberg models for iridates on the triangular, hyperkagome, kagome, fcc, and pyrochlore lattices’

[3]: Chaloupka et al. (2010), ‘Kitaev-Heisenberg Model on a Honeycomb Lattice’

[4]: Chaloupka et al. (2013), ‘Zigzag Magnetic Order in the Iridium Oxide Na_2IrO_3 ’

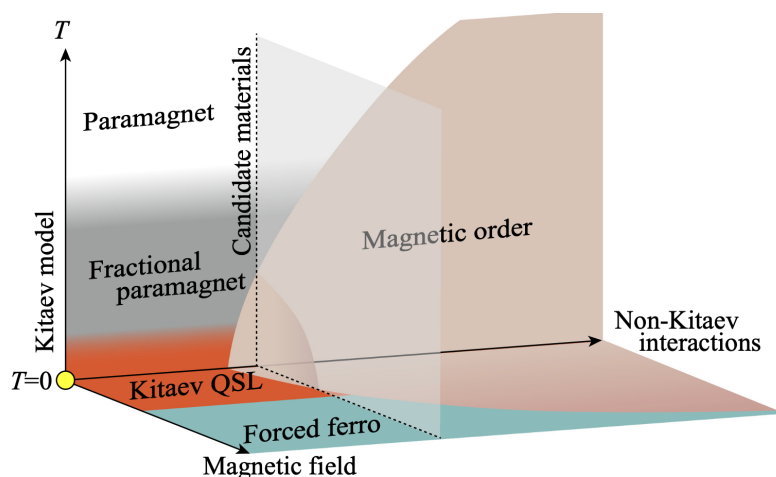


Figure 1.16: Schematic phase diagram of candidate QSL materials with ferromagnetic Kitaev interactions. Source: [54].

intermediate phase, often referred to as a fractional paramagnet. Figure 1.16 shows a schematic phase diagram for ferromagnetic Kitaev interactions, where the fractional paramagnetic phase is represented in grey. By slightly decreasing both the temperature and the non-Kitaev interactions, this intermediate phase seamlessly coalesces into the QSL phase, shown in red. At finite temperature, the latter is described by itinerant Majorana fermions in a disordered flux sector. As the temperature is increased, one finds the aforementioned crossover into the fractional paramagnet, which, in turn crosses over into a featureless paramagnet. The diagram of Figure 1.16 also allows for a small window of QSL behaviour upon increasing the magnetic field, which suppresses magnetic order. Eventually, the field forces the system into a ferromagnet regime. However, evidence from inelastic neutron scattering [160] in the form of spin excitations for varying magnetic field suggests that there might be an intermediate regime without any contribution from magnon excitations, which could correspond to a QSL.

[160]: Banerjee et al. (2018), ‘Excitations in the field-induced quantum spin liquid state of α – RuCl_3 ’

In the following chapters, the intricacies of emergent magnetism and QSL behaviour in strongly correlated matter are captured using a variety of numerical methods, well suited for quantum many-body systems, whose nature demands remarkably precise and robust approaches. Among the requirements for these methods are: the ability to pinpoint quantum criticality and to maintain numerical stability in the whole gamut of the range of parameters, *e.g.* very low temperatures, or very strong correlations.

Methods 2

Exact solutions of interacting quantum condensed matter models beyond one dimension are elusive. A well-known example of an exactly solvable one-dimensional model is the isotropic Heisenberg chain [12]. It took 37 years for the same pioneering technique used for the latter to be applied in the solution of the one-dimensional Hubbard model [161]. Although these are undoubtedly important examples, they are by no means the *only* examples. In fact, comprehensive lists of other examples have even been compiled, *e.g.* References [162, 163]. In contrast, there are only a few examples of exactly solvable interacting quantum models in two dimensions, *e.g.* References [56, 164, 165]. While the importance of these exact solutions cannot be overstated, in general, analytical calculations tend to rely on restrictive assumptions and approximations only justifiable for specific classes of systems.

The broad intractability of model Hamiltonians for many-body systems in dimensions larger than one demands a numerical approach. On the one hand, computational studies provide a testing ground for novel theories and analytical calculations. On the other hand, numerical simulations constitute a laboratory in themselves, in the sense that they create an opportunity to discover otherwise inaccessible phenomena. This is a consequence of the fact that the computational approach allows the exploration of more complex models than the analytical approach. For this reason, numerical results frequently inspire both theoretical and experimental developments.

The remainder of this chapter is organised as follows. In Section 2.1, I present an overview of the basic concepts of Monte Carlo methods in statistical physics, illustrating the ideas with the example of the classical Ising chain. Then, I review the main aspects of the DetQMC method that is used to study the intra-orbital Hubbard model of Equation 1.1 for zTMDNRs in Chapter 3. The following sections are devoted to a toolset of Chebyshev polynomial-based iterative methods developed in this work. These provide a unified framework to study the thermodynamical properties, critical behaviour and dynamics of frustrated quantum spin models with controlled accuracy. Similar to previous applications of the Chebyshev spectral methods to condensed matter systems, the algorithmic complexity scales linearly with the Hilbert space dimension and the Chebyshev truncation order.

In Section 2.3, I summarise the key concepts behind the Chebyshev

2.1	Classical Monte Carlo method	22
2.2	Determinant quantum Monte Carlo	25
2.3	Chebyshev spectral methods: rationale . .	29
2.4	Vector recursions and bit representation of the Hamiltonian	31
2.5	Lanczos exact diagonalisation	36
2.6	Kernel polynomial method	39
2.7	Microcanonical ensemble	50
2.8	Canonical ensemble .	58
2.9	Dynamical properties	64

[12]: Bethe (1931), ‘Zur Theorie der Metalle’

[161]: Lieb et al. (1968), ‘Absence of Mott Transition in an Exact Solution of the Short-Range, One-Band Model in One Dimension’

[162]: Baxter (1985), ‘Exactly Solved Models in Statistical Mechanics’

[163]: Mattis (1993), *The Many-Body Problem*

[56]: Kitaev (2006), ‘Anyons in an exactly solved model and beyond’

[164]: Sriram Shastry et al. (1981), ‘Exact ground state of a quantum mechanical antiferromagnet’

[165]: Affleck et al. (1988), ‘Valence bond ground states in isotropic quantum antiferromagnets’

approach in condensed matter physics and outline important differences with respect to competing methods. All of these methods are based on vector recursions, which are explained in detail in Section 2.4. The bit representation of the Hamiltonian that is used in these recursions is also discussed. Section 2.5 reviews the Lanczos method of exact diagonalisation for low-lying states. In Section 2.6, I review the kernel polynomial method (KPM), which is a competing Chebyshev spectral method. I use this section to establish some ideas concerning Chebyshev expansions. Section 2.7 covers the use of a target energy to probe the core of the spectrum of the Hamiltonian. In particular, the Chebyshev polynomial Green's function method (CPGF) is compared with alternative Lanczos and TPQ approaches. I review the microcanonical Lanczos method (MCLM) (Section 2.7.1), the microcanonical variant of TPQ (Section 2.7.2), and the Chebyshev polynomial Green's function method (CPGF) (Section 2.7.3); In Section 2.8, I present my newly developed finite temperature Chebyshev polynomial (FTCP) method, again in comparison with its Lanczos and TPQ counterparts. First, I review the finite temperature Lanczos method (FTLM) (Section 2.8.1) and the canonical variant of the TPQ (Section 2.8.2), and then I present the novel finite temperature Chebyshev polynomial (FTCP) that I introduce in this work (Section 2.8.3); Finally, in Section 2.9, another one of my newly developed methods is introduced: the hybrid Lanczos-Chebyshev (HLC) method. In Section 2.9.1, a review of the continued fraction Lanczos approach is given and the latter is compared with HLC for the study of spectral functions in Section 2.9.2.

2.1 Classical Monte Carlo method

[166]: Newman et al. (1999), *Monte Carlo Methods in Statistical Physics*

The Monte Carlo method is ubiquitous in statistical physics [166]. It is often employed to investigate collective properties of condensed matter systems with an exponentially large number of possible configurations. Most of these are extremely improbable, with a dramatically narrow subset of configuration space being responsible for the properties of the system. Monte Carlo makes use of *importance sampling* to efficiently draw samples from the target probability distribution, $p(X)$. This variance reduction technique ensures that more probable states are visited more often, effectively simulating the random fluctuations of a system oscillating between states. These fluctuations can be interpreted as thermal and/or quantum fluctuations depending on whether one considers a classical or a quantum model.

Suppose that one is interested in evaluating the expectation of a function of a random variable X , $f(X)$, in the probability distribu-

tion, p . The expected value can be expressed not only in terms of f and p , but also a separate distribution q . If one defines a weight function, w , as the ratio of the two probability distributions, *i.e.* $w(x) = p(x)/q(x)$, one has

$$\mathbb{E}[f(X)] = \int dx f(x)p(x) = \int dx f(x)q(x)w(x) = \mathbb{E}[f(Y)w(Y)], \quad (2.1)$$

where $Y \sim q$, *i.e.* random variable Y follows the q distribution. Notice that the variance obtained when drawing M independent and identically distributed samples from $q(Y)$ is

$$\text{Var}\left(\frac{1}{M} \sum_{k=1}^M f(y_k)w(y_k)\right) = \frac{1}{M} \text{Var}(f(y_1)w(y_1)), \quad (2.2)$$

which is proportional to M^{-1} . Thus, the error of Monte Carlo estimators for expected values scales as the inverse of the square root of the number of samples, $M^{-1/2}$. It is the freedom in the choice of q that can be exploited in importance sampling with the goal of achieving $\text{Var}(f(y_1)w(y_1)) \sim 1$.

The target distribution is sampled using a Markov chain¹ Monte Carlo algorithm. Once enough steps of this algorithm are completed, it starts to generate samples from an arbitrary target stationary distribution. This is guaranteed by the ergodic theorem. If the Markov chain obeys a certain set of conditions², its samples follow a distribution that approaches a target stationary distribution [166], which in this case is chosen to be $p(X)$. One of these conditions—detailed balance—is particularly relevant for the purposes of this thesis. It can be interpreted as introducing time-reversal symmetry in the simulation via the following constraint on the transition probabilities: $P_{\mu \rightarrow \nu}/P_{\nu \rightarrow \mu} = e^{-\beta(E_\nu - E_\mu)}$. This condition can be exploited to achieve importance sampling, *i.e.* maximising the efficiency of the sampling by making sure that one selects the portion of state space containing states that contribute more significantly to the expectation, but without introducing any bias.

Now, I outline the Metropolis-Hastings [167] sampling scheme used in this work. Suppose that one aims to evaluate the average of a given quantity, Q :

$$\langle Q \rangle = \frac{\sum_{\mu=1}^{|\Omega|} Q_\mu e^{-\beta E_\mu}}{\sum_{\mu=1}^{|\Omega|} e^{-\beta E_\mu}}. \quad (2.3)$$

It is not computationally feasible to evaluate it exactly if the state space is exponentially large. Instead, one makes use of Equation

1: A stochastic process with ‘extremely short term memory’, *i.e.* a sequence of events, where the probability of each event depends only on the state obtained before the current state. The distribution is represented by a vector (π_μ) , $\mu = 1, 2, \dots, |\Omega|$, where $|\Omega|$ is the number of possible states in the state space Ω . In turn, the Markov chain is represented by a matrix $\mathbf{P} = [P_{\mu \rightarrow \nu}]$, where each entry contains the probability of a transition from state μ to state ν at any given step.

2: The Markov chain must be irreducible, aperiodic, positive recurrent and satisfy the condition of detailed balance. The latter is defined as $\pi_\mu P_{\mu \rightarrow \nu} = P_{\nu \rightarrow \mu} \pi_\nu \forall \mu, \nu \in \Omega$. In statistical physics, one has $\pi_\mu = Z^{-1} e^{-\beta E_\mu}$, where E_μ is the energy of state μ and $\beta = k_B T$, with k_B being the Boltzmann constant and T the temperature. Z is the partition function.

[167]: Metropolis et al. (1949), ‘The Monte Carlo Method’

3: As $M \rightarrow \infty$, the estimator $Q_M \rightarrow \langle Q \rangle$. Yet, for a fixed number of samples, the accuracy of the estimator depends on the choice of the probabilities π . For example, the uniform distribution $\pi_\mu = 1/|\Omega|$ is a poor choice because most of the visited states have a negligible contribution to the expectation. In that case, achieving acceptable accuracy would imply exponential computational complexity because one would need to have $M \sim |\Omega|$.

2.1 to devise an estimator for the mean, given M samples³:

$$Q_M = \frac{\sum_{i=1}^M Q_i \pi_{\mu_i}^{-1} e^{-\beta E_{\mu_i}}}{\sum_{i=1}^M \pi_{\mu_i}^{-1} e^{-\beta E_{\mu_i}}}, \quad (2.4)$$

where π_μ is the probability of a state $\mu \in \{\mu_1, \mu_2, \dots, \mu_M\}$.

Markov Chain Monte Carlo is used to generate a probability distribution, π , optimised for the accuracy of Monte Carlo estimators with $M \ll |\Omega|$. The Markov process is designed as a ‘proposal-acceptance’ scheme. First, notice that the condition of detailed balance is not affected by the probability to ‘stay at home’, $P_{\mu \rightarrow \mu} \in [0, 1]$. The only constraint it imposes is that any change in $P_{\mu \rightarrow \nu}$ has to be compensated in $P_{\nu \rightarrow \mu}$, in order to guarantee that the ratio is fixed. New states are proposed according to the selection probabilities, $S_{\mu \rightarrow \nu}$, $\mu, \nu \in \Omega$. Then, they are either accepted or rejected with probability $A_{\mu \rightarrow \nu}$. Thus, the entries of the matrix describing the Markov chain are $P_{\mu \rightarrow \nu} = S_{\mu \rightarrow \nu} A_{\mu \rightarrow \nu}$. Ideally, all states are accepted and $S_{\mu \rightarrow \nu}$ contains all the information about the dependence of $P_{\mu \rightarrow \nu}$ on the states μ, ν . This is not possible because it is equivalent to knowing the solution of the problem *a priori*. In practice, the Metropolis-Hastings algorithm ensures that the acceptance ratio approaches unity. The selection probability is chosen to be uniform and the acceptance ratios are constrained by detailed balance:

$$\frac{P_{\mu \rightarrow \nu}}{P_{\nu \rightarrow \mu}} = \frac{A_{\mu \rightarrow \nu}}{A_{\nu \rightarrow \mu}} = e^{-\beta(E_\nu - E_\mu)}. \quad (2.5)$$

If $E_\mu < E_\nu$, $A_{\nu \rightarrow \mu} > A_{\mu \rightarrow \nu}$ and since only the ratio is fixed, one may freely set $A_{\nu \rightarrow \mu} = 1$, which implies that $A_{\mu \rightarrow \nu} = e^{-\beta(E_\nu - E_\mu)}$ for detailed balance to hold. If $E_\mu > E_\nu$, a similar argument gives $A_{\mu \rightarrow \nu} = 1$. This choice is optimal for optimising the accuracy of the estimator of Equation 2.4 [167]. Below, I outline the sampling scheme.

[167]: Metropolis et al. (1949), ‘The Monte Carlo Method’

Initialisation Start with a random initial state.

Propose new state Pick another state at random (the selection probability is uniform).

Accept or reject Accept the new state with probability $A_{\mu \rightarrow \nu} = \min(1, e^{-\beta(E_\nu - E_\mu)})$. If it gets rejected, propose another state chosen at random.

This scheme only samples from the correct distribution once the Markov chain reaches its stationary distribution. The number of steps of the algorithm required for correct sampling is known as equilibration time, τ_{eq} and is measured in steps of the algorithm. Given a lattice model with a discrete set of states at each site

$i = 1, 2, \dots, N$, one typically uses the number of ‘warm-up’ sweeps instead, $W \sim \tau_{\text{eq}}/N$.

For concreteness, consider an Ising chain ⁴ of N binary classical spins, $s_i = \pm 1$. The dimension of the state space is exponentially large ($D = 2^N$). To simulate this model with Monte Carlo, configurations are typically sampled using single-spin-flip dynamics, *i.e.* new states in the Metropolis-Hastings algorithm are proposed by flipping a single spin of the configuration at any given point. A sweep of the lattice is completed when a flip of every spin on the lattice is proposed. Although this strategy is efficient from the computational point of view, consecutive configurations are not truly chosen at random. Instead, they are heavily correlated. In order to estimate how many sweeps are required for samples to become uncorrelated, one must choose a representative quantity. An obvious choice for the Ising chain is the magnetisation per site, $m = \sum_i s_i/N$. Then, one studies the time-displaced self-correlator

$$\begin{aligned} \chi_m(t) = & \frac{1}{t_{\text{max}} - t} \sum_{t'}^{t_{\text{max}}-t} m(t')m(t' + t) \\ & - \left(\frac{1}{t_{\text{max}} - t} \sum_{t'}^{t_{\text{max}}} m(t') \right) \left(\frac{1}{t_{\text{max}} - t} \sum_{t'}^{t_{\text{max}}} m(t' + t) \right), \end{aligned} \quad (2.7)$$

which has exponentially vanishing long-time behaviour, $\chi_m(t) \sim e^{-t/\tau_c}$, where τ_c is the correlation time, in simulation steps. Here, it is assumed that after A sweeps, corresponding to $2\tau_c$, samples are virtually uncorrelated.

2.2 Determinant quantum Monte Carlo

This section contains a brief description of the implementation of the DetQMC method used in this work ⁵. A thorough discussion of all the technical details can be found in Reference [168]. I focus on the aspects that are most relevant for this thesis. In particular, I provide details on how to write the spin correlation operator in terms of the Green’s functions, which are the main object of DetQMC simulations.

In theory, expectations of quantum observables can be computed directly from the partition function. Unfortunately, in general it is not possible to obtain an explicit closed form expression for the latter. Instead, I use Monte Carlo sampling to compute expectations of the spin correlation operator with DetQMC. First, I map the model of Equation 1.1 to a noninteracting model. This is done by introducing an additional binary lattice field, which can be interpreted as the mediator of the Hubbard interaction. The original

4: Classical Ising spins interact via the model Hamiltonian

$$H = -J \sum_{\langle i,j \rangle} s_i s_j - B \sum_i s_i, \quad (2.6)$$

where J is a coupling constant, $\langle i, j \rangle$ denotes nearest neighbours on the lattice and B is an external magnetic field.

5: The code is publicly available at <https://github.com/fmonteir/tmd-nanoribbon-detQMC> (Accessed: 24 November 2023)

[168]: Brito (2018), *Development of a QMC code to tackle interacting electronic systems in 2D with application to TMD nanoribbons*

model is reduced to that of independent fermions coupled to an external field and the fermionic part of the partition function can then be traced out explicitly. One is left with the contribution of the binary external field, \mathbf{h} , yielding a problem analogous to the classical Ising chain of Section 2.1. Fermionic statistics imposes a crucial difference with respect to Ising spins. Some configurations of \mathbf{h} contribute to the partition function

$$Z = \sum_{\mathbf{h}} p(\mathbf{h}) \quad (2.8)$$

with a negative weight, $p(\mathbf{h})$. Thus they cannot be interpreted as probabilities in the mathematical sense. This minor setback can easily be solved by modifying the expression used to compute the expectation of a given observable, \hat{A} , which maps to a function of the field \mathbf{h} .

$$\begin{aligned} \langle A \rangle &= \frac{\sum_{\mathbf{h}} A(\mathbf{h})p(\mathbf{h})}{\sum_{\mathbf{h}} p(\mathbf{h})} = \frac{\sum_{\mathbf{h}} A(\mathbf{h})|p(\mathbf{h})|\text{sign}[p(\mathbf{h})]/\sum_{\mathbf{h}} p(\mathbf{h})}{\sum_{\mathbf{h}} |p(\mathbf{h})|\text{sign}[p(\mathbf{h})]/\sum_{\mathbf{h}} p(\mathbf{h})} \\ &= \frac{\langle As \rangle_{|p|}}{\langle s \rangle_{|p|}}, \end{aligned} \quad (2.9)$$

where $s(\mathbf{h}) \equiv \text{sign}[p(\mathbf{h})]$ and the subscript $|p|$ serves to remind the reader that the average is taken using the probability distribution $|p|$. Formally, the latter corresponds to a bosonic system with partition function $Z' = \sum_{\mathbf{h}} |p(\mathbf{h})|$. The average of the sign distribution depends exponentially on the difference between the free energies of bosonic and fermionic systems, Δf . This dependence is reflected in the relative error of the denominator of Equation 2.9:

$$\frac{\Delta s}{\langle s \rangle} = \frac{\sqrt{(\langle s^2 \rangle - \langle s \rangle^2)/M}}{\langle s \rangle} = \frac{\sqrt{1 - \langle s \rangle^2}}{\sqrt{M}\langle s \rangle} \propto e^{\beta N \Delta f} M^{-1/2}. \quad (2.10)$$

The consequence of this estimate is that the error of Monte Carlo estimators only has the advantageous scaling with $M^{-1/2}$ when $e^{\beta N \Delta f} \sim 1$, which is not guaranteed in general. The exponential scaling of the error is known as the sign problem because it causes a dramatic increase in the computational cost of Monte Carlo simulations, frequently making them unfeasible.

In the path integral formulation, with discretised imaginary time, the partition function contains a product of exponential functions of a sum of non-commuting operators. This product can be approximated by using the Trotter breakup. Dividing the imaginary time interval $[0, \beta]$ into L equal sub-intervals of smaller width $\Delta\tau = \beta/L$,

and using the inverse of the Baker–Campbell–Hausdorff formula, whilst keeping only the first order term in $\Delta\tau$, one obtains

$$Z = \text{Tr} \left[\prod_{l=0}^{L-1} e^{-\Delta\tau \hat{H}_{\text{TB}}} e^{-\Delta\tau \hat{H}_U^l} \right] + \mathcal{O}(\Delta\tau^2), \quad (2.11)$$

where \hat{H}_{TB} is the 3BTB Hamiltonian and \hat{H}_U^l is the intraorbital Hubbard term defined in the Hilbert space of the l -th imaginary time slice. The parameter $\Delta\tau^{-1}$ can be regarded as a high energy cutoff, and it must be larger than all other energy scales in the problem for the approximation to be valid.

Let one define the so called Hubbard-Stratonovich (HS) binary field \mathbf{h} as a $(L \times N)$ -dimensional, spin-1/2 field comprised of binary variables, where N is the total number of sites \times orbitals. The interaction term is eliminated by use of the discrete HS transformation for $U > 0$, which couples the local electronic spin $n_{i,\alpha,\uparrow} - n_{i,\alpha,\downarrow}$ to the field \mathbf{h} [169, 170]. $[n_{i,\alpha,\sigma}, n_{j,\beta,\sigma'}] = 0 \forall i, j, \alpha, \beta, \sigma, \sigma'$ implies that

$$e^{-\Delta\tau \hat{H}_U} = \prod_{\mu=1}^N e^{-U\Delta\tau(n_{\mu,\uparrow}-1/2)(n_{\mu,\downarrow}-1/2)}, \quad (2.12)$$

where the two indices i, α were absorbed into a single index μ to simplify the notation.

Consider a row of the matrix \mathbf{h} forming a vector of binary variables (± 1), denoted $\tilde{\mathbf{h}}_l = (h_{l,\mu=1,2,\dots,N})$. For simplicity, I momentarily fix an imaginary time slice and omit the l -index. Let $C = \frac{1}{2}e^{-\frac{U\Delta\tau}{4}}$ and $\nu = \text{arcosh}(e^{\frac{U\Delta\tau}{2}})$. Then, Equation 2.12 can be recast in terms of the local electronic spin as a non-interacting quadratic term⁶:

Discrete HS transformation

$$e^{-U\Delta\tau(n_{\mu,\uparrow}-1/2)(n_{\mu,\downarrow}-1/2)} = C \sum_{\tilde{h}_\mu} e^{\nu \tilde{h}_\mu (n_{\mu,\uparrow} - n_{\mu,\downarrow})}. \quad (2.15)$$

Equation 2.15 allows one to write the exponential of the Hubbard term as a trace over $\tilde{\mathbf{h}}_l$ (the l -th row of the HS field) at imaginary time slice l [169]. In principle, a more complicated transformation could allow one to simulate the model with interorbital, Hund and pair-hopping terms. However, it would require three spin-1 fields [45], thereby significantly increasing the computational cost, which I will show to be quite high already due to the sign problem in Chapter 3. Moreover, such a transformation would likely lead to a more severe sign problem [171], increasing the computational cost even more or impeding simulations altogether. For the sake of

[169]: Bai et al. (2009), ‘Numerical Methods for Quantum Monte Carlo Simulations of the Hubbard Model’
[170]: Hirsch (1983), ‘Discrete Hubbard-Stratonovich transformation for fermion lattice models’

6: A comparison of the action of the operators below suggests a relation between their exponentials:

$$\left(n_{\mu,\uparrow} - \frac{1}{2}\right) \left(n_{\mu,\downarrow} - \frac{1}{2}\right) |s_{\pm}\rangle = \mp \frac{1}{4} |s_{\pm}\rangle,$$

$$(n_{\mu,\uparrow} - n_{\mu,\downarrow}) |s_{\pm}\rangle = \frac{1 \pm 1}{2} |s_{\pm}\rangle,$$

where $|s_+\rangle \in \{|\uparrow\rangle, |\downarrow\rangle\}$ and $|s_-\rangle \in \{|\downarrow\rangle, |\uparrow\rangle\}$. In fact, one has

$$e^{-U\Delta\tau(n_{\mu,\uparrow}-1/2)(n_{\mu,\downarrow}-1/2)} |s_{\pm}\rangle = e^{\pm \frac{U\Delta\tau}{4}} |s_{\pm}\rangle, \quad (2.13)$$

$$\sum_{\tilde{h}_\mu = \pm 1} e^{\nu \tilde{h}_\mu (n_{\mu,\uparrow} - n_{\mu,\downarrow})} |s_{\pm}\rangle = \begin{cases} 2 |s_+\rangle, \\ (e^\nu + e^{-\nu}) |s_-\rangle, \end{cases} \quad (2.14)$$

where ν plays the role of a coupling constant. The right hand side of Equation 2.13 is recovered by multiplying Equation 2.14 by $\frac{1}{2}e^{-\frac{U\Delta\tau}{4}}$ and constraining the coupling via $\cosh \nu = e^{\frac{U\Delta\tau}{2}}$.

[45]: Huang et al. (2022), ‘Sign-free determinant quantum Monte Carlo study of excitonic density orders in a two-orbital Hubbard-Kanamori model’

[171]: Held et al. (1998), ‘Microscopic conditions favoring itinerant ferromagnetism: Hund’s rule coupling and orbital degeneracy’

simplicity and to avoid excessive computational cost, I have only included the intraorbital term in my simulations.

Let

$$\hat{H}_{U,\sigma} = \sum_{\mu} v \tilde{h}_{\mu} n_{\mu,\sigma} = \sigma v c_{\sigma}^{\dagger} \mathbf{U}(\tilde{\mathbf{h}}) c_{\sigma}, \quad (2.16)$$

where $\mathbf{U}(\tilde{\mathbf{h}}) \equiv \text{diag}(\tilde{h}_{\mu})$, *i.e.* \mathbf{U} is a diagonal matrix containing vector $\tilde{\mathbf{h}}$. Each imaginary time slice has a corresponding row of the HS matrix, $\tilde{\mathbf{h}}_l$, which in turn specifies the matrix \mathbf{U}_l and its corresponding operator $\hat{H}_{U,\sigma}^l$. Returning to Equation 2.11, one now has to include a trace over the field, which can be exchanged with the fermionic trace to give

$$Z = C^{NL} \text{Tr}_{\mathbf{h}} \text{Tr} \left[\prod_{l=0}^{L-1} \underbrace{e^{-\Delta\tau \hat{H}_{\text{TB},\uparrow}} e^{\hat{H}_{U,\uparrow}^l}}_{B_{l,\uparrow}(\tilde{\mathbf{h}}_l)} \underbrace{e^{-\Delta\tau \hat{H}_{\text{TB},\downarrow}} e^{\hat{H}_{U,\downarrow}^l}}_{B_{l,\downarrow}(\tilde{\mathbf{h}}_l)} \right], \quad (2.17)$$

where all operators are now quadratic in the fermion operators. The trace over the electronic degrees of freedom in the partition function may now be taken explicitly [172], turning the many-fermion problem into a single-particle problem:

Partition function in terms of the HS field

$$Z = C^{NL} \text{Tr}_{\mathbf{h}} \left[\prod_{\sigma} \det \left[\mathbf{I} + \prod_{l=L-1}^0 \mathbf{B}_{l,\sigma}(\tilde{\mathbf{h}}_l) \right] \right]. \quad (2.18)$$

[168]: Brito (2018), *Development of a QMC code to tackle interacting electronic systems in 2D with application to TMD nanoribbons*

[169]: Bai et al. (2009), ‘Numerical Methods for Quantum Monte Carlo Simulations of the Hubbard Model’
[172]: Hanke et al. (1993), ‘Electronic Phase Transitions. Modern Problems in Condensed Matter Sciences Vol. 32. North Holland’

[173]: Bai et al. (2011), ‘Stable solutions of linear systems involving long chain of matrix multiplications’

7: For each configuration of \mathbf{h} , I measure the observable $\langle S_{i,\alpha}^z S_{j,\beta}^z \rangle_{\mathbf{h}}$, defined in terms of $G^{\sigma}(\mathbf{h})$ as

$$\begin{aligned} \langle S_{i,\alpha}^z S_{j,\beta}^z \rangle_{\mathbf{h}} &= \\ & \sum_{\sigma} \left(G_{(i\alpha)(i\alpha)}^{\sigma}(\mathbf{h}) G_{(j\beta)(j\beta)}^{\sigma}(\mathbf{h}) \right. \\ & \left. - G_{(i\alpha)(i\alpha)}^{\sigma}(\mathbf{h}) G_{(j\beta)(j\beta)}^{-\sigma}(\mathbf{h}) \right). \end{aligned}$$

To multiply the chains of \mathbf{B} -matrices in a numerically stable manner, I use QR decompositions with partial pivoting [168, 169, 172, 173]. The determinant can be calculated with computational complexity $\mathcal{O}(LN^3)$ for a $N \times N$ matrix, leading to a naive $\mathcal{O}(L^2N^4)$ algorithm. Configurations of \mathbf{h} are sampled using single spin-flip dynamics, where the binary values of the HS field are analogous to classical spins. The acceptance/rejection scheme of the Metropolis-Hastings algorithm is implemented using a rank-one update of the matrices $\mathbf{I} + \prod_{l=L-1}^0 \mathbf{B}_{l,\sigma}(\tilde{\mathbf{h}}_l)$ [169], which reduces the complexity of the algorithm to order $\mathcal{O}(LN^3)$. Using Wick’s theorem, one may write any observable in terms of the matrix elements of the Green’s function for a fixed configuration of the HS field, which in turn is given by $G^{\sigma}(\mathbf{h}) = [\mathbf{I} + \prod_{l=L-1}^0 \mathbf{B}_{l,\sigma}(\tilde{\mathbf{h}}_l)]^{-1}$ [169, 172]. So, I use the Green’s function — the fundamental object of DetQMC — not only to sample configurations of the field \mathbf{h} , but also to measure spin correlations. I do so by averaging the spin correlator between site/orbital pairs i, α and j, β , over uncorrelated configurations of the HS field⁷ to obtain an estimator for $\langle S_{i,\alpha}^z S_{j,\beta}^z \rangle$.

2.3 Chebyshev spectral methods: rationale

Spectral methods are an increasingly popular tool for the simulation of condensed matter systems. This computational tool fulfills the requirement of general applicability [174–186] because — among other advantages — it is immune to the sign problem that plagues QMC simulations. A universal characteristic of these methods is that they rely on the iterative reconstruction of the target functions of interest (e.g. static or dynamic correlation functions), generally in terms of Chebyshev polynomial expansions due to their favourable convergence properties [187]. The iterative scheme is stable and can be made as accurate as required within a specified parameter. For example, if one is interested in computing expectations of quantum observables in the microcanonical ensemble, this parameter is the energy resolution. The canonical ensemble analogue of this parameter is the temperature.

Take the instructive case of the microcanonical ensemble. The spectral approach uses a coarse-grained description of energy states to provide estimates for quantum observables in large systems (see Figure 2.1). This is to be contrasted with full ED, which relies on the knowledge of individual states, and thus is limited to very small systems. In practical terms, spectral methods are combined with stochastic techniques for the computation of traces to further reduce the computational cost and are amenable to parallelisation in computational implementations, as the reader will see briefly.

The CPGF approach I exploit in this work to compute microcanonical averages [188, 189] has proven effective in dealing with tight-binding models, allowing unparalleled large-scale simulations with billions of atomic orbitals [189, 190]. Motivated by these developments, the main aim of this work is to introduce a finite-temperature spectral framework that can capture the physics of two-dimensional quantum spin models over a wide range of temperatures (of particular interest will be to probe the low-temperature behaviour of spin liquids).

The efficient evaluation of Chebyshev expansion moments relies on estimators for expectation values that use random vectors⁸ to evaluate traces of operators [191]. This technique, dubbed stochastic trace evaluation (STE), is ubiquitous in the study of condensed phases and is used in ED methods, such as those based on the Lanczos algorithm and TPQ [34, 35], and in KPM [174]. The rationale in the STE is to approximate the trace of an operator by an average of expectation values using $N_{\text{rd.vec.}}$ random vectors, $|\phi_0^{(r)}\rangle$ — where r is an index labelling a specific realisation of the random vector $|\phi_0\rangle$ — i.e. $\text{Tr}_{\text{STE}} \hat{O} := \frac{1}{N_{\text{rd.vec.}}} \sum_{r=1}^{N_{\text{rd.vec.}}} \langle \phi_0^{(r)} | \hat{O} | \phi_0^{(r)} \rangle$. The relative error scales favourably with the Hilbert space dimension, D (in fact the relative

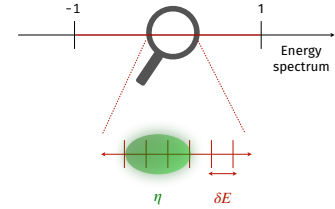


Figure 2.1: In the spectral approach, the energy spectrum is probed using a coarse-grained average of energy states within the required energy resolution η .

[189]: Ferreira et al. (2015), ‘Critical Delocalization of Chiral Zero Energy Modes in Graphene’

[190]: João et al. (2020), ‘KITE’

8: A random vector is defined as $|\phi_0\rangle = \sum_{i=1}^D \xi_i |i\rangle$, with $\{|i\rangle\}$ an arbitrary basis and $\xi_i \in \mathbb{C}$ random variables that satisfy $\overline{\xi_i} = 0$, $\overline{\xi_i \xi_j} = \delta_{ij}$ and $\overline{\xi_i^* \xi_j} = \delta_{ij}$ (here the bar denotes statistical average). The r -th realisation, $|\phi_0^{(r)}\rangle$ corresponds to a specific set of coefficients, $\{\xi_i^r, i = 1, 2, \dots, D\}$ and different sets are assumed to be uncorrelated.

[34]: Sugiura et al. (2012), ‘Thermal Pure Quantum States at Finite Temperature’

[35]: Sugiura et al. (2013), ‘Canonical Thermal Pure Quantum State’

[174]: Weisse et al. (2006), ‘The kernel polynomial method’

[187]: Boyd (1989), *Chebyshev & Fourier Spectral Methods*

[174]: Weisse et al. (2006), 'The kernel polynomial method'

9: The two variables x, y are defined as follows. x is the variable upon which the function one wishes to approximate depends on, say the energy. y is the integration variable used when the function is convoluted with the kernel.

[188]: Braun et al. (2014), 'Numerical evaluation of Green's functions based on the Chebyshev expansion'

[189]: Ferreira et al. (2015), 'Critical Delocalization of Chiral Zero Energy Modes in Graphene'

[34]: Sugiura et al. (2012), 'Thermal Pure Quantum States at Finite Temperature'

[35]: Sugiura et al. (2013), 'Canonical Thermal Pure Quantum State'

error is proportional to $1/\sqrt{D}$ for typical sparse operators) and, for a fixed system size, can be made as small as desired by increasing $N_{\text{rd.vec.}}$. Moreover, and perhaps most importantly, stochastic trace estimators are free from the sign problem.

A crucial feature of Chebyshev expansions is that they offer uniform convergence [187] (and in the case of CPGF this translates into an energy resolution that can be specified exactly [189]). This is appealing for studies of phase transitions, particularly when one wishes to characterise the critical behaviour of thermodynamic functions, among others. There are two ways to define a resolution. One of them uses a kernel that modifies the coefficients of the Chebyshev expansion. This modification smears out so called Gibbs oscillations which occur upon truncation of orthogonal polynomial series [174]. A resolution may then be defined as the spread of the kernel in the xy -plane⁹, and generally depends on the truncation order and energy. Here, instead, I use a Green's function-based method that was proposed independently in the works of Braun and Schmitteckert [188] and Ferreira and Mucciolo [189]. This approach, coined CPGF in Reference [189], has two main features:

1. It is based on a stable, asymptotically exact expansion of lattice Green's functions in Chebyshev polynomials;
2. The energy resolution is specified from the outset, in the form of a simple imaginary self-energy.

By extending these ideas to quantum spin models, I have developed a Chebyshev-based method for the computation of quantum expectations in the canonical ensemble, where the temperature plays the role of a resolution. This method — which I shall detail in this chapter — bypasses potential low-temperature convergence issues by using an adaptive temperature step, while maintaining rigorous control over convergence. Alternatively, TPQ-based methods can be used to approximate either microcanonical [34] or canonical [35] averages by successive application of the Hamiltonian operator onto an initial random state. In TPQ, the number of iterations is proportional to a quantity that plays the role of an effective temperature. Broadly speaking, this effective temperature acts similarly to a resolution that becomes finer as more iterations are completed. Yet, this annealing-like scheme is susceptible to slow convergence, particularly in the vicinity of critical points.

In the following sections, I will compare Lanczos, TPQ, and Chebyshev-based approaches since they all scale linearly with the dimension of the Hilbert space D . Moreover, all methods scale linearly with the number of polynomials required for spectral convergence (or iterations in the case of TPQ) $N_{\text{poly/it}}$ and with

the number of realisations of the initial random state required for statistical convergence $N_{\text{rd.vec.}}$.

The methods described here involve two main steps. First, a numerically exact or approximate spectral representation of the target state is obtained by means of algorithms with polynomial computational complexity. This is achieved by recursive application of the Hamiltonian, \hat{H} , to an initial random state, $|\phi_0\rangle$. Some examples of typical target states are the ground state, a microcanonical state (with energy restricted to an energy shell) or a canonical (finite temperature) state. After the target state is converged to the desired precision, physical observables may be computed by means of the STE technique introduced earlier in this section, *i.e.* by averaging the expectation value $\langle\phi_0|\hat{O}|\phi_0\rangle$ over an ensemble of random vectors.

These techniques are general in scope and can also be combined to provide a powerful means of accessing excited states, reconstructing Green's functions and computing the average and local density of states. Additionally, they can easily be extended to the study of quantum dynamics, either in the time domain, by exploiting a spectral approximation of the time evolution operator, or in the frequency domain, via the resolvent operator.

2.4 Vector recursions and bit representation of the Hamiltonian

All methods I shall discuss in the coming sections rely on matrix-vector products of the type $H|\phi\rangle$ ¹⁰. If done naively, these quickly become overly expensive from a computational point of view as the system size is increased. In fact, these matrix-vector operations constitute the bottleneck of all the algorithms discussed here. Thus, it is crucial to efficiently implement the operation $H|\phi\rangle$, both from the perspective of CPU time and memory usage. In particular, the latter grows exponentially with the system size for interacting quantum spins, thereby limiting not only the efficiency of the implementation, but also the available system sizes. Simulating a wide range of system sizes is important because finite-size scaling studies give insight on the properties of a system as the thermodynamic limit is approached. In this section, I discuss the computational optimisation of these $H|\phi\rangle$ operations.

The matrix at play is usually a representation of the Hamiltonian operator, \hat{H} , in some basis: a sparse $D \times D$ matrix, where I recall that $D = 2^N$ is the size of the Hilbert space for a system of N spins-1/2. However, this matrix can also be a representation of a quantum observable of interest, such as the nearest neighbour

10: Here, H is a matrix and the ϕ -vector is written in bra-ket notation

spin-spin correlation on a given lattice. One might think that using linear algebra libraries to manipulate these matrices in sparse form would be efficient enough for the purposes of this thesis, but that turns out not to be the case. Hence, I will introduce the so called bit-representation of the Hamiltonian, which helps to circumvent this issue by enabling the generation of the Hamiltonian (and other observables) ‘on-the-fly’.

Even though the H -matrices are sparse (with $\mathcal{O}(D)$ nonzero entries), storing their elements and corresponding indices still requires a lot of memory even for modest system sizes, *e.g.* $\mathcal{O}(10^2)$ GB for $N \sim 24$. Ultimately, the exponential growth of the Hilbert space with the system size for a system of interacting quantum spins deems the storage and access to the corresponding matrix entries too inefficient for the purposes of this thesis (tackling problems where $N > 20$). Fortunately, these matrix entries can be evaluated ‘on-the-fly’, *i.e.* every time a matrix-vector product is computed. Clearly, this dramatically reduces the memory usage, since one no longer needs to store $\mathcal{O}(D)$ nonzero entries of the relevant matrix (along with their corresponding indices) in some sparse matrix form. What is perhaps more surprising is that provided that the system is large enough ($N \gtrsim 20$), this strategy also reduces the CPU time because it turns out to be computationally cheaper to recompute the matrix entries and their corresponding indices every time a matrix-vector product occurs than to retrieve them from memory.

Now that I have outlined how the matrices involved in the $H|\phi\rangle$ operation will be handled, let me focus on the vectors. The algorithms discussed in the next few sections generate these vectors iteratively. This is done by repeatedly applying the Hamiltonian to previously generated vectors and combining a subset of them to form the new vector. Typically, algorithms start from an initial random vector $|\phi_0\rangle$. Then, various recursive rules can be used to generate order- n polynomials of the Hamiltonian acting on the initial random vector $p_n(H)|\phi_0\rangle$. I will discuss various types of vector recursions [13, 34, 189]. While these will generate different polynomials, $p_n(H)$, they have a crucial aspect in common: after M iterations, one obtains a vector in the so called Krylov subspace, defined below in Definition 2.4.1.

[13]: Lanczos (1950), ‘An iteration method for the solution of the eigenvalue problem of linear differential and integral operators’

[34]: Sugiura et al. (2012), ‘Thermal Pure Quantum States at Finite Temperature’

[189]: Ferreira et al. (2015), ‘Critical Delocalization of Chiral Zero Energy Modes in Graphene’

Definition 2.4.1 *The order- M Krylov subspace generated by the $D \times D$ matrix H and the D -dimensional vector $|\phi_0\rangle$ is the linear subspace spanned by the vectors obtained by applying the first M powers of H to $|\phi_0\rangle$, *i.e.**

$$\mathcal{K}_M(H, |\phi_0\rangle) = \text{span}\{|\phi_0\rangle, H|\phi_0\rangle, H^2|\phi_0\rangle, \dots, H^{M-1}|\phi_0\rangle\}.$$

The key to evaluating the interacting quantum spin Hamiltonian matrix — appearing in the algorithms discussed here in successive matrix-vector multiplications, as illustrated by Definition 2.4.1 — ‘on-the-fly’ is to notice that spin states can be mapped onto integer numbers. In order to set up this mapping, I start with a bit (with states 0,1) that represents two possible spin states (up and down):

$$\begin{aligned} |0\rangle &\equiv |\uparrow\rangle \equiv |+\rangle, \\ |1\rangle &\equiv |\downarrow\rangle \equiv |-\rangle. \end{aligned} \quad (2.19)$$

By using the binary representation of integers that are higher powers of 2, I can map quantum spin states in a D -dimensional Hilbert space onto integers in the following manner¹¹:

$$\begin{aligned} |\uparrow \dots \uparrow\uparrow\rangle &= |0 \dots 000\rangle \mapsto |0\rangle \\ |\uparrow \dots \uparrow\downarrow\rangle &= |0 \dots 001\rangle \mapsto |1\rangle \\ |\uparrow \dots \downarrow\uparrow\rangle &= |0 \dots 010\rangle \mapsto |2\rangle \\ |\uparrow \dots \downarrow\downarrow\rangle &= |0 \dots 011\rangle \mapsto |3\rangle \\ &\dots \\ |\downarrow \dots \downarrow\downarrow\rangle &= |11 \dots 11\rangle \mapsto |D-1\rangle \end{aligned} \quad (2.20)$$

Equation 2.20 can be used to define a ‘bit’-basis for a state of N spins (see Definition 2.4.2). Using this basis, one can systematically label each state non-ambiguously with an integer number. Using the bit representation of these integers, one can evaluate the matrix elements of any quantum spin Hamiltonian ‘on-the-fly’.

Definition 2.4.2 A state in the product state basis for a system of N spins is defined as

$$|\sigma\rangle = |\sigma_0 \sigma_1 \dots \sigma_i \dots \sigma_j \dots \sigma_{N-1}\rangle = |a\rangle,$$

where $\sigma_{0,1,\dots,N-1} = \pm 1$ and a is the integer represented by the set of bits $\frac{1}{2}(\sigma + \mathbf{1})$. Here, $\mathbf{1}$ is a vector with all entries equal to one.

Each of the D states in the basis of product states of individual spins of Definition 2.4.2 is encoded by an integer, a , between 0 and $D-1$, represented by a set of bits. Mapping the lattice sites to the N bit positions and the individual spin states to the value of the bit, the Hamiltonian acts on a basis state in one of the two ways. Either the state gets:

1. multiplied by a constant that depends on the value of two bits at different positions, or

11: The binary representation of a positive integer is obtained in a similar fashion to its decimal counterpart. For example, here’s the integer 86 in decimal and binary representation, respectively

$$\begin{aligned} 86_{10} &= 8 \cdot 10^1 + 6 \cdot 10^0 \\ &= 1 \cdot 2^6 + 0 \cdot 2^5 + 1 \cdot 2^4 + 0 \cdot 2^3 \\ &\quad + 1 \cdot 2^2 + 1 \cdot 2^1 + 0 \cdot 2^0 \\ &= 1010110_2. \end{aligned}$$

2. converted to a state encoded by a different integer, obtained by flipping only two bits, and then multiplied by a constant that depends on the values of the two flipped bits.

Once a model is translated into these simple rules — which are stored at virtually no memory cost — any matrix-vector multiplication boils down to applying the rules to basis states.

12: The Pauli matrices are defined as

Pauli matrices
$\sigma^x = \begin{pmatrix} 0 & 1 \\ 1 & 0 \end{pmatrix},$
$\sigma^y = \begin{pmatrix} 0 & -i \\ i & 0 \end{pmatrix},$
$\sigma^z = \begin{pmatrix} 1 & 0 \\ 0 & -1 \end{pmatrix}.$

Recall that the Pauli matrices¹² act on a single-spin state ($|\sigma = \pm\rangle$) as follows:

$$\begin{aligned} \hat{\sigma}^x |\sigma\rangle &= |-\sigma\rangle, \\ \hat{\sigma}^y |\sigma\rangle &= i\sigma |-\sigma\rangle, \\ \hat{\sigma}^z |\sigma\rangle &= \sigma |\sigma\rangle. \end{aligned} \quad (2.21)$$

Let one consider the example of the Heisenberg model to illustrate how the corresponding Hamiltonian can be evaluated ‘on-the-fly’. When considering the Heisenberg interaction, the relevant operator is $\hat{\sigma}_i \cdot \hat{\sigma}_j$, which acts as follows:

Given two spins at sites i and j of a lattice with N sites, and an arbitrary state $|\sigma\rangle$, a new state can be obtained by flipping those two spins:

$$\hat{\sigma}_i \cdot \hat{\sigma}_j |\sigma\rangle = (1 - \sigma_i \sigma_j) |\sigma'\rangle + \sigma_i \sigma_j |\sigma\rangle, \quad (2.22)$$

$$|\sigma'\rangle = |\sigma_0 \sigma_1 \dots -\sigma_i \dots -\sigma_j \dots \sigma_{N-1}\rangle$$

where $|\sigma'\rangle$ is simply $|\sigma\rangle$ with spins i and j flipped.

Equation 2.22 is obtained by gathering the contributions of the three types of exchange (labeled $\gamma = x, y, z$):

$$\hat{\sigma}_i^\gamma \hat{\sigma}_j^\gamma |\sigma\rangle = \begin{cases} |\sigma'\rangle, & \gamma = x \\ -\sigma_i \sigma_j |\sigma'\rangle, & \gamma = y \\ \sigma_i \sigma_j |\sigma\rangle, & \gamma = z. \end{cases} \quad (2.23)$$

Equation 2.23 will be useful when deriving the action of the Kitaev Hamiltonian on a spin state in Chapter 4.

Recalling that $\hat{S} = \frac{\hbar}{2} \hat{\sigma}$, the nonzero terms of the Heisenberg Hamiltonian

$$\hat{H} = -J \sum_{\langle i, j \rangle} \mathbf{S}_i \cdot \mathbf{S}_j, \quad (2.24)$$

where $\langle i, j \rangle$ means nearest neighbouring sites on a given lattice, can be obtained using Algorithm 1 (in units where $J = \hbar = 1$).

Finally, given a state written in the bit-basis

Algorithm 1: Generating the Heisenberg Hamiltonian using the bit-basis. See margin note for details.

Data: Simple rule of Equation 2.22 for the action of the Hamiltonian Matrix.

Result: $D \times D$ Sparse Hamiltonian Matrix filled with the relevant matrix elements.

```

1 for  $a = 0, \dots, D - 1$  do
2    $H(a, a) \leftarrow 0$ ;
3   for  $i = 0, \dots, N - 1$  do
4     for  $j \in \text{neighbours}(i)$  do
5       if  $a[i] = a[j]$  then
6          $H(a, a) \leftarrow H(a, a) - 0.25$ ;
7       else
8          $H(a, a) \leftarrow H(a, a) + 0.25$ ;
9          $b = \text{flip}(a[i], a[j])$ ;
10         $H(a, b) \leftarrow -0.5$ ;

```

$$|\psi_0\rangle = \sum_a c_a |a\rangle, \quad (2.25)$$

the state obtained by acting with \hat{H} on $|\psi_0\rangle$, $|\psi_1\rangle = \hat{H}|\psi_0\rangle$ can be computed using Algorithm 2. This is better than simply acting with the H -matrix obtained with Algorithm 1 upon state $|\psi_0\rangle$ written in the bit-basis because it does not require storing all the $\mathcal{O}(D)$ nonzero entries.

Algorithm 2: Acting with the Heisenberg Hamiltonian on a state written in the bit-basis.

Data: Simple rule of Equation 2.22 for the action of the Hamiltonian Matrix; D -dimensional state vector $|\psi_0\rangle$ written in the bit-basis.

Result: $|\psi_1\rangle = \hat{H}|\psi_0\rangle$

```

1 for  $a = 0, \dots, D - 1$  do
2    $\psi_1(a) = 0$ ;
3   for  $i = 0, \dots, N - 1$  do
4     for  $j \in \text{neighbours}(i)$  do
5       if  $a[i] = a[j]$  then
6          $\psi_1(a) \leftarrow \psi_1(a) - 0.25 * \psi_0(a)$ ;
7       else
8          $\psi_1(a) \leftarrow \psi_1(a) + 0.25 * \psi_0(a)$ ;
9          $b = \text{flip}(a[i], a[j])$ ;
10         $\psi_1(a) \leftarrow \psi_1(a) - 0.5 * \psi_0(b)$ ;

```

Detail of Algorithms 1 and 2

The function $\text{neighbours}(i)$ returns the neighbours of site i on a given lattice. The notation $a[i]$ refers to the i -th bit of the integer a . The function $\text{flip}(a[i], a[j])$ flips the i -th and j -th bits of integer a and returns the resulting integer. Finally, it is important to remark that in practice one does not fill the Hamiltonian matrix directly; this is only done in the pseudo-code for simplicity. Instead, triplets with the two matrix indices and the corresponding matrix element are stored and then the sparse matrix is initialised separately.

Now one has all the ingredients needed to carry out the operation $H|\phi\rangle$ 'on-the-fly'. I have outlined how it can be implemented for the specific case of the Heisenberg model, but the process is

general: first, I determine how the relevant interacting quantum spin Hamiltonian and potential observables of interest act on a generic spin state; then, one uses some version of Algorithm 2 for that quantum spin Hamiltonian (and desired observables) to define the relevant matrix-vector operations.

[192]: Sandvik (2010), ‘Computational Studies of Quantum Spin Systems’

In Reference [192], the author explains how the original matrix can be successively broken up into blocks systematically by using symmetry operations derived from the symmetries of the Hamiltonian. In practice, codes can be made faster and more memory-efficient by taking advantage of this block structure.

The following sections describe various iterative methods, specialising in distinct tasks, while sharing a main aspect: they are all based on polynomial expansions in terms of the Hamiltonian. Consequently, after M iterations, one always obtains a state in the Krylov subspace of Definition 2.4.1, $\mathcal{K}_M(\hat{h}, |\phi_0\rangle)$ where $\hat{h} = \hat{H}/N$ is the Hamiltonian normalised to the number of lattice sites (referred to as *Hamiltonian density* throughout) and $|\phi_0\rangle$ is a normalised initial random state.

2.5 Lanczos exact diagonalisation

The Lanczos method [13] converges quickly to the ground state and low-lying excitations. It consists of iteratively generating a set of orthonormal states, $\{|\phi_j\rangle, j = 0, 1, \dots, M\}$, spanning the Krylov space by using the following recursion. Let $\alpha_j = \langle\phi_j|\hat{h}|\phi_j\rangle$. First, α_0 is used to generate an unnormalised orthogonal state:

$$|\Phi_1\rangle = (\hat{h} - \alpha_0)|\phi_0\rangle, \quad (2.26)$$

which can then be normalised to obtain the second Lanczos state:

$$|\phi_1\rangle = \beta_1^{-1}|\Phi_1\rangle, \quad \beta_1 = \sqrt{\langle\Phi_1|\Phi_1\rangle}. \quad (2.27)$$

Subsequent Lanczos states are generated using the recursion and normalisation scheme:

$$\begin{aligned} |\Phi_{j+1}\rangle &= (\hat{h} - \alpha_j)|\phi_j\rangle - \beta_j|\phi_{j-1}\rangle \\ |\phi_{j+1}\rangle &= \beta_{j+1}^{-1}|\Phi_{j+1}\rangle, \quad j = 1, 2, \dots, M-1, \end{aligned} \quad (2.28)$$

with $\beta_j = \sqrt{\langle\Phi_j|\Phi_j\rangle}$.

Algorithm 3 summarises an implementation of the Lanczos vector recursion. Notice that considering $\beta = 0$ in the very first iteration eliminates the need to treat it as a special case.

Algorithm 3: Lanczos algorithm

Data: 3 vectors of size D . Declare two of them and fill the other one ($|v_1\rangle$) with randomly generated entries (e.g. drawn uniformly), then normalise it. Matrix-vector multiplication operation defined using the Hamiltonian per site \hat{h} .

Result: Ground state energy and corresponding quasi-eigenstate.

- 1 Declare two vectors $|v_0\rangle, |u\rangle$ arbitrary ;
 - 2 Declare α ;
 - 3 $\beta = 0$;
 - 4 $j = 0$;
 - 5 **while** convergence criterion and $j <$ maximum number of iterations
 do
 - 6 $|u\rangle \leftarrow \hat{h} |v_1\rangle$;
 - 7 $|u\rangle \leftarrow |u\rangle - \beta |v_0\rangle$;
 - 8 $\alpha \leftarrow \langle v_1 | u \rangle$;
 - 9 $|u\rangle \leftarrow |u\rangle - \alpha |v_1\rangle$;
 - 10 $\beta \leftarrow \sqrt{\langle u | u \rangle}$;
 - 11 $|v_0\rangle \leftarrow |v_1\rangle$;
 - 12 $|v_1\rangle \leftarrow \frac{1}{\beta} |u\rangle$;
-

The convergence criterion consists of analysing the convergence of the estimate of the ground state energy, computed as follows. Acting with $\langle \Phi_1 |$ upon Equation 2.26, yields $\langle \phi_1 | \hat{h} | \phi_0 \rangle = \beta_1$. Other nonzero matrix elements of the Hamiltonian are obtained by acting with either $\langle \phi_{j-1} |$, $\langle \phi_j |$, or $\langle \phi_{j+1} |$ on the recursion of Equation 2.28:

$$\langle \phi_{j-1} | \hat{h} | \phi_j \rangle = \beta_j, \quad \langle \phi_j | \hat{h} | \phi_j \rangle = \alpha_j, \quad \langle \phi_{j+1} | \hat{h} | \phi_j \rangle = \beta_{j+1}. \quad (2.29)$$

Thus, the representation of the Hamiltonian in the Lanczos basis is a tridiagonal matrix, which is exact when M coincides with the size of the Hilbert space, D . A low-energy approximation of the Hamiltonian is obtained by truncating the matrix at $M \ll D$:

$$T_M = \begin{pmatrix} \alpha_0 & \beta_1 & 0 & \dots & 0 \\ \beta_1 & \alpha_1 & \beta_2 & \ddots & \vdots \\ 0 & \beta_2 & \ddots & \ddots & 0 \\ \vdots & \ddots & \ddots & \ddots & \beta_M \\ 0 & \dots & 0 & \beta_M & \alpha_M \end{pmatrix}. \quad (2.30)$$

[193]: Dhillon (1997), *A New $O(n^2)$ Algorithm for the Symmetric Tridiagonal Eigenvalue/Eigenvector Problem*

[194]: Anderson et al. (1999), *LAPACK Users' Guide*

[195]: Dhillon et al. (2006), 'The design and implementation of the MRRR algorithm'

[196]: Demmel et al. (2008), 'Performance and Accuracy of LAPACK's Symmetric Tridiagonal Eigensolvers'

In my Lanczos implementation, T_M is diagonalised using the method of Multiple Relatively Robust Representations (MR) [193], implemented e.g. in LAPACK [194–196]. MR was chosen to maximise efficiency because it has $\mathcal{O}(M^2)$ computational complexity and allows one to specify a range of desired eigenpairs, rather than computing all eigenpairs. This is useful because here one is only interested in the lowest eigenvalues of T_M , $\{\varepsilon_{j=0,1,\dots,\lambda}\}$ (with $\lambda \ll M$), which accurately approximate the low-lying eigenvalues of \hat{h} . The corresponding eigenstates, $\{|\psi_j\rangle\}$ are obtained by transforming to the original basis using the eigenvectors of T_M , $\mathbf{v}_j = (v_{j0}, v_{j1}, \dots, v_{jM})$:

$$|\psi_j\rangle = \sum_{i=0}^M v_{ji} |\phi_i\rangle. \quad (2.31)$$

The dominant memory cost of the methods discussed throughout is incurred via the storage of vectors of dimension D (D -vectors). This is because the Hamiltonian is never stored in memory, e.g. as a sparse matrix. Instead, the matrix-vector multiplications encoding the action of the Hamiltonian on a state are carried out on-the-fly, based on the bit representation of spin states explained in Section 2.4. The Lanczos recursion requires only two D -vectors ($|\phi_i\rangle, |\phi_{i-1}\rangle$) to be stored in memory in each step, i . Consequently, constructing the corresponding eigenstates, $|\psi_j\rangle$ entails a second Lanczos recursion in order to regenerate the Lanczos vectors, while accumulating the weighted sum of Equation 2.31. This can only be done once the eigenvectors \mathbf{v}_j are obtained at the end of the first recursion. Suppose one is interested in constructing one of the low-lying states, $|\psi_j\rangle$. Then, an additional vector must be stored in memory so as to accumulate the weighted sum of Equation 2.31 during the second recursion, implying that the memory cost is dominated by three D -vectors.

Once a low-lying eigenstate, $|\psi_j\rangle$, is found, the static expectation value of a quantum observable in that state can be evaluated. If multiple low-lying states are desired, it is still possible to preserve the 3-vector memory cost by carrying out multiple Lanczos recursions to evaluate the relevant expectations for different low-lying states. In contrast, constructing the whole set of eigenstates, $\{|\psi_j\rangle\}$

during the second recursion requires as many extra vectors as desired eigenstates to be stored in memory. While the ground state and low-lying excitations are important, there are problems that require knowledge of higher excited states or even the whole spectrum. In what follows, I compare different approaches to go beyond low-lying states.

2.6 Kernel polynomial method

The key concept behind KPM [174] is that one may reliably characterise functions of the energy — such as the density of states $\rho(\varepsilon)$ — in terms of their moments

$$\mu_n = \int \rho(\varepsilon) \varepsilon^n d\varepsilon, \quad n = 0, 1, \dots \quad (2.32)$$

Naively gathering these moments tends to lead to a numerically unstable procedure and a modified moment approach is required. I will explain how to modify the moments in terms of Chebyshev expansions so that a numerically stable scheme is obtained, and quantities such as the density of states can be accurately approximated. The same approach can be used to compute moments of other observables, thus characterising their behaviour in a similar fashion. This approach treats all energies on equal footing and so, unlike the Lanczos algorithm described previously, it enables one to go well beyond low-lying states.

[174]: Weisse et al. (2006), ‘The kernel polynomial method’

2.6.1 Chebyshev expansions

Definition 2.6.1 *Let one define a scalar product in a vector space of functions*

$$\langle f | g \rangle \equiv \int_a^b w(x) f(x) g(x) dx, \quad (2.33)$$

where $f(x)$ and $g(x)$ are generic real functions and $w(x)$ is a real weight function. These three functions are defined in the interval $]a, b[$.

The Chebyshev polynomials of the first kind (T_n) are a basis set of the vector space defined with the weight function $w_1(x) = \pi^{-1}(1 - x^2)^{-1/2}$ in the interval $] -1, 1[$, corresponding to the scalar product

$$\langle f | g \rangle_1 = \int_{-1}^1 \frac{f(x)g(x)}{\pi\sqrt{1-x^2}} dx. \quad (2.34)$$

In order to constitute a basis set, the Chebyshev polynomials of the first kind must obey an orthogonality relation. The latter can easily be derived by using the scalar product defined in Equation 2.42, revealing the general form of the Chebyshev polynomials of the first kind.

$$\begin{aligned}
 \langle T_n | T_m \rangle &= \int_{-1}^1 \frac{T_n(x)T_m(x)}{\pi\sqrt{1-x^2}} dx \quad \text{let } x = \cos \theta \\
 &= \int_{\arccos(-1)}^{\arccos(1)} \frac{T_n(\cos \theta)T_m(\cos \theta)}{\pi \sin \theta} d(\cos \theta) \\
 &= \frac{1}{\pi} \int_{\pi}^0 \frac{T_n(\cos \theta)T_m(\cos \theta)}{\sin \theta} (-\sin \theta) d\theta \\
 &= \frac{1}{\pi} \int_0^{\pi} \cos(n\theta) \cos(m\theta) d\theta = 0 \text{ if } n \neq m,
 \end{aligned} \tag{2.35}$$

where $T_n(\cos \theta) = \cos(n\theta)$ is assumed. If $n = m = 0$, one has

$$\frac{1}{\pi} \int_0^{\pi} d\theta = 1. \tag{2.36}$$

On the other hand, if $n = m \neq 0$, one has

$$\frac{1}{\pi} \int_0^{\pi} \cos^2(n\theta) = \frac{1}{\pi} \int_0^{\pi} \frac{1 + \cos(2n\theta)}{2} d\theta = \frac{1}{2}. \tag{2.37}$$

Thus, one obtains the orthogonality relation

$$\int_{-1}^1 \frac{dx}{\pi\sqrt{1-x^2}} T_n(x)T_m(x) = \frac{1 + \delta_{0,n}}{2} \delta_{m,n}. \tag{2.38}$$

This is a direct consequence of the orthogonality of Fourier components, hinting at the connection between Chebyshev and Fourier series. The orthogonality relation of Equation 2.38 implies that any function can be expanded in Chebyshev polynomials.

Definition 2.6.2 *n*-th order Chebyshev polynomials of the first kind can be obtained directly using

$$T_n(x) = \cos(n \arccos x). \tag{2.39}$$

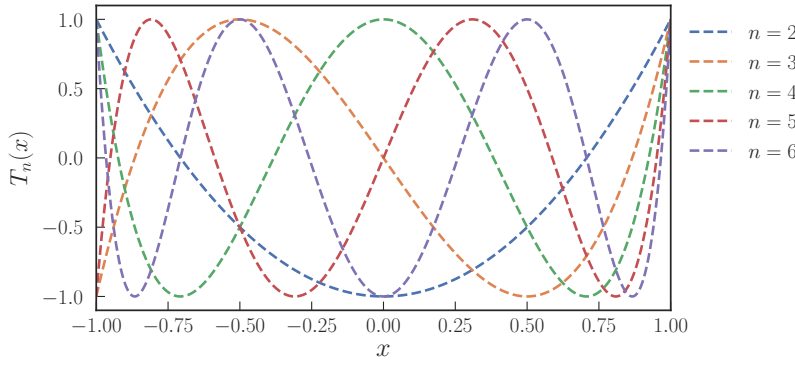


Figure 2.2: Chebyshev polynomials of the first kind for orders $n = 2, 3, \dots, 6$.

In Figure 2.2, I plot $\{T_n(x), n = 2, 3, \dots, 6\}$. I also list the first three Chebyshev polynomials of the first kind on the margin. Let $x = \cos \theta$. As outlined on the margin, the simplest way to derive the coefficients of the Chebyshev polynomials is to use the double angle formula repeatedly with the variable θ , *i.e.*

$$\cos(2\theta) = 2 \cos^2 \theta - 1$$

defines $T_2(x) = 2x^2 - 1$, and the rest of the sequence can be generated similarly by using Definition 2.6.2 and using trigonometric identities to reduce expressions to the double angle formula. If one uses this process to derive T_3 , the lower-order polynomials T_1 and T_2 appear, hinting at the existence of a recursion relation that allows one to generate higher order polynomials given lower order ones. It turns out that the full sequence $\{T_n, n \geq 0\}$, may be generated using the recursive rule

$$T_{n+1}(x) = 2xT_n(x) - T_{n-1}(x). \quad (2.40)$$

Proof. The Chebyshev recursive relation is easily proven by applying the cosine of the sum formula, together with the definition of Equation 2.39.

$$\begin{aligned} & T_{n+1}(\cos \theta) + T_{n-1}(\cos \theta) \\ &= \cos[(n+1)\theta] + \cos[(n-1)\theta] \\ &= \cos(n\theta) \cos \theta - \sin(n\theta) \sin \theta \\ &+ \cos(n\theta) \cos \theta + \sin(n\theta) \sin \theta \\ &= 2 \cos(n\theta) \cos \theta \\ &= 2 \cos \theta T_n(\cos \theta) \end{aligned}$$

□

It is also possible to derive a product relation for the Chebyshev polynomials of the first kind, which shall be useful later:

$$\begin{aligned} T_0(x) &= \cos(0) = 1 \\ T_1(x) &= \cos(\arccos x) = x \\ T_2(x) &= \cos(2 \arccos x) \\ &= 2 \cos^2(\arccos x) - 1 \\ &= 2x^2 - 1 \\ T_3(x) &= \cos(3 \arccos x) \\ &= \cos(2 \arccos x + \arccos x) \\ &= \cos(2 \arccos x) \cos(\arccos x) \\ &- \sin(2 \arccos x) \sin(\arccos x) \\ &= xT_2(x) \\ &- 2 \sin^2(\arccos x) \cos(\arccos x) \\ &= xT_2(x) + 2(\cos^2(\arccos x) - 1)x \\ &= xT_2(x) + (T_2(x) - 1)x \\ &= 2xT_2(x) - T_1(x) \\ &= 4x^3 - 3x \end{aligned}$$

$$T_m(x)T_n(x) = \frac{1}{2} \left(T_{m+n}(x) + T_{m-n}(x) \right). \quad (2.41)$$

Proof.

$$\begin{aligned} 2T_m(x)T_n(x) &= 2 \cos(n \arccos x) \cos(m \arccos x) \\ &= \cos[(n + m) \arccos x] \\ &\quad + \cos[(n - m) \arccos x] \\ &= T_{m+n}(x) + T_{m-n}(x). \end{aligned}$$

□

Similarly to T_n , the Chebyshev polynomials of the second kind (U_n) are a basis set of the vector space defined with the weight function $w_2(x) = \pi\sqrt{1-x^2}$ in the interval $] -1, 1[$.

$$\langle f | g \rangle_2 = \int_{-1}^1 f(x)g(x)\pi\sqrt{1-x^2}dx. \quad (2.42)$$

From now on, I focus on the Chebyshev polynomials of the first kind, taking into account that there is an intimate relation between Chebyshev polynomials of the first and second kinds.

Take an integrable function $f :] -1, 1[\rightarrow \mathbb{R}$. Its expansion in Chebyshev polynomials of the first kind

$$f(x) = \sum_{n=0}^{\infty} a_n T_n(x) \quad (2.43)$$

is found by using the orthogonality relation of Equation 2.38:

$$\begin{aligned} & \int_{-1}^1 \frac{dx}{\pi\sqrt{1-x^2}} T_m(x) f(x) \\ &= \sum_n a_n \int_{-1}^1 \frac{dx}{\pi\sqrt{1-x^2}} T_m(x) T_n(x) \\ &= \sum_n a_n \frac{1 + \delta_{0,n}}{2} \delta_{m,n} \\ &= a_m \frac{1 + \delta_{0,m}}{2}, \end{aligned} \quad (2.44)$$

yielding the coefficients

$$a_n = \frac{2}{1 + \delta_{0,n}} \int_{-1}^1 \frac{dx}{\pi\sqrt{1-x^2}} T_n(x) f(x). \quad (2.45)$$

Alternatively, one may use the set of coefficients $\{\mu_n\}$ defined by

$$\mu_n = \int_{-1}^1 dx T_n(x) f(x), \quad (2.46)$$

so that

$$f(x) = \frac{1}{\pi\sqrt{1-x^2}} \sum_n \frac{2}{1+\delta_{0,n}} \mu_n T_n(x), \quad (2.47)$$

which solidifies the claim that a modified moment approach would be obtained. Formally, this is equivalent to expanding in terms of the orthogonal functions

$$\phi_n(x) = \frac{T_n(x)}{\pi\sqrt{1-x^2}}, \quad (2.48)$$

which fulfill the orthogonality relation for the Chebyshev polynomials of the second kind: $\langle \phi_n | \phi_m \rangle_2 = \frac{1+\delta_{0,n}}{2} \delta_{m,n}$ [174]. Thus, they are also a valid basis set upon which one can expand $f(x)$.

[174]: Weisse et al. (2006), 'The kernel polynomial method'

2.6.2 Kernels and Gibbs oscillations

In practice, an approximation of the target function, f , is constructed by truncating the infinite series of Equation 2.47 for a finite number of polynomials, N_{poly} . Unfortunately, regardless of how much one increases N_{poly} , it remains challenging to achieve good precision since large fluctuations may set in as more polynomials are considered, *i.e.*

$$f(x) \approx \frac{1}{\pi\sqrt{1-x^2}} \left(\mu_0 + 2 \sum_{n=1}^{N_{\text{poly}}} \mu_n T_n(x) \right) \quad (2.49)$$

could be a poor approximation of f . The fluctuations leading to loss of precision are known as *Gibbs oscillations*. If f is discontinuous or has singularities, the situation worsens even more.

Gibbs oscillations are damped by modifying the expansion coefficients $\mu_n \rightarrow g_n \mu_n$, so that they depend on the order of the polynomial, leading to the KPM approximation of f :

$$f_{\text{KPM}}(x) = \frac{1}{\pi\sqrt{1-x^2}} \left(g_0 \mu_0 + 2 \sum_{n=1}^{N_{\text{poly}}} g_n T_n(x) \mu_n \right). \quad (2.50)$$

This potentially more stable KPM approximation of f corresponds to a convolution of f with a kernel of the form

$$K_{N_{\text{poly}}}(x, y) = g_0 \phi_0(x) \phi_0(y) + 2 \sum_{n=1}^{N_{\text{poly}}} g_n \phi_n(x) \phi_n(y), \quad (2.51)$$

so that the original expansion of f in terms of Chebyshev polynomials is modified to

$$\begin{aligned}
f_{\text{KPM}}(x) &= \int_{-1}^1 \pi \sqrt{1-y^2} K_{N_{\text{poly}}}(x, y) f(y) dy \\
&= \langle K_{N_{\text{poly}}}(x, y) | f(y) \rangle_2 \\
&= \frac{1}{\pi \sqrt{1-x^2}} \left(g_0 \underbrace{\int_{-1}^1 f(y) dy}_{\mu_0} + 2 \sum_{n=1}^{N_{\text{poly}}} g_n T_n(x) \underbrace{\int_{-1}^1 T_n(y) f(y) dy}_{\mu_n} \right)
\end{aligned} \tag{2.52}$$

Now the question is that of finding the optimal kernel for each application. In the following sections, I consider several kernels.

The Dirichlet kernel is obtained by setting $g_n^D = 1$. This is the simplest choice and is equivalent to truncating the series, which is not ideal, as was previously discussed. If the function to be approximated is continuous, this should actually be enough to obtain an acceptable result since the Gibbs oscillations typically never become too severe.

To obtain a quantity that measures the deviation of the KPM approximation from the actual function, one uses the definition of the norm $\|f\|_2 = \sqrt{\langle f | f \rangle_2}$ as $N_{\text{poly}} \rightarrow +\infty$, which is in general not sufficiently restrictive to ensure convergence. This is easily understood. Recall that power series converge absolutely inside their convergence radius. Given a point x_0 lying within the radius of convergence, the point-wise condition holds

$$\frac{\sum_{n=0}^{N_{\text{poly}}-1} \frac{2a_n}{1+\delta_{n,0}} T_n(x_0)}{\pi \sqrt{1-x_0^2}} \xrightarrow{N_{\text{poly}} \rightarrow +\infty} f(x_0). \tag{2.53}$$

Yet, the series may converge at different rates for different values of x . Different choices of kernel mitigate this problem. For example, the Fejér kernel is obtained by setting $g_n^F = 1 - \frac{n}{N_{\text{poly}}}$, so that

$$K_{N_{\text{poly}}}^F(x, y) = \frac{1}{N_{\text{poly}}} \sum_{\nu=1}^{N_{\text{poly}}} K_{\nu}^D(x, y), \tag{2.54}$$

Intuitively, it corresponds to assigning progressively less weight to higher-order polynomials, which presumably contribute less to the approximation of the target function. The advantage of this kernel is that for a continuous function, the approximation

has been shown to converge uniformly in any restricted interval $I = [-1 + \varepsilon, 1 - \varepsilon] \forall \varepsilon > 0$, *i.e.*

$$\|f - f_{\text{KPM}}\|_{\infty}^{\varepsilon} \equiv \max_I |f(x) - f_{\text{KPM}}(x)| \xrightarrow{N_{\text{poly}} \rightarrow +\infty} 0. \quad (2.55)$$

Uniform convergence is disrupted in the vicinity of the end points $x = \pm 1$ due to the presence of the factor $\sqrt{1 - x^2}$ in the denominator. For the applications I am interested in, it is generally possible to carry out a change of variable so that $x \in [-1/s, 1/s]$, with $s \gtrsim 1$. Normally this process is a rescaling of the Hamiltonian $H \rightarrow \tilde{H}$, where s can be chosen so that uniform convergence is ensured.

[174]: Weisse et al. (2006), 'The kernel polynomial method'

The conditions for uniform convergence are the following [174]:

Positive kernel $K_{N_{\text{poly}}}(x, y) > 0 \forall x, y \in]-1, 1[$;

Normalised kernel $\int_{-1}^1 K_{N_{\text{poly}}}(x, y) dx = \phi_0(y) \iff g_0 = 1$;

Limit of second coefficient $g_1 \rightarrow 1$ as $N_{\text{poly}} \rightarrow \infty$.

The second and third conditions can be verified by inspection of Equation 2.54. I explain the proof of the first condition in Appendix A.1. A few remarks are now in order.

- $g_{n>2}$ are restricted only through $K_{N_{\text{poly}}}(x, y) > 0$, which is equivalent to requiring the map to be monotonic:

$$f \rightarrow f_{\text{KPM}}, \text{ with } f \geq f' \implies f_{\text{KPM}} \geq f'_{\text{KPM}}. \quad (2.56)$$

- The conditions of positivity and normalisation are useful in practice. From the first, one may induce that the approximation of positive quantities is positive, and from the second, the integral of the expanded function is conserved:

$$\int_{-1}^1 f_{\text{KPM}}(x) dx = \int_{-1}^1 f(x) dx. \quad (2.57)$$

For example, if one applies the kernel to a density of states, one obtains a strictly positive, normalised approximation.

- A good measure of the error of an order- N_{poly} approximation for a continuous function is the modulus of continuity

$$w_f(\Delta) = \max_{|x-y| \leq \Delta} |f(x) - f(y)|. \quad (2.58)$$

The Fejér kernel leads to an error of order $\mathcal{O}(1/\sqrt{N_{\text{poly}}})$ for sufficiently smooth functions, since it satisfies

$$\|f - f_{\text{KPM}}\|_{\infty} \sim w_f(1/\sqrt{N_{\text{poly}}}). \quad (2.59)$$

The resolution or broadening that is obtained when expanding less regular functions containing discontinuities or singularities is also of order $\mathcal{O}(1/\sqrt{N_{\text{poly}}})$.

The Jackson kernel improves upon the Féjer kernel. It is based on demanding optimal resolution by minimising the so called variance of the kernel

$$Q \equiv \int_{-1}^1 \int_{-1}^1 (x - y)^2 K_{N_{\text{poly}}}(x, y) dx dy. \quad (2.60)$$

Since the kernel will peak for $x = y$, Q is approximated as the squared width of this peak. In Appendix A.2, I show that the weight that defines the Jackson kernel is given by

$$g_n^J = \frac{(N_{\text{poly}} - n + 1) \cos \frac{\pi n}{N_{\text{poly}} + 1} + \sin \frac{\pi n}{N_{\text{poly}} + 1} \cot \frac{\pi}{N_{\text{poly}} + 1}}{N_{\text{poly}} + 1}. \quad (2.61)$$

In my derivation, the quantity $\sqrt{Q_{\text{min}}} \sim 1/N_{\text{poly}}$ emerges as a measure of the spread of the Jackson kernel in the $x - y$ plane. In contrast, I have mentioned that when using the Féjer kernel, the error can be shown to scale as $1/\sqrt{N_{\text{poly}}}$, which illustrates the superiority of the Jackson kernel. For the Féjer kernel, I imposed the conditions $g_0 = 1$ and $g_1 \rightarrow 1$ as $N \rightarrow +\infty$. The calculation of Appendix A.2 gives some insight on the success of the Jackson kernel by revealing that it not only requires that $g_1 \rightarrow 1$ as $N \rightarrow +\infty$, but also that the rate at which this limit is approached is optimised.

In practice, the calculations I generally focus on often involve singular functions. The Jackson kernel has disadvantages for singular functions, which become apparent *e.g.* when examining the behaviour of its KPM approximation of the δ -function:

$$\begin{aligned} \delta_{\text{KPM}}(x - x_0) &= \langle K_{N_{\text{poly}}}(x, y) | \delta(y - x_0) \rangle_2 \\ &= g_0 \phi_0(x) T_0(x_0) + 2 \sum_{n=1}^{N_{\text{poly}}-1} g_n \phi_n(x) T_n(x_0). \end{aligned} \quad (2.62)$$

Under convolution with the kernel, the δ -function broadens. I will inspect the scaling of the width of the approximated δ -function and conclude that it behaves similarly to a Gaussian. In the following section, it will become clear that a more convenient approximation of the Dirac delta is obtained with a broader peak.

The broadening is defined by the variance $\sigma = \sqrt{\langle x^2 \rangle_{\text{KPM}} - \langle x \rangle_{\text{KPM}}^2}$. By writing the powers of x in terms of Chebyshev polynomials ($x = T_1(x)$ and $x^2 = \frac{T_2(x) + T_0(x)}{2}$), one can use Equation 2.38 to arrive at

$$\langle x \rangle_{\text{KPM}} = \int_{-1}^1 x \delta_{\text{KPM}}(x - x_0) dx = g_1 T_1(x_0), \quad (2.63)$$

$$\langle x^2 \rangle_{\text{KPM}} = \int_{-1}^1 x^2 \delta_{\text{KPM}}(x - x_0) dx = \frac{g_0 T_0(x_0) + g_2 T_2(x_0)}{2}. \quad (2.64)$$

Hence, the width of $\delta_{\text{KPM}}(x - x_0)$ is given by

$$\begin{aligned} \sigma^2 &= x_0^2 (g_2 - g_1^2) + \frac{g_0 - g_2}{2} \\ &= \frac{N_{\text{poly}} - x_0^2 (N_{\text{poly}} - 1)}{2(N_{\text{poly}} + 1)} \left(1 - \cos \frac{2\pi}{N_{\text{poly}} + 1} \right) \\ &\approx \left(\frac{\pi}{N_{\text{poly}}} \right)^2 \left(1 - x_0^2 + \frac{3x_0^2 - 2}{N_{\text{poly}}} \right). \end{aligned} \quad (2.65)$$

for large N_{poly} . An expansion of order N_{poly} of δ using the Jackson kernel results in a broadening of the peak, yielding a width $\sigma \sim \pi/N_{\text{poly}}$ for $x_0 \ll 1$. Close to the boundaries, one has $x_0 \lesssim 1$ and the last term now dominates, leading to $\sigma = \pi/N_{\text{poly}}^{3/2}$. This is consistent with a peak that closely approximates a Gaussian, as advertised above:

$$\delta_{\text{KPM}}^J(x) \approx \frac{1}{\sqrt{2\pi\sigma^2}} \exp\left(-\frac{x^2}{2\sigma^2}\right). \quad (2.66)$$

While the Jackson kernel is the most widely applicable one, some functions have special analytical properties, which can only be accounted for by other kernels. An example of such a function is the Dirac delta, which I am particularly interested in approximating. To this end, the most well suited kernel is the Lorentz kernel, which is normally used to compute Green's functions.

Recall the Sokhotski-Plemelj formula:

$$\lim_{\eta \rightarrow 0} \frac{1}{x \pm i\eta} = \text{P} \frac{1}{x} \mp i\pi\delta(x), \quad (2.67)$$

where $\eta > 0$ is an infinitesimal quantity and P is the principal value. As $\eta \rightarrow 0$, the δ -function is approached by means of a Lorentzian

$$\delta(x) = -\frac{1}{\pi} \lim_{\eta \rightarrow 0} \text{Im} \frac{1}{x + i\eta} = \lim_{\eta \rightarrow 0} \frac{\eta}{\pi(x^2 + \eta^2)}, \quad (2.68)$$

which has a broader shape compared with the Gaussian given by the Jackson kernel. The Lorentz kernel gives a better approximation of the Lorentzian, while remaining strictly positive, unlike the Jackson kernel. This is important because it ensures that some basic properties of the Green's function are obeyed, namely that poles are located in the lower (upper) half complex plane for retarded (advanced) Green functions.

The coefficients of the Lorentz kernel are given by

$$g_n^L = \frac{\sinh[\lambda(1 - n/N)]}{\sinh \lambda}. \quad (2.69)$$

λ is a free parameter that needs to be adjusted so as to achieve a balance between accuracy and convergence speed. A good compromise between sufficient damping of the Gibbs oscillations and resolution is typically given by $\lambda \sim 3 - 5$. Finally, notice that when $\lambda \rightarrow 0$, one recovers the Fejér kernel $K_N^F(x, y)$, with $g_n^F = 1 - n/N$. This suggests that the two kernels share some properties.

2.6.3 Delta function and density of states

I close this section with the concrete example of the density of states of a Heisenberg chain. The model Hamiltonian is given in Equation 2.24. I consider the one-dimensional case with periodic boundary conditions, *i.e.* each spin has two neighbours, one to the left and the other to the right and the first spin has the last spin as its neighbour, forming a 'ring'. The eigenvalues of the Hamiltonian for a 14-spin ring are shown in Figure 2.3.

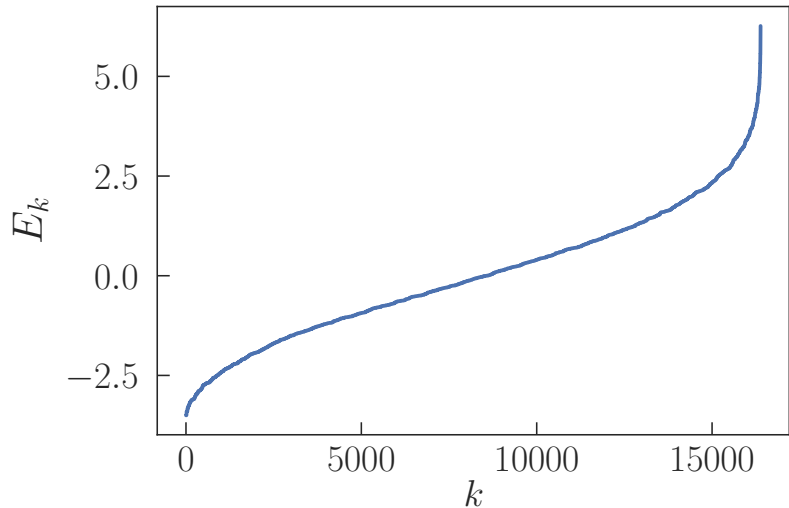


Figure 2.3: Eigenvalues of a 14-spin Heisenberg chain.

As a preliminary example, I consider a delta function centered at x_0 . Its expansion in Chebyshev polynomials of the first kind is given by Equation 2.47, with the coefficients μ_n as per Equation 2.46:

$$\mu_n = \int_{-1}^1 T_n(x) \delta(x - x_0) dx = T_n(x_0). \quad (2.70)$$

Thus, the Chebyshev expansion of the Dirac delta is

$$\delta(x - x_0) = \frac{1}{\pi \sqrt{1 - x^2}} \left(1 + 2 \sum_{n=1}^{N-1} T_n(x_0) T_n(x) \right). \quad (2.71)$$

In order to compute the density states of the Heisenberg chain, one would have to perform a sum of Dirac deltas over an exponentially large ($D = 2^N$) space involving the full spectrum:

$$\rho(E) = \frac{1}{D} \sum_{k=0}^{D-1} \delta(E - E_k). \quad (2.72)$$

The energy must be rescaled, so that it falls in the interval $]-1, 1[$. Here, I assume that the appropriate transformation has already been done. In Section 2.7.3, I shall provide more details about this transformation. In analogy with the Chebyshev expansion of the delta function, the μ_n coefficients of the Chebyshev expansion of the density of states are computed using Equation 2.46.

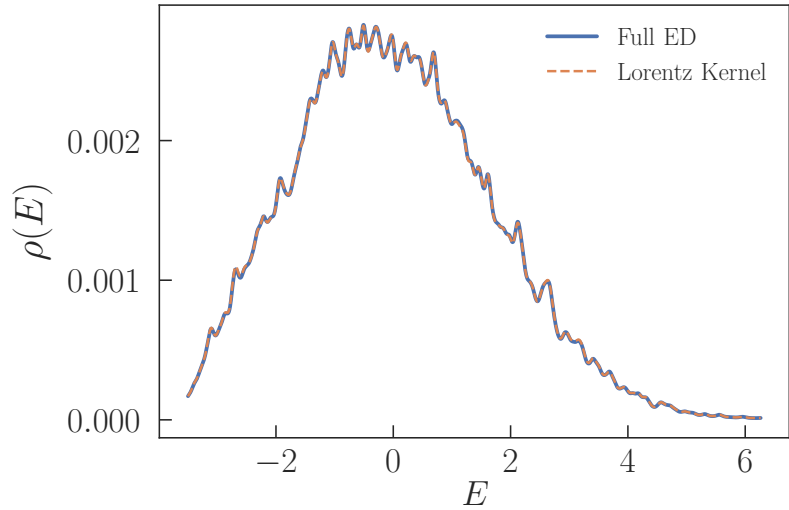
$$\begin{aligned} \mu_n &= \int_{-1}^1 \rho(E) T_n(E) dE \\ &= \frac{1}{D} \sum_{k=0}^{D-1} T_n(E_k) \\ &= \frac{1}{D} \sum_{k=0}^{D-1} \langle k | T_n(\hat{H}) | k \rangle \\ &= \frac{1}{D} \text{Tr}[T_n(\hat{H})]. \end{aligned} \quad (2.73)$$

One can use the STE to approximate the trace. The moments μ_n are modified using a suitable kernel in order to attenuate Gibbs oscillations. Here, the Lorentz kernel is the appropriate choice:

$$\rho_{\text{KPM}}(E) = \frac{1}{\pi D \sqrt{1 - E^2}} \sum_{n=0}^{N_{\text{poly}}} \sum_{r=0}^{N_{\text{rd, vec.}}} \frac{2}{1 + \delta_{n,0}} g_n^L \langle r | T_n(\hat{H}) | r \rangle T_n(E). \quad (2.74)$$

In the previous section, I have mentioned that the Lorentzian curve approaches a delta function as its width η is decreased. I will use Lorentzians as a benchmark for my expansion of the delta functions in the density of states in Chebyshev polynomials. The Lorentz kernel approximation of the delta function converges to a Lorentzian with width $\eta = \lambda/N_{\text{poly}}$, which in turn approaches a delta function as $\eta \rightarrow 0$. In this sense, λ is akin to the resolution of the calculation.

Figure 2.4: Density of states of a 14-spin Heisenberg chain. The blue curve is obtained via a sum of Lorentzians centered at the eigenvalues of the Hamiltonian. These are obtained by fully diagonalising the Hamiltonian numerically. The dotted orange curve is the kernel polynomial approximation obtained using the Lorentz kernel with $N_{\text{poly}} = 1500$, $N_{\text{rd. vec.}} = 100$ and $\eta = 5 \times 10^{-3}$.



In Figure 2.4, I compare the density of states obtained from a full diagonalisation of the Hamiltonian with the Lorentz kernel approximation. The results match perfectly. Yet, full diagonalisation required about 4000 times more computer memory than the Chebyshev approach.

2.7 Microcanonical ensemble

In the standard Lanczos algorithm described in detail in Section 2.5, the core of the spectrum of \hat{h} is inaccessible. Loss of orthogonality due to finite machine precision impedes convergence beyond low-lying excitations. To complicate matters further, reorthogonalisation schemes are computationally expensive [192]. In Section 2.6, I reviewed a method that can be used to access the energy dependence of quantities of interest, such as the density of states. An alternative approach is to set a target energy, construct a quasi-eigenstate corresponding to that energy and compute observables using the obtained microcanonical state. All of the methods I describe in this section follow that prescription, whilst using different schemes to construct the quasi-eigenstate. In particular, the last method I shall describe in this section has many aspects in common with the method of Section 2.6. Even though it is also based on

[192]: Sandvik (2010), ‘Computational Studies of Quantum Spin Systems’

Chebyshev expansions, crucially it does not require the use of a kernel and is based on a numerically exact expansion of the Green function.

2.7.1 Microcanonical Lanczos

In the MCLM [17, 197], excited states in the core of the spectrum — and thus inaccessible to the “ground state” Lanczos method — are probed by setting a target energy density, ε and finding the lowest-lying eigenpair of

$$\hat{v} = (\hat{h} - \varepsilon)^2. \quad (2.75)$$

The lowest eigenvalue found by performing a Lanczos recursion with \hat{v} approaches 0 and, using its corresponding Lanczos vectors, one can construct the quasi-eigenstate $|\psi_\varepsilon\rangle$. MCLM converges slower than the standard Lanczos approach in most applications. For example, the microcanonical variant was found to require $\mathcal{O}(10^3)$ iterations to construct a quasi-eigenstate in the spin-1/2 Heisenberg chain [197]. This is to be contrasted to the standard Lanczos algorithm, which typically requires $\mathcal{O}(10^2)$ iterations to retrieve a low-lying state [17]. The energy uncertainty reads

$$\sigma_\varepsilon = \sqrt{\langle \psi_\varepsilon | \hat{v} | \psi_\varepsilon \rangle}. \quad (2.76)$$

As a rule of thumb, in Reference [17], the authors state that in order to resolve the desired energy level with small energy spread $\sigma_\varepsilon/W < 10^{-3}$, where W is the spectrum width, $M' \sim 10^3$ iterations are typically needed. Then, the quasi-eigenstate can be used to compute observables reliably. The computational complexity is dominated by two main components. One of them comes from the diagonalisations of the tridiagonal matrices at each Lanczos iteration. Since I use MR [193, 195, 196] for these diagonalisations, the number of floating point operations for this part scale as

$$\sum_{m=1}^{M'} m^2 = M'(M' + 1)(2M' + 1)/6 \sim \mathcal{O}(M'^3). \quad (2.77)$$

The other component comes from the M' matrix-vector multiplications in the Lanczos recursion, each carried out “on-the-fly”, incurring a cost $\mathcal{O}(zD \log_2 D)$, where z is the coordination number of the lattice. Thus, the computational effort from matrix-vector multiplications scales as $\mathcal{O}(zM'D \log_2 D)$, where $D = 2^N$ for spin-1/2 systems.

[17]: Prelovšek et al. (2013), ‘Ground State and Finite Temperature Lanczos Methods’

[197]: Long et al. (2003), ‘Finite-temperature dynamical correlations using the microcanonical ensemble and the Lanczos algorithm’

[193]: Dhillon (1997), *A New $O(n^2)$ Algorithm for the Symmetric Tridiagonal Eigenvalue/Eigenvector Problem*

[195]: Dhillon et al. (2006), ‘The design and implementation of the MRRR algorithm’

[196]: Demmel et al. (2008), ‘Performance and Accuracy of LAPACK’s Symmetric Tridiagonal Eigensolvers’

For $N \gtrsim 20$, the ratio between the two costs is $zD \log_2 D/M'^2 \gtrsim 1$, and the computational complexity is dominated by the cost of matrix-vector multiplication. However, if the more standard implicit QR method is used for diagonalisation instead of MR, the complexity of the diagonalisation increases to $\mathcal{O}(M'^4)$. The relevant ratio of computational costs becomes $zD \log_2 D/M'^3$, which only becomes significantly larger than 1 for $N \gtrsim 30$.

As a final note on memory cost, I remark that the \hat{h}^2 -term in Equation 2.75 requires an additional vector to be stored in memory compared with the ‘ground state’ Lanczos, increasing the number of stored D -vectors to four.

2.7.2 Thermal pure quantum states

[34]: Sugiura et al. (2012), ‘Thermal Pure Quantum States at Finite Temperature’

In this subsection, I follow closely the work of Sugiura and Shimizu [34]. The rationale of the microcanonical variant of the TPQ method (MTPQ) is to find a pure state that faithfully captures the equilibrium properties of a quantum system at finite temperature as accurately as possible using microcanonical TPQ states with well defined energy, constructed as follows. First, one generates a random state

$$|\phi_0\rangle \equiv \sum_{i=1}^D \xi_i |i\rangle. \quad (2.78)$$

For simplicity, $\{|i\rangle\}$ is usually taken as the set of product states of individual spins. The distribution of energy in $|\phi_0\rangle$ is proportional to the density of states

$$g(u; N) = \exp[Ns(u; N)], \quad (2.79)$$

where $s(u; N)$ is the entropy density, which converges to a function of the energy density, $s(u; \infty)$, in the thermodynamic limit [34].

The basic procedure is an iterative one similar to minimisation annealing schemes. The goal is to modify the distribution of energy in the random state so that it becomes sharply peaked at the desired energy density, ε . In Section A.3, I detail how such a distribution is achieved and how a correspondence between energy densities and temperatures is readily available. A microcanonical TPQ state is achieved by operating with a suitable polynomial of the Hamiltonian density onto $|\phi_0\rangle$ iteratively. Take a constant $\varepsilon_{\text{upper}} \sim \mathcal{O}(1)$, such that $\varepsilon_{\text{upper}} \geq \varepsilon_M$, where ε_M is the maximum eigenvalue of the Hamiltonian density. Thus, $\varepsilon_{\text{upper}}$ is an upper bound on the spectrum of \hat{h} . Then, start from $|\phi_0\rangle$ and iteratively

compute, respectively the energy density, u_k and the (normalised) new state, $|\phi_{k+1}\rangle$ at iteration k :

$$u_k = \langle \phi_k | \hat{h} | \phi_k \rangle, \quad |\phi_{k+1}\rangle = \frac{|\Phi_{k+1}\rangle}{\sqrt{\langle \Phi_{k+1} | \Phi_{k+1} \rangle}}, \quad \text{where } |\Phi_{k+1}\rangle \equiv (\varepsilon_{\text{upper}} - \hat{h}) |\phi_k\rangle \quad (2.80)$$

iteratively for $k = 1, 2, \dots, N_{\text{it}}$, the maximum number of iterations. Later on, the reader will see that N_{it} plays a role analogous to the inverse of the resolution in the Chebyshev expansion. Since the microcanonical states are now generated directly, as opposed to being reconstructed via a Lanczos recursion, the memory cost is now dominated by two D -vectors rather than four.

The first energy density corresponds to the infinite temperature state at $\beta = 0$. Thus, $g(u; N)$ has its maximum at $u = u_0$. Then, the energy density decreases gradually towards the ground state energy, ε_m , as k is increased: $u_0 > u_1 > \dots > u_{N_{\text{it}}} \geq \varepsilon_m$. One stops iterating at $k = N_{\text{it}}$, when u_k gets close enough to the ground state energy density, ε_m . The obtained TPQ states in the sequence $|\phi_0\rangle, |\phi_1\rangle, \dots, |\phi_{N_{\text{it}}}\rangle$ correspond to decreasing thermal energy densities $u_0 > u_1 > \dots > u_{N_{\text{it}}}$. Thus, an estimate of the equilibrium average value of an arbitrary observable \hat{A} is obtained as $\langle \hat{A} \rangle_k = \langle \phi_k | \hat{A} | \phi_k \rangle$ as a function of u_k . Notably, in the large system limit, the effective temperature associated with each TPQ iteration, $1/\beta_k$, accurately reproduces the true thermodynamic temperature of a state with energy density u_k . In fact, it is possible to approximate the thermodynamic temperature with an error of order $\mathcal{O}(1/N^2)$ [34] (see also Appendix A.4).

Finally, the static expectation value $\langle \hat{A} \rangle_k$ obtained for each realisation of the random coefficients $\{\xi_i\}$ depends exponentially less on the number of sites, N , as the latter is increased, due to self averaging properties. Hence, accurate results are often obtained with a few or even a single random vector realisation [34, 35].

2.7.3 Chebyshev polynomial Green's function

CPGF consists of numerically evaluating the lattice resolvent operator

$$\hat{G}(z) = (z - \hat{h})^{-1} \quad (2.81)$$

via an exact expansion in terms of Chebyshev polynomials of the Hamiltonian density. Here, $z = \varepsilon + i\eta$ is a complex energy variable. A key aspect is that the Green's function is reconstructed with uniform energy resolution over the entire energy range.

[34]: Sugiura et al. (2012), 'Thermal Pure Quantum States at Finite Temperature'

[35]: Sugiura et al. (2013), 'Canonical Thermal Pure Quantum State'

For numerical stability, the resolution parameter should satisfy $\eta = \text{Im } z \gtrsim \delta \varepsilon$, where $\delta \varepsilon$ is the mean level spacing. To expand Equation 2.81 in Chebyshev polynomials, I consider the following linear transformation of the Hamiltonian and the energy variables: $\tilde{h} = (\hat{h} - b)/a$ and $\tilde{z} = \tilde{\varepsilon} + i\tilde{\eta}$, where $\tilde{\varepsilon} = (\varepsilon - b)/a$, $\tilde{\eta} = \eta/a$, and

$$a = f \frac{\varepsilon_M - \varepsilon_m}{2} \quad b = \frac{\varepsilon_M + \varepsilon_m}{2}, \quad (2.82)$$

where ε_M and ε_m are the extremal eigenvalues and $f \simeq 1.001$ is a safety factor to ensure that the spectrum of the reconstructed operator falls inside the Chebyshev domain of convergence at each iteration step. As customary, I work with Chebyshev polynomials of the first kind $\{T_n(x) = \cos(n \arccos x), n = 0, 1, 2, \dots\}$ due to their favourable convergence properties [187].

[187]: Boyd (1989), *Chebyshev & Fourier Spectral Methods*

Typical target functions of energy, including density of states and static expectations values, are evaluated by making use of the Chebyshev polynomial expansion of the imaginary part of the rescaled Green's function [189]

[189]: Ferreira et al. (2015), 'Critical Delocalization of Chiral Zero Energy Modes in Graphene'

$$\text{Im}[\hat{G}(\tilde{\varepsilon} + i\tilde{\eta})] = \sum_k \frac{\tilde{\eta}}{(\tilde{\varepsilon} - \tilde{\varepsilon}_k)^2 + \tilde{\eta}^2} |k\rangle \langle k| = \sum_{n=0}^{\infty} \text{Im}[g_n(\tilde{z})] T_n(\tilde{h}), \quad (2.83)$$

with

$$g_n(z) = \frac{-2i}{1 + \delta_{0,n}} \frac{(z - i\sqrt{1-z^2})^n}{\sqrt{1-z^2}}. \quad (2.84)$$

Below, I derive the closed form for the coefficients of the expansion of Equation 2.84.

Proof. I start by expressing the lattice Green's function using the eigenvalues $\{\varepsilon_k\}$ and the eigenstates $\{|k\rangle\}$. For convenience, in my notation, I assume that the energy has already been rescaled onto the appropriate interval, so I drop the tildes, e.g. ε is shorthand for $\tilde{\varepsilon}$.

$$\hat{G}(\varepsilon + i\eta) = \sum_k \frac{1}{\varepsilon - \varepsilon_k + i\eta} |k\rangle \langle k|. \quad (2.85)$$

Below, I prove that this operator can also be expressed as

$$\hat{G}(\varepsilon + i\eta) = -i \int_0^{\infty} dt e^{i(\varepsilon+i\eta)t} e^{-i\hat{H}t} \quad (2.86)$$

First, I express the Hamiltonian in terms of the eigenvalues and eigenstates. Then, I switch the integral and the summation:

$$\begin{aligned}
 -i \int_0^\infty dt e^{i(\varepsilon+i\eta)t} e^{-i\hat{H}t} &= -i \int_0^\infty dt e^{i(\varepsilon+i\eta)t} \sum_k e^{-i\varepsilon_k t} |k\rangle \langle k| \\
 &= \sum_k \left(-i \int_0^\infty dt e^{i(\varepsilon+i\eta-\varepsilon_k)t} \right) |k\rangle \langle k|.
 \end{aligned} \tag{2.87}$$

Now, it remains to prove that the quantity in brackets is equal to $(\varepsilon + i\eta - \varepsilon_k)^{-1}$:

$$\begin{aligned}
 -i \int_0^\infty dt e^{i(\varepsilon+i\eta-\varepsilon_k)t} &= -i \int_0^\infty dt e^{-\eta t} e^{i(\varepsilon-\varepsilon_k)t} \\
 &= \int_0^\infty dt e^{-\eta t} \sin(\varepsilon - \varepsilon_k)t - i \int_0^\infty dt e^{-\eta t} \cos(\varepsilon - \varepsilon_k)t \\
 &= \frac{1}{(\varepsilon - \varepsilon_k)^2 + \eta^2} \left\{ e^{-\eta t} \left[-\eta \sin(\varepsilon - \varepsilon_k)t - (\varepsilon - \varepsilon_k) \cos(\varepsilon - \varepsilon_k)t \right] \right\}_0^\infty \\
 &\quad - i \frac{1}{(\varepsilon - \varepsilon_k)^2 + \eta^2} \left\{ e^{-\eta t} \left[-\eta \cos(\varepsilon - \varepsilon_k)t + (\varepsilon - \varepsilon_k) \sin(\varepsilon - \varepsilon_k)t \right] \right\}_0^\infty \\
 &= \frac{\varepsilon - \varepsilon_k + i\eta}{(\varepsilon - \varepsilon_k)^2 + \eta^2} = \frac{1}{\varepsilon - \varepsilon_k + i\eta}.
 \end{aligned} \tag{2.88}$$

Notice that one can use the Jacobi-Anger identity

$$e^{-ixz} = \sum_{n=0}^{\infty} \frac{2i^{-n}}{1 + \delta_{0,n}} J_n(z) T_n(x), \quad |x| \leq 1, \tag{2.89}$$

where J_n is Bessel function of the first kind of order n , to write the lattice Green function in terms of a series of Chebyshev polynomials. To do that, one needs to use the Laplace transform of the Bessel function

$$\int_0^\infty dt e^{-st} J_n(t) = \frac{1}{\sqrt{1+s^2}} \left(\sqrt{1+s^2} - s \right)^n. \tag{2.90}$$

The lattice Green function can then be recast as a Chebyshev series:

$$\begin{aligned}
\hat{G}(z) &= -i \int_0^\infty dt e^{i(\varepsilon+i\eta)t} \left[\sum_{n=0}^\infty \frac{2i^{-n}}{1+\delta_{0,n}} J_n(t) T_n(\hat{H}) \right] \\
\text{let } s &= -i(\varepsilon+i\eta) \\
&= -i \sum_{n=0}^\infty \frac{2i^{-n}}{1+\delta_{0,n}} \frac{(\sqrt{1+s^2}-s)^n}{\sqrt{1+s^2}} T_n(\hat{H}) \\
&= \sum_{n=0}^\infty \frac{-2i}{1+\delta_{0,n}} \frac{(-i\sqrt{1+s^2}+is)^n}{\sqrt{1+s^2}} T_n(\hat{H}) \\
&= \sum_{n=0}^\infty g_n(z) T_n(\hat{H}), \text{ with } z = is
\end{aligned} \tag{2.91}$$

□

The operators $T_n(\tilde{h})$ of Equation 2.83 are constructed using the operator versions of the Chebyshev recursion relation

$$\begin{aligned}
T_0(\tilde{h}) &= 1, \\
T_1(\tilde{h}) &= \tilde{h}, \\
T_{n+1}(\tilde{h}) &= 2\tilde{h}T_n(\tilde{h}) - T_{n-1}(\tilde{h}).
\end{aligned} \tag{2.92}$$

The series is truncated when the desired accuracy is achieved for a given choice of resolution. The $(N_{\text{poly}} + 1)$ -th order approximation of the lattice Green's function is therefore

$$\hat{G}_{N_{\text{poly}}+1}(\tilde{\varepsilon} + i\tilde{\eta}) \equiv \sum_{n=0}^{N_{\text{poly}}} g_n(\tilde{\varepsilon} + i\tilde{\eta}) T_n(\tilde{h}). \tag{2.93}$$

[190]: João et al. (2020), 'KITE'

For most cases, $N_{\text{poly}} = c\tilde{\eta}^{-1}$, with $c = \mathcal{O}(1)$ sufficing to achieve machine precision [190].

The spectral operator within the CPGF approach can be defined as follows

$$\delta_{\tilde{\eta}}(\tilde{\varepsilon} - \tilde{h}) = -\frac{1}{\pi} \sum_n \text{Im}[g_n(\tilde{\varepsilon} + i\tilde{\eta})] T_n(\tilde{h}). \tag{2.94}$$

By applying this operator to the r -th realisation of the random state $|\phi_0^{(r)}\rangle$, I obtain $|\tilde{\varepsilon}, \tilde{\eta}\rangle_r$, a quasi-eigenstate with rescaled energy $\tilde{\varepsilon}$ (within the rescaled resolution $\tilde{\eta}$). To compute static expectation values, I start by defining

$$\{\hat{A}\}_r(\varepsilon, \eta) \equiv \langle \varepsilon, \eta | \hat{A} | \varepsilon, \eta \rangle_r = a^{-2} \langle \tilde{\varepsilon}, \tilde{\eta} | \hat{A} | \tilde{\varepsilon}, \tilde{\eta} \rangle_r. \tag{2.95}$$

Provided that the resolution η is adequate ($\eta \rightarrow \delta\varepsilon \Leftrightarrow \tilde{\eta} \rightarrow \delta\varepsilon/a$, where $\delta\varepsilon$ is the mean level spacing), one obtains an accurate estimate of the expectation value of \hat{A} for a given energy ε , $A(\varepsilon)$ by averaging over realisations of the initial random state and using Equation 2.95:

$$\langle A \rangle_{\text{STE}}(\varepsilon, \eta) = \frac{\sum_{r=1}^{N_{\text{rd.vec.}}} \{\hat{A}\}_r(\varepsilon, \eta)}{\sum_{r=1}^{N_{\text{rd.vec.}}} \{\hat{1}\}_r(\varepsilon, \eta)} \xrightarrow{\eta \rightarrow \delta\varepsilon^+} A(\varepsilon). \quad (2.96)$$

Similarly to the Lorentz kernel, CPGF allows one to choose the desired resolution *a priori*. However, unlike the former — which is only optimal for approximating functions with special analytical properties like the Dirac delta — the CPGF method is universally applicable. Moreover, it has better convergence properties because there is no need to use a kernel at all. These are significant advantages of CPGF with respect to KPM.

Below, I illustrate these ideas for the specific example of the density of states of the Heisenberg chain, which I have already computed with KPM using the Lorentz kernel. I compare CPGF with KPM and illustrate how in some cases, one can avoid constructing quasi-eigenstates and simply reconstruct the relevant quantity using Chebyshev moments. This process will also be used later on when studying dynamics.

It is possible to use the expansion of Equation 2.83 to recast the density of states as a Chebyshev series:

$$\rho(E) = -\frac{1}{\pi D} \lim_{\eta \rightarrow 0} \sum_{n=0}^{\infty} \text{Im}[g_n(E + i\eta)] \text{Tr}[T_n(\hat{H})], \quad (2.97)$$

where the energy, E , and the resolution, η , are assumed to have undergone the appropriate transformation which guarantees that $E \in]-1, 1[$. Then, the calculation of an approximate density of states using the Chebyshev expansion boils down to computing and storing a set of moments, which can then be used to stochastically reconstruct the trace. The series is truncated once convergence is achieved for the required resolution, *i.e.* adding more polynomials does not change the approximation of the density of states.

The results of Figure 2.5 show perfect matching between the density of states from full ED and CPGF. Unlike the Lorentz kernel approximation, which requires about 1500 polynomials for convergence, CPGF only requires about 300. These results suggest that CPGF is a promising method to tackle quantum spin models.

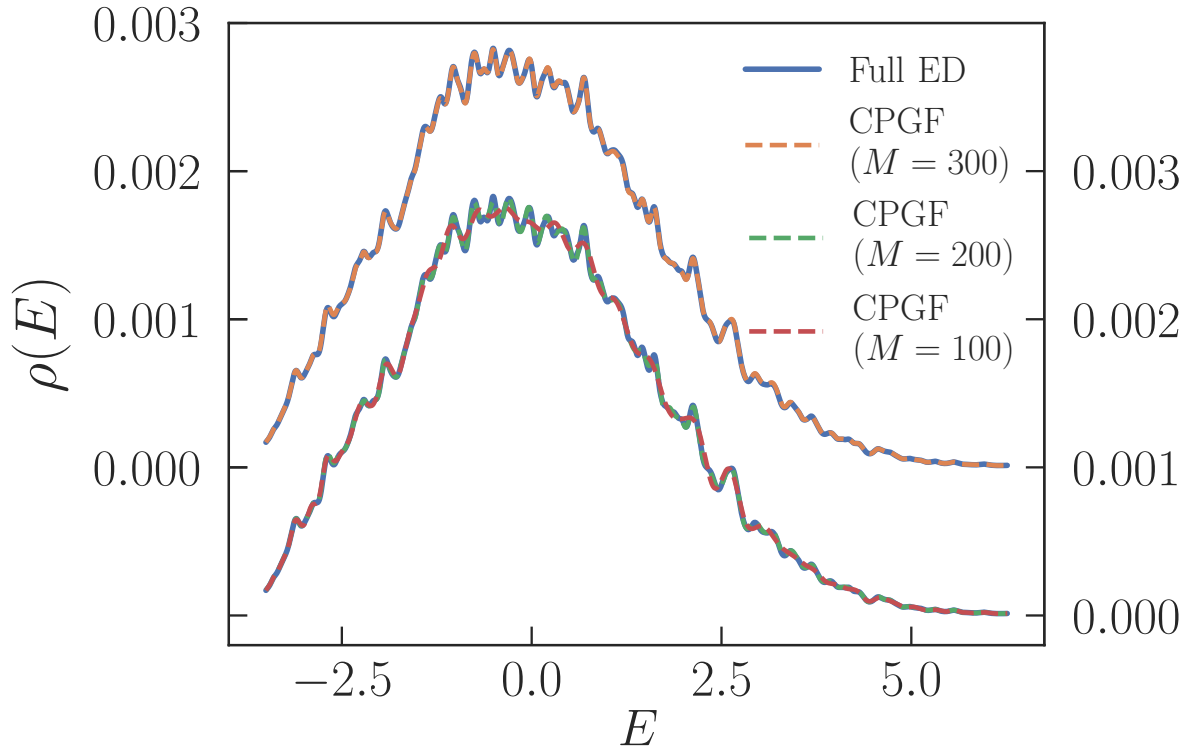


Figure 2.5: Density of states of a 14-spin Heisenberg chain. The blue curve is obtained from full exact diagonalisation of the Hamiltonian. The dotted orange curve is the CPGF result with $N_{\text{poly}} = 300$, $N_{\text{rd. vec.}} = 100$ and the same resolution as considered for KPM. In this case, CPGF converges about 5 times faster than KPM. Also shown are green and red curves corresponding to $N_{\text{poly}} = 200, 100$, respectively. The y-axis for these curves is the one on the right hand side. The convergence speed is remarkable. Even with just 100 moments, the shape of the density of states is already mostly reproduced. With 200 moments, only the sharpest peaks need to be resolved, and with 300 moments, CPGF matches the exact result.

2.8 Canonical ensemble

While microcanonical methods are useful, one might also be interested in evaluating observables using canonical states. In practice, one may decide which ensemble is more convenient to perform a given calculation because the principle of ensemble equivalence guarantees that results are consistent across statistical ensembles. For example, canonical methods have the advantage of allowing direct specification of temperature as an input, so they may be preferable to study temperature dependence of systems in thermal equilibrium. Moreover, for finite systems, calculations done with the microcanonical ensemble tend to show significant statistical fluctuations [17]. As temperature increases, higher energy states in the spectrum become increasingly important for determining the properties of the system and these statistical fluctuations are smeared out. The most interesting features of the systems I tackle in this work appear at low temperature, so the canonical methods detailed below are particularly useful in this context.

[17]: Prelovšek et al. (2013), ‘Ground State and Finite Temperature Lanczos Methods’

2.8.1 Finite temperature Lanczos method

The FTLM has been introduced in Reference [15] and discussed in depth in Reference [17]. The basic idea is to generate a set of eigenpairs $\{\varepsilon_{j,r}, |\psi_j^{(r)}\rangle\}$ using M_{FT} Lanczos steps and starting from different realisations of the initial random state. Throughout the recursion, one needs only store two sets of overlaps: $Q_{r,j} \equiv \langle \phi_0^{(r)} | \psi_j^{(r)} \rangle$ and $A_{r,j} \equiv \langle \psi_j^{(r)} | \hat{A} | \phi_0^{(r)} \rangle$. The memory cost is still dominated by the D -vectors: two for the recursion and one to store the initial random state so as to allow the computation of the overlaps, totaling three D -vectors. The STE estimator of the canonical average, $\langle A \rangle(\beta, N)$, defined as

$$\langle A \rangle(\beta, N) \equiv \frac{\text{Tr}[\hat{A}e^{-\beta\hat{H}}]}{\text{Tr}[e^{-\beta\hat{H}}]} = \frac{\text{Tr}[e^{-\beta\hat{H}/2}\hat{A}e^{-\beta\hat{H}/2}]}{\text{Tr}[e^{-\beta\hat{H}}]} \quad (2.98)$$

in the FTLM [15, 17] is obtained as

$$\langle A \rangle_{\text{STE}}(\beta, N) = \frac{\sum_{r=1}^{N_{\text{rd.vec.}}} \sum_{j=0}^{M_{\text{FT}}} e^{-N\beta\varepsilon_{j,r}} Q_{r,j} A_{r,j}}{\sum_{r=1}^{N_{\text{rd.vec.}}} \sum_{j=0}^{M_{\text{FT}}} e^{-N\beta\varepsilon_{j,r}} |Q_{r,j}|^2}. \quad (2.99)$$

Since the statistical fluctuations of this estimator increase significantly as the temperature is decreased, the need for an optimised low-temperature Lanczos method (LTLM) arose and this method has been introduced in Reference [16]. Apart from the $Q_{r,j}$ overlaps defined above, the computation of the STE estimator for this method requires the storage of $\mathcal{O}(M_{\text{FT}}^2)$ additional overlaps: $A'_{r,l,j} \equiv \langle \psi_j^{(r)} | \hat{A} | \psi_l^{(r)} \rangle$, with $l, j = 0, 1, \dots, M_{\text{FT}}$. In terms of these overlaps and using the symmetric form in the right hand side of Equation 2.98, the final estimator becomes

$$\langle A \rangle_{\text{STE}}(\beta, N) = \frac{\sum_{r=1}^{N_{\text{rd.vec.}}} \sum_{l,j=0}^{M_{\text{FT}}} e^{-N\beta(\varepsilon_{l,r} + \varepsilon_{j,r})/2} Q_{r,l} A'_{r,l,j} Q_{r,j}^*}{\sum_{r=1}^{N_{\text{rd.vec.}}} \sum_{j=0}^{M_{\text{FT}}} e^{-N\beta\varepsilon_{j,r}} |Q_{r,j}|^2}. \quad (2.100)$$

Notice that the LTLM requires a double sum with $\mathcal{O}(M_{\text{FT}}^2)$ terms. It becomes increasingly more expensive to compute these overlaps as the temperature is decreased and more Lanczos iterations M_{FT} are required. However, the estimator of Equation 2.100 has the advantage of reaching smoothly the zero temperature limit — as opposed to that of Equation 2.99 — which is the reason behind its advantageous statistical convergence properties. Below, I introduce other alternative methods to FTLM since LTLM has an inherently high cost.

[15]: Jaklič et al. (1994), ‘Lanczos method for the calculation of finite-temperature quantities in correlated systems’

[17]: Prelovšek et al. (2013), ‘Ground State and Finite Temperature Lanczos Methods’

2.8.2 Canonical thermal pure quantum states

[35]: Sugiura et al. (2013), ‘Canonical Thermal Pure Quantum State’

The microcanonical TPQ state I outlined previously is specified by the independent variables (u, N) . It can be shown [35] that its (unnormalised) canonical counterpart $|\beta, N\rangle$ — specified by the inverse temperature, β instead of u — is obtained as follows:

$$|\beta, N\rangle \equiv e^{-N\beta\hat{h}/2} |\phi_0\rangle. \quad (2.101)$$

A simple analytic transformation reminiscent of the principle of ensemble equivalence allows one to cast canonical TPQ states in terms of their microcanonical counterparts. This correspondence is obtained as follows. First, I assume that the minimum and maximum eigenvalues of \hat{h} , respectively ε_m and ε_M , are known. These can be obtained numerically, for example with Lanczos. Let one now define an unnormalised microcanonical TPQ state for a given realisation of the initial random state:

$$|k^{(r)}\rangle = \left(\frac{\varepsilon_M - \hat{h}}{W} \right)^k |\phi_0^{(r)}\rangle. \quad (2.102)$$

where $W = \varepsilon_M - \varepsilon_m$ is the spectrum width. Here, dividing by W ensures some degree of numerical stability since the operator inside parentheses is bounded. Multiplying and dividing Equation 2.101 by $e^{N\beta\varepsilon_M/2}$ and Taylor expanding the exponential, one finds:

$$|\beta, N\rangle = e^{-N\beta\varepsilon_M/2} \sum_{k=0}^{\infty} \frac{(N\beta W/2)^k}{k!} |k\rangle. \quad (2.103)$$

In the canonical TPQ formulation (CTPQ), the STE estimator is then given by

$$\langle A \rangle_{\text{STE}}(\beta, N) = \frac{\sum_{r=1}^{N_{\text{rd.vec.}}} \langle \beta, N | \hat{A} | \beta, N \rangle_r}{\sum_{r=1}^{N_{\text{rd.vec.}}} \langle \beta, N | \beta, N \rangle_r}, \quad (2.104)$$

where the subscript r means that the canonical states of Equation 2.103 have been constructed using the r -th realisation of the initial random state. Naively, one might expect that computing this expectation would involve performing a double sum over the iterations and storing $\mathcal{O}(N_{\text{it}}^2)$ overlaps, yielding a cost comparable to LTLM. This is because Equation 2.103 implies that

$$\langle \beta, N | \hat{A} | \beta, N \rangle_r \propto \sum_{k,q} \frac{(N\beta W/2)^{k+q}}{k!q!} \langle k | \hat{A} | q \rangle_r, \quad (2.105)$$

with $\langle k | \hat{A} | q \rangle_r = \langle k^{(r)} | \hat{A} | q^{(r)} \rangle$.

If the observable of interest is a constant of motion (i.e. $[\hat{A}, \hat{h}] = 0$), Equation 2.105 simplifies significantly.

Let $A_{k,r} = \langle k|\hat{A}|k\rangle_r$, $A'_{k,r} = \langle k|\hat{A}|k+1\rangle_r$. Then, one has

$$\begin{aligned} \langle \beta, N|\hat{A}|\beta, N\rangle_r &\propto \sum_k \left[\frac{(N\beta W/2)^{2k}}{(2k)!} A_{k,r} + \frac{(N\beta W/2)^{2k+1}}{(2k+1)!} A'_{k,r} \right] \\ &\equiv \{\hat{A}\}_r(\beta, N). \end{aligned} \quad (2.106)$$

In such cases, one only needs to store $4N_{\text{it}} \ll D$ overlaps for each random vector:

$$A_{k,r} = \langle k|\hat{A}|k\rangle_r, A'_{k,r} = \langle k|\hat{A}|k+1\rangle_r, N_{k,r} = \langle k|k\rangle_r, N'_{k,r} = \langle k|k+1\rangle_r.$$

Finally, for each inverse temperature, the STE expectation of Equation 2.104 can be reconstructed using the stored overlaps:

$$\langle A \rangle_{\text{STE}}(\beta, N) = \frac{\sum_{r=1}^{N_{\text{rd.vec.}}} \{\hat{A}\}_r(\beta, N)}{\sum_{r=1}^{N_{\text{rd.vec.}}} \{\hat{1}\}_r(\beta, N)}. \quad (2.107)$$

While this derivation is only strictly valid when $[\hat{A}, \hat{h}] = 0$, in Reference [35], the authors show that it holds remarkably well in general. I shall confirm this in practice later.

[35]: Sugiura et al. (2013), 'Canonical Thermal Pure Quantum State'

Memory-wise, CTPQ is similar to its microcanonical counterpart, requiring two D -vectors. Unfortunately, numerical instabilities build up rapidly as k increases. Lower-temperature properties are thus challenging to probe.

2.8.3 A novel finite temperature Chebyshev polynomial approach

So far, I have reviewed the generalisation of the ideas behind Lanczos and TPQ to the study of canonical expectations. In what follows, I introduce the FTCP method, a new approach that I developed to extend CPGF to the canonical ensemble description of interacting quantum systems.

In Reference [189], the g -coefficients of Equation 2.83 are obtained by exploiting the operator version of the Jacobi-Anger identity

[189]: Ferreira et al. (2015), 'Critical Delocalization of Chiral Zero Energy Modes in Graphene'

$$e^{-iz\tilde{h}} = \sum_{n=0}^{\infty} \frac{2i^{-n}}{1 + \delta_{n,0}} J_n(z) T_n(\tilde{h}), \quad (2.108)$$

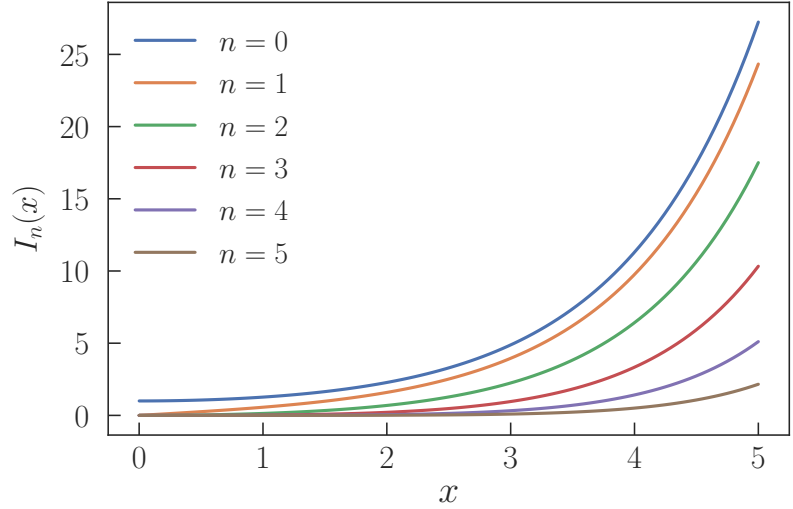


Figure 2.6: Modified Bessel functions up to order five.

[198]: Ikeuchi et al. (2015), ‘Computation of ESR spectra from the time evolution of the magnetization’

where $J_n(z)$ is the Bessel function of order n . I follow a similar route, and seek a Chebyshev expansion of the operator $e^{-\beta\tilde{h}/2}$. Suppose one is interested in low temperature behaviour, *i.e.* a high inverse temperature, β_{\max} . One could expand the operator $e^{-\beta_{\max}\tilde{h}/2}$ in Chebyshev polynomials directly as done *e.g.* in Reference [198]. However, such an expansion is vulnerable to numerical instabilities for large β_{\max} (low temperature) due to the rapid growth of the Bessel functions. Using

$$e^{-\beta_{\max}\tilde{h}/2} = \prod_{k=1}^L e^{-\delta\beta_k\tilde{h}}, \quad (2.109)$$

where $\sum_{k=1}^L \delta\beta_k = \beta_{\max}/2$, one can decompose $e^{-\beta_{\max}\tilde{h}/2}$ into a string of L operators. This expansion enables one to bypass the divergent behaviour of $J_n(z)$ in Equation 2.108 for large negative imaginary arguments $z = -i\beta_{\max}$ (see Figure 2.6). Moreover, the inverse temperature steps, $\delta\beta_k$ need not be uniform, but may instead vary for each operator, $e^{-\delta\beta_k\tilde{h}}$, in the string of L operators. This opens the door to the use of an adaptive temperature step.

Using the modified Bessel functions — which obey the relation $I_n(x) = i^{-n}J_n(ix)$, $x \in \mathbb{R}$ — one can use the Jacobi-Anger identity to cast each operator in the string of operators as a Chebyshev series:

$$e^{-\delta\beta_k\tilde{h}} = \sum_{n=0}^{\infty} \frac{2}{1 + \delta_{n,0}} I_n(-\delta\beta_k) T_n(\tilde{h}). \quad (2.110)$$

Applying Equation 2.110 to a random state $|\phi_0^{(r)}\rangle$ produces a sequence of approximate finite temperature states (with inverse

temperatures $\beta_l = 2 \sum_{k=1}^l \delta\beta_k$ with $l = 1, \dots, L$), with accuracy controlled by the truncation order. In practice, a Chebyshev truncation order $N_{\text{poly},k} \sim \mathcal{O}(10)$ ensures convergence for a typical inverse temperature step of $\delta\beta \lesssim 10^2$ (in rescaled units). The l -th finite temperature state reads

$$|\phi_l^{(r)}\rangle \equiv \sum_{n=0}^{N_{\text{poly},l}} \frac{2}{1 + \delta_{0,n}} I_n(-\delta\beta_l) T_n(\tilde{h}) |\phi_{l-1}^{(r)}\rangle, \quad (2.111)$$

where, as customary, the Chebyshev vectors are generated starting from the r -th realisation of the initial random state. Notice that, at all steps, the arguments of the fast growing modified Bessel functions need to be kept small in order to avoid numerical instabilities.

As the l -th operator in the string of operators is applied to $|\phi_{l-1}^{(r)}\rangle$, the canonical average of a quantum observable, \hat{A} , can be evaluated for the l -th inverse temperature. In order to compute a thermal average, it suffices to notice that

$$\langle \phi_0^{(r)} | e^{-\beta_l \tilde{h}/2} \hat{A} e^{-\beta_l \tilde{h}/2} | \phi_0^{(r)} \rangle = \langle \phi_l^{(r)} | \hat{A} | \phi_l^{(r)} \rangle. \quad (2.112)$$

Then, using the right hand side of Equation 2.98, one obtains the STE expectation with the FTCP method:

$$\langle A \rangle_{\text{STE}}(\beta_l, N) = \frac{\sum_{r=1}^{N_{\text{rd.vec.}}} \langle \phi_l^{(r)} | \hat{A} | \phi_l^{(r)} \rangle}{\sum_{r=1}^{N_{\text{rd.vec.}}} \langle \phi_l^{(r)} | \phi_l^{(r)} \rangle}, \quad (2.113)$$

where $2 \sum_{k=1}^l \delta\beta_k = \beta_l \leq \beta_{\text{max}}$. The adaptive inverse temperature step used in this work allows one to maximise efficiency by focusing the computational effort at low temperature, where a finer temperature grid (and thus a larger spacing $\delta\beta_k$) is required to capture the key features of the systems at play. The reconstruction of $\langle A \rangle_{\text{STE}}(\beta_l, N)$ for a discrete set of L inverse temperatures, $\{\beta_l, l = 1, 2, \dots, L\}$ involves storing $2L$ overlaps, $\langle \phi_l^{(r)} | \hat{A} | \phi_l^{(r)} \rangle$ and $\langle \phi_l^{(r)} | \phi_l^{(r)} \rangle$ for each random vector realisation. The total number of Chebyshev iterations is thus $N_{\text{Cheb}} = \sum_{l=1}^L N_{\text{poly},l} \sim 10^3$. As shown shortly in Chapter 4, the favourable convergence properties of FTCP will allow one to reach very low temperatures that are hard to access with FTLM and CTPQ. Finally, FTCP has the same memory requirement of three D -vectors as CPGF: two for the Chebyshev recursion and one to cumulatively generate the finite temperature state at each inverse temperature.

2.9 Dynamical properties

The prototype simulation aimed at studying the dynamics of a quantum system starts from a well defined initial state $|\Psi(t = 0)\rangle$, such as the ground state of the model Hamiltonian at play, $|\text{GS}\rangle$, which can be obtained, *e.g.* using the Lanczos method. This initial state is then evolved using the time evolution operator. Successive small time steps are taken in order to maintain enough numerical accuracy, while keeping track of the evolution of quantities of interest, such as time-domain correlators of the type

$$G^{\hat{B}\hat{A}}(t) = \langle \text{GS} | \hat{B}(t) \hat{A}(0) | \text{GS} \rangle, \quad (2.114)$$

where \hat{A}, \hat{B} are two generic quantum observables in the Heisenberg picture. Both Lanczos and a Chebyshev-based approaches exist to approximate the time evolution operator. Within the Lanczos approach, the time evolution operator for a short time step δt is approximated as

$$e^{-iN\delta t\hat{h}} \approx \sum_{j=0}^{M_t} e^{-iN\varepsilon_j\delta t} |\psi_j\rangle\langle\psi_j|, \quad (2.115)$$

where $\{\varepsilon_j\}$ and $\{|\psi_j\rangle\}$ are sets of energies and corresponding eigenstates obtained using M_t Lanczos steps and starting the Lanczos procedure from a previously computed state $|\Psi(t')\rangle$. On the other hand, the Chebyshev approximation of the time evolution operator — which is used *e.g.* in Reference [199] in combination with CTPQ¹³ — relies on Equation 2.108:

$$e^{-iN\delta t\hat{h}} \approx \sum_{n=0}^{N_t} \frac{2i^{-n}}{1 + \delta_{n,0}} J_n(N\delta t) T_n(\tilde{h}). \quad (2.116)$$

Both methods require $\mathcal{O}(10)$ iterations for a standard time step $\delta t \approx W^{-1}$ [17]. Yet, the Chebyshev approach has an important advantage. Unlike Lanczos, where a tridiagonal matrix has to be diagonalised at each time step to generate the coefficients of the Lanczos expansion, the coefficients in the Chebyshev expansion in Equation 2.116 can be easily and efficiently evaluated using freely available numerical libraries.

The efficiency of the Chebyshev approximation of the time evolution operator suggests that a Chebyshev approach can also be advantageous when studying zero-temperature spectral functions, $\mathcal{C}^{\hat{B}\hat{A}}(\omega)$, obtained by Fourier transforming the time-domain correlators of Equation 2.114:

[199]: Endo et al. (2018), ‘From Linear to Nonlinear Responses of Thermal Pure Quantum States’

13: In Reference [199], CTPQ is used to generate an initial thermal state at $t = 0$. Time evolution is carried out using the Chebyshev approximation of $e^{-it\hat{H}}$.

[17]: Prelovšek et al. (2013), ‘Ground State and Finite Temperature Lanczos Methods’

$$\begin{aligned}
\mathcal{C}^{\hat{B}\hat{A}}(\omega) &= \int \frac{dt}{2\pi} e^{i\omega t} G^{\hat{B}\hat{A}}(t) \\
&= \langle \text{GS} | \hat{B} \delta(\omega - \hat{h} + \varepsilon_m) \hat{A} | \text{GS} \rangle \\
&= -\frac{1}{\pi} \lim_{\eta \rightarrow 0} \langle \text{GS} | \hat{B} \text{Im} \left(\frac{1}{\omega - \hat{h} + \varepsilon_m + i\eta} \right) \hat{A} | \text{GS} \rangle,
\end{aligned} \tag{2.117}$$

where I recall that ε_m is the ground state energy density, obtained *e.g.* with Lanczos.

2.9.1 Dynamical autocorrelation response functions with Lanczos

In the particular case where $\hat{B} = \hat{A}^\dagger$, the spectral function $\mathcal{C}^{\hat{A}^\dagger \hat{A}}$ is referred to as the autocorrelation response function for observable \hat{A} and is defined as follows (with $z = \omega + \varepsilon_m + i\eta$):

$$\mathcal{A}(\omega) = -\frac{1}{\pi} \lim_{\text{Im } z \rightarrow 0} \langle \text{GS} | \hat{A}^\dagger \text{Im} [(z - \hat{h})^{-1}] \hat{A} | \text{GS} \rangle. \tag{2.118}$$

Once the ground state, $|\text{GS}\rangle$, is reconstructed with Lanczos, the response function above can be computed by performing an additional Lanczos recursion (where the number of iterations needed for satisfactory convergence is typically $\tilde{M} \sim 10^3$) with the initial state

$$|\tilde{\phi}_0\rangle = \frac{\hat{A}|\text{GS}\rangle}{\sqrt{\langle \text{GS} | \hat{A}^\dagger \hat{A} | \text{GS} \rangle}}. \tag{2.119}$$

Similarly to Section 2.5, this recursion also generates a (now much larger) tridiagonal matrix

$$\tilde{T}_{\tilde{M}} = \begin{pmatrix} \tilde{\alpha}_0 & \tilde{\beta}_1 & 0 & \dots & 0 \\ \tilde{\beta}_1 & \tilde{\alpha}_1 & \tilde{\beta}_2 & \ddots & \vdots \\ 0 & \tilde{\beta}_2 & \ddots & \ddots & 0 \\ \vdots & \ddots & \ddots & \ddots & \tilde{\beta}_{\tilde{M}} \\ 0 & \dots & 0 & \tilde{\beta}_{\tilde{M}} & \tilde{\alpha}_{\tilde{M}} \end{pmatrix}, \tag{2.120}$$

whose entries can be used to compute the response function [17] with no need to compute the eigenpairs $\{\varepsilon_j, \mathbf{v}_j, j = 0, 1, \dots, \tilde{M}\}$. The resolvent $(z - \hat{h})^{-1}$, can be approximated using a continued fraction, thus giving the ‘‘Lanczos’’ response function

[17]: Prelovšek et al. (2013), ‘Ground State and Finite Temperature Lanczos Methods’

$$\mathcal{A}(\omega, \eta) = -\frac{1}{\pi} \text{Im} \frac{\langle \text{GS} | \hat{A}^\dagger \hat{A} | \text{GS} \rangle}{z - \tilde{\alpha}_0 - \frac{\tilde{\beta}_1^2}{z - \tilde{\alpha}_1 - \frac{\tilde{\beta}_2^2}{z - \dots}}}, \quad (2.121)$$

where the continued fraction is terminated with $\tilde{\beta}_{\tilde{M}+1} = 0$. This procedure is significantly more expensive computationally than simply approximating the ground state with Lanczos as described in Section 2.5. This is due to the accumulated cost of matrix-vector multiplications as more iterations are completed, which is $\mathcal{O}(z\tilde{M}D \log_2 D)$. Unlike Section 2.7.1, the accumulated cost of diagonalising the tridiagonal matrix at each iteration using MR [193, 195, 196] only applies to the first recursion. This diagonalisation cost is $\mathcal{O}(M^3) \sim 10^6$, which is very small compared to the cost of matrix-vector multiplications, *e.g.* $\mathcal{O}(z\tilde{M}D \log_2 D) \sim 10^{12}$ for $N = 24$.

[193]: Dhillon (1997), *A New $O(n^2)$ Algorithm for the Symmetric Tridiagonal Eigenvalue/Eigenvector Problem*

[195]: Dhillon et al. (2006), ‘The design and implementation of the MRRR algorithm’

[196]: Demmel et al. (2008), ‘Performance and Accuracy of LAPACK’s Symmetric Tridiagonal Eigensolvers’

2.9.2 Original hybrid Lanczos-Chebyshev method for spectral functions

Here, I use the Chebyshev expansion of the resolvent operator of Equation 2.93 to compute spectral functions directly in the frequency domain. This approach is inspired by a similar technique described in Reference [174], where a kernel polynomial approximation based on Chebyshev polynomials is used. This approach was further exploited in References [178, 200], where Chebyshev expansions were combined with Matrix Product States (MPS) and DMRG to investigate one-dimensional strongly correlated systems. Yet, this technique has so far relied on the use of a kernel convolutions to damp Gibbs oscillations in the Chebyshev expansion. Here, I combine the numerically exact Chebyshev expansion of Equation 2.93, which avoids the use of a kernel, with Lanczos. The key advantage of this approach is the rigorous control over resolution, a feature that is shared with the CPGF method that was described above in Section 2.7.3. In principle, the ideas of the method described below could be combined with MPS and DMRG as well, but that is outside the scope of this work.

Similarly to Lanczos, I start the procedure with the state $|\tilde{\phi}_0\rangle$ — obtained from two prior Lanczos recursions — and, instead of a third Lanczos recursion, one carries out a Chebyshev recursion to generate the polynomials $T_n(\tilde{h})$ using Equation 2.92, while storing the moments

$$\mu_n = \langle \tilde{\phi}_0 | T_n(\tilde{h}) | \tilde{\phi}_0 \rangle. \quad (2.122)$$

[174]: Weisse et al. (2006), ‘The kernel polynomial method’

[178]: Lado et al. (2019), ‘Topological spin excitations in Harper-Heisenberg spin chains’

[200]: Holzner et al. (2011), ‘Chebyshev matrix product state approach for spectral functions’

The autocorrelation response function is then obtained as follows:

$$\mathcal{A}(\omega, \eta) = -\langle \text{GS} | \hat{A}^\dagger \hat{A} | \text{GS} \rangle \sum_n \text{Im}[g_n(\tilde{z})] \mu_n, \quad (2.123)$$

with $\tilde{z} = (\omega + \varepsilon_m + i\eta - b)/a$, where a, b are defined in Equation 2.82 and I recall that ε_m is the ground state energy density. This procedure has significant advantages. The first is that two moments can be obtained per matrix-vector multiplication, which implies that the numerical effort is halved if one assumes the same number of iterations. Thus, the computational effort is proportional to the number of iterations, $\tilde{N}_{\text{it}} = \tilde{N}_{\text{poly}}/2$, where \tilde{N}_{poly} is the number of Chebyshev moments needed for convergence. This is derived by applying the product identity of Equation 2.41 to the overlaps $\langle \tilde{\phi}_n | \tilde{\phi}_n \rangle$ and $\langle \tilde{\phi}_{n+1} | \tilde{\phi}_n \rangle$, where $|\tilde{\phi}_n\rangle = T_n(\tilde{h})|\tilde{\phi}_0\rangle$:

$$\begin{aligned} \langle \tilde{\phi}_n | \tilde{\phi}_n \rangle &= \frac{1}{2} \langle \tilde{\phi}_0 | (T_{2n}(\tilde{h}) + \mathbb{1}) | \tilde{\phi}_0 \rangle \\ &= \frac{1}{2} (\mu_{2n} + \mu_0) \\ \langle \tilde{\phi}_{n+1} | \tilde{\phi}_n \rangle &= \frac{1}{2} \langle \tilde{\phi}_0 | (T_{2n+1}(\tilde{h}) + T_1(\tilde{h})) | \tilde{\phi}_0 \rangle \\ &= \frac{1}{2} (\mu_{2n+1} + \mu_1) \end{aligned} \quad (2.124)$$

For a given iteration, given a new $|\tilde{\phi}_n\rangle$, two moments can now be computed:

$$\begin{aligned} \mu_{2n} &= 2 \langle \tilde{\phi}_n | \tilde{\phi}_n \rangle - \mu_0, \\ \mu_{2n+1} &= 2 \langle \tilde{\phi}_{n+1} | \tilde{\phi}_n \rangle - \mu_1. \end{aligned} \quad (2.125)$$

Two remarks are now in order:

- \tilde{N}_{it} is typically of the same order of magnitude as \tilde{M} , which guarantees that CPGF is at least as fast as Lanczos. In practice, I observe faster performance with CPGF. I attribute this to the possibility of better parallelisation with CPGF because it requires half as many vector update loops. These loops are needed in order to carry out the Lanczos and CPGF recursions with only two vectors of dimension D stored in memory. They incur a cost that, whilst not dominating over that of matrix-vector multiplications, still compares closely. In fact, the complexity of each of these loop is proportional to D . With Lanczos, the two steps of Equation 2.28 involve two of these loops that need to be executed one after the other, in opposition to CPGF, which needs only a single loop vector update.

- CPGF can easily be modified to compute more general spectral functions (for which one might have $\hat{B} \neq \hat{A}^\dagger$) without a significant additional memory or computer time cost. The 3-vector memory cost is preserved because the vector used to generate $|\text{GS}\rangle$ during the second Lanczos recursion is not used in CPGF once the initial state, $|\tilde{\phi}_0\rangle$ is generated. Thus, this vector can be used to store $|\varphi\rangle \equiv \hat{B}^\dagger|\text{GS}\rangle/\sqrt{\langle\text{GS}|\hat{B}\hat{B}^\dagger|\text{GS}\rangle}$, which in turn can be used to compute the modified moments, $\mu'_n = \langle\varphi|T_n(\tilde{h})|\tilde{\phi}_0\rangle$ needed to Chebyshev-expand $\mathcal{G}^{\hat{B}\hat{A}}(\omega)$:

$$\mathcal{G}^{\hat{B}\hat{A}}(\omega, \eta) = -\sqrt{\langle\text{GS}|\hat{A}^\dagger\hat{A}|\text{GS}\rangle\langle\text{GS}|\hat{B}\hat{B}^\dagger|\text{GS}\rangle} \sum_n \text{Im}[g_n(\tilde{z})]\mu'_n. \quad (2.126)$$

In contrast, the continued fraction Lanczos approach does not work in the case $\hat{B} \neq \hat{A}^\dagger$. One must then resort to Equation 2.115 to directly study the behaviour of the time-domain correlator. This leads to short time expansions with M_t Lanczos vectors and the initial state $|\Psi(t=0)\rangle = |\tilde{\phi}_0\rangle$:

$$\begin{aligned} G^{\hat{B}\hat{A}}(\delta t) &= \langle\text{GS}|e^{iN\delta t\hat{h}}\hat{B}e^{-iN\delta t\hat{h}}\hat{A}|\text{GS}\rangle \\ &\approx \sqrt{\langle\text{GS}|\hat{A}^\dagger\hat{A}|\text{GS}\rangle} \sum_{j=0}^{M_t} e^{-Ni(\varepsilon_j - \varepsilon_m)\delta t} \langle\text{GS}|\hat{B}|\tilde{\psi}_j\rangle \langle\tilde{\psi}_j|\tilde{\phi}_0\rangle \end{aligned} \quad (2.127)$$

The eigenvectors of the tridiagonal matrix of Equation 2.120, $\{\mathbf{v}_j\}$ give $\langle\tilde{\psi}_j|\tilde{\phi}_0\rangle = \tilde{v}_{j0}$. However, the overlaps of the type $\langle\text{GS}|\hat{B}|\tilde{\psi}_j\rangle$ must be evaluated explicitly using the vector $\hat{B}|\text{GS}\rangle$, which now has to be stored in memory separately, thus adding to the memory cost:

$$\langle\text{GS}|\hat{B}|\tilde{\psi}_j\rangle = \sum_{i=0}^{M_t} \tilde{v}_{ji} \langle\text{GS}|\hat{B}|\tilde{\phi}_i\rangle. \quad (2.128)$$

Moreover, one must update the initial state of the Lanczos expansion at each time interval, $|\Psi(t)\rangle$ using short time Lanczos expansions. Then, one re-computes the eigenvectors of a new tridiagonal matrix and re-evaluate $\langle\text{GS}|\hat{B}|\tilde{\psi}_j\rangle$ for each time step. This process becomes computationally expensive very quickly since one may require a large number of time steps to capture important features of $G^{\hat{B}\hat{A}}(t)$. On the other hand, the CPGF treats the cases $\hat{B} \neq \hat{A}^\dagger$ and $\hat{B} = \hat{A}^\dagger$ on equal footing. Therefore, the CPGF is a general purpose approach, which accesses spectral functions for

the case $\hat{B} \neq \hat{A}^\dagger$ using the same methodology and with the same computational complexity and memory requirements as the case $\hat{B} = \hat{A}^\dagger$.

**PART 1 — MEAN FIELD THEORY AND
DETERMINANT QUANTUM MONTE CARLO: A
COMPARATIVE STUDY FOR A
TWO-DIMENSIONAL NANOSTRUCTURE**

Edge magnetism in transition metal dichalcogenide nanoribbons

3

In this chapter, edge magnetism in z TMDNRs is studied using the 3BTB with local electron-electron interactions of Equation 1.1. The study is conducted using two separate methods: MFT and the unbiased, numerically exact DetQMC. Then, the results of these two methods are compared and their respective limitations are discussed.

MFT predicts the onset of different phases as the edge filling is varied, broadly classified as gapped or gapless. Gapped spin dimer and antiferromagnetic phases appear for two specific fillings. Away from these two edge fillings, there is a tendency towards metallic edge-ferromagnetism.

DetQMC simulations confirm the stability of the antiferromagnetic gapped phase at the same edge filling as MFT, despite being sign-problematic for other fillings. The obtained results point at edge filling as yet another key ingredient to understand the observed magnetism in nanosheets. Moreover, the filling dependent edge magnetism gives rise to spin-polarised edge currents in zigzag nanoribbons which could be tuned through a back gate voltage, with possible applications to spintronics.

The remainder of this chapter is organised as follows. Section 3.1 gives a brief overview of the MFT and DetQMC methods in the context of the minimal model presented in Section 1.1.2. In Section 3.2, I present my MFT and DetQMC results separately, closing the section with a critical comparison of the two methods. Conclusions are presented in Section 3.3.

3.1 Overview

In what follows, I present a study of the magnetism of z TMDNRs using MFT and DetQMC [170, 172, 201], based on a widely used 3BTB [122, 202], to which I add electron-electron interactions. Within the minimal intraorbital Hubbard model presented in Equation 1.1, I find evidence for the existence of magnetic order at the zigzag edges from both MFT and DetQMC, analogously to z GNRs. MFT provides evidence for the existence of a metallic ferromagnetic phase and two gapped phases with antiferromagnetic order, depending on the edge filling. This result is confirmed within MFT using a more elaborate model — suitable for transition metal atoms — which considers multiorbital interactions. The DetQMC results

3.1	Overview	73
3.2	Results	78
3.3	Discussion and conclusion	89

[122]: Liu et al. (2013), ‘Three-band tight-binding model for monolayers of group-VIB transition metal dichalcogenides’

[202]: Chu et al. (2014), ‘Spin-orbit-coupled quantum wires and Majorana fermions on zigzag edges of monolayer transition-metal dichalcogenides’

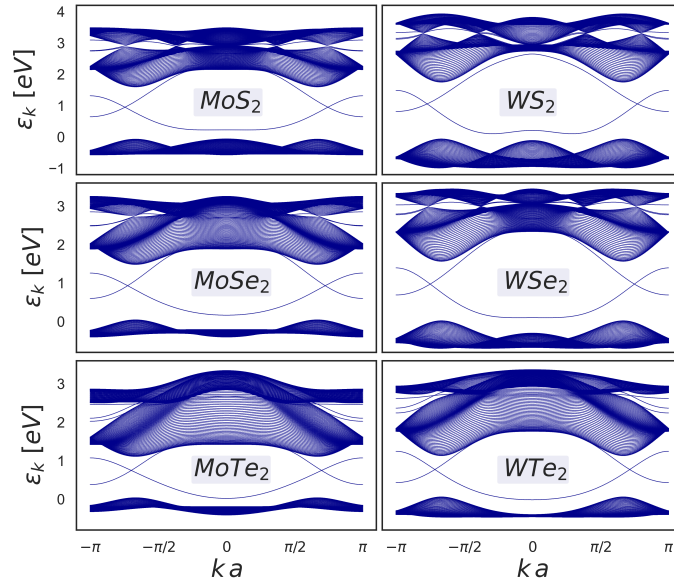
corroborate the existence of one of the gapped phases predicted with MFT for a specific edge filling. For other edge fillings, the DetQMC algorithm suffers from the sign problem and a direct comparison with MFT is not possible.

In Figure 3.1, I show the energy bands obtained with the noninteracting 3BTB for zTMDNRs with a width of 64 transition metal atoms, from now on referred to as M atoms. Similarly, chalcogen atoms are designated X atoms. The two in-gap, spin-degenerate bands at around 1 eV correspond to states localised at the M and X-terminated edges. It should be noted that the minimal model considered here correctly reproduces the edge bands derived from d_{z^2} , d_{xy} , and $d_{x^2-y^2}$ orbitals [122, 202].

[122]: Liu et al. (2013), ‘Three-band tight-binding model for monolayers of group-VIB transition metal dichalcogenides’

[202]: Chu et al. (2014), ‘Spin-orbit-coupled quantum wires and Majorana fermions on zigzag edges of monolayer transition-metal dichalcogenides’

Figure 3.1: Band structures of the 3BTB, i.e. Equation 1.1 with $U = 0$, for various infinitely long zTMDNRs with a width of 64 M atoms. Here, a is the lattice constant of the M atom triangular lattice.



[122]: Liu et al. (2013), ‘Three-band tight-binding model for monolayers of group-VIB transition metal dichalcogenides’

[203]: Mermin et al. (1966), ‘Absence of Ferromagnetism or Antiferromagnetism in One- or Two-Dimensional Isotropic Heisenberg Models’

TMDs have a sizeable SOC, ranging from several tens to a few hundreds of meV [122]. Yet, as the reader shall see later, the minimum Hubbard interaction required for magnetic ordering, U_c , is approximately an order of magnitude larger than the SOC energy scale. Thus, while SOC is a crucial feature of the real material, it can be safely neglected for the purposes of this thesis. This relatively weak SOC (compared to the critical Hubbard- U required for magnetic ordering) further justifies the use of the rotationally invariant Coulomb interaction vertex of Equations 1.2-1.4. Another important remark is that SU(2) spin-rotation symmetry is broken by SOC and the Mermin-Wagner theorem does not apply [203]. Therefore edge-magnetic ordering at finite temperature is not ruled out in TMD nanoribbons.

3.1.1 Mean field theory

The Gibbs-Bogolyubov-Feynman inequality [204] states that the variational grand potential Ω_V — computed with a quadratic mean field Hamiltonian \hat{H}_{MF} — is an upper bound on the grand potential Ω computed with a corresponding interacting Hamiltonian \hat{H} :

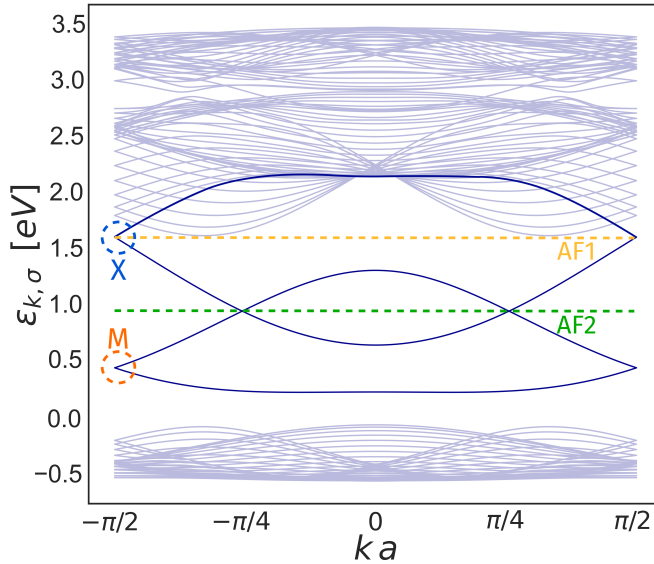
$$\Omega \leq \Omega_{\text{MF}} + \langle \hat{H} - \hat{H}_{\text{MF}} \rangle_{\text{MF}} \equiv \Omega_V, \quad (3.1)$$

where $\Omega_{\text{MF}} = -k_B T \log \text{Tr} \left\{ e^{-\beta(\hat{H}_{\text{MF}} - \mu \hat{N}_e)} \right\}$ is the mean field grand potential, T is the temperature and $\beta = (k_B T)^{-1}$, \hat{N}_e is the total electron number operator and $\langle \dots \rangle_{\text{MF}}$ is a thermodynamical average with respect to \hat{H}_{MF} . The chemical potential μ is set by fixing the electron density.

Starting from the mean field Hamiltonian family

$$\hat{H}_{\text{MF}} = \hat{H}_{\text{TB}} + U \sum_{i,\alpha,\sigma} n_{i,\alpha,\sigma} f_{i,\alpha,\sigma}, \quad (3.2)$$

where \hat{H}_{TB} is the 3BTB Hamiltonian and $f_{i,\alpha,\sigma}(\langle \mathbf{n} \rangle)$ is a variational field, one applies the variational principle of Equation 3.1 to find the \hat{H}_{MF} that best approximates the model Hamiltonian of Equation 1.1. The variational field f that minimises Ω_V is obtained by self-consistently solving the set of mean field equations $f_{i,\alpha,\sigma}(\langle \mathbf{n} \rangle) = \langle n_{i,\alpha,\sigma} \rangle \forall i, \alpha, \sigma$.



[204]: Feynman (2019), *Statistical Mechanics*

Figure 3.2: Folded band structure of the 3BTB, *i.e.* Equation 1.1 with $U = 0$, for a MoS₂ nanoribbon with a width of 20 M atoms and a doubled unit cell in the longitudinal direction. The bands corresponding to bulk states are faded. The dashed horizontal lines indicate band fillings for which two different types of antiferromagnetic order develop.

To simplify the mean field analysis, I assume that the mean field Hamiltonian of Equation 3.2 has translational symmetry along the longitudinal direction. A discrete Fourier transform decouples the mean field Hamiltonian into a set of effective one dimensional chains in the transverse direction, one for each longitudinal quasimomentum, k . The choice of periodicity in the longitudinal

direction restricts the self-consistent fields, and consequently the types of magnetic ordering that can be obtained by minimising Ω_V . Let p be the number of M atom columns in the unit cell. Taking $p = 1$ only allows paramagnetic or ferromagnetic solutions, while $p = 2$ also allows alternating spins (i.e. ferrimagnetic or antiferromagnetic solutions). In order to capture more complex forms of magnetic ordering one has to consider larger periods. In particular, to detect the spin dimers I shall encounter later, one has to set $p = 4$. Upon taking a unit cell with $p > 1$, the first Brillouin zone is reduced by a factor of p and energy bands fold p times. In Figure 3.2, I highlight the bands of the 3BTB with $p = 2$. The bands labeled M, X correspond to the M and X-terminated edges, respectively. The green and yellow lines indicate band fillings where — as the reader shall see later — gaps will be opened due to the Hubbard term in MFT. These gaps correspond to an edge-dimer (AF2) and an edge-antiferromagnetic phase (AF1), respectively.

[63]: Feldner et al. (2010), ‘Magnetism of finite graphene samples’

[118]: Yang et al. (2016), ‘Room-temperature magnetism on the zigzag edges of phosphorene nanoribbons’

[119]: Raczkowski et al. (2017), ‘Interplay between the edge-state magnetism and long-range Coulomb interaction in zigzag graphene nanoribbons’

[120]: Yang et al. (2017), ‘Strain-tuning of edge magnetism in zigzag graphene nanoribbons’

[205]: Varney et al. (2009), ‘Quantum Monte Carlo study of the two-dimensional fermion Hubbard model’

[206]: Golor et al. (2013), ‘Quantum Monte Carlo studies of edge magnetism in chiral graphene nanoribbons’

[207]: Johnston et al. (2013), ‘Determinant quantum Monte Carlo study of the two-dimensional single-band Hubbard-Holstein model’

[208]: Cheng et al. (2015), ‘Strain-induced edge magnetism at the zigzag edge of a graphene quantum dot’

[39]: Troyer et al. (2005), ‘Computational Complexity and Fundamental Limitations to Fermionic Quantum Monte Carlo Simulations’

[169]: Bai et al. (2009), ‘Numerical Methods for Quantum Monte Carlo Simulations of the Hubbard Model’

In order to study the effect of the multiorbital terms of Equations 1.2 -1.4, I further simplify the MFT approach by using a minimal set of variational fields. This set is obtained by making educated assumptions following the results obtained with the thorough MFT analysis of the intraorbital Hamiltonian of Equation 3.2. Firstly, I assume that the mean field solution is such that the bulk magnetisation $\langle \hat{S}_{i,\alpha}^z \rangle \equiv \langle n_{i,\alpha,\uparrow} - n_{i,\alpha,\downarrow} \rangle$ (for i, α on every row other than the two edge rows) vanishes. Then, I assume that magnetic order is primarily sensitive to electron spin. Thus, I ignore any orbital dependence. Finally, I compare the value of Ω_V in Equation 3.1 for the following phases: paramagnetic, (anti)ferromagnetic on each of the edges — labeled as Ferro-X, Ferro-M, AF-X, AF-M — or on both — labeled as Ferro-MX, AF-MX.

3.1.2 Determinant quantum Monte Carlo

DetQMC is commonly used to simulate interacting models of two-dimensional nanostructures [63, 118–120, 205–208]. As discussed in Section 2.2, it is based on the Hubbard-Stratonovich transformation, which allows one to map the Hubbard model onto a Hamiltonian of independent fermions coupled to a binary auxiliary field. Averages of quantum operators $\langle \hat{A} \rangle$ are evaluated by employing importance sampling over configurations of the auxiliary field. Each field configuration contributes to the expectation value with a weight that can be negative, leading to the fermion-sign problem. For sign-problematic models, the distribution of the sign variable is such that the variance of QMC estimators increases exponentially with the system size and the inverse temperature [39, 169]. In my case, a strong Hubbard interaction U deems the model severely sign-problematic. The severity of the sign problem also varies with

the chemical potential. The average of the sign distribution $\langle \text{sign} \rangle$ is a good measure of the severity of the sign problem for a given set of parameters β, μ, U, N (the latter being the total number of sites/orbitals). As $\langle \text{sign} \rangle \rightarrow 0$, the sign problem becomes more severe and the QMC estimators are no longer reliable.

I measure the \hat{S}^z spin-spin correlator between sites i and j with DetQMC:

$$C(\mathbf{R}_i, \mathbf{R}_j) = \sum_{\alpha, \beta} \langle (n_{i, \alpha, \uparrow} - n_{i, \alpha, \downarrow})(n_{j, \beta, \uparrow} - n_{j, \beta, \downarrow}) \rangle. \quad (3.3)$$

Notice that I use the following definition throughout: $\hat{S}^z = n_{\uparrow} - n_{\downarrow}$. Translational invariance and mirror symmetry are used to maximise the amount of information extracted from the measured values of the observable $C(\mathbf{R}_i, \mathbf{R}_j)$.

The discrete Fourier transform of the spin-spin correlator, known as the magnetic structure factor,

$$S(\mathbf{q}) = \frac{1}{N} \sum_{i, j} e^{i\mathbf{q} \cdot (\mathbf{R}_j - \mathbf{R}_i)} C(\mathbf{R}_i, \mathbf{R}_j), \quad (3.4)$$

is used to carry out finite-size scaling analysis and probe the system for long-range order in the thermodynamic limit. Peaks at $\mathbf{q} = (0, 0)$ and $\mathbf{q} = (\pi/a, \pi/a)$, where a is the lattice constant, correspond to ferromagnetic and antiferromagnetic order, respectively. Other types of order yield different peaks.

I inspect the zTMDNR for edge magnetism by restricting the sum in Equation 3.4 to the rows corresponding to the M- and X-terminated edges, or simply M- and X edges. If N_x is the ribbon length, and setting $q_x = \pi/a$ to study antiferromagnetic order, the structure factor for row y can be written as:

$$S_{\text{row}}(\pi, y) = \frac{1}{N_x} \sum_{x_i, x_j=0}^{N_x-1} (-1)^{|x_i - x_j|} C(x_i, y, x_j, y). \quad (3.5)$$

In practice, for finite-size systems, one aims to obtain an estimate of the correlation length, ξ , and compare it with N_x . When $\xi \ll N_x$, one is sufficiently close to the thermodynamic limit to identify an ordered phase. Due to translational invariance, one has that $C(x_i, y, x_j, y) = C(|x_i - x_j|, y)$, *i.e.* the 'edge' correlator depends solely on two variables. Defining $x \equiv |x_i - x_j|$, I hypothesise that

$$\frac{(-1)^x}{N_x} C(x, y) = f\left(\frac{x}{\xi}\right) + m_s^2(y), \quad (3.6)$$

where $m_s^2(y)$ is the row-dependent staggered magnetisation and

f is an integrable, monotonically decreasing function. Then, one may evaluate whether or not an ordered phase appears by testing the consistency of the hypothesis.

Replacing Equation 3.6 in Equation 3.5, one obtains

$$S_{\text{row}}(\pi, y) = \sum_{x=0}^{N_x-1} \left(f\left(\frac{x}{\xi}\right) + m_s^2(y) \right). \quad (3.7)$$

If $\xi \ll N_x$, the quantity $(-1)^x C(x, y)/N_x$ becomes constant at long distances and converges to the squared staggered magnetisation. Defining $A \equiv \sum_x f(x/\xi)$, one obtains

$$\frac{S_{\text{row}}(\pi, y)}{N_x} = \frac{A}{N_x} + m_{st}^2(y). \quad (3.8)$$

Equation 3.8 can be used to obtain an estimate of the staggered magnetisations in the thermodynamic limit. One starts by considering a temperature that is low enough to find signs of magnetic ordering, but high enough to avoid convergence problems (see Figure 3.10). Then, one simulates systems with varying longitudinal length, N_x , and uses Equation 3.8 to extrapolate to the thermodynamic limit.

3.2 Results

A central aspect of the work described in this chapter is the study of magnetic instabilities in zTMDNRs as a function of electron occupation of the edge bands. To be specific, I define the edge filling, ν_{edge} , as the fraction of electrons filling edge bands relative to the total number of available edge states within the noninteracting three-band tight-binding model, *i.e.* $\nu_{\text{edge}} \in [0, 1]$. Defining the spin-dependent electron density as $\langle n_\sigma \rangle = N^{-1} \sum_{i,\alpha} \langle n_{i,\alpha,\sigma} \rangle$, where N is the total number of sites \times orbitals, such that $\langle n_\sigma \rangle \in [0, 1]$, one may write the electron density as $\langle n \rangle = \langle n_\uparrow \rangle + \langle n_\downarrow \rangle$, which then ranges from 0 to 2. After simple algebra, the edge filling can be written in terms of the electron density as

$$\nu_{\text{edge}} = \frac{3N_y}{4} \langle n \rangle - \frac{1}{2}(N_y - 1), \quad (3.9)$$

where N_y is the width of the ribbon. For example, charge neutrality in this model corresponds to $\langle n \rangle = 2/3$, which corresponds to $\nu_{\text{edge}} = 1/2$, *i.e.*, half-filling of the edge.

3.2.1 Mean field theory: intraorbital interaction

I start by presenting MFT results for the intraorbital Hubbard- U model given by Equation 1.1. Only results for MoS₂ parameters are shown, but similar results are found for other TMDs of the family (see Appendix B.1).

Long-range edge-magnetic order emerges as the intraorbital Hubbard interaction, U , is increased. The type of magnetic ordering depends on the edge filling ν_{edge} . In particular, two gapped phases emerge: AF2 at $\nu_{\text{edge}} = 1/2$ and AF1 at $\nu_{\text{edge}} = 3/4$. These two edge fillings are indicated by dashed lines in Figure 3.2. Both below $\nu_{\text{edge}} = 1/2$ and between the two gapped phases, MFT predicts edge-ferromagnetic order. As can be seen in Figure 3.2, for $\nu_{\text{edge}} > 3/4$, bulk conduction bands start to be populated and the physics is no longer edge dominated.

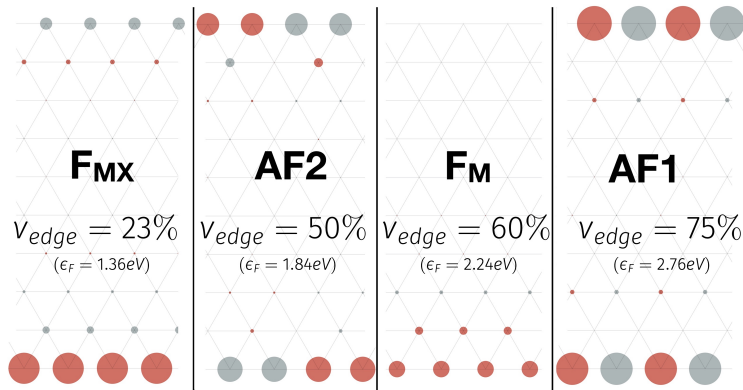
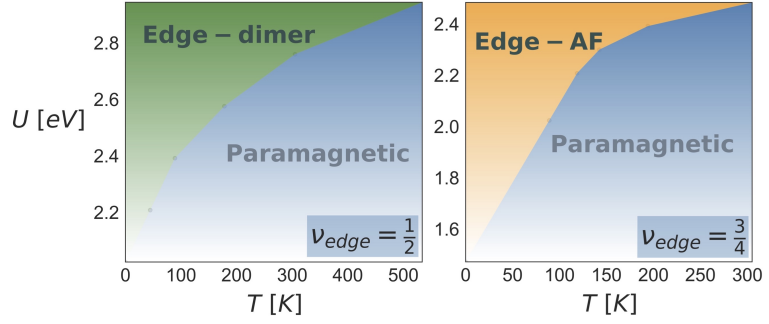


Figure 3.3: Mean field magnetic ordering for $U = 2.94$ eV at zero temperature for varying edge filling. The size of the circles indicates the magnitude of the local spin density. Red corresponds to spin-up and grey to spin-down. Left to right: ferromagnetic phase on both edges (FMX); edge-dimer (AF2); ferromagnetic phase on the M-edge (FM); edge-antiferromagnetic phase (AF1).

On the basis of the free edge bands shown in Figure 3.2, one can see that the gapped antiferromagnetic phases AF1 and AF2 are associated with the nesting vectors $Qa = \pi$ and $Qa = \pi/2$, respectively. Nesting favours gap opening instabilities such as these two types of antiferromagnetic ordering. For other generic fillings, a splitting of the spin-up and spin-down bands is preferred, which in turn induces Stoner-like edge-ferromagnetism. The three different types of edge-magnetic phases are shown in Figure 3.3, where the profile of the local magnetisation can be seen along the rows of the ribbon. At the edges, it is higher in magnitude, decreasing rapidly and eventually vanishing in the bulk.

The $U - T$ phase diagrams for the AF1 and AF2 phases are shown in Figure 3.4. The latter makes it apparent that these gapped phases exist at and below room temperature at the mean field level. Although this stability might be overestimated in MFT, my findings suggest that DetQMC calculations are worth doing for this model. Moreover, even though the Coulomb repulsion parameters are largely unknown for TMDs, the modest values of the Hubbard

Figure 3.4: $U - T$ mean field phase diagrams at: half edge filling (left); three-quarter edge filling (right). As indicated, blueish regions correspond to the paramagnetic phase. A ribbon of width $N_y = 5$ M atoms was used.



[209]: Roldán et al. (2013), ‘Interactions and superconductivity in heavily doped MoS₂’

interaction obtained are well within current parameter estimates [209]. Let me also mention that, due to the asymmetry between the two edges, the critical parameter, U_c , for magnetic order to develop is different for each of the two edges. In particular, for the AF1 phase, only the X edge is magnetised in the phase diagram of Figure 3.4 (right panel). The M edge becomes polarised only for $U \gtrsim 2.8$ eV, as will become clear shortly.

In Figure 3.5, I show the mean field band structures for the two gapped phases AF1 and AF2 and two representative edge-ferromagnetic phases. Both AF1 and AF2 band structures show an interaction-induced band gap (right panels). The AF2 phase (top right) occurs at $\nu_{\text{edge}} = 1/2$ and, correspondingly, half of the edge-bands are filled (in this case, since $p = 4$, this corresponds to 4 out of 8 spin-degenerate bands). The AF1 phase (bottom right) occurs at $\nu_{\text{edge}} = 3/4$. Since now I take $p = 2$, this corresponds to 3 out of 4 spin-degenerate edge bands. For the two representative edge-ferromagnetic phases (left panels), I took $p = 2$ to accommodate the possibility of (anti)ferrimagnetic ordering, but I consistently obtained ferromagnetism (other types of magnetic ordering or paramagnetism were also energetically excluded). At $\nu_{\text{edge}} = 0.23$ (top left), both edges become magnetised since the spin-degeneracy of all edge bands is lifted. For $\nu_{\text{edge}} = 0.60$ (bottom left), the bands corresponding to the X edge remain spin-degenerate, unlike the ones corresponding to the M edge. Thus, only the M edge becomes magnetised.

The phases I have obtained are independent of the width of the ribbon. To illustrate this, I consider the AF1 phase at $\nu_{\text{edge}} = 3/4$. In Figure 3.6, I show the staggered magnetisation m_{st} and the electron density $\langle n \rangle$ (top and middle panels) as a function of the row position y for two different ribbon widths $N_y = 10$ and $N_y = 20$ M atoms. The results are numerically indistinguishable. On the bottom panel of Figure 3.6, I show the variation of m_{st} with U at $T = 0$ for the ribbon widths $N_y = 5, 10, 20$.

As pointed out earlier, edge-antiferromagnetism is more robust on the X edge for the three N_y values considered, consistently appearing for lower critical values of U compared to the M edge.

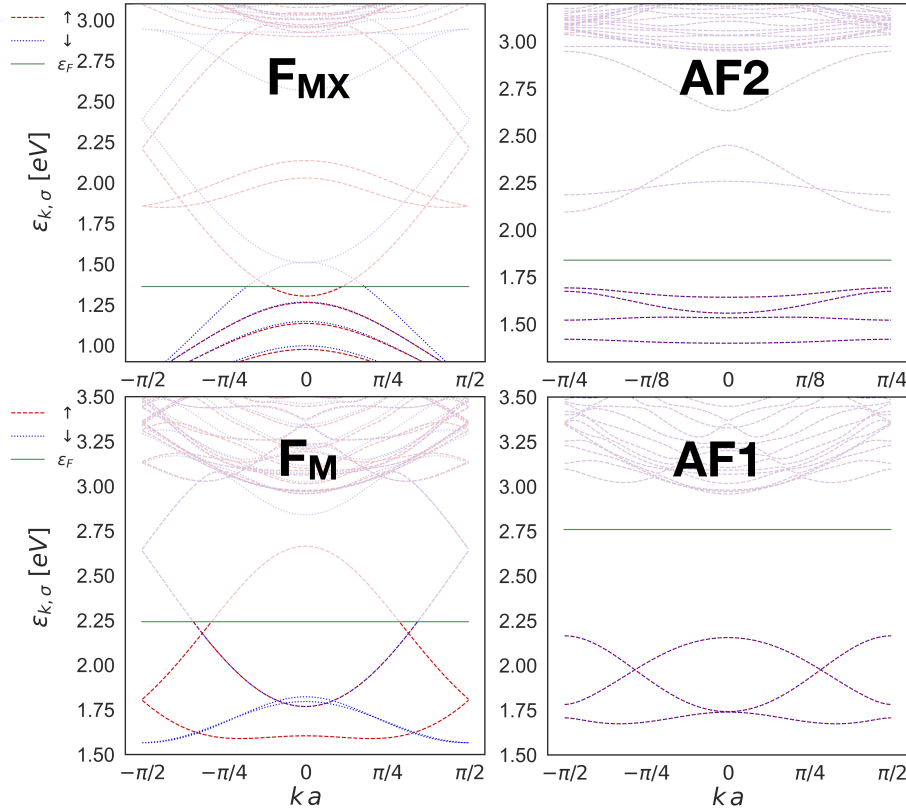


Figure 3.5: Mean field band structure for edge fillings of $\nu_{\text{edge}} = 0.23$ (top left - F_{MX}), $\nu_{\text{edge}} = 0.5$ (AF2), $\nu_{\text{edge}} = 0.60$ (F_{M}) and $\nu_{\text{edge}} = 0.75$ (AF1). I used $U = 2.94$ eV and $T = 0$, and a ribbon width of 10 M atoms. Spin-up bands are in dashed-red and spin-down in dotted-blue. Unoccupied bands are faded and the horizontal green line marks the Fermi energy, ε_F . Ferromagnetic phases (left panels) are characterised by spin-splitting of edge bands and present edge-metallicity (absence of a gap). In the F_{MX} phase both edges are polarised while in the F_{M} phase only the M-edge hosts magnetic ordering. The antiferromagnetic phases AF1 and AF2 (right panels) are insulating.

The differences in the critical values of U for different N_y are related to the change in $\langle n \rangle$ required to keep ν_{edge} fixed as N_y is changed, according to Equation 3.9. It is reasonable to assume that systems with larger widths would behave similarly. In fact, for the system with the smaller width of 5 M atoms, the edge staggered magnetisations are the same as those depicted on the top panel of Figure 3.6. The fact that there is no significant qualitative change justifies the use of a system with $N_y = 5$ M atoms for the DetQMC calculations in Section 3.2.3 (it becomes too computationally expensive to simulate larger systems using DetQMC due to the sign problem).

To close this section, I point out that the edge physics behind the magnetism found in Figure 3.3 is the result of two competing mechanisms: gap opening instabilities and Stoner-like edge-ferromagnetism. The winning mechanism depends on the edge filling, which is set via the Fermi energy. If the two Fermi points of the noninteracting system are connected through a wave vector which spans an integer fraction of the Brillouin zone (dashed green and yellow lines of Figure 3.2, the addition of a mean field in-

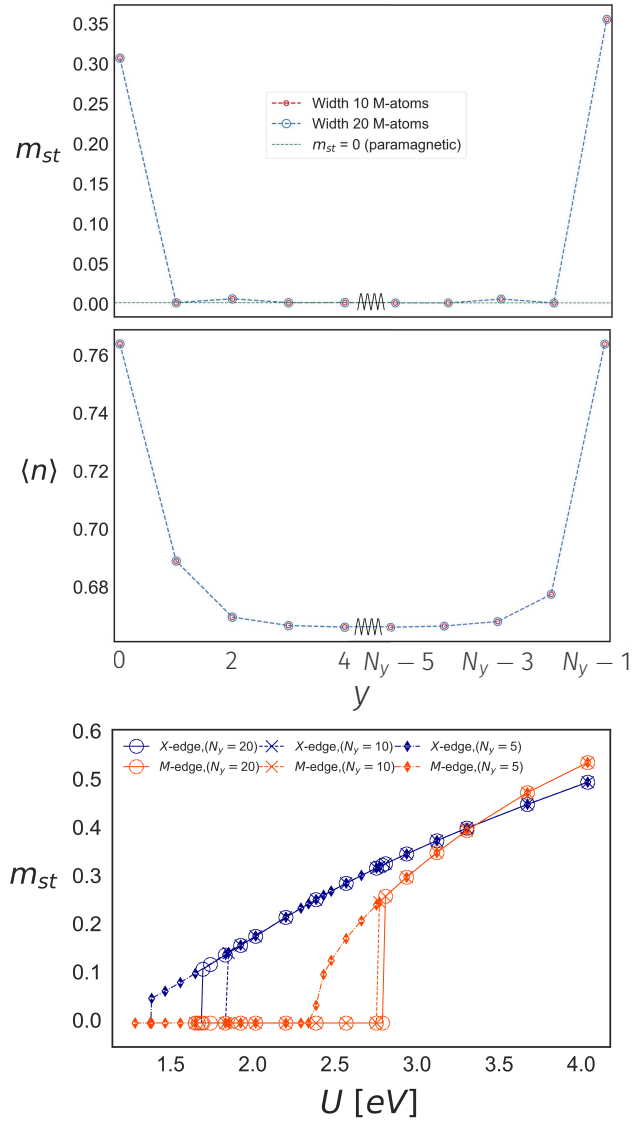


Figure 3.6: Comparison between ribbons with widths $N_y = 5, 10, 20$ M atoms at $T = 0$. (Top) Staggered magnetisation m_{st} and electron density $\langle n \rangle$ profiles as the row position y is changed for $U = 2.94$ eV. Results for $N_y = 10$ and $N_y = 20$ are indistinguishable. (Bottom) m_{st} vs U at the X edge (blue) and M edge (orange).

traorbital Hubbard interaction induces a nesting instability which opens a gap (see right panels of Figure 3.5). Other fillings favour Stoner-like edge-ferromagnetism (see left panels of Figure 3.5), with metallic edges and spin-split edge bands. On the other hand, entropy gain due to thermal fluctuations tends to counteract magnetic ordering. This is illustrated in Figure 3.4, where I observe that the critical Hubbard interaction required for magnetic ordering increases as the temperature is increased. The critical Hubbard interaction depends slightly on the width (see bottom panel of Figure 3.6), converging rapidly for wider ribbons. Once the system becomes magnetic, the order parameters coincide regardless of the width (see top panel of Figure 3.6), which is consistent with edge-dominated physics.

3.2.2 Mean field theory: multiorbital interaction

In Figure 3.7, I show the mean field phase diagrams for the multiorbital Hamiltonian, which includes both the minimal intraorbital model and the terms of Equations 1.2-1.4. As stated in Section 3.1.1, I consider a smaller set of mean field parameters by assuming that only the edges get magnetised. This is a justified approach based on the results of the previous section (in particular, the top panel of Figure 3.6). The results obtained with multiorbital interactions are compiled in Figure 3.7, where I show phase diagrams in the plane $U - U'$ at $T = 0$, obtained with a ribbon of width $N_y = 16$.

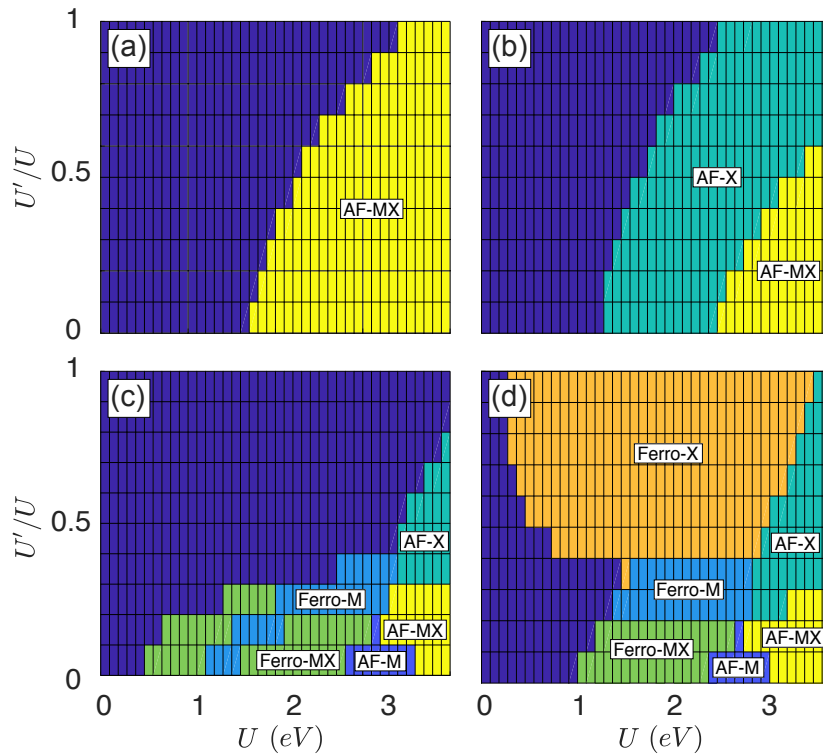


Figure 3.7: $U' - U$ phase diagrams at $T = 0$ for the multiorbital case, obtained for a ribbon width $N_y = 16$ at the edge fillings $\nu_{\text{edge}} = 75\%$ (a)-(b), $\nu_{\text{edge}} = 62.5\%$ (c), and $\nu_{\text{edge}} = 65\%$ (d). On panel (a) I consider $J = J' = 0$ and assume that both edges become polarised simultaneously. On the remaining panels, I consider $J = J' = (U - U')/2$. Dark-blue regions are paramagnetic, and the labels in the remaining phases stand for ferromagnetic on the X edge (Ferro-X), on the M edge (Ferro-M), or on both edges (Ferro-MX), and antiferromagnetic on the X edge (AF-X), on the M edge (AF-M), or on both edges (AF-MX).

I start by focusing on the AF1 phase at $\nu_{\text{edge}} = 3/4$. In Figure 3.7(a) I consider $J = J' = 0$ and assume both edges are simultaneously magnetised. It is clear that the interorbital term U' counteracts the tendency for antiferromagnetic order since the critical U value required for the onset of AF1 phase increases as U' is increased. Figure 3.7(b) shows the effect of including J and J' , now allowing for edge magnetisation independently on each edge. According to Section 3.1.1, I consider $J = J' = (U - U')/2$. It can be seen that the X edge becomes polarised first, in agreement with the results of the previous section. When $U' = 0$ and $J = J' = U/2$, notice that

the critical U for the onset of X edge magnetisation (AF-X), as well as for the onset of magnetisation on both edges (AF-MX), is lower than the case when $U' = J = J' = 0$ shown in Figure 3.6 (bottom panel). This indicates that J and J' favour magnetic order. Similarly to the case of panel Figure 3.7(a), as U' increases, the critical value of U for the onset of antiferromagnetism increases.

I now consider two representative edge fillings between $\nu_{\text{edge}} = 1/2$ and $\nu_{\text{edge}} = 3/4$. In Figure 3.7(c) I set $\nu_{\text{edge}} = 62.5\%$. Two ferromagnetic phases can be seen, one on both edges (Ferro-MX) and the other solely on the M edge (Ferro-M). Even though ferromagnetic phases appear for lower values of U , antiferromagnetic phases eventually appear as U is increased. Yet, the interorbital interaction U' still suppresses magnetic ordering quite significantly. The edge filling $\nu_{\text{edge}} = 65\%$ is considered in Figure 3.7(d). Ferromagnetism becomes more prominent on the phase diagram, with a ferromagnetic phase on the X edge (Ferro-X) appearing. Moreover, the tendency for the interorbital interaction to suppress magnetic ordering is weakened, with the Ferro-X and AF-X phases still surviving even as U' approaches U . Notably, the Ferro-X phase becomes favourable for lower values of U as U' is increased.

3.2.3 Determinant quantum Monte Carlo simulations

I now turn to the DetQMC approach. For the minimal Hubbard studied here, the method is severely limited by the sign problem, with the average sign going to zero in most regions of interest of the phase diagram. Notwithstanding, I am able to confirm the appearance of the AF1 phase predicted with MFT.

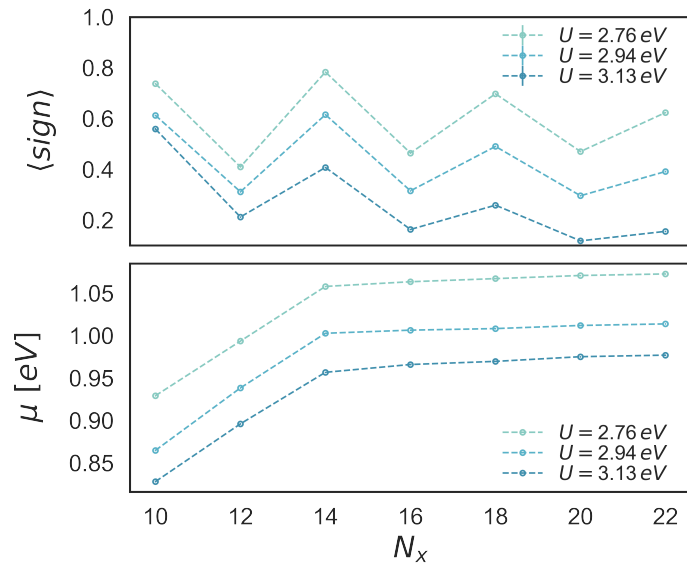


Figure 3.8: (Top) Average sign obtained in the Monte Carlo sampling for varying N_x and U at fixed temperature $T = 267$ K, for MoS₂ nanoribbons of 5 M atoms of width for electron densities corresponding to $\nu_{\text{edge}} \approx 0.75$ (error bars are negligibly small). (Bottom) Chemical potential used in the DetQMC algorithm to obtain the required edge filling for each system size (other parameters are kept the same as on the top panel).

Here, a relevant remark must be made about computational effort. These simulations are plagued by the sign problem — which exponentially increases the variance of Monte Carlo estimators — deeming them very computationally intensive.

In order to give the reader a concrete idea of just how intensive these simulations are, I compared two of the points shown in Figure 3.8: I fixed $N_x = 20$ and compared the data points shown for $U = 2.76, 2.94 \text{ eV}$. Since the average sign for $U = 2.94 \text{ eV}$ ($\langle \text{sign} \rangle = 0.2963 \pm 0.0007$) is lower than for $U = 2.76 \text{ eV}$ ($\langle \text{sign} \rangle = 0.470 \pm 0.002$), I expected to need more CPU hours in the case of the former in order to obtain similar accuracy to the case of the latter. This expectation was confirmed: 2930 CPU hours were required in order to obtain an error of $\Delta n = 0.005$ in the electron density $\langle n \rangle$ for $U = 2.76 \text{ eV}$, whilst 26093 CPU hours (almost 9 times more) were required in order to obtain an error of $\Delta n = 0.003$ for $U = 2.94 \text{ eV}$. The data points $N_x = 20$, $U = 2.76, 2.94 \text{ eV}$ were chosen to illustrate the computational cost because they were some of the most statistically demanding parts of this study.

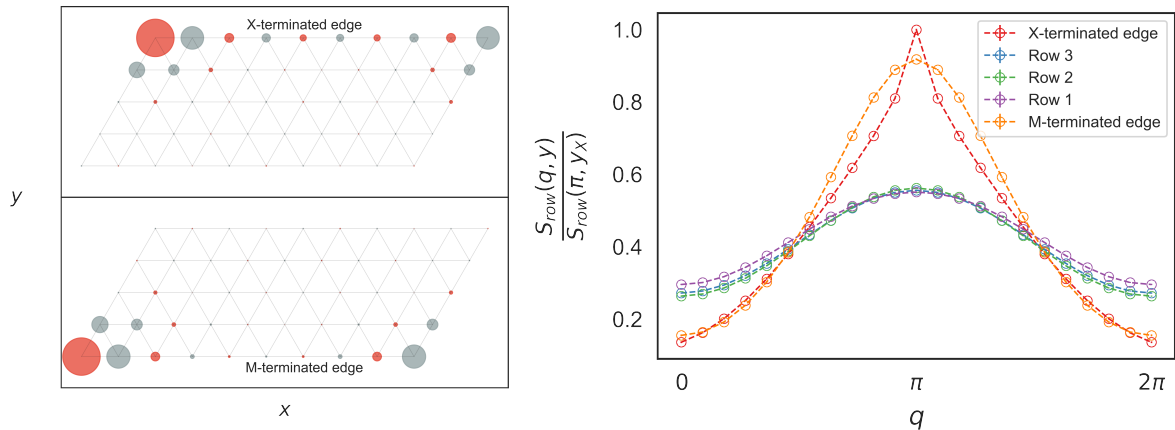


Figure 3.9: Evidence for the AF1 phase obtained with DetQMC for MoS₂ nanoribbons, with $U = 2.76 \text{ eV}$ and $T = 267 \text{ K}$. (Left) Spin-spin correlations for a 10×5 ribbon for edge filling $\nu_{\text{edge}} = 0.75 \pm 0.01$, measured with respect to the leftmost site of the X(M) edge. The size of the circles indicates the magnitude of the correlations (stronger on the X edge). Red corresponds to a positive correlation and blue to a negative correlation. (Right) Magnetic structure factor per row, normalised to its maximum value ($q = \pi$, at the X edge). Here, I consider a 22×5 MoS₂ ribbon with $\nu_{\text{edge}} = 0.745 \pm 0.008$. The error bars are negligibly small.

On the top panel of Figure 3.8, I show the average sign for some of the parameters (N_x, U) I use throughout this section. The width is $N_y = 5$ M atoms. According to Equation 3.9, the electron density corresponding to $\nu_{\text{edge}} = 3/4$ is $\langle n \rangle = 11/15$. For each system size N_x in the longitudinal direction, I fix the chemical potential so as to approximate this electron density, measured with DetQMC, as closely as possible. On the bottom panel of Figure 3.8, I show the chemical potential required in order to obtain $\langle n \rangle_{\text{QMC}} \approx 11/15$. Note that it initially grows with the system size, but then tends to stabilise. This is already apparent for $N_x = 16$.

On the left panel of Figure 3.9, I show the spin-spin correlator along the edges measured with DetQMC. For $\nu_{\text{edge}} \approx 0.75$ — for which the AF1 phase appears in MFT — my DetQMC results show that the spin-spin correlator has an alternating pattern that signals antiferromagnetic ordering. The staggered pattern corresponds to a peak at π in $S_{\text{row}}(q, y)$ computed for the edges of the ribbon ($y = 0, y = N_y - 1$), shown on the right panel of Figure 3.9. This peak is considerably more pronounced on the edges than on the other rows of the ribbon, indicating a tendency towards edge-antiferromagnetic ordering. The sharper peak for the X edge compared to the M edge confirms that antiferromagnetism is more robust on the former.

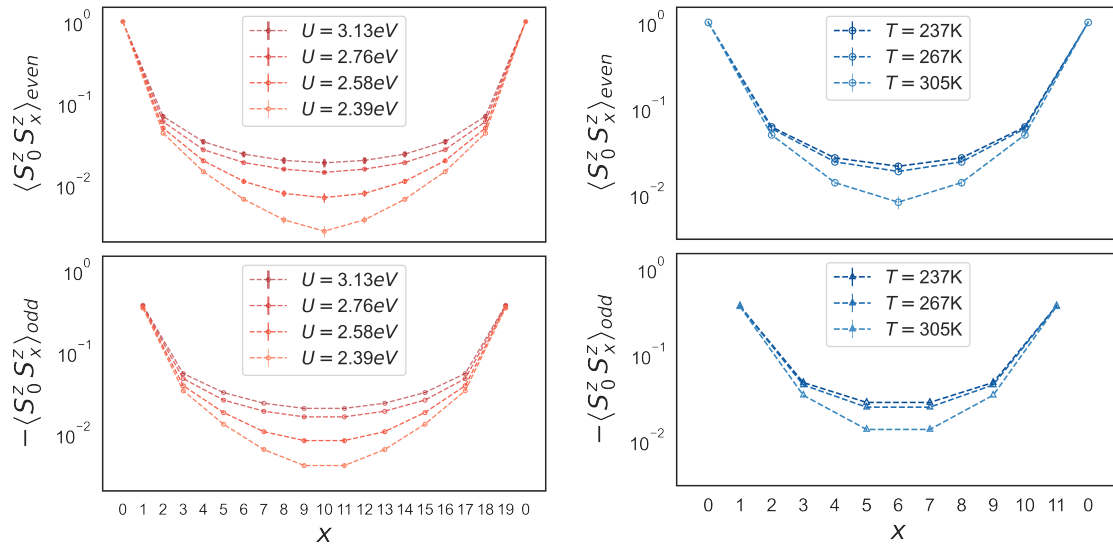


Figure 3.10: Spin-spin correlators between even and odd sites, along the X edge of MoS₂ nanoribbons measured with DetQMC for $\nu_{\text{edge}} \approx 0.75$. On the left panels, I vary the Hubbard interaction U and fix the temperature $T = 267\text{K}$ for a 20×5 ribbon. On the right panels, I vary T and fix $U = 2.94\text{eV}$ for a 12×5 ribbon.

In Figure 3.10, I show that as the Hubbard interaction U (left panels) or the inverse temperature β (right panels) increase, the spin-spin correlations at the X edge increase in magnitude. As can be seen on the right panels, for $T = 267\text{K}$ the behaviour of the spin-spin correlations does not differ significantly from those of the system at lower temperature $T = 237\text{K}$. As the temperature increases, the average sign gets closer to 1, yielding less statistical fluctuations. Thus, in the remainder of this section, I fix $T = 267\text{K}$ since it gives statistically relevant results which are already sufficiently close to the zero temperature limit. Note that, taking the semiconducting bulk gap $\Delta \sim 1\text{eV}$ in two-dimensional TMDs as an estimate for the bandwidth of edge states, I obtain $\beta\Delta \sim 43$ at $T = 267\text{K}$, which is well within typical values used to simulate ground state properties with DetQMC.

By varying the longitudinal dimension of the ribbon, N_x , one is able to extrapolate the value of the staggered magnetisation to

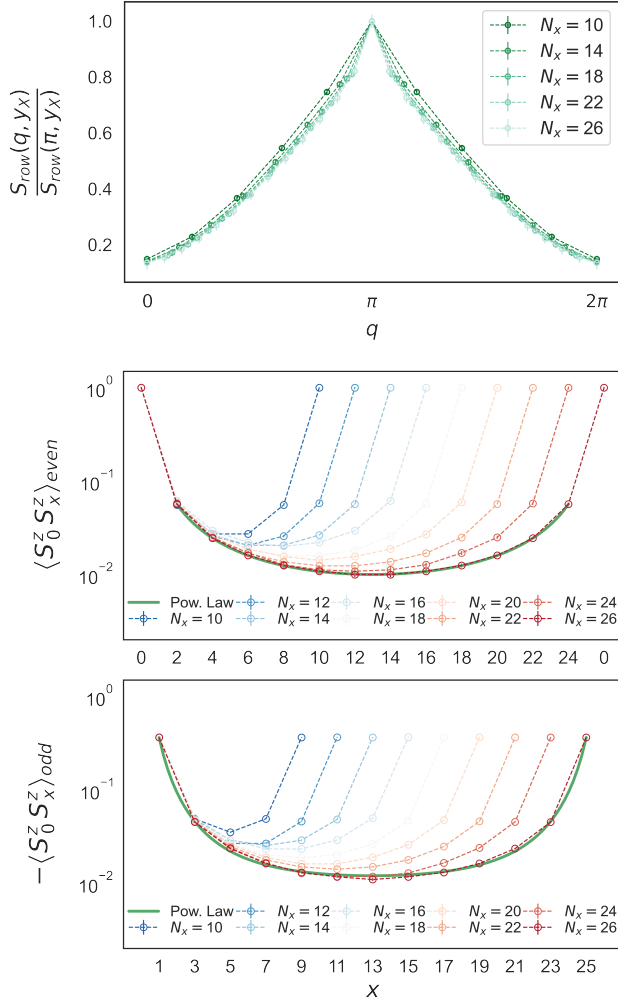


Figure 3.11: (Top) Magnetic structure factor $S_{\text{row}}(q, y_X)$ normalised to the peak $S_{\text{row}}(\pi, y_X)$ for nanoribbons with a width $N_y = 5$ M atoms and $U = 2.76$ eV at $T = 267$ K for $\nu_{\text{edge}} \approx 0.75$. The $q = \pi$ peak sharpens as N_x increases. (Bottom) Spin-spin correlations corresponding to the curves on the top panel with additional data shown. I use $N_x = 10, \dots, 26$ in steps of 2. The error bars are smaller than the symbols. The green curves are fits to the DetQMC data using functions that decrease as a power law.

the thermodynamic limit using the method outlined in Section 3.1.2. In Figure 3.11, I show finite-size scaling data for $U = 2.76$ eV. On the top panel, one can see that the $q = \pi$ peak of $S_{\text{row}}(q, y_X)$ sharpens as N_x increases. On the bottom panel, it is seen that the staggered spin-spin correlation on the X edge tends to a constant as the system size is increased, which signals antiferromagnetic ordering.

I find that the spin-spin correlations decay algebraically, indicating quasi long-range order. To fit the results, I use the power law:

$$(-1)^x \langle S_0^z S_x^z \rangle = \left(\frac{x}{\xi} \right)^{1-\eta} + \left(\frac{N_x - x}{\xi} \right)^{1-\eta} + \text{constant}, \quad (3.10)$$

where ξ and η are respectively the correlation length and the critical exponent, with $\xi = \xi_{\text{even}}, \xi_{\text{odd}}$ and $\eta = \eta_{\text{even}}, \eta_{\text{odd}}$ depending on whether x is odd or even. By fitting to the DetQMC data for $N_x = 26$, I find the correlation lengths: $\xi_{\text{even}} = 0.225 \pm 0.003$ and $\xi_{\text{odd}} = 0.605 \pm 0.003$. These are consistent with the scaling hypothesis in Equation 3.6 since $\xi_{\text{even/odd}} \ll N_x$. I also find the

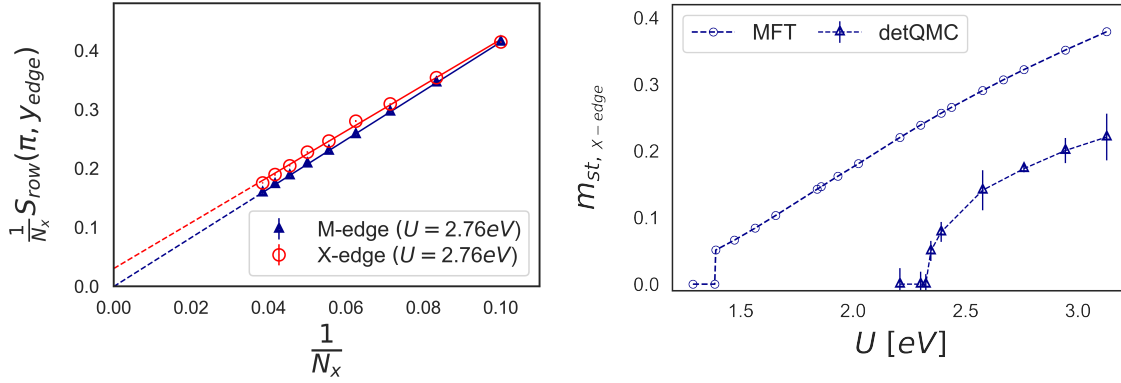


Figure 3.12: (Left) DetQMC results for $S_{\text{row}}(\pi, y)/N_x$, with $y = y_{\text{edge}}$, as a function of $1/N_x$, for nanoribbons with a width of $N_y = 5$ M atoms at $T = 267 \text{ K}$ and $v_{\text{edge}} \approx 3/4$. Red circles are for X edge and blue triangles for M edge. The lines are fits to the data using Equation 3.8. Dashed lines are extrapolations to the thermodynamic limit (I repeat the extrapolation illustrated on this panel for varying Hubbard interaction U to produce the bottom panel). (Right) Comparison between the staggered magnetisations on the X edge obtained with MFT (circles) and DetQMC (triangles) as a function of U . MFT results are for $N_y = 5$ and $T = 0$.

critical exponents $\eta_{\text{even}} = 2.343 \pm 0.008$ and $\eta_{\text{odd}} = 3.06 \pm 0.02$.

3.2.4 Comparison between mean field theory and quantum Monte Carlo

I close this section with a critical comparison of the results obtained from MFT and DetQMC at $v_{\text{edge}} = 3/4$, where the AF1 phase emerges. In order to obtain the staggered magnetisation based on the DetQMC results, I plot $S_{\text{row}}(\pi, y)/N_x$ for $y = y_{\text{edge}}$ as a function of $1/N_x$, and use Equation 3.8 to extrapolate to the thermodynamic limit. Representative results are shown on the left panel of Figure 3.12.

Notice that although I observe antiferromagnetic correlations at the M edge with DetQMC, these do not signal magnetic ordering in the thermodynamic limit: the blue dashed line on the top panel intersects the y -axis approximately at zero. It is possible that antiferromagnetism on the M edge appears for higher values of U , similarly to what is observed with MFT. However, one cannot confirm this suspicion because the sign problem becomes too severe beyond $U = 3.13 \text{ eV}$ (at which point the DetQMC simulations show no sign of antiferromagnetic order on the M edge).

On the right panel of Figure 3.12, I compare the extrapolated staggered magnetisation obtained with DetQMC to the MFT results. I considered the same ribbon width $N_y = 5$ in MFT but used $T = 0$. As expected, DetQMC predicts a higher critical interaction, $U_{c, \text{QMC}} \approx 2.33 \pm 0.02 \text{ eV}$, compared to the MFT result, $U_{c, \text{MFT}} = 1.387 \pm 0.004 \text{ eV}$. The agreement becomes better if one considers wider ribbons and/or $T > 0$ in the MFT calculation. Qualitatively, the MFT and DetQMC results are similar in the sense

that edge-antiferromagnetic ordering is established for values of the interaction that are of the same order of the band gap $U_c \sim \Delta$, with MFT overestimating long-range ordering. DetQMC unveils quasi-long-range order, with algebraic behaviour of the spin-spin correlations.

3.3 Discussion and conclusion

I have used MFT and DetQMC to probe edge magnetism in zTMDNRs via a minimal three-band Hubbard model. Three main questions have been addressed:

1. How does changing the edge filling affect the phase diagram?
2. What is the effect of multiorbital interactions?
3. Can one use the numerically exact DetQMC approach to probe edge magnetism in zTMDNRs in spite of the well known sign problem?

To answer the first question, I considered an intraorbital Hubbard- U interaction, which I treated at the mean field level. I found two gapped phases: an edge-dimer, when the edges are half filled, and an edge-antiferromagnetic phase at three-quarter edge filling. For other edge fillings, there is a tendency towards edge-ferromagnetism. As shown in Figure 3.5, the ferromagnetic phases are metallic and the edge magnetisation depends on the edge filling. Such magnetic edge states give rise to spin-polarised edge currents which could be tuned by changing the Fermi level through a back gate voltage. In particular, when the gapped phases are reached, these currents are suppressed. Similar behaviour has been explored in zTMDNRs in the presence of magnetic proximity effect produced by ferromagnetic [210, 211] and antiferromagnetic [212] substrates. My results indicate that intrinsic magnetism could also be used to induce spin-polarised edge currents.

The second question has been answered by considering not only the intraorbital Hubbard interaction, U , but also an interorbital interaction term (U'), as well as Hund (J) and pair-hopping (J') terms, characteristic of transition metal atoms. Within MFT, I obtained rich phase diagrams shown in Figure 3.7, which corroborate and further complement the phases obtained with the simpler intraorbital Hubbard- U interaction. Generically, the interorbital (U') term tends to suppress the magnetic phases, while J and J' tend to enhance them. However, there are fillings for which U' stabilises the ferromagnetic phase in a large portion of the phase diagram, as shown in Figure 3.7(d).

[210]: Cortés et al. (2019), ‘Tunable Spin-Polarized Edge Currents in Proximitized Transition Metal Dichalcogenides’

[211]: Correa et al. (2020), ‘Anisotropy of the spin-polarized edge current in monolayer transition metal dichalcogenide zigzag nanoribbons’

[212]: Cortés et al. (2020), ‘Reversible edge spin currents in antiferromagnetically proximitized dichalcogenides’

As far as the third question is concerned, I have successfully applied DetQMC to the intraorbital Hubbard model of Equation 1.1 for zTMDNRs, finding that edge magnetism depends strongly on the edge filling. In particular, at three-quarter edge filling – where the AF1 phase appears at mean field level – DetQMC has only a moderate sign problem and accurate results can be obtained. I have found edge-antiferromagnetic quasi-long-range order with spin-spin correlations behaving algebraically, reinforcing the AF1 phase predicted by MFT. The extrapolated staggered magnetisation from DetQMC is consistent with the MFT result, as shown in Figure 3.12. Even though in MFT long-range order is slightly overestimated, DetQMC and MFT agree that antiferromagnetism is more robust on the X edge.

[210]: Cortés et al. (2019), ‘Tunable Spin-Polarized Edge Currents in Proximitized Transition Metal Dichalcogenides’

[211]: Correa et al. (2020), ‘Anisotropy of the spin-polarized edge current in monolayer transition metal dichalcogenide zigzag nanoribbons’

[212]: Cortés et al. (2020), ‘Reversible edge spin currents in antiferromagnetically proximitized dichalcogenides’

[213]: Čadež et al. (2019), ‘Robust one dimensionality at twin grain boundaries in MoSe₂’

[214]: Ávalos-Ovando et al. (2019), ‘Lateral heterostructures and one-dimensional interfaces in 2D transition metal dichalcogenides’

Finally, let me point out that the dependence of edge magnetism on edge filling that I found might be relevant when interpreting experimental results. Often, the density of zigzag edges is used to explain how the ferromagnetic response varies between different nanosheet samples. My results point to the edge filling as yet another key ingredient, since structural defects or chemisorbed adatoms may effectively change the filling of the edge. Finally, an important aspect for further study is the impact of a magnetic substrate — which induces magnetic exchange fields as considered in References [210–212] — on the edge magnetism of zTMDNRs. The methods I use in this work could be used to determine whether the edge magnetism I have found survives the presence of a substrate, and whether phase transitions can be induced by tuning the coupling to the substrate. Searching for edge magnetism at twin grain boundaries in two-dimensional TMDs [213] and at one-dimensional interface-states in TMD heterostructures [214] is another interesting direction.

**PART 2 — REAL-SPACE SPECTRAL SIMULATION
OF GENERALISED KITAEV MODELS**

Kitaev-Heisenberg Model

4

In the second part of this thesis, I apply a toolset of spectral methods to compute both static (*e.g.* spin correlations) and dynamic (*e.g.* spin susceptibility) quantum observables in paradigmatic frustrated systems with competing interactions. Spectral methods based upon Chebyshev expansions have recently proven useful in different contexts [174, 177, 180, 181, 184–186, 189, 190, 200, 215, 216], and here I will be interested in whether similar approaches would be effective in the context of strongly correlated matter. I focus on generalised honeycomb Kitaev models, *i.e.* systems that combine Kitaev interactions with other types of magnetic exchange.

In Section 1.2.3, I have discussed the Kitaev model on the honeycomb lattice, one of the rare examples of an exactly solvable microscopic model [56] showing exchange frustration, *i.e.* nearest neighbour interactions that cannot be simultaneously minimised. This is similar to geometric frustration which notably occurs in the case of the antiferromagnetic Ising model on the triangular lattice [217]. I remind the reader that in the Kitaev case, frustration is created by bond-directional interactions which were found to give way to a fractionalised excitation spectrum of Majorana fermions coupled to a gauge field [56]. This has attracted great attention because it opens up the possibility of synthesising spin liquid materials with exotic topological orders, and which can be used as experimental probes of the fundamental physics of Majorana fermions and gauge fields [53–55].

A prevalent class of materials for the physical realisation of Kitaev physics are honeycomb iridates, which are transition metal oxides with partially filled *d*-shells. In Chapter 1, I reviewed how a subtle interplay of spin–orbit coupling and electronic correlations generates the type of bond-directional interactions that appear in the Kitaev model within these QSL candidates, known as Kitaev magnets. The latter are spin-orbit assisted Mott insulators, for which the Kitaev exchange interaction is thought to be responsible for the appearance of spin liquid physics [3, 51, 55, 218, 219]. The Kitaev exchange interaction also plays a key role in the modelling of other compounds such as the van der Waals ruthenate α -RuCl₃. A recent study proposes a minimal microscopic 2D spin model for α -RuCl₃ [220]. The model at play is an extension of the *JKT* model of Section 1.2.4, which also takes into account third neighbour exchange. The authors treat this extension of the K-H model using a mean-field random-phase approximation, aiming at extracting quantities such as the dynamical structure factor [220]. The use of

4.1 Numerical implementation of the model . . .	95
4.2 Zero-temperature consistency and micro-canonical approaches .	99
4.3 Canonical approaches: finite temperature . . .	108
4.4 Bench-marking the hybrid Lanczos-Chebyshev method against the continued fraction Lanczos approach	113

[217]: Wannier (1950), ‘Antiferromagnetism. The Triangular Ising Net’

[56]: Kitaev (2006), ‘Anyons in an exactly solved model and beyond’

[220]: Maksimov et al. (2020), ‘Rethinking α -RuCl₃’

[14]: Winter et al. (2018), ‘Probing α -RuCl₃ Beyond Magnetic Order’

[61]: Nasu et al. (2021), ‘Spin dynamics in the Kitaev model with disorder’

[221]: Nasu et al. (2020), ‘Thermodynamic and transport properties in disordered Kitaev models’

1: The scheme in Refs. [61, 221] requires the partial diagonalisation of the original Hamiltonian in terms of Majorana fermions. On the other hand, a direct QMC simulation of the Kitaev model suffers from the sign problem.

[15]: Jaklič et al. (1994), ‘Lanczos method for the calculation of finite-temperature quantities in correlated systems’

[16]: Aichhorn et al. (2003), ‘Low-temperature Lanczos method for strongly correlated systems’

[34]: Sugiura et al. (2012), ‘Thermal Pure Quantum States at Finite Temperature’

[35]: Sugiura et al. (2013), ‘Canonical Thermal Pure Quantum State’

[17]: Prelovšek et al. (2013), ‘Ground State and Finite Temperature Lanczos Methods’

[3]: Chaloupka et al. (2010), ‘Kitaev-Heisenberg Model on a Honeycomb Lattice’

[4]: Chaloupka et al. (2013), ‘Zigzag Magnetic Order in the Iridium Oxide Na₂IrO₃’

[5]: Gotfryd et al. (2017), ‘Phase diagram and spin correlations of the Kitaev-Heisenberg model’

[59]: Nasu et al. (2017), ‘Spin-Liquid-to-Spin-Liquid Transition in Kitaev Magnets Driven by Fractionalization’

this mean-field approach is justified by comparing its results with ED [14]. However, ED is limited to relatively small system sizes (for example, in Reference [14], a 24-site cluster is used). Thus, this approach runs into the risk of overlooking large scale properties of the model. In fact, in References [61, 221], the authors detect finite-size effects when computing the dynamical spin structure factor using QMC simulations of the Kitaev model in the presence of disorder — which deems the study of large scale properties crucial — even for clusters of 288 sites¹. These developments illustrate the need to develop accurate, general purpose computational methods that scale favourably with the system size, while remaining unbiased.

The Chebyshev polynomial methods I shall discuss below have a comparable complexity to Lanczos-based methods. They both share the advantage of being free of the sign problem, even though they cannot reach the same system sizes as QMC. Yet, Chebyshev expansions have a few key features that can make them more advantageous than their Lanczos counterparts, namely superior robustness and accuracy. For example, as seen in Section 2.8.1, the finite temperature generalisation of the Lanczos method [15] has a low-temperature counterpart [16] that was developed to tackle loss of accuracy due to statistical convergence issues at low-temperature. In contrast, in Section 2.8.3, I introduce a seamless Chebyshev approach (dubbed FTCP) that is accurate and does not require a low-temperature counterpart. Moreover, as I will show in this chapter, FTCP has advantages even over TPQ [34, 35]. Another application is to study dynamics (*e.g.* spectral functions), where the Chebyshev approach can be used as a more flexible and efficient alternative to its Lanczos-based counterpart, which approximates the resolvent operator in continued fraction form [17].

To summarise, the aim of this part of the thesis is to compare the convergence properties and performance of the Lanczos, TPQ and Chebyshev methods in detail in practical applications. I shall demonstrate the advantages of the Chebyshev framework in the study of two paradigmatic quantum spin models on the honeycomb lattice that were mentioned previously in Section 1.2.4: the K-H model [3–5], to which this chapter is devoted to, and the K-I model [59], which will be the subject of the next chapter.

This chapter is organised as follows. Section 4.1 gives a succinct description of the K-H model and its implementation in terms of matrix-vector multiplication in the iterative methods used here. In Section 4.2, I check that my results are consistent at zero temperature by computing the ground state energy and nearest-neighbour spin-spin correlation function of the K-H model on a 24-spin hexagonal cluster with PBCs using all methods and comparing

them with previously known results that I reproduced using the ED Lanczos technique [3, 4]. The transitions between a variety of magnetic phases, namely ferromagnetic, Néel, zigzag and stripy antiferromagnetic and quantum spin liquid phases — that were originally found in References [3, 4] — are identified accurately and efficiently. I also present a detailed analysis of the dependence of the estimators for the the spin–spin correlation on the relevant parameters: the number of initial random states, truncation order and, in the case of the CPGF, also the energy resolution. Going beyond ground state properties, in Section 4.3, I study the temperature dependence of the nearest-neighbour spin–spin correlation, specific heat and entropy of the K-H model and show that my results match the tensor network results of Reference [10]. Moreover, I accurately obtain the temperature dependence of these quantities over more than three decades in temperature in the vicinity of a QSL — where Kitaev interactions dominate over Heisenberg exchange — by means of the FTCP method introduced earlier. The low-temperature numerical robustness of FTCP enables the discovery of as-yet-unknown signs of thermal fractionalisation in the vicinity of the pure Kitaev limit of the K-H model: I present novel results indicating a three-stage release of entropy in the vicinity of the Kitaev limit, accompanied by a three-peak structure of the specific heat. Here, I emphasise that the efficiency of FTCP enables these numerically intensive calculations, which would be extremely costly with alternative methods, such as TPQ. Lastly, in Section 4.4, I bench-mark my implementation of the HLC method and compute the dynamical spin susceptibility for the K-H model, reproducing results from Reference [5], originally obtained with the continued fraction Lanczos method [17]. Here, I show that HLC, its Chebyshev counterpart, gives identical results, thereby validating my implementation. My findings suggest that the low-temperature stability, efficiency and versatility of the Chebyshev framework developed here could pave the way for previously unattainable studies of two-dimensional quantum spin models.

[3]: Chaloupka et al. (2010), ‘Kitaev-Heisenberg Model on a Honeycomb Lattice’

[4]: Chaloupka et al. (2013), ‘Zigzag Magnetic Order in the Iridium Oxide Na_2IrO_3 ’

[10]: Li et al. (2020), ‘Universal thermodynamics in the Kitaev fractional liquid’

[5]: Gotfryd et al. (2017), ‘Phase diagram and spin correlations of the Kitaev-Heisenberg model’

[17]: Prelovšek et al. (2013), ‘Ground State and Finite Temperature Lanczos Methods’

4.1 Numerical implementation of the model

The K-H model combines Kitaev and Heisenberg interactions. The Hamiltonian can be cast as a sum over nearest neighbouring bonds $\langle i, j \rangle^\gamma$ on the honeycomb lattice (the superscript refers to the type of bond, see Figure 1.8):

$$\hat{H} = A \sum_{\langle i, j \rangle^\gamma} \left(K \hat{S}_i^\gamma \hat{S}_j^\gamma + J \hat{\mathbf{S}}_i \cdot \hat{\mathbf{S}}_j \right). \quad (4.1)$$

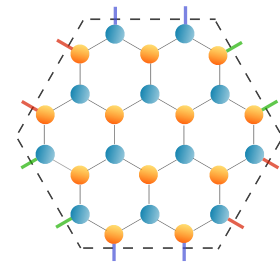


Figure 4.1: 24-spin hexagonal cluster with PBCs on the honeycomb lattice. The red, green and purple bonds illustrate the periodic boundary conditions.

[5]: Gotfryd et al. (2017), 'Phase diagram and spin correlations of the Kitaev-Heisenberg model'

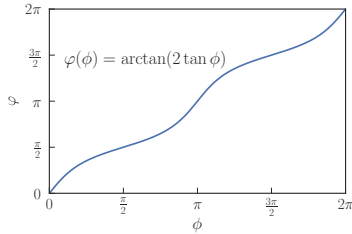


Figure 4.2: Conversion between the two widely used parameterisations of the K-H model in the literature.

with $K = \sin \varphi$, $J = \cos \varphi$, and where $\gamma = x, y, z$ is one of the three types of bond on the honeycomb lattice. I use the conventions of Reference [5]: $\varphi \in [0, 2\pi]$ parameterises the strength of each term and ensures that all possible ratios of the Heisenberg and Kitaev interactions are considered, and an overall energy scale is defined and set to unity throughout: $A = \sqrt{J^2 + K^2} \equiv 1$. The bond-directionality of the Kitaev interaction implies that for each distinct type of bond $\gamma = x, y, z$, there is a correspondent interaction (respectively $S^x S^x$, $S^y S^y$, $S^z S^z$), as shown in Figure 1.8. Here, $\varphi \in [0, 2\pi]$ is a parameter, which can be varied so as to exhaust all possible ratios of the K and J coupling constants, *i.e.* the relative strengths of the Kitaev and Heisenberg interactions and their signs.

Comment 4.1.1

The Kitaev term favours local bond correlations of the γ spin component, while the Heisenberg term on its own would lead to either antiferromagnetic or ferromagnetic long range order, depending on whether $J > 0$ or $J < 0$, respectively.

The parameterisation $K = 2 \sin \phi$, $J = \cos \phi$ is also commonly used in the literature, but one can easily convert between the two using the relation $\varphi = \arctan(2 \tan \phi)$ (see Figure 4.2).

In order to implement the honeycomb K-H Hamiltonian in my vector recursions, I need to derive its action on a generic spin state $|\sigma\rangle$. For convenience, I define the Hamiltonian per site as

$$\hat{h} = \frac{1}{4N} \sum_{\langle i,j \rangle^\gamma} \hat{h}_{\langle i,j \rangle^\gamma}, \quad (4.2)$$

where $\hat{h}_{\langle i,j \rangle^\gamma} = \cos \varphi \hat{\sigma}_i \cdot \hat{\sigma}_j + \sin \varphi \hat{\sigma}_i^\gamma \hat{\sigma}_j^\gamma \equiv \hat{j}_{\langle i,j \rangle} + \hat{k}_{\langle i,j \rangle}^\gamma$.

Using Equation 2.22, one can show that the Heisenberg component, $\hat{j}_{\langle i,j \rangle}$ acts as follows:

$$\hat{j}_{\langle i,j \rangle} |\sigma\rangle = \begin{cases} \sigma_i \sigma_j = +1 : & \cos \varphi |\sigma\rangle \\ \sigma_i \sigma_j = -1 : & \cos \varphi (2 |\sigma'\rangle - |\sigma\rangle), \end{cases} \quad (4.3)$$

where $|\sigma'\rangle$ differs from $|\sigma\rangle$ only in that it has spins i and j flipped, a notation inherited from Section 2.4.

Similarly, using Equation 2.23, one can show that the Kitaev component, $\hat{k}_{\langle i,j \rangle}^\gamma$ acts as follows:

Algorithm 4: Generate the Kitaev Hamiltonian. The function *neighbours* is assumed to return the index j of the neighbour and its corresponding type of bond γ . Constants h_0, h_1, h_2, h_3, h_4 are given in Equation 4.5.

Data: $2^N \times 2^N$ Hamiltonian Matrix initialised with zeros.

Result: $2^N \times 2^N$ Hamiltonian Matrix filled with the relevant matrix elements.

```

1 for  $a = 0, \dots, 2^N - 1$  do
2   for  $i = 0, \dots, N - 1$  do
3     for  $j, \gamma \leftarrow neighbours(i)$  do
4       if  $a[i] = a[j]$  then
5         if  $\gamma = z$  then
6            $h(a, a) \leftarrow h(a, a) + h_1;$ 
7         else
8            $h(a, a) \leftarrow h(a, a) + h_0;$ 
9            $b = flip(a[i], a[j]);$ 
10          if  $\gamma = y$  then
11             $h(a, b) \leftarrow -h_2;$ 
12          else
13             $h(a, b) \leftarrow h_2;$ 
14        else
15          if  $\gamma = z$  then
16             $h(a, a) \leftarrow h(a, a) - h_1;$ 
17             $b = flip(a[i], a[j]);$ 
18             $h(a, b) \leftarrow h_4;$ 
19          else
20             $h(a, a) \leftarrow h(a, a) - h_0;$ 
21             $b = flip(a[i], a[j]);$ 
22             $h(a, b) \leftarrow h_3;$ 

```

$$\hat{k}_{(i,j)\gamma} |\sigma\rangle = \begin{cases} \gamma = x, \sigma_i \sigma_j = \pm : & \sin \varphi |\sigma'\rangle \\ \gamma = y, \sigma_i \sigma_j = \pm : & \mp \sin \varphi |\sigma'\rangle \\ \gamma = z, \sigma_i \sigma_j = \pm : & \pm \sin \varphi |\sigma\rangle \end{cases} \quad (4.4)$$

Let me define the following constants:

$$\begin{aligned} h_0 &= \cos \varphi, \\ h_1 &= \cos \varphi + \sin \varphi, \\ h_2 &= \sin \varphi, \\ h_3 &= 2 \cos \varphi + \sin \varphi, \\ h_4 &= 2 \cos \varphi. \end{aligned} \quad (4.5)$$

I now gather the Heisenberg and Kitaev contributions, thus completing the derivation of the action of $\hat{h}_{\langle i,j \rangle}^\gamma$ in terms of the constants above:

$$\hat{h}_{\langle i,j \rangle}^\gamma |\sigma\rangle = \begin{cases} \gamma = x, \sigma_i \sigma_j = +1 : & h_0 |\sigma\rangle + h_2 |\sigma'\rangle \\ \gamma = x, \sigma_i \sigma_j = -1 : & -h_0 |\sigma\rangle + h_3 |\sigma'\rangle \\ \gamma = y, \sigma_i \sigma_j = +1 : & h_0 |\sigma\rangle - h_2 |\sigma'\rangle \\ \gamma = y, \sigma_i \sigma_j = -1 : & -h_0 |\sigma\rangle + h_3 |\sigma'\rangle \\ \gamma = z, \sigma_i \sigma_j = +1 : & h_1 |\sigma\rangle \\ \gamma = z, \sigma_i \sigma_j = -1 : & h_4 |\sigma'\rangle - h_1 |\sigma\rangle \end{cases} \quad (4.6)$$

The Hamiltonian can be generated using Algorithm 4. Yet, in my calculations, I never explicitly generate the Hamiltonian. Instead, a generalisation of Algorithm 4 similar to Algorithm 2 is used to carry out matrix-vector multiplications on-the-fly.

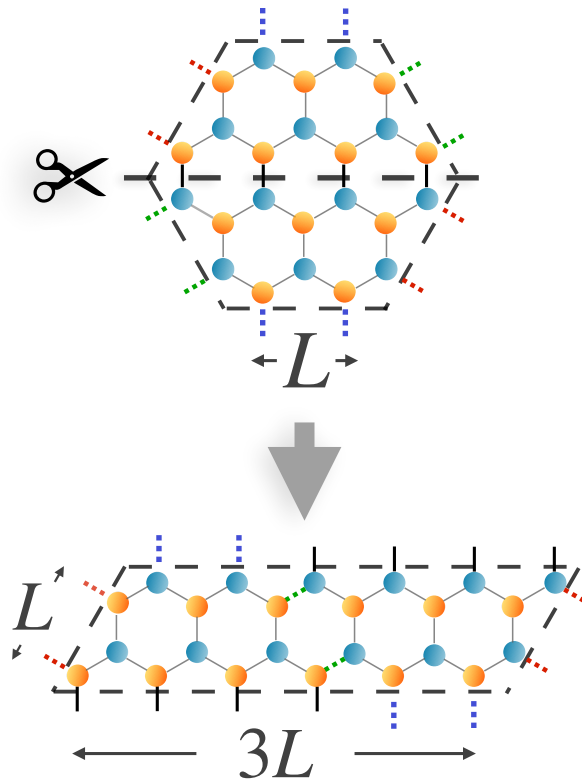


Figure 4.3: PBCs for a 24-spin hexagonal cluster. The figure illustrates the general procedure to create a hexagonal cluster of arbitrary size. To obtain, $N = 24$, I set $L = 2$. The dotted red, green and purple links represent nearest neighbouring spins. Standard PBCs on the parallelogram are modified solely by a shift in the connectivity of two spins along each of the two longitudinal edges.

Another important detail of the implementation is the indexing of sites in the 24-spin hexagonal cluster with PBCs. The cluster can be thought of as 6×2 parallelogram with carefully tailored boundary conditions, so as to obtain the same connectivity as the hexagon. This is illustrated in Figure 4.3.

4.2 Zero-temperature consistency and microcanonical approaches

The calculations presented throughout the next subsections serve two purposes: to prove that the classes of methods considered in this work are consistent and correctly capture the physics of frustrated quantum magnets and, more importantly, to show that the Chebyshev polynomial-based approaches offer significant advantages in terms of performance, stability and generality, especially when combined with Lanczos algorithms.

Firstly, I reproduced the results of References [3–5] using ED (via the “ground state” Lanczos algorithm), as used in the original references. Then, I recovered these results using both microcanonical and canonical approaches based on Lanczos, TPQ and Chebyshev recursions.

[3]: Chaloupka et al. (2010), ‘Kitaev-Heisenberg Model on a Honeycomb Lattice’

[4]: Chaloupka et al. (2013), ‘Zigzag Magnetic Order in the Iridium Oxide Na_2IrO_3 ’

[5]: Gotfryd et al. (2017), ‘Phase diagram and spin correlations of the Kitaev-Heisenberg model’

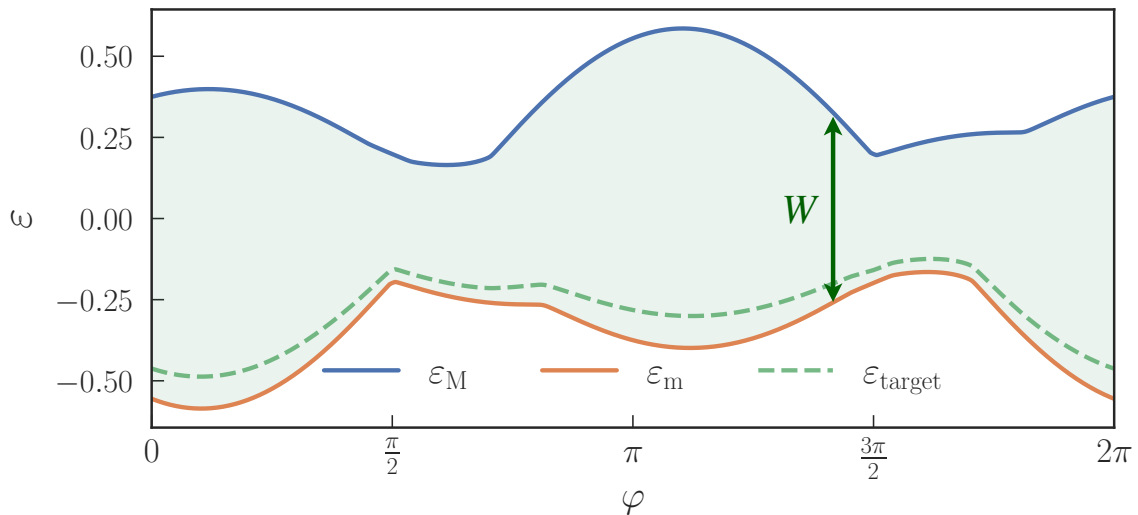


Figure 4.4: Minimum (ε_m) and maximum (ε_M) eigenvalues of the K-H Hamiltonian on a 24-spin periodic hexagonal cluster on the honeycomb lattice, computed with the ground state variant of Lanczos ED. The energy is normalised to the number of spins and the shaded green area represents the spectrum width $W = \varepsilon_M - \varepsilon_m$ for each value of φ . $\varepsilon_{\text{target}} = \varepsilon_m + 0.1W$ are target energies used later to compare MCLM and CPGF.

In order to bench-mark the microcanonical approaches — MCLM, MTPQ and CPGF — I set the ground state energy obtained from Lanczos as the target energy. Crucially, MTPQ and CPGF (and their canonical counterparts) require an estimate of the maximum eigenvalue as well. Although I could have applied Lanczos to the operator $-\hat{h}$ to obtain it, the Hamiltonian of Equation 4.1 happens to have a symmetry that can be used to avoid this additional computation: $-\hat{h}(\varphi) = \hat{h}((\varphi + \pi) \bmod (2\pi))$. Thus, the maximum eigenvalues can be obtained by simply reorganising the minimum eigenvalues as a function of φ and switching their sign (see Figure 4.4). These are the minimum and maximum energies that are then

used as inputs to the TPQ and Chebyshev methods. I remark that even though the ground state energy can be accurately estimated solely using MTPQ, the method requires an upper bound on the maximum eigenvalue (that one would normally obtain from Lanczos anyway). Moreover, MTPQ has much slower convergence to the ground state than Lanczos, as I will also show later, so it is simply more efficient to use Lanczos to obtain extremal eigenvalues. Still, MTPQ provides one with a useful consistency check, while being less memory-intensive — requiring two rather than three vectors of size D — and giving access to good approximations of finite temperature states.

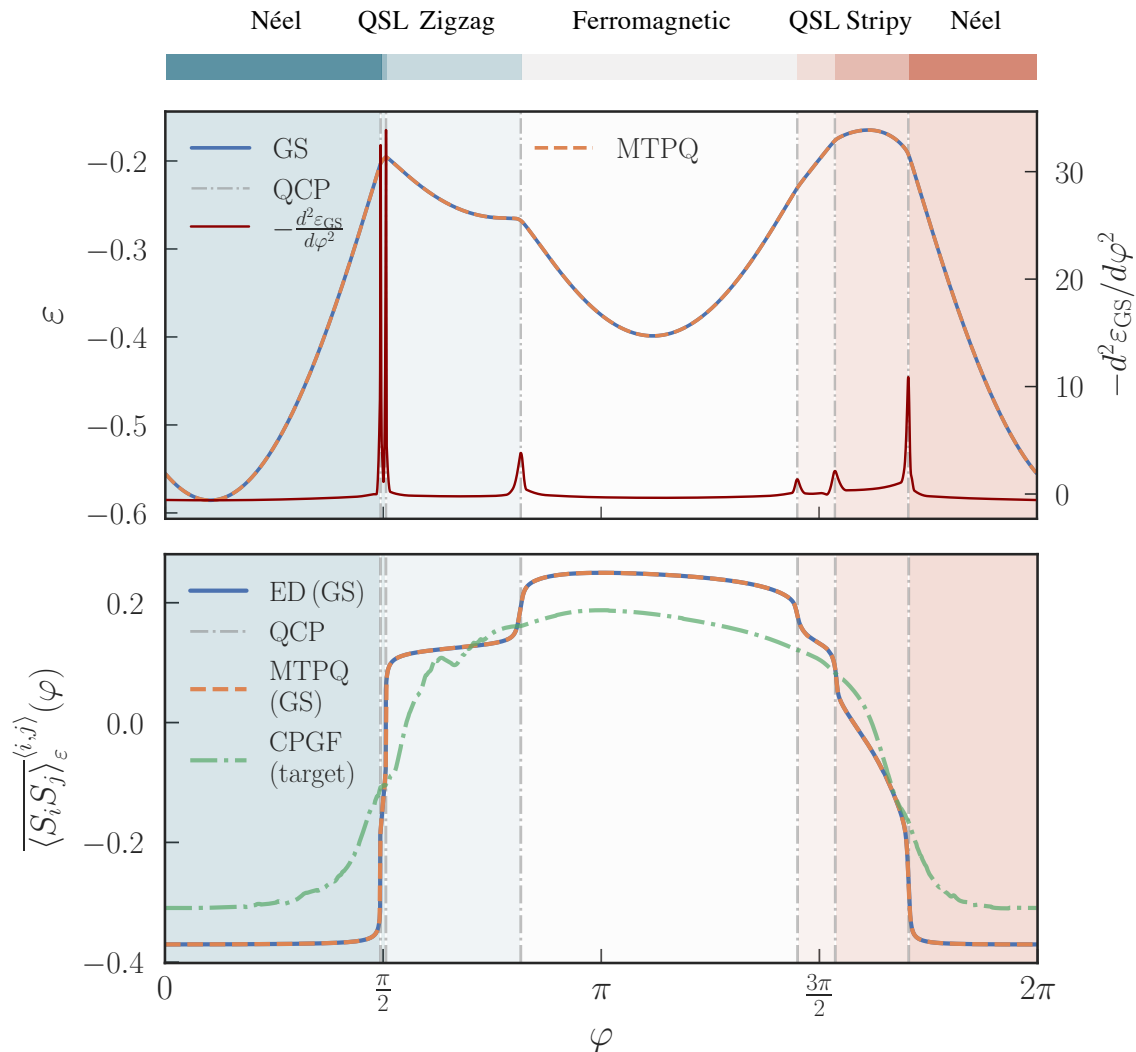


Figure 4.5: Top panel — Ground state energy density obtained with Lanczos ED (solid blue line) and MTPQ (dashed orange line). The two curves show excellent agreement. The solid red line is minus the second derivative of the Lanczos ED curve obtained via finite differences. Its peaks allow one to identify the quantum critical points labeled ‘QCP’. Bottom panel — Ground state nearest neighbour spin–spin correlation computed with Lanczos ED compared with MTPQ. The average of the same observable is also computed with CPGF for states with target energy ϵ_{target} . MCLM results match CPGF, so they are not shown in order to preserve clarity. The symbol $\overline{\langle S_i S_j \rangle}_{\epsilon}^{(i,j)}$ denotes an average over all nearest neighbours $\langle i, j \rangle$ on the honeycomb lattice.

The results I present throughout this section are for the ground

state energy density and nearest neighbour spin–spin correlation of the K-H model. The nearest neighbour spin–spin correlation is used for my bench-mark for two reasons. Firstly, in Reference [5], the authors show that longer-range correlations vanish in the vicinity of the spin liquid phases. Given that I am particularly interested in this region of the phase diagram, it is reasonable to focus on nearest neighbour correlations. Secondly, the step-like behaviour of the nearest neighbour spin–spin correlation coincides with quantum critical points [5]. Moreover, the behaviour of the nearest neighbour correlation as a function of the temperature is intimately connected to peaks in the specific heat [10] — that I also compute using Lanczos, TPQ and Chebyshev — and that are particularly relevant experimentally [222].

For each value of φ , I computed the minimum eigenvalue, or ground-state energy of the Hamiltonian, ε_{GS} , using the Lanczos ED technique. In the top panel of Figure 4.5, I show these results, along with the second derivative $-d^2\varepsilon_{\text{GS}}/d\varphi^2$, which accurately detects quantum phase transitions between magnetically ordered phases (Néel, stripy and zigzag antiferromagnets and a ferromagnet) and two spin liquid phases, which I refer to as antiferromagnetic quantum spin liquid (AFQSL), for ($\varphi \sim \pi/2$) and ferromagnetic quantum spin liquid (FQSL), for ($\varphi \sim 3\pi/2$).

QCP	φ/π	QCP	φ/π
Néel-AFQSL	0.4940	Ferromagnet-FQSL	1.4500
AFQSL-Zigzag	0.5064	FQSL-Stripy	1.5364
Zigzag-Ferromagnet	0.8156	Stripy-Néel	1.7048

The phase boundaries I obtained are summarised in Table 4.1 and agree well with Reference [5]. The Lanczos algorithm shows small statistical fluctuations, enabling one to use a single realisation of the initial random state across the entire phase diagram. As mentioned in Section 2.7.2, a single random vector suffices to achieve good accuracy in the MTPQ approach as well due to the self-averaging properties of the TPQ estimator. In fact, error bars obtained with more realisations are negligibly small and thus are not shown in my plots.

I now move on to the spin correlator. Figure 4.5 shows excellent agreement between the spin–spin correlation computed with Lanczos and MTPQ. As mentioned earlier, the step discontinuities in the correlator signal the quantum phase transitions of the K-H model [3–5]. MTPQ achieves its maximum effective resolution at low-temperatures (*i.e.* large N_{it}) where Figure 4.5 shows that it accurately approximates the ground state [34–36, 223]. These methods are designed to reconstruct the ground state in a recursive fashion. Thus, it is perhaps not too surprising that the energy and

[10]: Li et al. (2020), ‘Universal thermodynamics in the Kitaev fractional liquid’

[222]: Widmann et al. (2019), ‘Thermodynamic evidence of fractionalized excitations in α -RuCl₃’

Table 4.1: Phase boundaries of the K-H model on a periodic 24-spin hexagonal cluster obtained with Lanczos. ‘QCP’ stands for quantum critical point. The uncertainty in φ is 0.0004π .

[3]: Chaloupka et al. (2010), ‘Kitaev-Heisenberg Model on a Honeycomb Lattice’

[4]: Chaloupka et al. (2013), ‘Zigzag Magnetic Order in the Iridium Oxide Na₂IrO₃’

[5]: Gotfryd et al. (2017), ‘Phase diagram and spin correlations of the Kitaev-Heisenberg model’

[34]: Sugiura et al. (2012), ‘Thermal Pure Quantum States at Finite Temperature’

[35]: Sugiura et al. (2013), ‘Canonical Thermal Pure Quantum State’

[36]: Laurell et al. (2020), ‘Dynamical and thermal magnetic properties of the Kitaev spin liquid candidate α -RuCl₃’

[223]: Catuneanu et al. (2018), ‘Path to stable quantum spin liquids in spin-orbit coupled correlated materials’

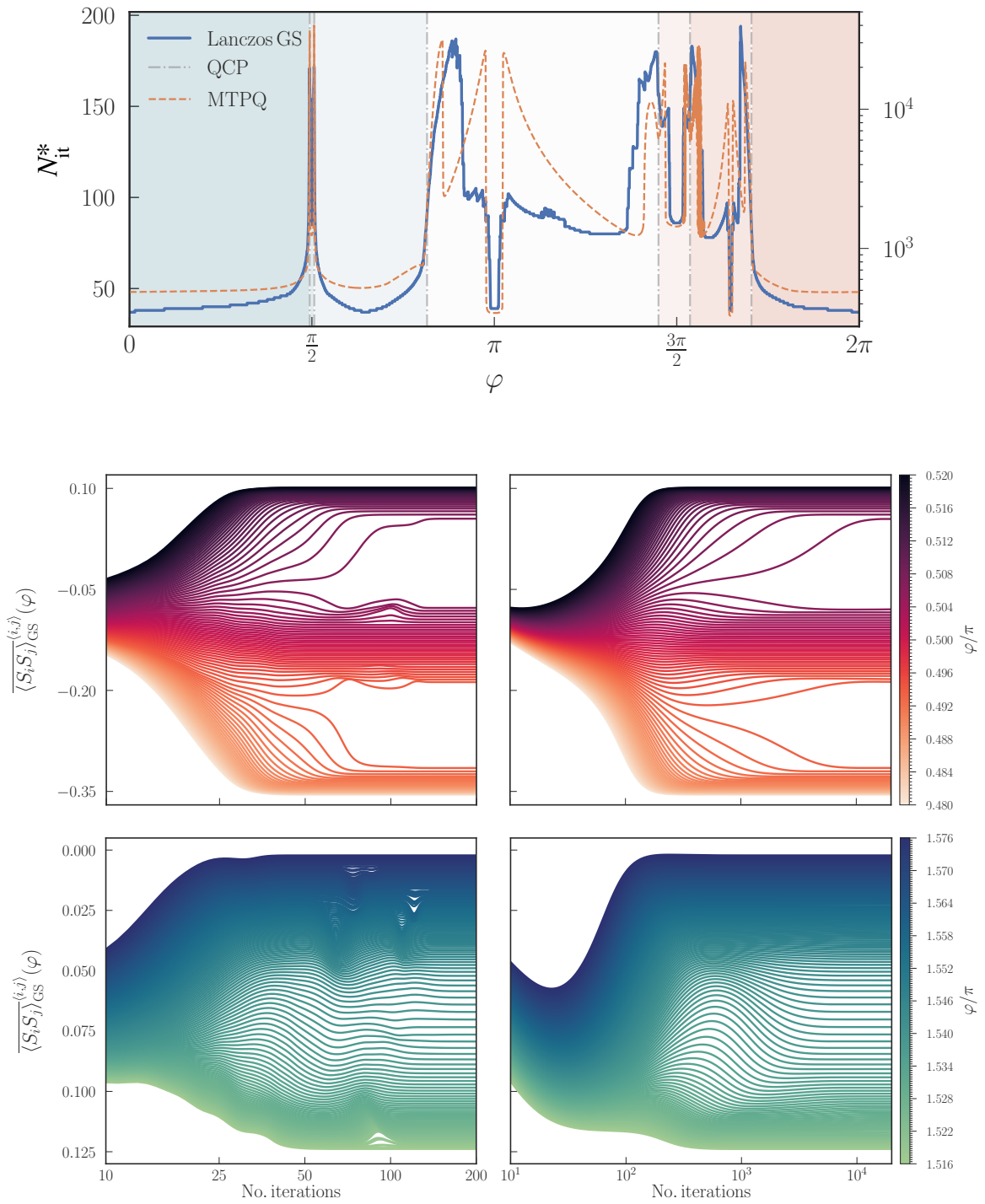


Figure 4.6: Convergence in computations of ground state nearest neighbour spin–spin correlations. Top panel – Dependence of N_{it}^* with φ in Lanczos and MTPQ (left and right vertical axes, respectively). Bottom panel – Convergence of Lanczos (left) and MTPQ (right) around the Kitaev limits: AFQSL on top and FQSL on the bottom.

nearest neighbour spin correlation can be both computed with great accuracy provided enough iterations are completed. Also shown in the bottom panel of Figure 4.5 is the behaviour of the spin correlation for the target energies larger than the ground

state by 10% of the spectrum width, obtained with CPGF (the MCLM results coincide, and thus are omitted to avoid unnecessary clutter on the figure). Interestingly, these excited states are still close enough to the ground state that the spin correlation preserves its general shape, albeit with some broadening of its sharper features. The top panel in Figure 4.6 summarises a careful convergence study aimed at understanding how the optimal² number of iterations, N_{it}^* , depends on the microscopic details of the model. My simulations show that convergence is relatively fast in the purely Heisenberg limits ($\varphi = 0, \pi$) and becomes slower as one approaches the quantum phase transitions and, in particular the Kitaev limits ($\varphi = \pi/2, 3\pi/2$), in both Lanczos and MTPQ. Note that in spite of the strong dependence of N_{it}^* with φ , Lanczos converges considerably faster throughout the K-H parameter space, requiring about two orders of magnitude less iterations for convergence than MTPQ.

2: Here, optimal convergence is defined as a variation of less than 10^{-9} in the energy density between consecutive iterations.

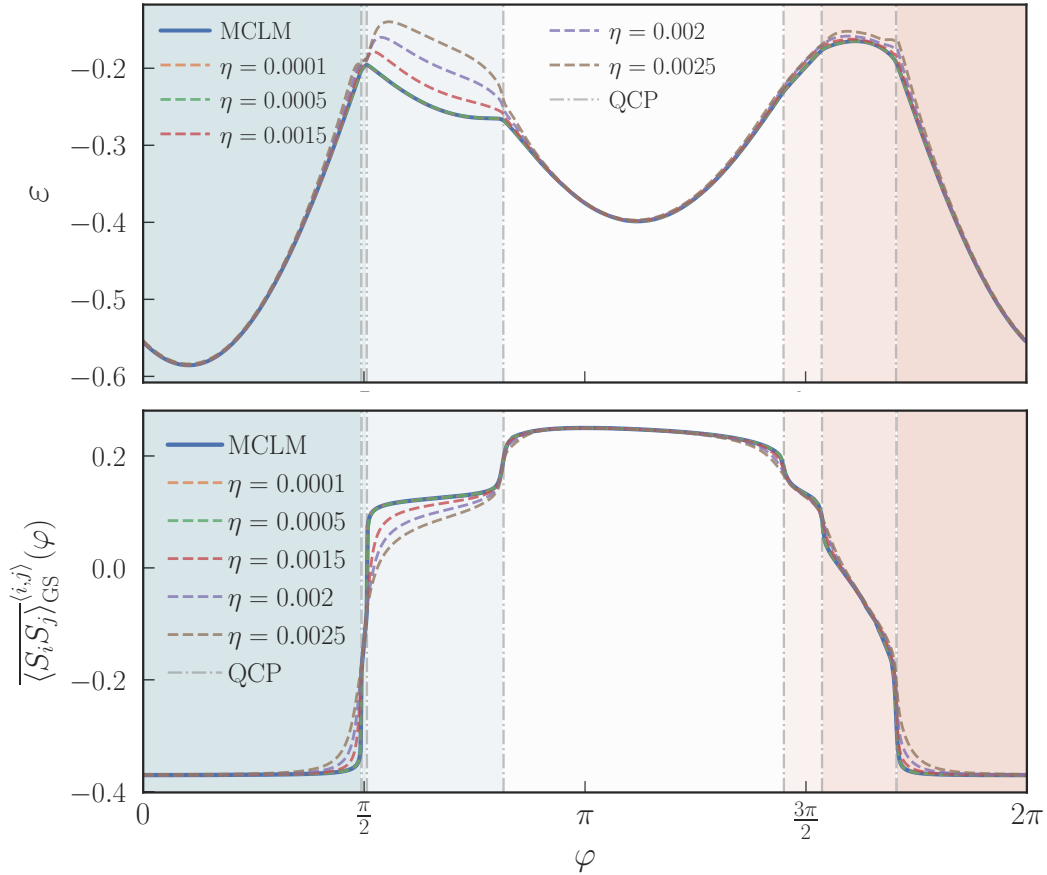


Figure 4.7: Comparative study between CPGF and MCLM. Top panel — Ground state energy density obtained with MCLM (solid blue line) and CPGF (dashed lines) with varying resolution as a function of φ . The two methods show excellent agreement provided that the CPGF resolution is sufficiently fine. Bottom panel — Ground state nearest neighbour spin–spin correlation as a function of φ . I used a single realisation of the initial random state for both methods. The results shown here also match the Lanczos and MTPQ results shown in Figure 4.5.

Next, I address convergence around the quantum critical points near the Kitaev limits in more detail; see Figure 4.6 (bottom panel).

The convergence of the Lanczos and TPQ estimators for the spin-spin correlation is found to slow down notably as the Kitaev term on the Hamiltonian becomes dominant ($|K|/|J| \gg 1$) and the ground state energy per site $\varepsilon_{GS}(\varphi)$ and the nearest neighbour spin-spin correlation $\overline{\langle S_i S_j \rangle}_{GS}^{(i,j)}(\varphi)$ start to differ significantly. As a result of the slower convergence away from the purely Heisenberg points, the computational effort grows substantially, notably so close to the Kitaev points. For example, for $\varphi \simeq 0.506\pi \iff |K|/|J| \simeq 53$, MTPQ requires around 4×10^4 iterations for optimal convergence as defined earlier to be achieved.

Figure 4.7 shows the energy density and spin correlation function of the 24-site cluster across the phase diagram calculated with CPGF. I compare the latter with MCLM, which also has the ability to probe an input target energy. I also establish the accuracy of the STE of Equation 2.96 using CPGF. An in-depth analysis which I now detail confirms that the standard deviation of the estimate for the nearest neighbour spin-spin correlation function scales as expected, *i.e.* as the inverse square root of the number of realisations of the initial random state. Statistical convergence is obtained when the error bars become acceptably small. This information is encoded in the scaling of the standard deviation with the number of used initial random states. In Figure 4.8, I confirm that one obtains the expected scaling ($\sigma \propto N_{rd.vec.}^{-1/2}$) [174], that is my error bars can be made as small as required by simply averaging over more realisations of the initial random state. This calculation was carried out with CPGF for a point in the phase diagram of the K-H model with the parametrisation of Reference [3].

[174]: Weisse et al. (2006), 'The kernel polynomial method'

[3]: Chaloupka et al. (2010), 'Kitaev-Heisenberg Model on a Honeycomb Lattice'

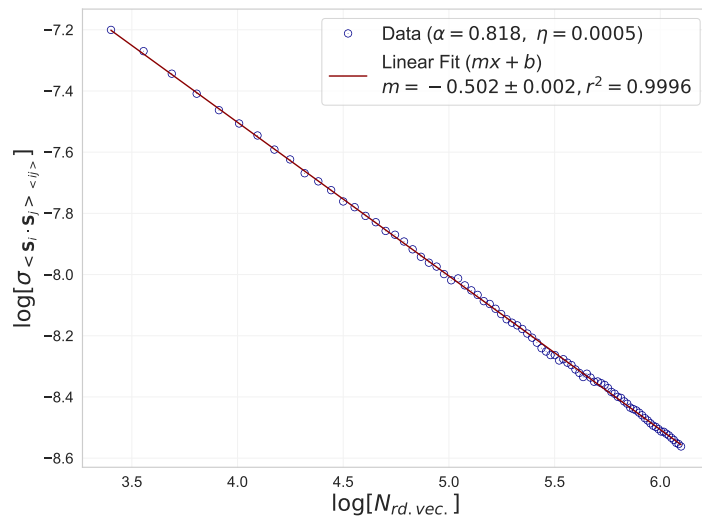
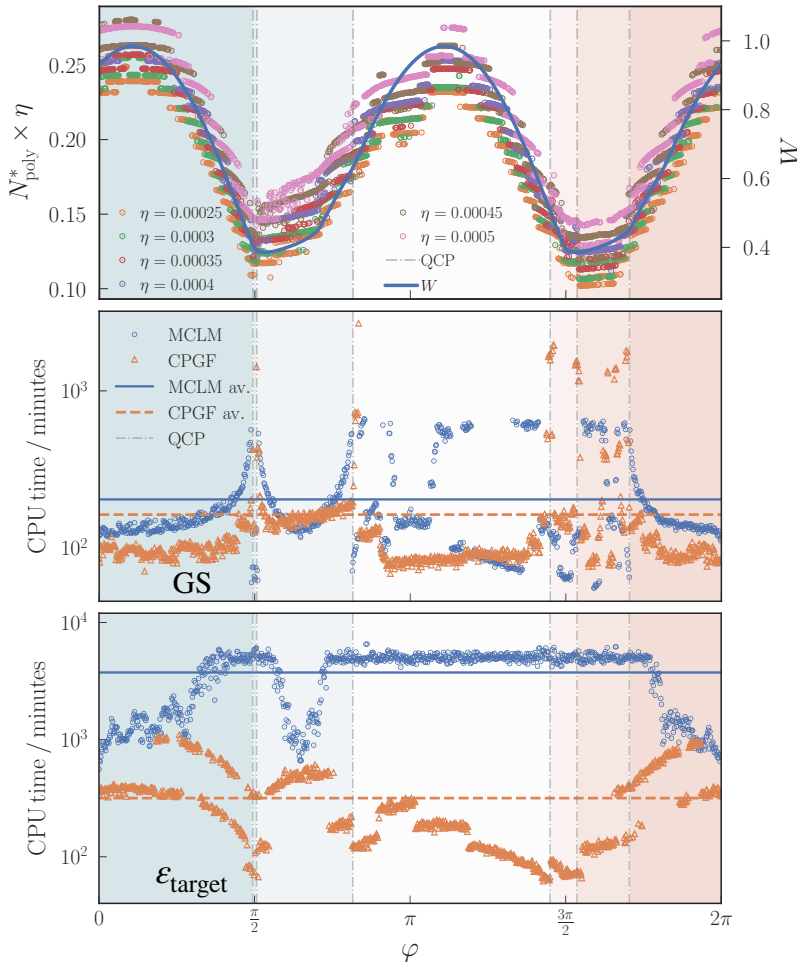


Figure 4.8: Behaviour of the standard deviation of the nearest neighbour spin correlation with the number of realisations of the initial random state for the CPGF method. Here, I consider a specific point of the phase diagram ($\alpha = 0.818$ in the parametrisation of Reference [3]). I obtain the expected scaling: $\sigma \propto N_{rd.vec.}^{-1/2}$.

The results of Figure 4.7 also show that finer CPGF resolutions are needed to probe the phase diagram around the Kitaev points

($\varphi = \pi/2, 3\pi/2$). On the contrary, near the Heisenberg limits ($\varphi = 0, \pi$), convergence occurs with comparatively coarse resolution. A useful feature of the CPGF method is that the optimal number of Chebyshev iterations, $N_{\text{poly}}^* = N_{\text{poly}}^*(\eta)$, follows a predictable pattern: it is roughly proportional to the spectrum width and inversely proportional to the required resolution [189, 190]. The results I shall now report confirm this expected behaviour.

My results shown in the top panel of Figure 4.9 confirm that the spectral convergence of CPGF follows a predictable pattern: the optimal number of polynomials needed for convergence, N_{poly}^* , is inversely proportional to the resolution, η . In the CPGF, I used a stricter definition of convergence than before: a variation of less than 10^{-9} in the energy density between *three* consecutive iterations. This is necessary because convergence occurs in a ‘damped oscillatory’ manner in CPGF (as I will show shortly in Figure 4.10).



[189]: Ferreira et al. (2015), ‘Critical Delocalization of Chiral Zero Energy Modes in Graphene’

[190]: João et al. (2020), ‘KITE’

Figure 4.9: Top panel: Number of iterations required for convergence with CPGF times the required resolution (left vertical axis) and spectrum width (right vertical axis). N_{poly}^* is approximately proportional to the spectrum width and inversely proportional to the required resolution. Thus, the number of iterations required for convergence can be estimated in advance, unlike in other approaches. Centre panel: Computer time required for convergence using MCLM and CPGF. Bottom panel: Similar to the centre panel, but now targeting excited states with energy $\mathcal{E}_{\text{target}}$. Here, I allowed a maximum of 10000 iterations with MCLM. In comparison, CPGF never required more than 3195 polynomials for convergence.

For the ground state, I find that the convergence speed of MCLM and CPGF compares very differently throughout the phase diagram. MCLM seems to show unpredictable behaviour as some points of the phase diagram require significantly more computational effort than others. CPGF behaves more intuitively, requiring a

greater effort for points close to the phase transitions, which need finer resolutions and, consequently more iterations and thus more computer time. Although the CPGF approach is significantly faster in some regions of the K-H parameter space, the MCLM approach is faster close to the transitions. Nevertheless, when targeting the ground state, CPGF is 25% faster on average. For the excited states, the difference in performance is much more dramatic and the results of the bottom panel of Figure 4.9 show that CPGF is the method of choice due to its faster overall convergence (about an order of magnitude less CPU time required).

When targeting the ground state, the convergence of the CPGF method slows down close to critical points, despite showing comparably faster convergence in other parts of the phase diagram (bottom panel of Figure 4.9). Surprisingly, MCLM behaves in a complementary fashion: convergence tends to become faster near a phase transition. Furthermore, each iteration is faster overall with CPGF, so even in cases where both require comparable numbers of iterations for convergence, CPGF tends to be faster. Thus, the CPGF is faster than MCLM at reproducing the complete phase diagram.

The cost of targeting the excited states with CPGF is comparable to targeting the ground state. In contrast, MCLM requires significantly more iterations for convergence, resulting in a total CPU time about an order of magnitude larger than CPGF. The complementary behaviour of the convergence properties of the two methods persists, *i.e.* the convergence speed of MCLM increases for the parts of the phase diagram where the convergence speed of CPGF decreases. Still, CPGF remains faster for the whole of the phase diagram when targeting the excited states. In conclusion, CPGF is the method of choice for targeting excited states.

Next, I bench-mark the MCLM and CPGF methods around the Kitaev limits in detail, *i.e.* for spreads of φ -values in the intervals $[0.4800, 0.5200]\pi$ and $[1.5160, 1.5760]\pi$. To assess convergence in the K-H model, I carefully track the evolution of the correlation function as more iterations are completed with each of the two methods.

In Figure 4.10, I show the dependence of the nearest neighbour spin correlation on the number of iterations in the MCLM and CPGF approaches. Here, I focused on a range of resolutions in the interval $[2.5 \times 10^{-5}, 5 \times 10^{-4}]$, but only plotted the curves corresponding to the energy resolutions that yield convergence. In this case, I consider that a given resolution yields convergence when the energy density and spin correlation no longer change appreciably as finer resolutions are considered. To ensure that convergence has indeed occurred, I compute the difference between

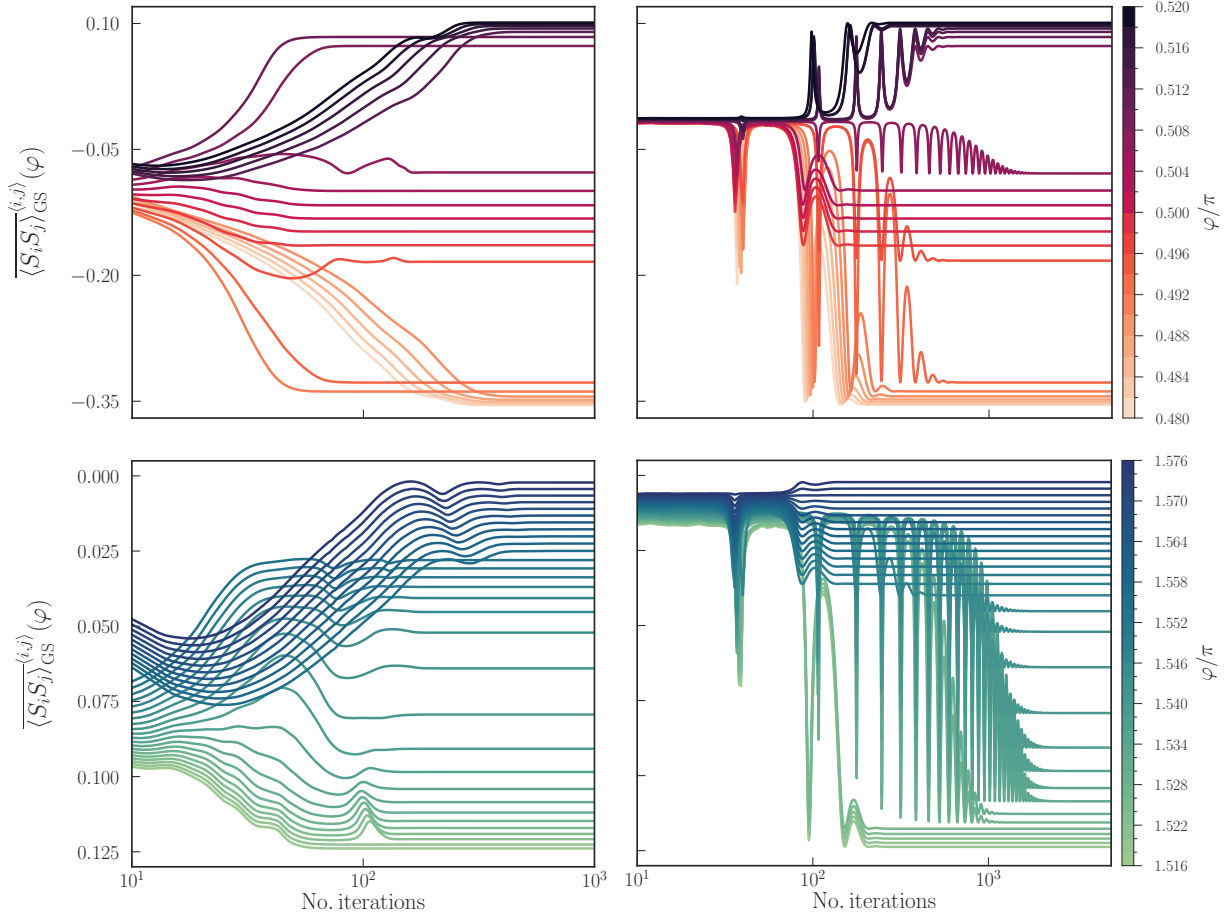


Figure 4.10: Convergence of the ground state nearest neighbour spin–spin correlation computed with MCLM (left) and CPGF (right) around the Kitaev limits.

the energy density for two consecutive resolutions and ensure that the difference is smaller than the resolution itself. As it turns out, convergence is achieved for $N_{\text{poly}} \sim 10^2 - 10^3$ depending on the value of φ . Figure 4.10 confirms that enhanced resolutions are crucial in the vicinity of quantum critical points. Moreover, it also shows that MCLM and CPGF have complementary convergence behaviour. The top left panel shows that MCLM converges quicker around 0.500π , but dramatically slows down around 0.480π and 0.520π . The top right panel shows that CPGF has more consistent and faster convergence, with only the points closest to the transition ($0.494\pi, 0.506\pi$) requiring more iterations due to the need for a finer resolution. The bottom panels exhibit a similar tendency. The points near 1.576π display faster convergence with CPGF than with MCLM, while the curves in the centre of the two plots show that convergence is faster with MCLM due to the increased resolution that is needed with CPGF. Here, I emphasise that I found each iteration to be faster with CPGF due to a lower number of necessary operations than with MCLM. Thus, CPGF is still faster even in situations where the number of iterations required for

convergence is similar, *e.g.* for the points near 1.516π in the bottom panels. The main contribution to the extra time per iteration in MCLM is the action of \hat{h}^2 upon a state at each iteration. Since the Hamiltonian is generated on-the-fly, one must act with \hat{h} twice in order to obtain the action of \hat{h}^2 . Thus, each iteration incurs an extra cost due to the additional matrix-vector multiplication, which is the most computationally expensive operation in these methods.

4.3 Canonical approaches: finite temperature

In what follows, I discuss the performance of the finite temperature approaches introduced in Section 2.8. I also include the microcanonical variant of the TPQ method in this analysis and confirm that the temperature corresponding to each energy density can be accurately estimated as explained in Reference [34]. For concreteness, I focus on the Kitaev point at $\varphi = 1.5\pi$ and restrict the temperature to the range $T = [0.004, 24]$ in units of the Kitaev coupling, which suffices to capture the relevant features of the model.

[34]: Sugiura et al. (2012), ‘Thermal Pure Quantum States at Finite Temperature’

Table 4.2: Number of iterations (or Chebyshev polynomials) required for convergence for each method and CPU time per core per iteration.

Method	No. iterations	CPU time / core / it. [s]
MTPQ ($e_{\text{upper}} = e_M$)	1200	0.56
MTPQ ($e_{\text{upper}} = 35e_M$)	22000	0.57
FTLM	200	2.05
CTPQ	500	0.58
FTCP ($5 < N_{\text{poly}} < 20$)	7515	0.98

I set out to obtain the nearest neighbour spin correlation, specific heat and entropy with all methods, with a careful convergence analysis. Thus, I compute the minimum (*i.e.* optimal) number of iterations, such that the target functions are reliably captured within the desired accuracy at all temperatures. Naturally, the relevant convergence parameters need to be adjusted separately for each method due to their different characteristics. These are summarised in Table 4.2. It is important to note that the results presented below not only agree with each other, but also with QMC and exponential tensor renormalisation group studies of Reference [10], thus supporting the validity of my implementation for all methods. The specific heat is computed as follows: $c = N\beta^2(\langle \hat{h}^2 \rangle - \langle \hat{h} \rangle^2)$. Similarly to Reference [158], the entropy density is computed by integrating c/T . I perform the integral numerically using Simpson’s rule.

[10]: Li et al. (2020), ‘Universal thermodynamics in the Kitaev fractional liquid’

[158]: Yamaji et al. (2016), ‘Clues and criteria for designing a Kitaev spin liquid revealed by thermal and spin excitations of the honeycomb iridate Na_2IrO_3 ’

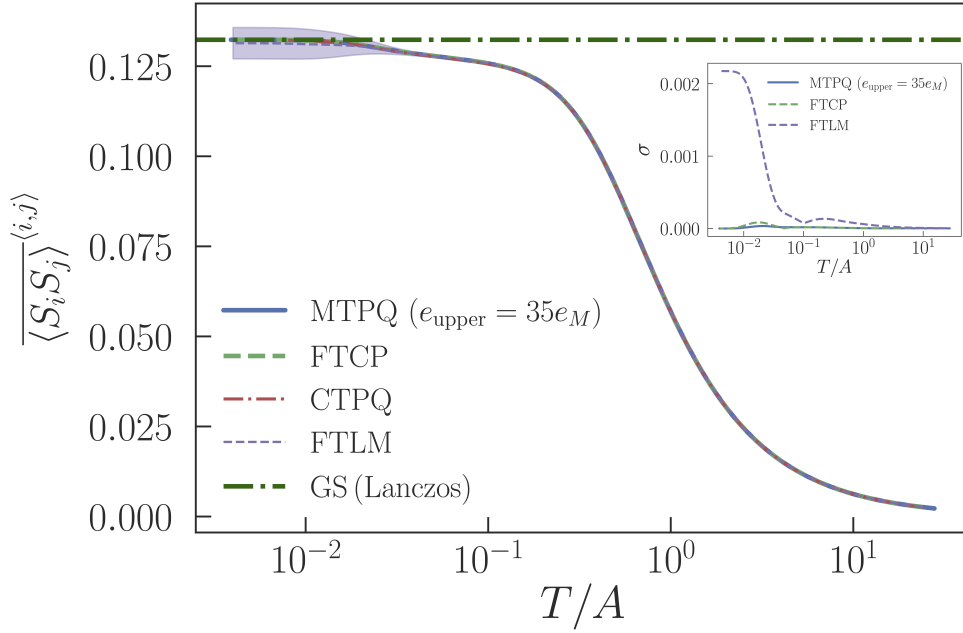


Figure 4.11: Finite temperature nearest neighbour spin correlator computed with the MTPQ, FTCP, CTPQ, and FTLM for the 24-site hexagonal cluster at the Kitaev limit $\varphi = 3\pi/2$. I used 50 random vector realisations in all cases. Error bars are negligibly small, except for FTLM. Inset: Standard deviation of the nearest neighbour spin correlator. CTPQ is not shown because the fluctuations are comparable to MTPQ.

At first sight, Table 4.2 seems to indicate that FTLM is the most efficient method. However, notice that in Figure 4.11, FTLM shows large low-temperature fluctuations, reaching about 26 times the fluctuations of FTCP (calculated from root-mean-square deviations). The inset of Figure 4.11 shows that these fluctuations are larger for FTLM than for the other methods throughout the temperature range. Here, I note that the same initial random vectors are used in all methods so that statistical fluctuations can be directly compared. Moreover, the total computational cost is dictated not only by the number of iterations, but also by the number of matrix-vector multiplications per iteration. This number is higher for FTLM than FTCP, leading to about twice the average computer time per iteration (2.05 seconds with FTLM compared to 0.98 seconds with FTCP).

Figure 4.12 shows a very important shortcoming of the CTPQ method. Unlike the nearest neighbour spin correlation, the specific heat has an important feature that cannot be reproduced with CTPQ, namely the decay to zero of the low-temperature peak as $T \rightarrow 0$. The limitation is related to the need to consider more terms in the summation of Equation 2.106 so as to achieve convergence. I find that when I considered 500 terms, I reached the limit of machine precision (80-bit floating-point on an Intel Core i5 processor) before reaching enough accuracy. The CTPQ results gradually lose accuracy as temperature decreases and at some point between 10^{-1} and 10^{-2} , they are no longer reliable. The entropy also shows

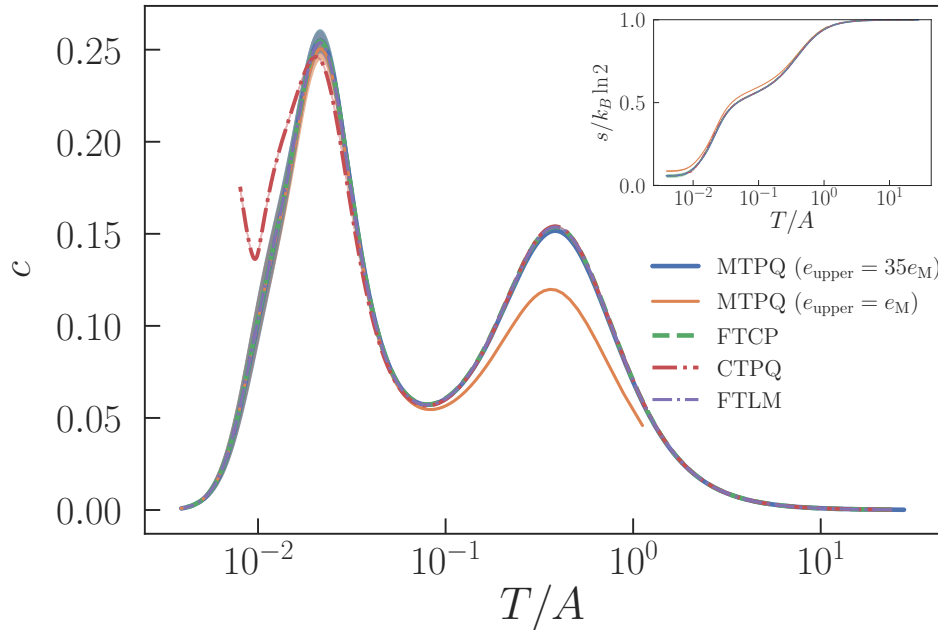


Figure 4.12: Specific heat (entropy density on the inset) computed with MTPQ, FTCP, CTPQ, and FTLM. I use 50 realisations of the initial random state for all methods. The error bars are negligibly small in most of the temperature range, except for temperatures below that of the low-temperature peak. The error bars are of comparable size for every method (except for CTPQ, for which their meaning is ill-defined due to a numerical instability). Model parameters as in Figure 4.11.

signs of the numerical instability of CTPQ (see inset of Figure 4.12). The operator break-up into the product of Equation 2.109 ensures that each Chebyshev expansion in Equation 2.111 is stable. The arguments of the fast growing modified Bessel functions are guaranteed to remain in check because they can be controlled via the inverse temperature step. This is to be contrasted with Equation 2.106, where the also fast growing functions of the inverse temperature and the number of iterations are not controlled, leading to the numerical instability visible in Figure 4.12.

Having discussed the limitations of FTLM (large low-temperature fluctuations) and CTPQ (numerical instability), I now move on to MTPQ. An often omitted detail in the literature is that the upper bound on the maximum eigenvalue of the Hamiltonian density, e_M , given as an input to MTPQ determines: i) the temperature range that is covered, and ii) how much accuracy is achieved for a given temperature. The strong influence of e_M can be traced back to the evolution of the TPQ energy density distribution with the number of iterations [34]. I found that in order to cover the desired temperature range with enough accuracy in MTPQ, I had to increase the upper bound to 35 times the maximum eigenvalue of the Hamiltonian density (computed with Lanczos). I consider that enough accuracy has been reached when the specific heat and entropy computed with MTPQ match the FTCP and FTLM results.

[34]: Sugiura et al. (2012), ‘Thermal Pure Quantum States at Finite Temperature’

The results of Figure 4.12 indicate that the disparity between MTPQ with $e_{\text{upper}} = e_M$ and the other methods is solely due to insufficient accuracy at high temperature. While MTPQ captures the high-temperature peak of the specific heat even with $e_{\text{upper}} = e_M$, the amplitude of this peak is severely underestimated. As more iterations are completed, the accuracy of the method increases and the low-temperature peak matches the results of other methods better, but still not perfectly. Moreover, even though the MTPQ result with $e_{\text{upper}} = e_M$ captures the general behaviour of the entropy density, there is not enough accuracy because of accumulated error from the lack of accuracy at high temperature and the reduced temperature range (note that I compute the entropy as an integral over temperature). The other methods match perfectly and show comparable fluctuations. Since there are only small error bars of approximately the same size for all methods at low temperature, the disparity can only be due to insufficient accuracy for MTPQ with $e_{\text{upper}} = e_M$. By probing higher values of e_{upper} , I find that it is necessary to input $e_{\text{upper}} \approx 35e_M$ for the high and low-temperature peaks to reproduce the correct behaviour. When I consider this upper bound, MTPQ requires about twice the total computer time compared to FTCP in order to achieve comparable results (14268 versus 7376 seconds per core). Even though the number of iterations is nearly 3 times higher in MTPQ compared to FTCP, the former requires 40 % less matrix-vector operations per iteration. Still, FTCP remains about two times faster due to its significantly faster convergence.

Finally, notice that for both the specific heat and the entropy in Figure 4.12, FTLM does not show the low-temperature fluctuations of Figure 4.11. I attribute this to the fact that Lanczos methods are designed to quickly achieve an approximation of the Hamiltonian in a subspace restricted to the ground state and low-lying excitations. The specific heat and the entropy are calculated solely in terms of averages of the Hamiltonian density, $\langle \hat{h} \rangle$ and $\langle \hat{h}^2 \rangle$. Thus, convergence is better for these quantities than for more general observables, such as the nearest neighbour spin correlation, which are not as closely associated with the Hamiltonian.

In Figure 4.13, I show FTCP results for the specific heat of the K-H model on the 24-spin hexagonal cluster. 100 initial random vectors were used for each value of the model parameter, φ . I find a three-peak structure of the specific heat that had not been described in the literature until this work. These results are consistent with thermal fractionalisation [8], suggesting a high temperature release of the entropy of the Majorana fermions, followed by a low-temperature two-stage reconfiguration of the flux degrees of freedom inherited from the pure Kitaev model. The latter leads to the ground state configuration asymptotically for $T \lesssim 10^{-3}A$. As the pure Kitaev

[8]: Nasu et al. (2015), ‘Thermal fractionalization of quantum spins in a Kitaev model’

model at $\varphi = 1.5\pi$ is approached, the low-temperature peak diminishes, as it shifts towards lower temperature. In the Kitaev limit, the specific heat has a two-peak structure.

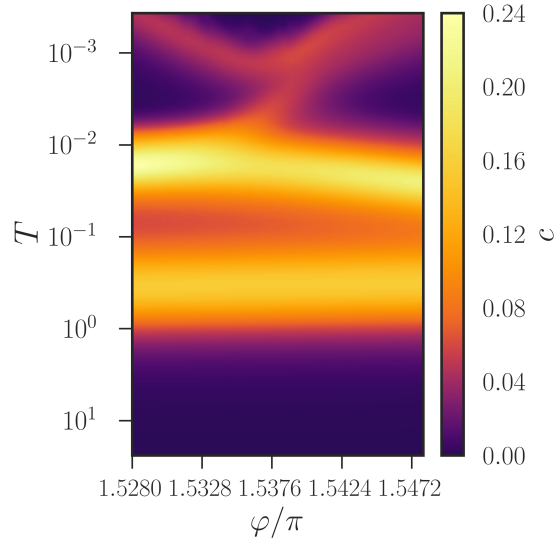


Figure 4.13: Three-peak structure of the specific heat near the FQSL-stripy transition of the K-H model.

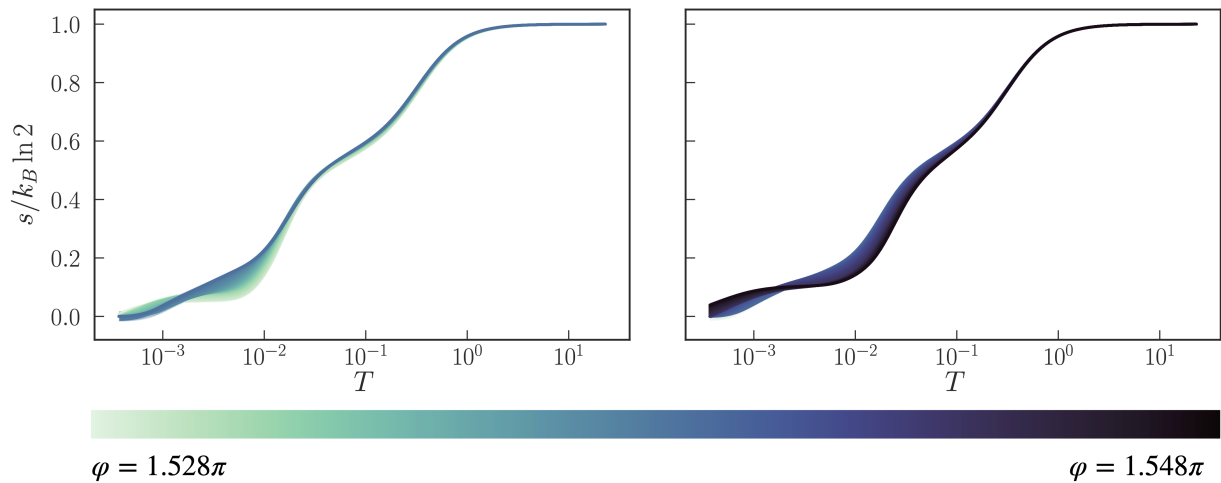


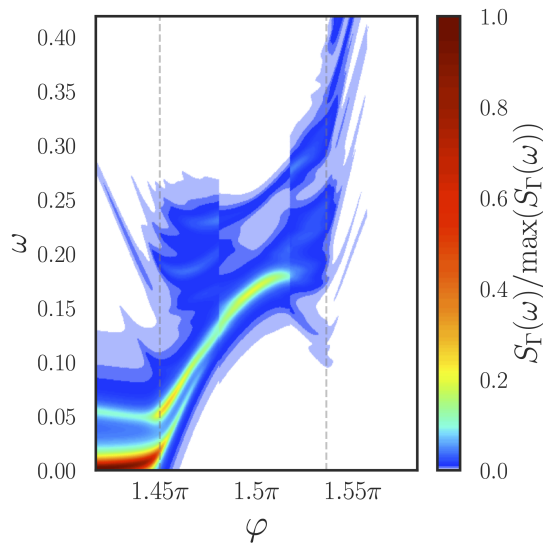
Figure 4.14: Three-stage release of the entropy density near the FQSL-stripy transition of the K-H model. I plot results for 52 values of $\varphi \in [1.528, 1.548]\pi$. The colours correspond to the varying parameter, φ , as indicated on the legend in the bottom. The results are separated in two panels to aid with visualisation.

Figure 4.14 shows the three-stage release of entropy density corresponding to the three peaks of the specific heat. The results are also consistent with signs of spin fractionalisation at finite temperature. My results suggest that near the Kitaev limit, the Heisenberg term might not completely modify the picture of Majorana fermions coupled to a gauge field. Instead, flux excitations could simply change in energy as φ is varied, with Figure 4.14 pointing at the possibility of a frozen flux configuration for $T \in [10^{-3}, 10^{-2}]A$ for some values of φ . Interestingly, signs of thermal fractionalisation are seen even within the stripy phase (above $\varphi = 1.5364\pi$, see Table 4.1). This is consistent with one of the hypotheses of Figure 1.16, which is that QSL candidate materials ordering at low temperature

may still shows signs of spin fractionalisation above the critical temperature for magnetic ordering.

4.4 Bench-marking the hybrid Lanczos-Chebyshev method against the continued fraction Lanczos approach

I computed the dynamical spin susceptibility at the Γ -point for the K-H model on the 24-spin hexagonal cluster for a range of model parameters φ around the ferromagnetic-liquid and liquid-stripy antiferromagnetic transitions. My Lanczos and hybrid Lanczos-Chebyshev results reproduce those already obtained in Reference [5]. The latter is shown in Figure 4.15 (the Lanczos result is virtually indistinguishable so I do not show it here). These results display the expected dynamical signatures of the two phase transitions, as discussed in Reference [5]. Having validated my hybrid approach by reproducing a known result, I then compared the performance of the two algorithms. I find my hybrid method to be more efficient overall, namely 33% faster on average in the range of φ -points shown in Figure 4.15.



[5]: Gotfryd et al. (2017), ‘Phase diagram and spin correlations of the Kitaev-Heisenberg model’

Figure 4.15: Dynamical spin susceptibility obtained with the HLC method for the K-H model on the hexagonal 24-spin cluster in the interval of φ -parameters containing, respectively, the ferromagnetic, spin-liquid and stripy antiferromagnetic phases. The quantum phase transitions are identified by grey dashed lines.

I close this section with a note on computational resources and memory cost. Throughout this second part of the thesis, my calculations are done using Intel Xeon Gold 6138 processors running at 2 GHz and each simulation requires between 0.5 and 1 GB of memory. All Chebyshev methods show improved performance. In the case of the dynamics studies of this section, I found that under the exact same circumstances, my HLC method is 33 % faster than the continued fraction Lanczos approach. This estimate was obtained as follows. When reproducing the previously known

[5]: Gotfryd et al. (2017), 'Phase diagram and spin correlations of the Kitaev-Heisenberg model'

result [5] for the dynamical spin susceptibility of the K-H model, I used the same number of Lanczos iterations/polynomials and averaged over ~ 400 simulations, each running with parallelisation enabled with 16 cores using the aforementioned processors. I used my own implementation of Lanczos in both cases, so my results are implementation-independent. Then, I measured CPU time for both methods. I emphasise that my newly introduced Chebyshev approach is not only faster overall compared with the traditional Lanczos approach, but also remarkably flexible, in the sense that it allows the study of generic (not necessarily autocorrelation) spectral functions.

Kitaev-Ising Model

5

In Reference [224], the authors argue that spiral magnetic order in Li_2IrO_3 could be explained in terms of a minimal model which adds an Ising interaction to the K-H model of the previous chapter. In fact, the authors find that their theoretical minimal model matches experimental predictions of spiral order for a dominant Kitaev interaction, with the Ising interaction corresponding to about 38% of the Kitaev interaction and the Heisenberg contribution only about 5%. This motivates me to consider an even more minimal model combining only Kitaev and Ising interactions.

Interestingly, in Reference [59], the authors report a liquid-to-liquid transition in this minimal model. Among the methods used to characterise the phase diagram are Lanczos ED and TPQ. This provides one with an avenue for comparison with FTCP and an opportunity to study the dynamics of the model using HLC. Within the K-I model, I discover signatures of the quantum phase transitions described in Reference [59] in the spin dynamics using HLC.

This chapter is organised as follows. Section 5.1 establishes the notation by introducing the Hamiltonian and its parametrisation. Section 5.2 validates my implementation, with my Lanczos ED results recovering the quantum phase transitions of Reference [59]. In Section 5.3, I provide further evidence for the two-fold speed-up with FTCP in comparison to TPQ that was already obtained in Chapter 4. I use my own implementation of MTPQ to recover results of Reference [59]. Then, I repeat the calculation and obtain FTCP results that perfectly match TPQ. I compare the CPU time required by each approach. Once again, FTCP is found to be about two times faster than MTPQ. In Section 5.4, I present new results for the dynamical spin susceptibility of the K-I model, identifying clear signatures of the quantum phase transitions discussed in the previous sections. I close the chapter with Section 5.5, where I study a quench protocol: the time evolution of a Néel state under the Kitaev model. Here, I do not consider the Ising interaction, but still allow for an anisotropy in the Kitaev couplings. My results are consistent with the Monte Carlo study of Reference [225], which describes a prethermal regime in which the staggered magnetisation persists for an exponentially long timescale as a function of the anisotropy.

5.1 Model Hamiltonian	116
5.2 Lanczos bench-mark	117
5.3 Finite temperature: Comparing Thermal Pure Quantum States and Chebyshev	118
5.4 Dynamics: Hybrid Lanczos-Chebyshev approach	119
5.5 Dynamics: Chebyshev approximation of the time evolution operator	120

[224]: Kimchi et al. (2015), ‘Unified theory of spiral magnetism in the harmonic-honeycomb iridates Li_2IrO_3 ’

[59]: Nasu et al. (2017), ‘Spin-Liquid-to-Spin-Liquid Transition in Kitaev Magnets Driven by Fractionalization’

[225]: Rademaker (2019), ‘Quenching the Kitaev honeycomb model’

5.1 Model Hamiltonian

The K-I model combines Kitaev and Ising interactions. The model Hamiltonian is:

$$\hat{H} = - \sum_{\langle i,j \rangle^\gamma} \left(K_\gamma \hat{\sigma}_i^\gamma \hat{\sigma}_j^\gamma + J_I \hat{\sigma}_i^z \hat{\sigma}_j^z \right), \quad (5.1)$$

[59]: Nasu et al. (2017), ‘Spin-Liquid-to-Spin-Liquid Transition in Kitaev Magnets Driven by Fractionalization’

where I use the parametrisation of Reference [59]. I allow not only for the isotropic case, but also an anisotropy, casting the Kitaev couplings as: $K_x = 1 - 2\alpha/3$, $K_y = K_z \equiv K_{yz} = \alpha/3$, where $\alpha \in [0, 1.5]$ is a parameter that measures the anisotropy and the relevant energy scale is set by $K_x + K_y + K_z = 1$, $K_y \geq 0$.

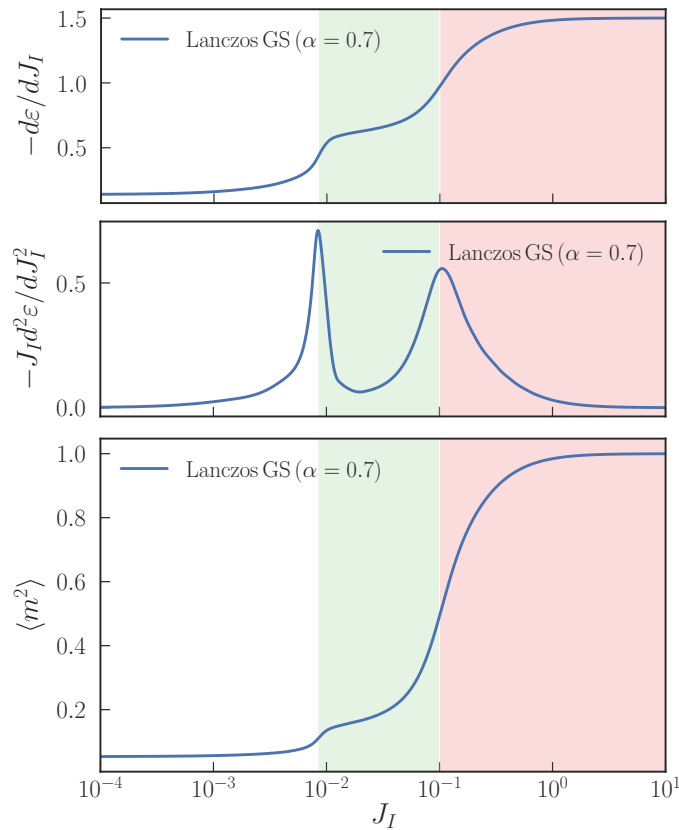


Figure 5.1: Top and centre panels – Negative first (top) and second (centre) derivatives of the Lanczos ground state energy density. Bottom panel – Mean square of the magnetisation, $\langle m^2 \rangle \equiv \langle [(1/N) \sum_i \sigma_i^z]^2 \rangle$. These results match those of Reference [59] and illustrate transitions between ferromagnetic (red), nematic (green) and QSL (blue) phases. Here, a single realisation of the initial random state was found to be sufficient due to negligible statistical fluctuations.

In Reference [59], the authors study this model for the 24-spin hexagonal cluster of the left panel of Figure 4.1 using Lanczos at zero temperature. I start by reproducing some of their results so as to validate my implementation. Then, I present a new study displaying dynamical signatures of the phase transitions described in Reference [59]. These signatures are found in the σ^z spin sus-

ceptibility, which I obtain using both the Lanczos and the HLC approach that I introduced in Section 2.9.2.

5.2 Lanczos bench-mark

Figure 5.1 summarises my Lanczos results and reproduces those of Reference [59]. The top panel shows two steps in the first derivative of the ground state energy density for fixed $\alpha = 0.7$ and varying $J_I \in [10^{-4}, 10]$. Correspondingly, the centre panel displays two peaks in the second derivative. These steps/peaks indicate two quantum phase transitions. From left to right, the first quantum critical point separates a QSL (blue) from a nematic (green) phase and the second one separates the latter from a ferromagnetic phase (red). Similarly to how the steps in the spin-spin correlation signal transitions for the K-H model (see bottom panel of Figure 4.5), the mean squared magnetisation also signals transitions in the K-I model, with its value approaching saturation very quickly as one enters the ferromagnetic phase.

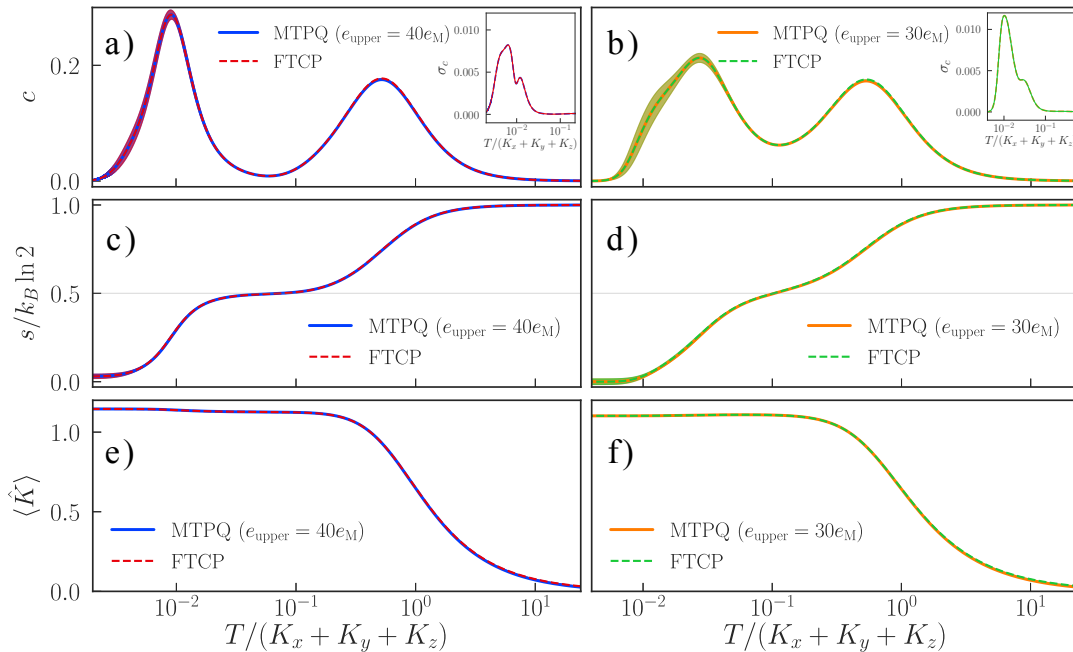


Figure 5.2: MTPQ and FTCP results for the K-I model on a 24-spin hexagonal cluster with PBCs, for $\alpha = 0.7$ and $J_I = 0.001$ (left panels) and $J_I = 0.03$ (right panels). I used 50 and 100 random vector realisations for $J_I = 0.001$ and $J_I = 0.03$, respectively. Panels a) and b) show the specific heat, with a zoom-in on the standard deviations — from which the error bars are derived — at low temperature; panels c) and d) show the entropy density, with the grey lines marking $s = 0.5k_B \ln 2$; panels e),f) show the finite temperature expectation of the kinetic energy of the Majorana fermions c .

5.3 Finite temperature: Comparing Thermal Pure Quantum States and Chebyshev

In Section 4.3, I bench-marked the FTCP approach by computing the temperature dependence of the specific heat, entropy density and nearest neighbour spin correlation. In principle, MTPQ could be the most viable competitor of FTCP (despite being a microcanonical method) because it avoids the shortcomings of FTLM and CTPQ. Yet, I found that MTPQ required about twice the computer time of FTCP in the context of the K-H model. Here, I further bench-mark FTCP by considering the K-I model. I also seek to clarify whether FTCP outperforms MTPQ in terms of computer time for a different model, which would suggest that the advantages of FTCP are not problem-dependent. I start by recovering the MTPQ results of Reference [59] using my own implementation. Then, I repeat the calculation using FTCP. These results — shown in Figure 5.2 — are for two specific points of the phase diagram: $(\alpha, J_I) = \{(0.7, 0.001), (0.7, 0.03)\}$. Going back to Figure 5.1, I can see that these two points are located within the Kitaev QSL and nematic regions of the phase diagram, respectively.

[59]: Nasu et al. (2017), ‘Spin-Liquid-to-Spin-Liquid Transition in Kitaev Magnets Driven by Fractionalization’

[8]: Nasu et al. (2015), ‘Thermal fractionalization of quantum spins in a Kitaev model’

In Reference [59], the authors remark that — similarly to what I found in Section 4.3 for the K-H model — the well known results for the pure Kitaev model that I recovered in Figure 4.11 and Figure 4.12 remain qualitatively valid even when $J_I \neq 0$, and even within the nematic phase (see right panels of Figure 5.2 with results for $(\alpha, J_I) = (0.7, 0.03)$). The specific heat has a two-peak structure, corresponding to a two-step release of entropy. At high temperature ($T \sim 0.5$), the Majorana fermions c (defined in [59]) release their entropy ($0.5k_B \ln 2$). The other half of the entropy is released by \mathbb{Z}_2 fluxes at low temperature ($T \lesssim 10^{-2}$) [8]. The high temperature crossover coincides with an enhancement of the expectation of the kinetic energy of the Majorana fermions c , defined in terms of the spin operators as follows:

$$\hat{K} = \frac{2}{N} \sum_{\gamma=x,y} \sum_{\langle j,k \rangle_\gamma} \hat{\sigma}_j^\gamma \hat{\sigma}_k^\gamma. \quad (5.2)$$

Table 5.1: Average CPU times, t_{CPU} , for MTPQ and FTCP calculations for the K-I model on a periodic 24-spin hexagonal cluster with $\alpha = 0.7$ and $J_I = 0.001, 0.03$.

J_I	t_{CPU} / hours	
	MTPQ	FTCP
0.001	142	77
0.03	61	29

The features mentioned above are all apparent in Figure 5.2 and my MTPQ and FTCP results match nearly perfectly. The striking difference between the two approaches is that once again, FTCP cuts the computer time in approximately half. To be more precise, for $J_I = 0.03$, FTCP is around 2.1 times faster and for $J_I = 0.001$, it is around 1.8 times faster. Table 5.1 summarises these differences in computer time.

Panels a),b) of Figure 5.2 confirm the two-peak behaviour of the specific heat. In the right panel ($J_I = 0.03$), statistical fluctuations are more apparent and even doubling the number of random vectors compared with the case $J_I = 0.001$ (going from 50 to 100), I find that statistical fluctuations remain higher. This is illustrated in the low-temperature behaviour of the standard deviation of the specific heat estimator, which is shown on the insets. MTPQ and FTCP show identical statistical properties, with these standard deviations matching remarkably well. Notice that the optimal value for the upper bounds on the maximum eigenvalue of Hamiltonian used in MTPQ were different in each case ($40e_M$ for $J_I = 0.001$ and $30e_M$ for $J_I = 0.03$). These were chosen so as to ensure enough accuracy throughout the chosen temperature ranges ($T \in [0.002, 24]$ for $J_I = 0.001$ and $T \in [0.004, 24]$ for $J_I = 0.03$, in units of $K_x + K_y + K_z$). Panels c),d) of Figure 5.2 show the two-step release of entropy. Compared with the pure Kitaev case of Figure 4.12, the left panel (c) shows a much more pronounced plateau-like behaviour between $T = 10^{-1}$ and $T = 10^{-2}$, ending in an abrupt decrease of entropy. In contrast, the right panel (d) shows no plateau at all, with a gentler decrease in entropy between $T = 10^{-1}$ and $T = 10^{-2}$. This is a manifestation of the intrinsic differences between the two liquid phases (Kitaev QSL and nematic). Finally, panels e), f) of Figure 5.2 illustrate the high temperature enhancement of the kinetic energy of the Majorana fermions c , a behaviour that is shared between the two phases. Here, statistical fluctuations are very small for both MTPQ and FTCP, with negligible error bars.

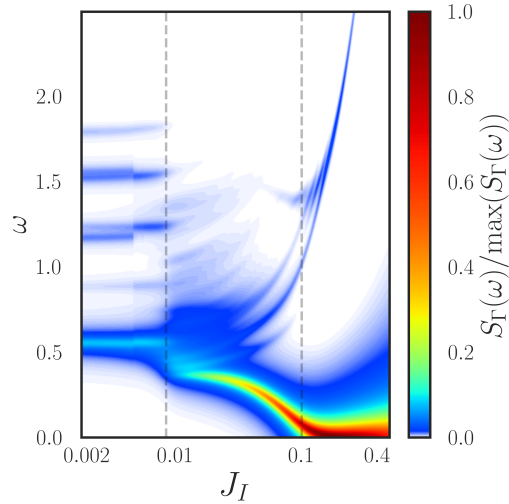
5.4 Dynamics: Hybrid Lanczos-Chebyshev approach

In this section, I present novel results that elaborate on the picture of the K-I system that was outlined in Reference [59]. I find that the signatures of the quantum phase transitions are present not only in static quantities, such as the energy and squared magnetisation, but also in the dynamical spin susceptibility. This spectral function is obtained by considering the relevant observable in Equation 2.123 to be the Fourier-transformed spin operator, *i.e.* $\hat{A} = \sum_{\mathbf{r}} e^{-i\mathbf{q}\cdot\mathbf{r}} \hat{S}_{\mathbf{r}}^z / \sqrt{N}$, where \mathbf{r} is a position on the lattice and \mathbf{q} is the wave vector.

In Figure 5.3, I show the variation of the $\mathbf{q} = (0, 0)$ dynamical spin susceptibility, $S_{\Gamma}(\omega)$, with the model parameter J_I . These results are obtained with the HLC method. The initial Lanczos run is stopped when the variation between the ground state energy density computed for consecutive iterations is less than 10^{-9} in units of $K_x + K_y + K_z$. I compute 3000 Chebyshev moments,

[59]: Nasu et al. (2017), ‘Spin-Liquid-to-Spin-Liquid Transition in Kitaev Magnets Driven by Fractionalization’

Figure 5.3: Dynamical spin susceptibility of the K-I system for varying J_I and $\alpha = 0.7$, normalised to its maximum value. The phase transitions are marked as grey dashed lines. The results obtained with the continued fraction Lanczos and hybrid Lanczos-Chebyshev methods are identical. The white space corresponds to a vanishing $S_\Gamma(\omega)$, as shown on the bottom of the colour bar.



which is enough to achieve convergence for all the values of η considered. Specifically, for each J_I , the resolution parameter is fixed to 0.1% of the spectrum width, which translates to values in the interval $\eta \in [0.0011, 0.0036](K_x + K_y + K_z)$. In terms of statistical sampling, I find that lower values of J_I require more random vectors for the peaks of the dynamic susceptibility to be resolved satisfactorily. Thus, for $J_I < 0.0057$, I use 16, rather than the 4 initial random vectors that I use for $J_I > 0.0057$. My interpretation of these results is in line with a similar reasoning for the K-H model presented in Reference [5], albeit with a crucial difference due to the specifics of the liquid-to-liquid transition. In the ferromagnetic limit ($J_I \gtrsim 10^{-1}$), the $\omega = 0$ component dominates because of the strong ferromagnetic correlations. As J_I is lowered and the transition to the nematic phase occurs, the gapless magnon mode gradually turns into a gapped mode. Moreover, there is a proliferation of sharp well-defined excitations in the nematic phase, which abruptly collapse onto a smaller set of modes as the transition to the Kitaev phase occurs ($J_I \sim 10^{-2}$). This rapid change in the spin susceptibility is consistent with the $T = 0$ first order topological phase transition described in Reference [59]. The gap is found to peak for the Kitaev liquid, at which point the lowest- ω mode occurs for a larger ω than in the nematic phase.

[5]: Gotfryd et al. (2017), 'Phase diagram and spin correlations of the Kitaev-Heisenberg model'

[59]: Nasu et al. (2017), 'Spin-Liquid-to-Spin-Liquid Transition in Kitaev Magnets Driven by Fractionalization'

5.5 Dynamics: Chebyshev approximation of the time evolution operator

Lastly, I study a quench protocol using the Chebyshev approximation of the time evolution operator of Equation 2.116. I consider a periodic 4×3 cluster and $J_I = 0$, *i.e.* the honeycomb Kitaev

model with anisotropic interactions. I also change the sign of the Hamiltonian, and modify my parametrisation as follows:

$$\hat{H} = \sum_{\langle i,j \rangle} K_{\gamma} \hat{\sigma}_i^{\gamma} \hat{\sigma}_j^{\gamma}, \quad (5.3)$$

with $K_z = 1$ setting the energy scale and $K_x = K_y \equiv K_{xy}$ serving as a measure of the anisotropy.

I seek to reproduce results of Reference [225], which uses the decomposition of the Kitaev model into Majorana fermions coupled to a gauge field to devise a Monte Carlo approach to time evolution. My approach is more general, *e.g.* it allows the study of generalised Kitaev models, unlike the Monte Carlo method of Reference [225]. However, here I am interested in checking consistency across the Chebyshev and Monte Carlo approaches, so I limit myself to the model of Equation 5.3 for the sake of simplicity.

An important consequence of the long-range entanglement in QSLs is that they cannot be smoothly converted to a non-entangled magnetic product state [225]. One of the simplest examples of such a state is the antiferromagnetic Néel state. In Reference [225], the author investigates whether the non-entangled Néel state can be connected to the highly entangled QSL ground state of the Kitaev model via a sudden change in the Hamiltonian. This so called quantum quench [226] could lead to a dynamical phase transition [227]. An example of a dynamical phase transition occurs in the transverse field Ising model [228], where an initial magnetic state evolving under a model with a paramagnetic ground state eventually shows nonanalytic behaviour of the overlap between the initial state and the state at time t , known as the return amplitude.

The quench setup I treat here is designed as follows. I start with the Néel state and time evolve it under the isotropic and anisotropic versions of the Hamiltonian of Equation 5.3. Despite the absence of a dynamical phase transition reported in Reference [225], the author describes a long prethermal regime in the anisotropic case. The latter is characterised, *e.g.* via the time evolution of the staggered magnetisation, $m_{\text{st}} = \sum_i (-1)^{a_i} \langle \hat{\sigma}_i^z(t) \rangle / N$, where $a_i = \pm 1$, depending on whether site i belongs to sublattice \mathcal{A} or \mathcal{B} . The staggered magnetisation vanishes after the quench for both the isotropic and anisotropic cases, but persists for a longer time for the latter. My results for the time evolution of the staggered magnetisation on the 4×3 periodic cluster are shown in Figure 5.4. I use between 5 and 10 Chebyshev polynomials for each time step, computing the staggered magnetisation for 200 evenly spaced points in the logarithmic x -axis of Figure 5.4.

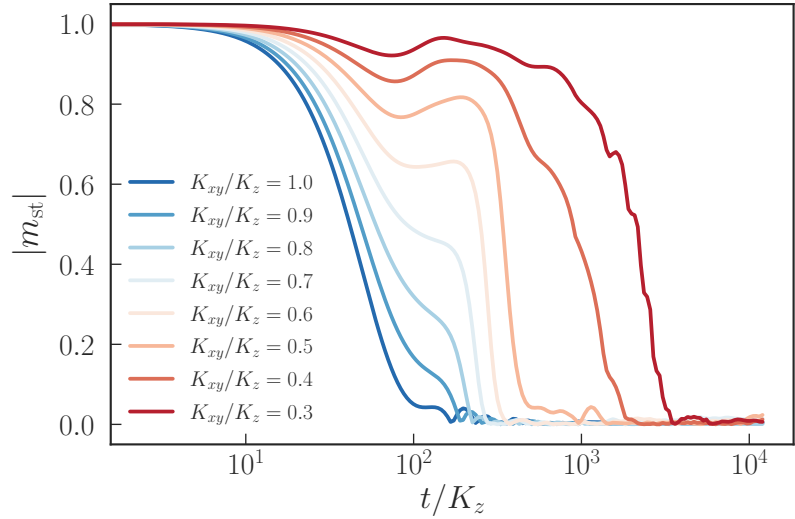
[225]: Rademaker (2019), ‘Quenching the Kitaev honeycomb model’

[226]: Polkovnikov et al. (2011), ‘Colloquium’

[227]: Heyl (2018), ‘Dynamical quantum phase transitions’

[228]: Heyl et al. (2013), ‘Dynamical Quantum Phase Transitions in the Transverse-Field Ising Model’

Figure 5.4: Staggered magnetisation after the quench at $t = 0$ for varying anisotropy. In the isotropic case, the magnetisation dies out quicker than in the anisotropic case, persisting for longer as the anisotropy becomes more pronounced.



The time required for the magnetisation to reach 0.1% of its original value is plotted as a function of the anisotropy ratio K_{xy}/K_z in Figure 5.5. The behaviour is approximately exponential in the anisotropy ratio, indicating the appearance of a characteristic timescale, t^* , for which the magnetisation persists long after the quench.

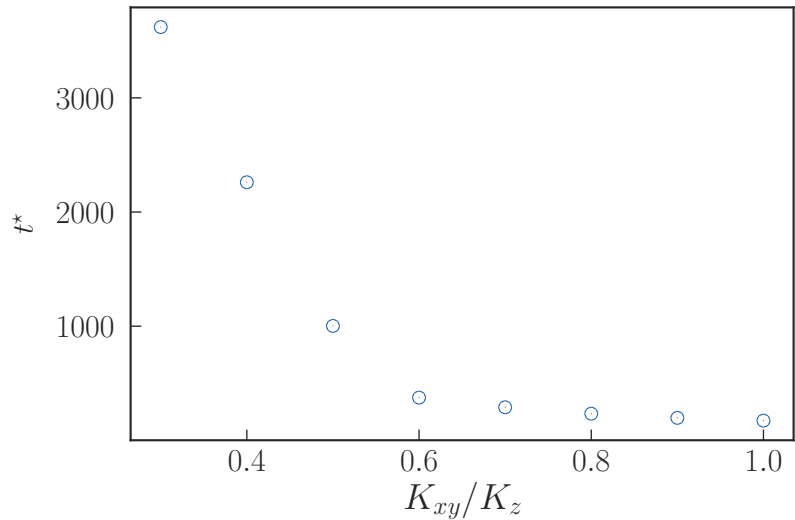


Figure 5.5: Timescale for the loss of 99.9% of the staggered magnetisation for varying anisotropy.

[229]: Bertini et al. (2015), ‘Prethermalization and Thermalization in Models with Weak Integrability Breaking’

The author of Reference [225] interprets these results in light of the concept of prethermalisation. For example, in Reference [229], the authors consider nonequilibrium evolution of many-body quantum systems, reporting the appearance of plateaux for local observables when systems are driven away from integrability by a perturbation. As the perturbation is increased, the system crosses over from this so called prethermal regime onto ‘thermal’ behaviour, *e.g.* the quick loss of magnetisation in the isotropic case seen in Figure 5.4.

As the anisotropy becomes more accentuated, the Kitaev model can

be regarded as having a dominant contribution from the z -bonds, with the terms corresponding to the x - and y -bonds serving as a perturbation. The Hamiltonian may then be approximated as the contribution of the z -bonds plus an effective Hamiltonian that does not couple spins linked by z -bonds [225]. Reference [230] describes how one may devise an appropriate unitary transformation that yields a perturbed Hamiltonian with new conservation laws compared to the original Hamiltonian. These laws affect the long time dynamics, leading to the appearance of a characteristic timescale that grows exponentially with the ratio K_z/K_{xy} .

The results of this section serve as further illustration of the versatility of the Chebyshev approach, which can be used to study dynamics either:

1. in the frequency domain, where it can access spectral functions, such as the dynamical spin susceptibility of Figure 5.3, displaying dynamical signatures of quantum criticality in the K-I model;
2. in the time domain, where it can be used *e.g.* to study quench protocols and characterise the time evolution of observables, such as the persisting staggered magnetisation after a Néel state is time evolved under the anisotropic Kitaev model, as shown in Figure 5.4.

[230]: Abanin et al. (2017), ‘A Rigorous Theory of Many-Body Prethermalization for Periodically Driven and Closed Quantum Systems’

Concluding remarks **6**

In this chapter, I point out the pros and cons of each method used in the second part of this thesis. In particular, I summarise how this work highlights the efficiency of the CPGF, FTCP and the HLC methods and I explain in which situations they could be particularly useful.

I studied the K-H and K-I models on the honeycomb lattice for 24-spin clusters with PBCs using three distinct approaches: Lanczos, TPQ and Chebyshev. The work is presented in the previous two chapters.

In Chapter 4, I started by reproducing the results of References [3–5] for the K-H model using Lanczos ED. Then, I recovered those results using microcanonical variants of the Lanczos (MCLM) and TPQ methods and the CPGF method, independently of each other. For these three methods, I carefully examined the spectral and statistical convergence properties. While Lanczos is found to be ideal to approximate the ground state, I find that CPGF is the most efficient method capable of probing an arbitrary target energy with well controlled accuracy, proving to be faster than both MTPQ and MCLM on average throughout the phase diagram of the K-H model.

Still within Chapter 4, I computed the temperature dependence of the nearest neighbour spin correlation, specific heat and entropy density. Again, the aim of this study was to compare three methods based on Lanczos, TPQ and Chebyshev ideas, respectively: the FTLM, the canonical variant of TPQ and the FTCP, introduced in Chapter 2. The MTPQ method is also considered because it is capable of estimating the temperature corresponding to each energy density remarkably accurately. My implementations are bench-marked against the exponential tensor renormalisation group results of Reference [10]. I find my newly introduced FTCP method to be the most efficient and versatile of the three, namely showing a two-fold increase in speed compared to TPQ, while also avoiding the large low-temperature statistical fluctuations of FTLM.

I opened Chapter 5 with a reproduction of Lanczos ED and TPQ results for the K-I model [59]. This bench-mark allowed me to validate my implementation and carry out a novel dynamical study for the K-I model, where I used the HLC method introduced here. The latter was also shown to be more flexible and about 33% faster than Lanczos on average. My detailed calculation of the dynamical spin susceptibility identifies signatures of the quantum phase transitions in the K-I model. This chapter also provides further evidence for the efficiency of FTCP, confirming the two-fold speed-up with respect to TPQ in finite temperature calculations for the K-I model. Finally, I bench-mark the Chebyshev approximation of the time evolution operator in a sudden quench, where a Néel state is time evolved under the Kitaev model. My results match those of a Monte Carlo approach to the same problem [225].

In what follows, I summarise the key aspects that support the conclusions above for each aspect of my work.

All microcanonical methods show low statistical fluctuations and considering even just a single realisation of the initial random state seems to suffice to achieve negligible deviations from the ED results throughout the phase diagram of the K-H model. Unlike the number of realisations, the resolution plays a central role when comparing the performance of the three microcanonical

approaches. In CPGF, finer resolutions always require more polynomials to achieve convergence. There is no one-to-one correspondence between the CPGF resolution and the effective resolutions of MTPQ and MCLM (which vary as more iterations are completed). Nonetheless, I managed to compare the three methods. TPQ showed an erratic convergence speed, with particularly significant slow-down for $\varphi = 0.506\pi$ in the K-H model, at which point around 4×10^4 polynomials/iterations are needed to achieve convergence and thus match the Lanczos ED results satisfactorily. On the other hand, CPGF requires very fine resolution to recover the ED results near the quantum phase transitions, thus converging relatively slower (but still faster than MTPQ) at these points of the phase diagram. Yet, away from quantum critical points, comparatively coarse resolutions are enough to reproduce the ED results. For most points of the phase diagram, CPGF has fast convergence and a relatively coarse input resolution suffices to match the results of ED. Even though the convergence behaviour of MCLM throughout the phase diagram is not as predictable as CPGF, the convergence speed is comparable to that of CPGF and both typically converge faster than MTPQ. Overall, I find that CPGF requires less computer time and has well controlled accuracy through the resolution and number of polynomials, thus having a slight edge over MCLM. In spite of not being ideal for probing target energies with well controlled accuracy, I still find that MTPQ is very useful because of its ability to estimate the temperature corresponding to each energy density over the course of the iteration. This means that MTPQ is a viable method to carry out studies that would otherwise only be possible using canonical methods.

Regarding finite-temperature studies, I find shortcomings in both MTPQ and its canonical counterpart, CTPQ. Both seem advantageous at first sight due to their lower memory cost. However, in the case of MTPQ, this implies a trade-off that I show to greatly increase the computer time. On the other hand, in the case of CTPQ, a numerical instability limits its ability to probe very low temperatures. I show that the main competitor of TPQ, the Lanczos-based FTLM, has comparatively larger statistical fluctuations when studying the low-temperature behaviour of the nearest neighbour spin correlations. These fluctuations, along with a high number of matrix-vector multiplications per iteration in FTLM, limit the method's efficiency. Finally, I show that the newly introduced FTCP method circumvents the shortcomings of the other methods. Its statistical fluctuations are smaller than FTLM and comparable to the TPQ methods. Whilst FTCP's memory cost is the same as FTLM (but slightly higher than TPQ), the trade-off is that the method is more efficient, i.e. twice as fast as MTPQ. This can be a crucial advantage in practical applications. Moreover, when using FTCP, accuracy can be controlled at each iteration, unlike in MTPQ, where the only way to guarantee sufficient accuracy is to increase the upper bound on the maximum eigenvalue of the spectrum by trial-and-error and carry out more costly, longer simulations. This is a demanding process, where one considers that accuracy is sufficient when no changes are detected in the relevant quantities for the desired temperature range as the upper bound is increased and the simulations are repeated. FTCP provides one with the option of choosing the number of polynomials for convergence in each Chebyshev expansion throughout the iterative process, thereby ensuring that accuracy is maintained in the whole temperature range, without dramatically increasing the computational cost.

My results show clear trade offs that must be taken into account when choosing which method to use. For example, MTPQ is designed to achieve maximum accuracy for the ground state. However, it cannot isolate excited states nor can it ensure uniform accuracy throughout large temperature windows. Concomitantly, the additional control afforded by the CPGF approach — which can access excited states directly — could be useful for studying non equilibrium systems, such as those studied in Reference [9]. Another example is that of canonical methods. While I find Lanczos to be

efficient for the computation of observables closely related to the Hamiltonian, it has large statistical fluctuations for more generic observables that might be of interest, such as the nearest neighbour spin correlation in the K-H model.

A particularly powerful competing method is DMRG, originally devised to investigate one-dimensional interacting systems [27–29]. DMRG aims to systematically truncate the exponentially large Hilbert space basis. The basis is rotated in the process in order to improve the accuracy of the truncation. This rotation is achieved via a series of global rotations generated by sweeping the lattice and thus focusing on a few sites at a time. The wide applicability of the DMRG procedure means that it can be used as a general purpose, sign problem free method. Moreover, it yields results that are competitive with QMC. However, the application of DMRG to two-dimensional systems remains challenging [30]. The Chebyshev-based methods used throughout this paper are a potential alternative to DMRG because, unlike the latter, they pose no restrictions on boundary conditions and their accuracy can be precisely controlled by ensuring statistical convergence and, in the case of CPGF, by adjusting the spectral resolution. As far as the system size is concerned, Reference [192] details the use of conservation laws to improve the efficiency of ED methods, particularly from the computer memory point of view. For example, translational symmetry implies that some configurations of the spins are equivalent up to a phase factor. This is a consequence of the block structure of the Hamiltonian, which gives forth to a reduced basis approach, enabling the study of larger system sizes. The only caveat is that systems with open boundary conditions and/or random couplings cannot be tackled with this approach.

To sum up, my results show that Chebyshev methods are more versatile and efficient than their Lanczos and TPQ counterparts, unless one is interested in properties that are well described using solely the ground state, or a small set of low-lying excitations. While in that case, Lanczos is still the method of choice, Chebyshev methods have significant advantages in various other scenarios, namely for the study of: properties that depend on an arbitrary target energy; finite temperature behaviour of observables of interest that cannot be expressed in terms of the Hamiltonian and low-order polynomials of the latter; and dynamical quantities, such as spectral functions and time-dependent observables.

FUTURE WORK AND CONCLUSION

Integration with the open-source software KITE

KITE is an open-source software offering computational tools for the simulation of electronic structure and quantum transport for tight-binding models [190]. Similarly to the codes that were written for this thesis, the core of KITE is a high-performance software written in C++. It uses Python as a user interface, particularly relying on the library `PyBinding` for generating the lattice and building the model, along with setting target functions.

Following KITE's footsteps, the codes developed for this thesis are implementations of my novel Chebyshev-based methods, designed with the capability to use `PyBinding` to build the lattice and the model, rather than hard-coding specific lattices or models. Following a notation similar to that of Reference [54], a generic Hamiltonian for the candidate compounds for a physical realisation of the Kitaev interaction can be written as follows

$$\hat{H}_{\text{generic}} = \sum_{\langle i,j \rangle^\gamma} \hat{S}_i^T J_\gamma \hat{S}_j, \quad (7.1)$$

where J_x, J_y, J_z are three 3×3 matrices which parametrise all possible spin interactions. For example, recalling the model outlined in Section 1.2.4, for z -bonds, the matrix reads

$$J_z = \begin{pmatrix} J & \Gamma & \Gamma' \\ \Gamma & J & \Gamma' \\ \Gamma' & \Gamma' & J + K_z \end{pmatrix} \quad (7.2)$$

In Appendix C, I show a minimal example of a Python script that uses `PyBinding` to generate the necessary inputs to simulate the honeycomb Kitaev model on a 4×3 cluster with periodic boundary conditions. A representation of the cluster from `PyBinding` is shown in Figure 7.1. Figures 7.2-7.5 represent hexagonal clusters generated with `PyBinding`, with increasing number of spins, respectively 24, 36, 42, 54. The cluster of Figure 7.5 is beyond reach for Lanczos, TPQ and Chebyshev approaches due to excessive memory requirements. An interesting direction for future research is the development of strategies to unlock larger system sizes, such as the cluster of Figure 7.5. In fact, even the cluster of Figure 7.3 already requires a computer memory of the order of the terabyte if no symmetries of the Hamiltonian are directly implemented in ED codes.

The evaluation of matrix-vector products 'on-the-fly' is the most computationally expensive operation in Lanczos, TPQ and Chebyshev methods, such as the FTCP and HLC introduced for the first time here. Similarly, KITE relies on the CPGF method, for which matrix-vector multiplication constitutes the bottleneck as well. The information needed to carry out the matrix-vector products on-the-fly is encoded via a set of arrays indexing nearest neighbouring spins on the honeycomb lattice, their corresponding types of bond and the matrices J_γ . These arrays can then be input

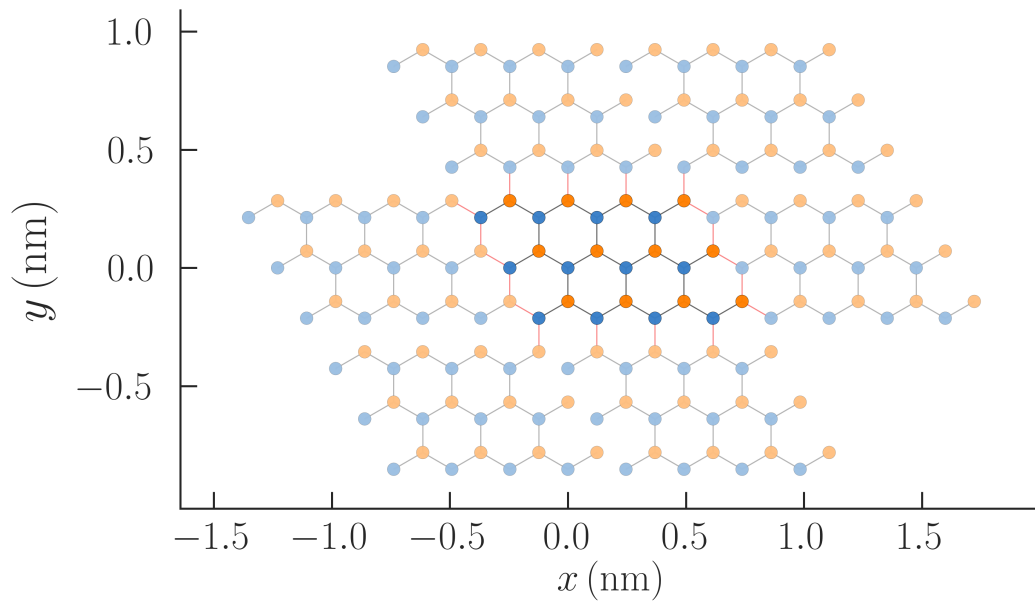


Figure 7.1: Periodic 4×3 cluster on the honeycomb lattice, generated with PyBinding.

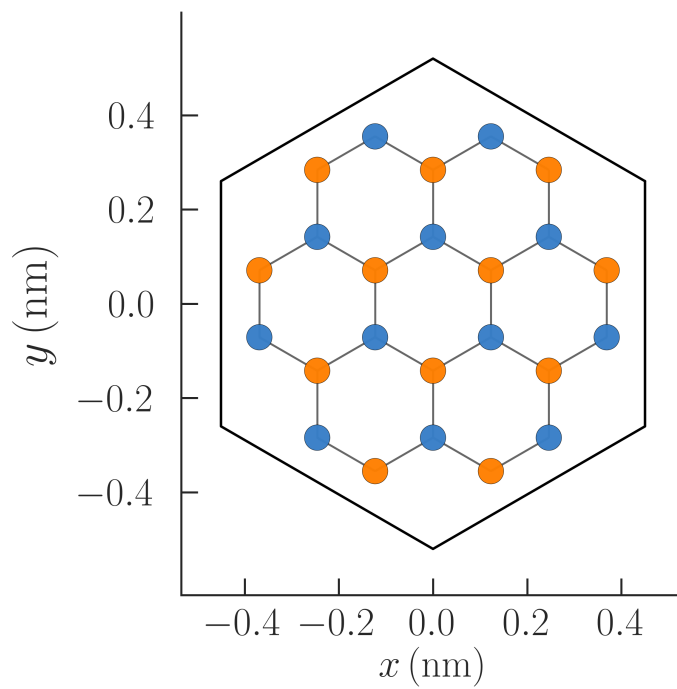


Figure 7.2: 24-spin hexagonal cluster on the honeycomb lattice, generated with PyBinding.

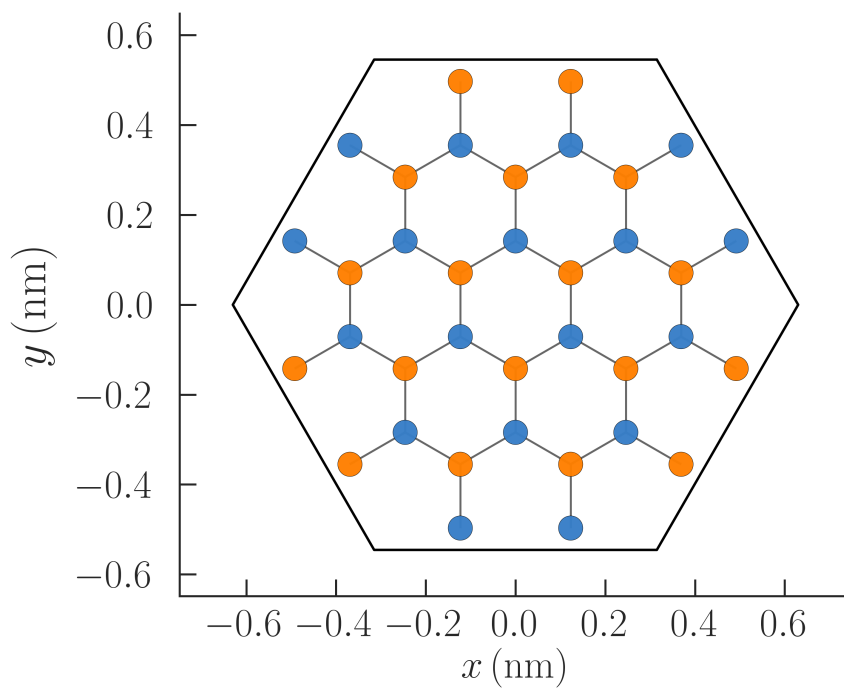


Figure 7.3: 36-spin hexagonal cluster on the honeycomb lattice, generated with PyBinding.

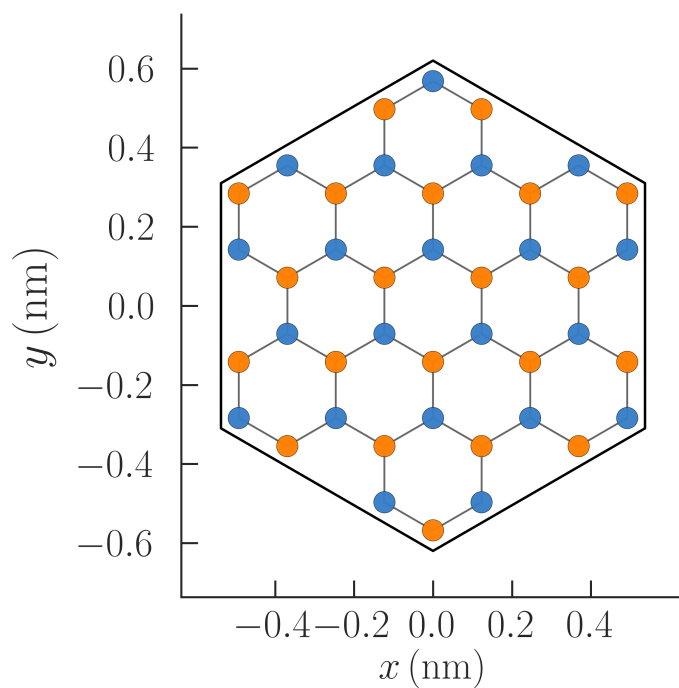


Figure 7.4: 42-spin hexagonal cluster on the honeycomb lattice, generated with PyBinding.

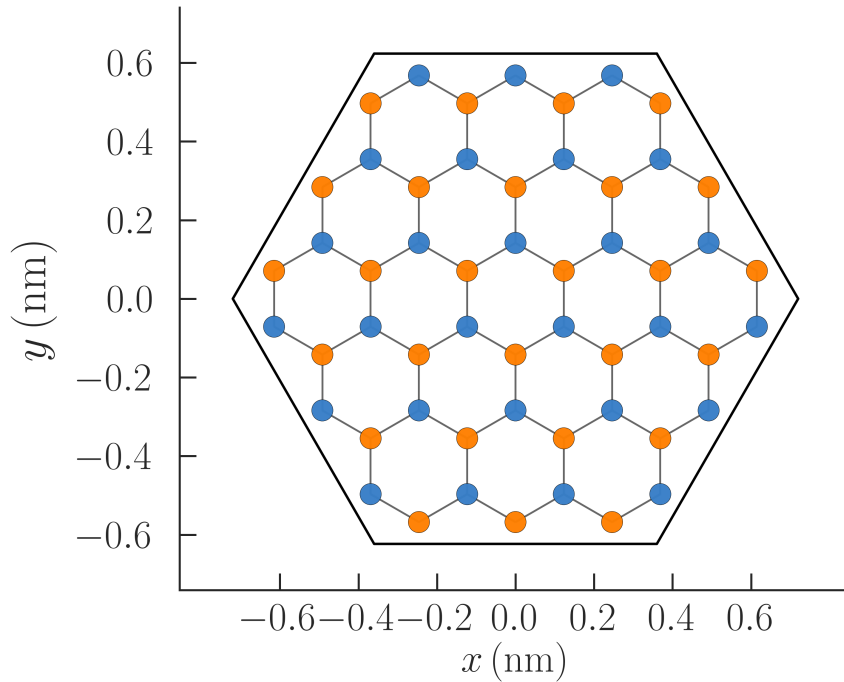


Figure 7.5: 54-spin hexagonal cluster on the honeycomb lattice, generated with PyBinding.

into the high-performance C++ software developed in this work in the exact same manner that tight-binding parameters are input into KITE. The flexibility afforded by this approach is invaluable, in particular to study the effect of various spin interactions, bond disorder, or even special boundary conditions.

The results obtained with the software developed in this work were carried out on a shared memory multi-node CPU architecture. The on-the-fly evaluation of matrix-vector multiplications allows one to reach very good multi-threading performance by parallelising the most costly outer loops involved in these operations (see *e.g.* Algorithm 2, where I parallelise the very first loop). KITE uses a more sophisticated domain decomposition technique to thread partitions of the lattice, boosting the performance of its parallelisation. However, this technique is specifically designed for the non-interacting Hamiltonians simulated by KITE. A direct generalisation for interacting Hamiltonians, such as the ones studied in this work is not trivial because of the exponential growth of the Hilbert space with the number of spins and is beyond the scope of this work. Still, by employing a similar workflow to KITE, I have enabled the integration of my codes with KITE and these are being prepared in coordination with the KITE team to appear in a future release of a new KITE version.

I believe that the addition of the software developed in this work to KITE represents a significant benefit to the community because it provides a user-friendly platform for the simulation of interacting quantum spin models with general purpose, numerically exact, unbiased methods. The user-friendliness of the KITE workflow is attributed to the prescription of the model Hamiltonian and details of the lattice with an intuitive Python script, followed by a high-performance simulation. The work of the thesis extends the possibilities created by this approach from the tight-binding models, included in the initial release of KITE, to many-body systems. In particular, the two novel Chebyshev methods for many-body systems presented here (FTCP and HLC) will become available to the public via the unified workflow of KITE.

Conclusion

In this work, two generalised models of interacting quantum condensed matter systems in two spatial dimensions are simulated. Both models serve as minimal models for transition metal compounds with underlying honeycomb lattice structures and strong electron correlations. The thesis is divided in two parts, corresponding to the aforementioned distinct classes of models. In the first part of the thesis, electron-electron interactions are treated directly using MFT and DetQMC approaches. In the second part, interactions are treated via effective quantum spin models, probed with methods based on Lanczos ED, TPQ and numerically exact expansions in Chebyshev polynomials. The first part is devoted to the search for emerging magnetism at the edges of a strongly correlated nanostructure, while the second part highlights the properties of phases with no magnetic order in a family of QSL candidate materials known as Kitaev magnets. Rather than ordering magnetically, in these phases, fluctuating quantum spins remain disordered even at zero temperature, fractionalising into fermionic and gauge field degrees of freedom. This process leaves traces in the thermodynamics, for example in the specific heat and entropy, but also in the dynamics, in the form of distinct excitations, which can be probed, *e.g.* with inelastic neutron scattering.

Part 1 illustrates the need for unbiased, numerically exact methods in a system of interacting electrons: a zTMDNR, modeled via a generalised multi-orbital Hubbard model. The model is first approached using MFT, which points at a strong dependence of the ground state on the occupation of electronic states localised at the edges of the sample. This so called edge filling dramatically affects the variance of QMC estimators, which is exponentially large for most fillings of interest. Luckily, for one of the phases predicted by MFT (an edge-antiferromagnetic phase), the sign problem does not impede QMC simulations and although they remain computationally intensive, it is still possible to extract insight.

QMC confirms the stability of an antiferromagnetic phase at the chalcogen-terminated edge of a molybdenum disulfide zTMDNR. Yet, upon comparison with QMC, the MFT approach is found to overestimate magnetic ordering, predicting long-range order, *i.e.* constant antiferromagnetic spin correlations on the edges of the nanoribbon. Moreover, the onset of edge-magnetism occurs for lower values of the Hubbard interaction than in QMC. A finite-size scaling study of the QMC results reveals *quasi* long-range order with algebraic decay of the spin correlations at the one of the edges of the ribbon. Moreover, on the transition metal-terminated edge, MFT predicts that antiferromagnetism only sets in for a larger value of the Hubbard interaction compared to the chalcogen-terminated edge, suggesting that ordering is not as robust on the transition metal-terminated edge. Again, QMC results validate this suspicion by revealing antiferromagnetic correlations with a faster decay at the transition metal-terminated edge; a finite-size scaling study of the QMC results points at no magnetic ordering for a wide range of Hubbard interactions, with spin correlations dying off as the thermodynamic limit is approached. Strong Hubbard interactions intensify the sign problem and eventually QMC simulations become prohibitively expensive, so magnetic order is only confirmed

for the chalcogen-terminated edge. Although QMC results do not preclude magnetic order at both edges, the required strength of the Hubbard term is likely unrealistic for TMDs.

Part 2 tackles generalised honeycomb Kitaev models, namely the K-H and K-I models. Unlike the pure Kitaev case, these evade an analytical approach. These models have been studied intensively in the last decade because of their relevance for the modelling of QSL candidate materials, such as the Kitaev magnets, which are the subject of this work. I have used a toolset of general purpose methods based on Chebyshev polynomial expansions devised to treat these models with improved efficiency and flexibility, and with remarkable numerical stability and tightly controlled accuracy. Similarly to ED and QMC, the Chebyshev methods are unbiased and numerically exact. Despite being unable to tackle the large system sizes achieved by QMC, or other competing methods, such as DMRG, Chebyshev methods do not suffer from the sign problem plaguing QMC. Moreover, they allow for any choice of boundary conditions, unlike DMRG. Finally, they have some advantages with respect to Lanczos and TPQ approaches, which I summarise below.

Using the FTCP method, I have characterised thermal spin fractionalisation into Majorana fermions and a gauge field in the K-H and K-I models in terms of a multi-stage release of entropy of the relevant quasiparticles. This is accompanied by a multi-peak structure of the specific heat. I compare the computational performance of FTCP with that of a state-of-the-art TPQ method, observing a two-fold decrease in computer time, despite a minor trade-off in memory usage (a 50% increase with the Chebyshev approach, *i.e.* a similar memory requirement to Lanczos). Additionally, FTCP offers more control over accuracy than TPQ throughout the temperature range.

Finally, I use the HLC method to study the dynamics of the K-H and K-I models, finding dynamical signatures of QSL and magnetically ordered phases in both cases. Here, I highlight novel results for the spin susceptibility of the K-I model. These have enabled the identification of clear signs of the quantum phase transitions in this model via a smooth change in the spin excitations at the quantum critical points. In particular, I analyse the liquid-to-liquid transition in the K-I model in terms of this change.

The excitations of the Kitaev spin liquid phase in the K-I model are attributed to the introduction of a π -flux pair and subsequent reconfiguration of the Majorana fermions in this new background gauge field, which corresponds to a discrete peak structure in the spin susceptibility. Near zero frequency, the response vanishes due to the gapped nature of flux excitations. This characteristic peak structure of the Kitaev model fades away as a nematic liquid phase of the K-I model is approached, and, in particular, the gap decreases and its distinctive low-frequency mode splits into a set of several low-frequency modes concentrated in a small range, precisely at the quantum critical point for the Kitaev QSL-nematic transition. The identification of dynamical signatures, such as the one described for the K-I model, is relevant for the interpretation of experimental data (*e.g.* inelastic neutron scattering) that could potentially point at the existence of QSL phases in real compounds.

In conclusion, this work highlights the power of unbiased methods, such as the Chebyshev framework that is used extensively in Part 2. An important avenue for future research is the development of strategies to conduct larger scale simulations, possibly by combining the virtues of Chebyshev spectral methods and variational methods, such as tensor networks.

APPENDICES

A

Appendix to Chapter 2

A.1 Coefficients of the Fejér kernel

I start by defining the positive function with period 2π

$$p(\varphi) = \left| \sum_{v=0}^{N-1} a_v e^{iv\varphi} \right|^2, \quad a_v \in \mathbb{R}. \quad (\text{A.1})$$

It is now possible to make appear the definition of the Chebyshev polynomials.

$$\begin{aligned} p(\varphi) &= \sum_{\mu, v=0}^{N-1} a_\mu a_v e^{i(v-\mu)\varphi} \\ &= \sum_{\mu, v=0}^{N-1} a_\mu a_v \cos(v - \mu)\varphi \\ &= \sum_{v=0}^{N-1} a_v^2 + 2 \sum_{n=1}^{N-1} \sum_{v=0}^{N-1-n} a_v a_{v+n} \cos(n\varphi). \end{aligned} \quad (\text{A.2})$$

Defining the weights in terms of the a -coefficients,

$$g_n = \sum_{v=0}^{N-1-n} a_v a_{v+n} \quad (\text{A.3})$$

one may rewrite the function of Equation A.1 as

$$p(\varphi) = g_0 + 2 \sum_{n=1}^{N-1} g_n \cos(n\varphi). \quad (\text{A.4})$$

Since $p(\varphi)$ is positive, then one has that the quantity

$$\begin{aligned} &\frac{1}{2}[p(\arccos x + \arccos y) + p(\arccos x - \arccos y)] \\ &= p(\arccos x)p(\arccos y) \end{aligned} \quad (\text{A.5})$$

is positive for all $x, y \in]-1, 1[$. Thus, the kernel defined in Equation 2.51 is positive for all $x, y \in]-1, 1[$, as long as the weights depend on the a -coefficients as specified in Equation A.3. The Fejér kernel is obtained by setting $a_v = 1/\sqrt{N}$. Thus, it is positive.

A.2 Coefficients of the Jackson kernel

Q can be expressed in terms of g_n and a_ν by noting that

$$\begin{aligned} (x - y)^2 &= [T_1(x) - T_1(y)]^2 \\ &= \frac{1}{2} \left\{ [T_2(x) + T_0(x)]T_0(y) + T_0(x)[T_2(y) + T_0(y)] \right\} - 2T_1(x)T_1(y), \end{aligned} \quad (\text{A.6})$$

which is derived using the product identity of Equation 2.41.

Now I use the definition of a kernel to obtain

$$\begin{aligned} Q &= \int_{-1}^1 \int_{-1}^1 dx dy (x - y)^2 \left[g_0 \phi_0(x) \phi_0(y) + 2 \sum_{n=1}^{N-1} g_n \phi_n(x) \phi_n(y) \right] \\ &= g_0 \int_{-1}^1 T_0(x) \frac{T_0(x)}{\pi \sqrt{1-x^2}} dx \int_{-1}^1 T_0(y) \frac{T_0(y)}{\pi \sqrt{1-y^2}} dy \\ &\quad - 4g_1 \int_{-1}^1 T_1(x) \frac{T_1(x)}{\pi \sqrt{1-x^2}} dx \int_{-1}^1 T_1(y) \frac{T_1(y)}{\pi \sqrt{1-y^2}} dy \\ &= g_0 (\langle T_0 | T_0 \rangle_1)^2 - 4g_1 (\langle T_1 | T_1 \rangle_1)^2 \\ &= g_0 - g_1, \end{aligned} \quad (\text{A.7})$$

where the fact that Chebyshev polynomials are a basis set makes it so that terms with $n \neq 0, 1$ vanish by inspection and the factor of 2 of the second term cancels out with the factor of 1/2 appearing in Equation 2.38.

I minimise $Q = g_0 - g_1$ under the constraint $C = g_0 - 1$ using the Lagrange multiplier method. The relevant condition is

$$\frac{\partial Q}{\partial a_\nu} = \lambda \frac{\partial C}{\partial a_\nu}, \quad (\text{A.8})$$

and using $g_n = \sum_{\nu=0}^{N-1-n} a_\nu a_{\nu+n}$ and setting $a_{-1} = a_N = 0$, one obtains the eigenvalue problem for a harmonic chain with fixed boundary conditions

$$2a_\nu - a_{\nu-1} - a_{\nu+1} = \lambda a_\nu, \quad (\text{A.9})$$

which has a well known solution:

$$a_\nu = \bar{a} \sin \frac{\pi k(\nu+1)}{N+1}, \quad \lambda = 1 - \cos \frac{\pi k}{N+1}, \quad (\text{A.10})$$

where $\nu = 0, \dots, N-1$ and $k = 1, 2, \dots, N$. The g 's may now be computed, given a_ν and using the notation $q = \frac{\pi k}{N+1}$. First, one writes them in terms of the a 's:

$$\begin{aligned}
g_n &= \sum_{v=0}^{N-1-n} a_v a_{v+n} \\
&= \bar{a}^2 \sum_{v=1}^{N-n} \sin(qv) \sin[q(v+n)].
\end{aligned} \tag{A.11}$$

Then, one may use the identity $\cos(a+b) = \cos a \cos b - \sin a \sin b$ to obtain

$$\begin{aligned}
g_n &= \frac{\bar{a}^2}{2} \sum_{v=1}^{N-n} [\cos(qn) - \cos[q(2v+n)]] \\
&= \frac{\bar{a}^2}{2} \left((N-n) \cos(qn) - \operatorname{Re} \sum_{v=1}^{N-n} e^{iq(2v+n)} \right) \\
&= \frac{\bar{a}^2}{2} ((N-n+1) \cos(qn) + \sin(qn) \cot q),
\end{aligned} \tag{A.12}$$

where in the last step I did the following manipulations

$$\begin{aligned}
& - \operatorname{Re} \left[\sum_{v=1}^{N-n} e^{iq(2v+n)} \right] = - \operatorname{Re} \left[e^{iqn} \sum_{v=1}^{N-n} e^{2iqv} \right] \\
&= - \operatorname{Re} \left[e^{iqn} \left(\frac{1 - e^{2iq(N-n+1)}}{1 - e^{2iq}} - 1 \right) \right] \\
&= \cos(qn) - \operatorname{Re} \left[e^{iqn} \frac{1 - e^{2iq(N-n+1)}}{1 - e^{2iq}} \right] \\
& \quad \left(\text{using } e^{2iq(N+1)} = 1 \right) \\
&= \cos(qn) - \operatorname{Re} \left[\frac{e^{iqn} - e^{-iqn}}{e^{2iq} - 1} \right] = \cos(qn) - \operatorname{Re} \left[e^{-iq} \frac{e^{iqn} - e^{-iqn}}{e^{iq} - e^{-iq}} \right] \\
&= \cos(qn) - \operatorname{Re} \left[e^{-iq} \frac{\sin(qn)}{\sin q} \right] = \cos(qn) - \cos q \frac{\sin(qn)}{\sin q} \\
&= \cos(qn) - \sin(qn) \cot q.
\end{aligned} \tag{A.13}$$

The normalisation condition ($g_0 = 1$) is obtained by setting $\bar{a}^2 = \frac{2}{N+1}$. Noticing that $g_1 = \cos q$, one can conclude that the optimal value of Q is

$$\begin{aligned}
Q = g_0 - g_1 &= 1 - \cos \frac{\pi}{N_{\text{poly}} + 1} \\
&\approx \frac{1}{2} \left(\frac{\pi}{N_{\text{poly}}} \right)^2 \equiv Q_{\text{min}},
\end{aligned} \tag{A.14}$$

where I took only the leading contribution for large N_{poly} .

A.3 A prescription to generate a sequence of microcanonical pure quantum states

Here, I show that the states obtained using the procedure above are TPQ states. One is free to choose a particular basis set for this proof since the results are independent of the chosen basis set. Let one choose the one comprised of the energy eigenstates $\{|n\rangle\}$, defined by $\hat{h}|n\rangle = \varepsilon_n|n\rangle$. After k iterations, one obtains the state

$$|\psi_k\rangle \propto (l - \hat{h})^k |\psi_0\rangle = \sum_n c_n (l - \varepsilon_n)^k |n\rangle. \quad (\text{A.15})$$

Let one look at the energy density distribution in this state. The distribution function of u is given by

$$r_k(u; N) \propto \delta_r^{-1} \sum_n' |c_n|^2 (l - \varepsilon_n)^{2k}, \quad (\text{A.16})$$

where δ_r is a constant of order $\mathcal{O}(1)$ and \sum_n' is a sum over eigenstates such that $\varepsilon_n \in [u - \frac{\delta_r}{2}, u + \frac{\delta_r}{2}]$. Since $g(u; N)$ is exponential in N , $r_k(u; N)$ converges exponentially fast to its average (with high probability):

$$r_k(u; N) = D^{-1} \exp[N\xi(u; N)], \quad (\text{A.17})$$

where $\xi(u; N) \equiv s(u; N) + \frac{2k}{N} \ln(l - u)$. $\xi_k(u; N)$ has a maximum at u_k^* , such that

$$\beta(u_k^*; N) = \frac{2k}{N(l - u_k^*)}. \quad (\text{A.18})$$

Equation A.18 immediately defines the inverse temperature up to some error of order $\mathcal{O}(\frac{1}{N})$. One can improve upon this estimate by expanding $\xi_k(u; N)$ around u_k^* . This is also the first step that will allow one to prove that this method yields TPQ states. First, notice that

$$\xi_k'' \equiv \left. \frac{\partial^2 \xi_k}{\partial u^2} \right|_{u=u_k^*} = \beta'(u_k^*; N) - \frac{2k}{N(l - u_k^*)^2} < 0. \quad (\text{A.19})$$

Then, expand up to third order, to obtain

$$\xi_k(u; N) = \xi_k(u_k^*; N) - \left| \xi_k'' \right| \frac{(u - u_k^*)^2}{2} + \xi_k''' \frac{(u - u_k^*)^3}{6} + \dots \quad (\text{A.20})$$

The third order derivative may be recast as

$$\xi_k''' \equiv \left. \frac{\partial^3 \xi_k}{\partial u^3} \right|_{u=u_k^*} = \beta''(u_k^*; N) - \frac{4k}{N(l - u_k^*)^3} < 0. \quad (\text{A.21})$$

By replacing the expansion of Equation A.20 in Equation A.17, one can conclude that $r_k(u; N)$ behaves approximately as a Gaussian distribution peaking at $u = u_k^*$. The variance goes to zero as N increases: $\sigma^2 = 1/N|\xi_k''|$.

Now let one define the density operator

$$\hat{\rho}_k \equiv \frac{(l - \hat{h})^{2k}}{\text{Tr}[(l - \hat{h})^{2k}]} \quad (\text{A.22})$$

This operator has the same energy distribution $r_k(u; N)$. $\hat{\rho}_k$ represents an equilibrium state specified by the tuple u_k, N , since $r_k(u; N)$ has a sharp peak at $u = u_k$. It may be shown (similarly to what is done in Reference [231]) that the conditions for $|\psi_k\rangle$ to be a TPQ state are obeyed, that is

$$P\left(|\langle\psi_k|\hat{A}|\psi_k\rangle - \text{Tr}[\hat{\rho}_k\hat{A}]| \geq \varepsilon\right) \leq \frac{\|\hat{A}\|^2 r_k(e_{\min}; N)}{\varepsilon^2 r_k(u_k^*; N)}, \quad (\text{A.23})$$

where $\|\hat{A}\|$ is the norm of the operator \hat{A} , and

$$\overline{\langle\psi_k|\hat{A}|\psi_k\rangle} = \text{Tr}[\hat{\rho}_k\hat{A}], \quad (\text{A.24})$$

where $\overline{\langle\psi_k|\hat{A}|\psi_k\rangle}$ is the average over realisations of the random vector. This is valid for every mechanical variable \hat{A} .

As N increases, the $\|\hat{A}\|$ grows at most as a low degree polynomial. On the other hand, the ratio of distributions $r_k(e_{\min}; N)/r_k(u_k^*; N)$ decreases exponentially at finite temperature, that is for $u_k^* > e_{\min}$.

I have obtained an order $\mathcal{O}(1/N)$ expression for the inverse temperature:

$$\beta(u_k; N) = \frac{2k}{N(l - u_k)} + \mathcal{O}\left(\frac{1}{N}\right). \quad (\text{A.25})$$

However, in practice the energy density that one obtains at each iteration is not the exactly the one that maximises $\xi_k(u; N)$. A more general expression is obtained by using the expansion of $\xi_k(u; N)$. This is done in Section A.4 below.

A.4 Estimating temperature with microcanonical pure quantum states

Any two consecutive vectors obtained during the iterative TPQ procedure contain enough information to enable one to compute the inverse temperature, energy density and specific heat. Given a normalised TPQ vector, $|\psi_k\rangle$, the next (unnormalised) vector in the sequence, $|\phi_{k+1}\rangle^*$ is obtained similarly to Equation 2.80:

$$|\phi_{k+1}\rangle = (l - \hat{h})|\psi_k\rangle. \quad (\text{A.26})$$

* Its normalised counterpart is simply $|\psi_{k+1}\rangle = |\phi_{k+1}\rangle/||\phi_{k+1}\rangle||$

Let me start by obtaining the energy density in terms of the following two overlaps: $\langle \psi_k | \phi_{k+1} \rangle$ and $\langle \phi_{k+1} | \phi_{k+1} \rangle$. Acting with $\langle \psi_k |$ on the left both on the left and right hand sides of Equation A.26 and reorganising the terms, one obtains

$$u_k = l - \langle \phi_{k+1} | \psi_k \rangle. \quad (\text{A.27})$$

Similarly, if one acts with $\langle \phi_{k+1} |$ on the left both on the left and right hand sides of Equation A.26 and reorganise the terms, one obtains

$$v_k \equiv \langle \psi_k | \hat{h}^2 | \psi_k \rangle = -l^2 + 2lu_k \langle \phi_{k+1} | \phi_{k+1} \rangle, \quad (\text{A.28})$$

which can be used to obtain the specific heat per spin, c for a system with N spins as

$$c_k = N(\langle \psi_k | \hat{h}^2 | \psi_k \rangle - \langle \psi_k | \hat{h} | \psi_k \rangle^2) = N(v_k - u_k^2) \quad (\text{A.29})$$

Equation A.25 gives an expression for the inverse temperature of a finite system of N spins that holds to order $\mathcal{O}(1/N)$. The two partial derivatives defined in Equation A.19 and Equation A.20 can be used to obtain better approximations [34].

The first improvement to the $\mathcal{O}(1/N)$ formula of Equation A.25 is to derive a $\mathcal{O}(1/N^2)$ formula. The first step of the derivation is to notice that the partial derivatives of Equation A.19 and Equation A.20 can be recast using the following expectations over TPQ states [34]:

$$\begin{aligned} \frac{c_k}{N} &= \langle \psi_k | (\hat{h} - u_k)^2 | \psi_k \rangle = \frac{1}{N|\xi_k''|} + \mathcal{O}(1/N^2), \\ \Delta_k &\equiv \langle \psi_k | (\hat{h} - u_k)^3 | \psi_k \rangle = \xi_k''' / N^2 |\xi_k''|^3 + \mathcal{O}(1/N^3). \end{aligned} \quad (\text{A.30})$$

From Equation A.19, one has that $\xi_k'' < 0$. The latter can be cast as $\xi_k'' = -1/c_k$. Using this relation, one may now cast the third derivative as $\xi_k''' = N^2 \Delta_k / c_k^3$. Still, it remains to derive a practical formula for Δ_k . Fortunately, it can be obtained efficiently using u_k , v_k , l , and u_{k+1} :

$$\Delta_k = -l^2 u_k - 3u_k v_k - 2l v_k + u_{k+1} (l^2 - 2l u_k + v_k). \quad (\text{A.31})$$

Proof. I start by using the binomial theorem to rewrite Δ_k as

$$\begin{aligned} \Delta_k &= \langle \psi_k | \hat{h}^3 | \psi_k \rangle - 3\langle \psi_k | \hat{h}^2 | \psi_k \rangle u_k + 3\langle \psi_k | \hat{h} | \psi_k \rangle u_k^2 - u_k^3 \\ &= \langle \psi_k | \hat{h}^3 | \psi_k \rangle - 3v_k u_k + 2u_k^3. \end{aligned}$$

In what follows, I will apply the relations:

$$\hat{h} | \psi_k \rangle = l | \psi_k \rangle - | \phi_{k+1} \rangle, \quad \langle \psi_k | \hat{h} = l \langle \psi_k | - \langle \phi_{k+1} |,$$

which are derived from Equation A.26. These will be used several times.

$$\begin{aligned}
\Delta_k &= \langle \psi_k | \hat{h}^2 (|\psi_k\rangle - |\phi_{k+1}\rangle) - 3v_k u_k + 2u_k^3 \\
&= lv_k - \langle \psi_k | \hat{h}^2 | \phi_{k+1} \rangle - 3v_k u_k + 2u_k^3 \\
&= lv_k - (l\langle \psi_k | - \langle \phi_{k+1} |) \hat{h} | \phi_{k+1} \rangle - 3v_k u_k + 2u_k^3 \\
&= lv_k - l\langle \psi_k | \hat{h} | \phi_{k+1} \rangle + \langle \phi_{k+1} | \hat{h} | \phi_{k+1} \rangle - 3v_k u_k + 2u_k^3 \\
&= lv_k - l(l\langle \psi_k | - \langle \phi_{k+1} |) | \phi_{k+1} \rangle + \langle \phi_{k+1} | \hat{h} | \phi_{k+1} \rangle - 3v_k u_k + 2u_k^3 \\
&= lv_k - l^2 \langle \psi_k | \phi_{k+1} \rangle + l \langle \phi_{k+1} | \phi_{k+1} \rangle + \langle \phi_{k+1} | \hat{h} | \phi_{k+1} \rangle - 3v_k u_k + 2u_k^3
\end{aligned}$$

In terms of the variables of Equation A.27 and Equation A.28, one has

$$\langle \phi_{k+1} | \psi_k \rangle = l - u_k, \quad \langle \phi_{k+1} | \phi_{k+1} \rangle = v_k + l^2 - 2lu_k.$$

Moreover, the energy density at the $(k + 1)$ -th step is given by

$$u_{k+1} = \frac{\langle \phi_{k+1} | \hat{h} | \phi_{k+1} \rangle}{\langle \phi_{k+1} | \phi_{k+1} \rangle}.$$

Thus, one has

$$\langle \phi_{k+1} | \hat{h} | \phi_{k+1} \rangle = (v_k + l^2 - 2lu_k)u_{k+1}.$$

Finally, one obtains

$$\begin{aligned}
\Delta_k &= lv_k - l^2(l - u_k) + (v_k + l^2 - 2lu_k)(l + u_{k+1}) - 3v_k u_k + 2u_k^3 \\
&= -l^2 u_k - 3u_k v_k - 2lv_k + u_{k+1}(l^2 - 2lu_k + v_k).
\end{aligned}$$

□

Let $u_k^\bullet \equiv u_k - \xi_k''' / 2N \xi_k''^2 = u_k - N \Delta_k / c_k$. Then, in Reference [34], the authors show that the $\mathcal{O}(1/N^2)$ formula for the inverse temperature is

$$\beta(u_k^\bullet, N) = 2k/N(l - u_k^\bullet) + \mathcal{O}(1/N^2). \quad (\text{A.32})$$

The authors of Reference [34] also state that the canonical average of the energy density, \tilde{u}_k^c can be estimated more accurately by considering an enlarged Hilbert space of C identical copies of the N -spin system and then taking the limit $C \rightarrow \infty$. When this is done, one obtains an estimate for the inverse temperature of an infinite system comprised of infinitely many N -spin systems, $\tilde{\beta}(u; \infty)$. In order to obtain a practical formula, the authors of Reference [34] remark that the canonical average of the energy density may be approximated as $\tilde{u}_k^c = \tilde{u}_k^\bullet + \mathcal{O}(1/N^2)$, with

$$\tilde{u}_k^\bullet \equiv u_k^\bullet + \frac{\xi_k''' + 4k/N(l - u_k^\bullet)^3}{2N[\xi_k'' + 2k/N(l - u_k^\bullet)^2]}. \quad (\text{A.33})$$

The estimate for the inverse temperature of the infinite system, $\tilde{\beta}(u; \infty)$ then becomes

$$\tilde{\beta}(\tilde{u}_k^\bullet; \infty) = 2k/N(l - \tilde{u}_k^\bullet) + \mathcal{O}(1/N^2). \quad (\text{A.34})$$

To sum up, the inverse temperature can be computed similarly to Equation A.25, but with a ‘corrected’ energy density, \tilde{u}_k^\bullet . Let me now rewrite this quantity solely in terms of $k, N, l, u_k, \Delta_k, c_k$:

$$\tilde{u}_k^\bullet = u_k - \frac{N\Delta_k}{c_k} + \frac{\frac{N^2\Delta_k}{c_k^3} + \frac{4k}{N(l-u_k-N\Delta_k/c_k)^3}}{2N\left[\frac{2k}{N(l-u_k-N\Delta_k/c_k)^2} - \frac{1}{c_k}\right]^2}. \quad (\text{A.35})$$

Appendix to Chapter 3

B.1 Effect of edge bandwidth on edge magnetic order of zig zag transition metal dichalcogenide nanoribbons

In this appendix, I discuss the impact of using different TMDs in my calculations, therefore changing the edge bandwidth, *i.e.* the portion of the spectrum corresponding to edge bands. Using different TMDs has only a slight impact on the edge magnetic ordering because the edge bandwidth is similar (~ 1 eV) among group 6 TMDs, as I show in Figure 3.1.

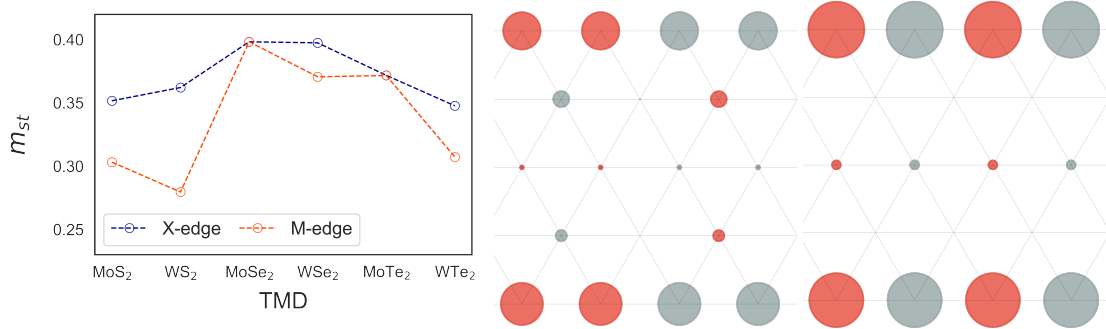


Figure B.1: (Left) Variation of the mean field staggered magnetisations at the M edge (orange) and the X edge (blue) for the AF1 phase for different TMD nanoribbons, all of them with a width of 5 M atoms and with $U = 2.94$ eV. (Right) Example of the gapped AF2 (left) and AF1 (right) phases obtained with MFT at $\nu_{edge} = 0.5$ for a WSe₂ nanoribbon with a width of 5 M atoms and considering $U = 2.94$ eV. I also recover the edge ferromagnetic phases for $\nu_{edge} \neq 0.5, 0.75$ shown in Figure 3.3 for all TMDs in the family, but I omit them here for the sake of brevity.

I obtain the edge antiferromagnetic phases AF2 and AF1, respectively at $\nu_{edge} = 0.5, 0.75$ for all the TMDs I considered. For other edge fillings, I find edge ferromagnetism. Even though there are slight differences in the specific values of the order parameters on each edge between the TMDs, the general qualitative conclusions do not change. I illustrate this for the AF1 phase in the left panel of Figure B.1. Notice that for MoSe₂ and MoTe₂ the two edges have the same value of the staggered magnetisation. This is because these two TMDs have the narrowest edge bandwidths. Thus, for this specific Hubbard- U , the magnetisations are likely already saturated, *i.e.* they have already reached their maximum value. On the right panel of Figure B.1, I show an example of the aforementioned edge antiferromagnetic phases for WSe₂.

Appendix to Chapter 7

C.1 Setting up the honeycomb Kitaev model with PyBinding: a minimal example

The Python script below is a minimal example of the preliminary build of the lattice and model using PyBinding. The script sets up the honeycomb Kitaev model on a periodic 4×3 cluster. This is the first step in the preparation of simulations using Chebyshev methods.

```
import numpy as np
import pybinding as pb
from pybinding.repository.graphene.constants import a

def spins_honeycomb(Jx, Jy, Jz):
    '''
    Defines the generic nearest neighbour quantum spin model on a honeycomb lattice.
    '''
    # Initialise lattice object with primitive translation vectors
    lat = pb.Lattice( a1=[ -a, 0 ], a2=[ a/2, -a/2 * np.sqrt(3) ] )

    # Initialise sublattices A and B
    lat.add_sublattices(
        ( 'A', a * np.array( [0., 0.] ), [0., 0., 0.] ),
        ( 'B', a * np.array( [1 / 2, np.sqrt(3) / 6] ), [ 0., 0., 0. ] ) )

    # Add three different matrices with input magnetic couplings, i.e. define the model
    # with function inputs.
    lat.register_hopping_energies( { 'Jx': Jx, 'Jy': Jy, 'Jz': Jz } )

    # Add couplings. Arguments are: neighbour coordinates, initial and final sublattice
    # and coupling matrix.
    lat.add_hoppings( ( [0, 0], 'A', 'B', 'Jx' ),
                      ( [1, 0], 'A', 'B', 'Jy' ),
                      ( [1, 1], 'A', 'B', 'Jz' ) )

    return lat

# This definition of coupling matrices yields the pure, isotropic Kitaev model.
Jx, Jy, Jz = np.diag([1, 0, 0]), np.diag([0, 1, 0]), np.diag([0, 0, 1])

# Construct the lattice object
lattice = spins_honeycomb(Jx, Jy, Jz)
```

```

# Construct a 4 x 3 periodic cluster
model = pb.Model( lattice,
                  pb.primitive(4, 3),
                  pb.translational_symmetry(4 * a, 3 * a) )

# Obtain the row, col and data variables, which contain the indices of the
# interacting spins
row = model.system.hoppings.tocoo().row
col = model.system.hoppings.tocoo().col
data = model.system.hoppings.tocoo().data

# Extract three matrices from the lattice object containing the couplings that define the
# model
jx = np.real(model.lattice.hoppings['Jx'].energy)
jy = np.real(model.lattice.hoppings['Jy'].energy)
jz = np.real(model.lattice.hoppings['Jz'].energy)

# This variable contains the sites on the boundaries of the cluster
bounds = model.system.boundaries

# Concatenate arrays of indices for sites in the bulk and boundaries for three different
# nearest neighbour directions
start_idx = np.concatenate([row, bounds[0].hoppings.tocoo().row, bounds[1].hoppings.tocoo(
    ).row, bounds[2].hoppings.tocoo().row])
end_idx = np.concatenate([col, bounds[0].hoppings.tocoo().col, bounds[1].hoppings.tocoo(
    ).col, bounds[2].hoppings.tocoo().col])
bond = np.concatenate([data, bounds[0].hoppings.tocoo().data, bounds[1].hoppings.tocoo().
    data, bounds[2].hoppings.tocoo().data])

print(start_idx)
print(end_idx)
print(bond)
print(jx, jy, jz)

```

In this case, I suppose that I aim to simulate the isotropic honeycomb Kitaev model, so the J_x , J_y , J_z matrices are diagonal with only one nonzero entry. The script generates two arrays of indices labeling each pair of nearest neighbouring sites on the lattice, `start_idx` and `end_idx`. Notice that the `bounds` object contains the indices corresponding to the sites on the boundaries. Moreover, the type of bond is stored in the variable `bond`, which takes on the values 0, 1, 2, corresponding to x -, y - and z -bonds, respectively. Finally, j_x , j_y , j_z are the J_γ matrices, which define the model. The script produces the following output

```

[ 0  1  2  3  4  4  4  5  5  5  6  6  6  7  7  8  8  8  9  9  9 10 10 10
11 11  0  0  1  1  2  2  3  7 11  3]
[12 13 14 15 12 13 16 13 14 17 14 15 18 15 19 16 17 20 17 18 21 18 19 22
19 23 20 21 21 22 22 23 23 12 16 20]
[0 0 0 0 2 1 0 2 1 0 2 1 0 2 0 2 1 0 2 1 0 2 0 2 1 0 2 1 0 2 0 2 1 2 1 2 1 2 1 1 1]
[[1.  0.  0.]
 [0.  0.  0.]
 [0.  0.  0.]] [[0.  0.  0.]
 [0.  1.  0.]
 [0.  0.  0.]] [[0.  0.  0.]
 [0.  0.  0.]
 [0.  0.  0.]

```


[0. 0. 1.]

which can be saved into a file, which in turn is read as an input of my Lanczos, TPQ or Chebyshev codes.

Glossary

Numbers

3BTB three-band tight-binding model. 6, 27, 73–76

A

AF1 edge-antiferromagnetic phase. 76, 79–81, 83–86, 88–90, 147

AF2 edge-dimer. 76, 79–81, 89, 147

AFQSL antiferromagnetic quantum spin liquid. 101, 102

C

CPGF Chebyshev polynomial Green's function method. x–xii, 22, 29, 30, 53, 56–58, 61, 63, 66–68, 95, 99, 100, 103–107, 125–127, 131

CPU central processing unit. ix, 31, 32, 85, 106, 108, 114, 115, 118, 134

D

DetQMC determinant quantum Monte Carlo. iii, x, xi, 2, 3, 5, 21, 25, 28, 73, 74, 76, 77, 79, 81, 84–90, 135

DFT density functional theory. 5

DMRG density matrix renormalisation group. 1, 66, 127, 136

E

ED exact diagonalisation. v, xi, 1, 2, 18, 21, 29, 36, 37, 57, 94, 95, 99–101, 115, 125–127, 131, 135, 136

F

FQSL ferromagnetic quantum spin liquid. xii, 101, 102, 112

FTCP finite temperature Chebyshev polynomial. iii, ix, xii, 22, 61, 63, 94, 95, 108–111, 115, 117–119, 125, 126, 131, 134, 136

FTLM finite temperature Lanczos method. xii, 22, 59, 63, 108–111, 118, 125, 126

H

HLC hybrid Lanczos-Chebyshev. iii, vi, xii, 22, 93, 95, 113, 115, 117, 119, 120, 125, 131, 134, 136

HS Hubbard-Stratonovich. 27, 28

I

iPEPS infinite Projected Entangled Pair States. 1

K

K-H Kitaev-Heisenberg. xii, 18, 19, 93–96, 99, 101, 103, 104, 106, 111–115, 117, 118, 120, 125–127, 136

K-I Kitaev-Ising. xii, 18, 94, 115–120, 123, 125, 136

KPM kernel polynomial method. ix, 22, 29, 39, 43, 44, 46, 57, 58

L

LTLM low-temperature Lanczos method. 59, 60

M

MCLM microcanonical Lanczos method. xi, 22, 51, 99, 100, 103–108, 125, 126

MFT mean field theory. iii, vi, xi, xiii, 1–6, 73, 74, 76, 79, 84, 86, 88–90, 135, 147

MPS Matrix Product States. 66

MR Multiple Relatively Robust Representations. 38, 51, 52, 66

O

OBC open boundary condition. 6

P

PBC periodic boundary condition. xi, 6, 94, 95, 98, 117, 125

Q

QMC quantum Monte Carlo. vi, 1–3, 29, 76, 77, 88, 94, 108, 127, 135, 136

QSL quantum spin liquid. iii, ix, xii, 1, 3, 4, 7, 10, 12–14, 16, 19, 20, 93, 95, 112, 116–119, 121, 135, 136

S

SOC spin-orbit coupling. ix, 8–10, 74

STE stochastic trace evaluation. 29, 31, 49, 59–61, 63, 104

T

TMD transition metal dichalcogenide. ix, 3–8, 74, 79, 86, 90, 136, 147

TPQ thermal pure quantum states. ix, xi, xii, 1, 22, 29, 30, 52, 53, 60, 61, 63, 64, 94, 95, 99–104, 108–111, 115, 117–119, 125–127, 131, 135, 136, 142–144, 151

Z

zGNR zig zag graphene nanoribbon. 4, 5, 73

zTMDNR zig zag transition metal dichalcogenide nanoribbon. iii, vii, x, xiii, 4–6, 8, 21, 73, 74, 77, 78, 89, 90, 135, 147

Bibliography

Below, I list the references in citation order.

1. Carr LD. Understanding Quantum Phase Transitions. 1st ed. CRC Press, 2010 (cited on page 1)
2. Sachdev S. Quantum Phase Transitions. 2nd ed. Cambridge University Press, 2011 (cited on page 1)
3. Chaloupka J, Jackeli G, and Khaliullin G. Kitaev-Heisenberg Model on a Honeycomb Lattice: Possible Exotic Phases in Iridium Oxides A_2IrO_3 . Physical Review Letters. 2010 Jul 9; 105. doi: [10.1103/PhysRevLetters105.027204](https://doi.org/10.1103/PhysRevLetters105.027204) (cited on pages 1, 3, 19, 93–95, 99, 101, 104, 125)
4. Chaloupka J, Jackeli G, and Khaliullin G. Zigzag Magnetic Order in the Iridium Oxide Na_2IrO_3 . Physical Review Letters. 2013 Feb 28; 110:097204. doi: [10.1103/PhysRevLetters110.097204](https://doi.org/10.1103/PhysRevLetters110.097204) (cited on pages 1, 3, 19, 94, 95, 99, 101, 125)
5. Gotfryd D, Rusnačko J, Wohlfeld K, Jackeli G, Chaloupka J, and Oleś AM. Phase diagram and spin correlations of the Kitaev-Heisenberg model: Importance of quantum effects. Physical Review B. 2017 Jan 23; 95:024426. doi: [10.1103/PhysRevB.95.024426](https://doi.org/10.1103/PhysRevB.95.024426) (cited on pages 1, 3, 94–96, 99, 101, 113, 114, 120, 125)
6. Price CC and Perkins NB. Critical Properties of the Kitaev-Heisenberg Model. Physical Review Letters 2012; 109(18):187201. doi: [10.1103/PhysRevLetters109.187201](https://doi.org/10.1103/PhysRevLetters109.187201) (cited on page 1)
7. Nasu J, Udagawa M, and Motome Y. Vaporization of Kitaev Spin Liquids. Physical Review Letters. 2014 Nov 7; 113:197205. doi: [10.1103/PhysRevLetters113.197205](https://doi.org/10.1103/PhysRevLetters113.197205) (cited on pages 1–3)
8. Nasu J, Udagawa M, and Motome Y. Thermal fractionalization of quantum spins in a Kitaev model: Temperature-linear specific heat and coherent transport of Majorana fermions. Physical Review B. 2015 Sep 9; 92:115122. doi: [10.1103/PhysRevB.92.115122](https://doi.org/10.1103/PhysRevB.92.115122) (cited on pages 1–3, 12, 16, 111, 118)
9. Nasu J and Motome Y. Nonequilibrium Majorana dynamics by quenching a magnetic field in Kitaev spin liquids. Physical Review Research. 2019 Oct 3; 1:033007. doi: [10.1103/PhysRevResearch.1.033007](https://doi.org/10.1103/PhysRevResearch.1.033007) (cited on pages 1, 3, 126)
10. Li H, Qu DW, Zhang HK, Jia YZ, Gong SS, Qi Y, and Li W. Universal thermodynamics in the Kitaev fractional liquid. Physical Review Research. 2020 Oct 2; 2:043015. doi: [10.1103/PhysRevResearch.2.043015](https://doi.org/10.1103/PhysRevResearch.2.043015) (cited on pages 1, 95, 101, 108, 125)
11. Hickey C, Berke C, Stavropoulos PP, Kee HY, and Trebst S. Field-driven gapless spin liquid in the spin-1 Kitaev honeycomb model. Physical Review Research. 2020 Jun 18; 2:023361. doi: [10.1103/PhysRevResearch.2.023361](https://doi.org/10.1103/PhysRevResearch.2.023361) (cited on page 1)
12. Bethe H. Zur Theorie der Metalle. Zeitschrift für Physik. 1931 Mar 1; 71:205–26. doi: [10.1007/BF01341708](https://doi.org/10.1007/BF01341708) (cited on pages 1, 21)

13. Lanczos C. An iteration method for the solution of the eigenvalue problem of linear differential and integral operators. *Journal of Research of the National Bureau of Standards* 1950 Oct; 45:255. doi: [10.6028/jres.045.026](https://doi.org/10.6028/jres.045.026) (cited on pages 1, 32, 36)
14. Winter SM, Riedl K, Kaib D, Coldea R, and Valentí R. Probing α -RuCl₃ Beyond Magnetic Order: Effects of Temperature and Magnetic Field. *Physical Review Letters*. 2018 Feb 15; 120:077203. doi: [10.1103/PhysRevLetters120.077203](https://doi.org/10.1103/PhysRevLetters120.077203) (cited on pages 1, 94)
15. Jaklič J and Prelovšek P. Lanczos method for the calculation of finite-temperature quantities in correlated systems. *Physical Review B* 1994 Feb 15; 49:5065–8. doi: [10.1103/PhysRevB.49.5065](https://doi.org/10.1103/PhysRevB.49.5065) (cited on pages 1, 59, 94)
16. Aichhorn M, Daghofer M, Evertz HG, and Linden W von der. Low-temperature Lanczos method for strongly correlated systems. *Physical Review B* 2003 Apr 24; 67:161103. doi: [10.1103/PhysRevB.67.161103](https://doi.org/10.1103/PhysRevB.67.161103) (cited on pages 1, 59, 94)
17. Prelovšek P and Bonča J. Ground State and Finite Temperature Lanczos Methods. *Strongly Correlated Systems: Numerical Methods*. Ed. by Avella A and Mancini F. Springer Series in Solid-State Sciences. Berlin, Heidelberg: Springer, 2013 :1–30. doi: [10.1007/978-3-642-35106-8_1](https://doi.org/10.1007/978-3-642-35106-8_1) (cited on pages 1, 51, 58, 59, 64, 65, 94, 95)
18. Rigol M, Bryant T, and Singh RRP. Numerical Linked-Cluster Approach to Quantum Lattice Models. *Physical Review Letters*. 2006 Nov 3; 97:187202. doi: [10.1103/PhysRevLetters97.187202](https://doi.org/10.1103/PhysRevLetters97.187202) (cited on page 1)
19. Kallin AB, Hyatt K, Singh RRP, and Melko RG. Entanglement at a Two-Dimensional Quantum Critical Point: A Numerical Linked-Cluster Expansion Study. *Physical Review Letters*. 2013 Mar 26; 110:135702. doi: [10.1103/PhysRevLetters110.135702](https://doi.org/10.1103/PhysRevLetters110.135702) (cited on page 1)
20. Devakul T and Singh RR. Early Breakdown of Area-Law Entanglement at the Many-Body Delocalization Transition. *Physical Review Letters*. 2015 Oct 28; 115:187201. doi: [10.1103/PhysRevLetters115.187201](https://doi.org/10.1103/PhysRevLetters115.187201) (cited on page 1)
21. Schäfer R, Hagymási I, Moessner R, and Luitz DJ. Pyrochlore $S = \frac{1}{2}$ Heisenberg antiferromagnet at finite temperature. *Physical Review B*. 2020 Aug 4; 102:054408. doi: [10.1103/PhysRevB.102.054408](https://doi.org/10.1103/PhysRevB.102.054408) (cited on page 1)
22. Richter J, Heitmann T, and Steinigeweg R. Quantum quench dynamics in the transverse-field Ising model: A numerical expansion in linked rectangular clusters. *SciPost Physics* 2020 Sep 3; 9:031. doi: [10.21468/SciPostPhysics9.3.031](https://doi.org/10.21468/SciPostPhysics9.3.031) (cited on page 1)
23. Hagymási I, Schäfer R, Moessner R, and Luitz DJ. Possible Inversion Symmetry Breaking in the $S = 1/2$ Pyrochlore Heisenberg Magnet. *Physical Review Letters*. 2021 Mar 18; 126:117204. doi: [10.1103/PhysRevLetters126.117204](https://doi.org/10.1103/PhysRevLetters126.117204) (cited on page 1)
24. Kuwahara T, Alhambra ÁM, and Anshu A. Improved Thermal Area Law and Quasilinear Time Algorithm for Quantum Gibbs States. *Physical Review X*. 2021 Mar 9; 11:011047. doi: [10.1103/PhysRevX.11.011047](https://doi.org/10.1103/PhysRevX.11.011047) (cited on page 1)
25. Ghorbani E, Tocchio LF, and Becca F. Variational wave functions for the $S = \frac{1}{2}$ Heisenberg model on the anisotropic triangular lattice: Spin liquids and spiral orders. *Physical Review B*. 2016 Feb 5; 93:085111. doi: [10.1103/PhysRevB.93.085111](https://doi.org/10.1103/PhysRevB.93.085111) (cited on pages 1, 2)
26. Sato T and Assaad FF. Quantum Monte Carlo simulation of generalized Kitaev models. *Physical Review B*. 2021 Aug 10; 104:L081106. doi: [10.1103/PhysRevB.104.L081106](https://doi.org/10.1103/PhysRevB.104.L081106) (cited on pages 1, 2)

27. White SR. Density matrix formulation for quantum renormalization groups. *Physical Review Letters*. 1992 Nov 9; 69:2863–6. doi: [10.1103/PhysRevLetters69.2863](https://doi.org/10.1103/PhysRevLetters69.2863) (cited on pages 1, 127)
28. Schollwöck U. The density-matrix renormalization group. *Reviews of Modern Physics*. 2005 Apr 26; 77:259–315. doi: [10.1103/RevModPhysics77.259](https://doi.org/10.1103/RevModPhysics77.259) (cited on pages 1, 127)
29. Hallberg KA. New trends in density matrix renormalization. *Advances in Physics* 2006; 55:477–526. doi: [10.1080/00018730600766432](https://doi.org/10.1080/00018730600766432) (cited on pages 1, 127)
30. Stoudenmire EM and White SR. Studying Two Dimensional Systems With the Density Matrix Renormalization Group. *Annual Review of Condensed Matter Physics*. 2012 Mar; 3:111–28. doi: [10.1146/annurev-conmatphys-020911-125018](https://doi.org/10.1146/annurev-conmatphys-020911-125018) (cited on pages 1, 127)
31. Verstraete F, Murg V, and Cirac J. Matrix product states, projected entangled pair states, and variational renormalization group methods for quantum spin systems. *Advances in Physics* 2008 Mar 1; 57:143–224. doi: [10.1080/14789940801912366](https://doi.org/10.1080/14789940801912366) (cited on page 1)
32. Wietek A, Corboz P, Wessel S, Normand B, Mila F, and Honecker A. Thermodynamic properties of the Shastry-Sutherland model throughout the dimer-product phase. *Physical Review Research*. 2019 Oct 21; 1:033038. doi: [10.1103/PhysRevResearch.1.033038](https://doi.org/10.1103/PhysRevResearch.1.033038) (cited on page 1)
33. Orús R. A practical introduction to tensor networks: Matrix product states and projected entangled pair states. *Annals of Physics*. 2014 Oct 1; 349:117–58. doi: [10.1016/j.aop.2014.06.013](https://doi.org/10.1016/j.aop.2014.06.013) (cited on page 1)
34. Sugiura S and Shimizu A. Thermal Pure Quantum States at Finite Temperature. *Physical Review Letters*. 2012 Jun 11; 108:240401. doi: [10.1103/PhysRevLetters108.240401](https://doi.org/10.1103/PhysRevLetters108.240401) (cited on pages 1, 29, 30, 32, 52, 53, 94, 101, 108, 110, 144, 145)
35. Sugiura S and Shimizu A. Canonical Thermal Pure Quantum State. *Physical Review Letters*. 2013 Jul 1; 111:010401. doi: [10.1103/PhysRevLetters111.010401](https://doi.org/10.1103/PhysRevLetters111.010401) (cited on pages 1, 29, 30, 53, 60, 61, 94, 101)
36. Laurell P and Okamoto S. Dynamical and thermal magnetic properties of the Kitaev spin liquid candidate α -RuCl₃. *npj Quantum Materials* 2020 Jan 10; 5:1–10. doi: [10.1038/s41535-019-0203-y](https://doi.org/10.1038/s41535-019-0203-y) (cited on pages 1, 101)
37. Hu WJ, Gong SS, and Sheng DN. Variational Monte Carlo study of chiral spin liquid in quantum antiferromagnet on the triangular lattice. *Physical Review B*. 2016 Aug 15; 94:075131. doi: [10.1103/PhysRevB.94.075131](https://doi.org/10.1103/PhysRevB.94.075131) (cited on page 2)
38. Wang J, Zhao Q, Wang X, and Liu ZX. Multinode quantum spin liquids on the honeycomb lattice. *Physical Review B*. 2020 Oct 19; 102:144427. doi: [10.1103/PhysRevB.102.144427](https://doi.org/10.1103/PhysRevB.102.144427) (cited on page 2)
39. Troyer M and Wiese UJ. Computational Complexity and Fundamental Limitations to Fermionic Quantum Monte Carlo Simulations. *Physical Review Letters* 2005 May 4; 94:170201. doi: [10.1103/PhysRevLetters94.170201](https://doi.org/10.1103/PhysRevLetters94.170201) (cited on pages 2, 76)
40. Nakamura T. Vanishing of the negative-sign problem of quantum Monte Carlo simulations in one-dimensional frustrated spin systems. *Physical Review B* 1998 Feb; 57:R3197–R3200. doi: [10.1103/PhysRevB.57.R3197](https://doi.org/10.1103/PhysRevB.57.R3197) (cited on page 2)

41. Honecker A, Wessel S, Kerkdyk R, Pruschke T, Mila F, and Normand B. Thermodynamic properties of highly frustrated quantum spin ladders: Influence of many-particle bound states. *Physical Review B* 2016 Feb; 93:054408. doi: [10.1103/PhysRevB.93.054408](https://doi.org/10.1103/PhysRevB.93.054408) (cited on page 2)
42. Alet F, Damle K, and Pujari S. Sign-Problem-Free Monte Carlo Simulation of Certain Frustrated Quantum Magnets. *Physical Review Letters* 2016 Nov; 117:197203. doi: [10.1103/PhysRevLetters117.197203](https://doi.org/10.1103/PhysRevLetters117.197203) (cited on page 2)
43. Li ZX and Yao H. Sign-Problem-Free Fermionic Quantum Monte Carlo: Developments and Applications. *Annual Review of Condensed Matter Physics* 2019; 10:337–56. doi: [10.1146/annurev-conmatphys-033117-054307](https://doi.org/10.1146/annurev-conmatphys-033117-054307) (cited on page 2)
44. Levy R and Clark BK. Mitigating the Sign Problem through Basis Rotations. *Physical Review Letters* 2021 May 24; 126:216401. doi: [10.1103/PhysRevLetters126.216401](https://doi.org/10.1103/PhysRevLetters126.216401) (cited on page 2)
45. Huang XX, Moritz B, Claassen M, and Devereaux TP. Sign-free determinant quantum Monte Carlo study of excitonic density orders in a two-orbital Hubbard-Kanamori model. *Physical Review B*. 2022 Apr 15; 105:165124. doi: [10.1103/PhysRevB.105.165124](https://doi.org/10.1103/PhysRevB.105.165124) (cited on pages 2, 27)
46. Weber L, Honecker A, Normand B, Corboz P, Mila F, and Wessel S. Quantum Monte Carlo simulations in the trimer basis: first-order transitions and thermal critical points in frustrated trilayer magnets. en. *SciPost Physics* 2022 Feb; 12:054. doi: [10.21468/SciPostPhysics12.2.054](https://doi.org/10.21468/SciPostPhysics12.2.054) (cited on page 2)
47. Hen I. Resolution of the sign problem for a frustrated triplet of spins. *Physical Review E* 2019 Mar 29; 99:033306. doi: [10.1103/PhysRevE.99.033306](https://doi.org/10.1103/PhysRevE.99.033306) (cited on page 2)
48. Brito FMO, Li L, Lopes JMVP, and Castro EV. Edge magnetism in transition metal dichalcogenide nanoribbons: Mean field theory and determinant quantum Monte Carlo. *Physical Review B* 2022 May 20; 105:195130. doi: [10.1103/PhysRevB.105.195130](https://doi.org/10.1103/PhysRevB.105.195130) (cited on page 2)
49. Witzak-Krempa W, Chen G, Kim YB, and Balents L. Correlated Quantum Phenomena in the Strong Spin-Orbit Regime. *Annual Review of Condensed Matter Physics* 2014; 5:57–82. doi: [10.1146/annurev-conmatphys-020911-125138](https://doi.org/10.1146/annurev-conmatphys-020911-125138) (cited on pages 3, 8, 9)
50. Rau JG, Lee EKH, and Kee HY. Spin-Orbit Physics Giving Rise to Novel Phases in Correlated Systems: Iridates and Related Materials. *Annual Review of Condensed Matter Physics* 2016; 7:195–221. doi: [10.1146/annurev-conmatphys-031115-011319](https://doi.org/10.1146/annurev-conmatphys-031115-011319) (cited on pages 3, 8, 10, 11, 18)
51. Savary L and Balents L. Quantum spin liquids: a review. *Reports on Progress in Physics*. 2016 Nov; 80:016502. doi: [10.1088/0034-4885/80/1/016502](https://doi.org/10.1088/0034-4885/80/1/016502) (cited on pages 3, 8, 12, 13, 93)
52. Winter SM, Tsirlin AA, Daghofer M, Brink Jvd, Singh Y, Gegenwart P, and Valentí R. Models and materials for generalized Kitaev magnetism. en. *Journal of Physics: Condensed Matter* 2017 Nov; 29:493002. doi: [10.1088/1361-648X/aa8cf5](https://doi.org/10.1088/1361-648X/aa8cf5) (cited on pages 3, 8, 11, 18)
53. Hermanns M, Kimchi I, and Knolle J. Physics of the Kitaev Model: Fractionalization, Dynamic Correlations, and Material Connections. *Annual Review of Condensed Matter Physics*. 2018 Mar 10; 9:17–33. doi: [10.1146/annurev-conmatphys-033117-053934](https://doi.org/10.1146/annurev-conmatphys-033117-053934) (cited on pages 3, 8, 12, 93)
54. Motome Y and Nasu J. Hunting Majorana Fermions in Kitaev Magnets. *Journal of the Physical Society of Japan* 2020 Jan; 89:012002. doi: [10.7566/JPSJ.89.012002](https://doi.org/10.7566/JPSJ.89.012002) (cited on pages 3, 8, 10, 14, 16, 18, 20, 93, 131)

55. Trebst S and Hickey C. Kitaev materials. *Physics Reports*. Kitaev materials 2022 Mar 4; 950:1–37. doi: [10.1016/j.physrep.2021.11.003](https://doi.org/10.1016/j.physrep.2021.11.003) (cited on pages 3, 8–10, 13, 93)
56. Kitaev A. Anyons in an exactly solved model and beyond. *Annals of Physics*. January Special Issue 2006 Jan 1; 321:2–111. doi: [10.1016/j.aop.2005.10.005](https://doi.org/10.1016/j.aop.2005.10.005) (cited on pages 3, 7, 21, 93)
57. Rau JG, Lee EKH, and Kee HY. Generic Spin Model for the Honeycomb Iridates beyond the Kitaev Limit. *Physical Review Letters* 2014 Feb; 112:077204. doi: [10.1103/PhysRevLetters112.077204](https://doi.org/10.1103/PhysRevLetters112.077204) (cited on pages 3, 18, 19)
58. Kitagawa K, Takayama T, Matsumoto Y, Kato A, Takano R, Kishimoto Y, Bette S, Dinnebier R, Jackeli G, and Takagi H. A spin–orbital-entangled quantum liquid on a honeycomb lattice. *en. Nature* 2018 Feb; 554:341–5. doi: [10.1038/nature25482](https://doi.org/10.1038/nature25482) (cited on pages 3, 12, 13)
59. Nasu J, Kato Y, Yoshitake J, Kamiya Y, and Motome Y. Spin-Liquid-to-Spin-Liquid Transition in Kitaev Magnets Driven by Fractionalization. *Physical Review Letters* 2017 Mar 31; 118:137203. doi: [10.1103/PhysRevLetters118.137203](https://doi.org/10.1103/PhysRevLetters118.137203) (cited on pages 3, 94, 115–120, 125)
60. Hickey C and Trebst S. Emergence of a field-driven U(1) spin liquid in the Kitaev honeycomb model. *en. Nature Communications* 2019 Jan; 10:530. doi: [10.1038/s41467-019-08459-9](https://doi.org/10.1038/s41467-019-08459-9) (cited on page 3)
61. Nasu J and Motome Y. Spin dynamics in the Kitaev model with disorder: Quantum Monte Carlo study of dynamical spin structure factor, magnetic susceptibility, and NMR relaxation rate. *Physical Review B*. 2021 Jul 8; 104:035116. doi: [10.1103/PhysRevB.104.035116](https://doi.org/10.1103/PhysRevB.104.035116) (cited on pages 3, 94)
62. Fujita M, Wakabayashi K, Nakada K, and Kusakabe K. Peculiar Localized State at Zigzag Graphite Edge. *Journal of the Physical Society of Japan* 1996 Jul 15; 65:1920–3. doi: [10.1143/JPSJ.65.1920](https://doi.org/10.1143/JPSJ.65.1920) (cited on page 4)
63. Feldner H, Meng ZY, Honecker A, Cabra D, Wessel S, and Assaad FF. Magnetism of finite graphene samples: Mean-field theory compared with exact diagonalization and quantum Monte Carlo simulations. *Physical Review B* 2010 Mar 11; 81:115416. doi: [10.1103/PhysRevB.81.115416](https://doi.org/10.1103/PhysRevB.81.115416) (cited on pages 4–6, 76)
64. Feldner H, Meng ZY, Lang TC, Assaad FF, Wessel S, and Honecker A. Dynamical Signatures of Edge-State Magnetism on Graphene Nanoribbons. *Physical Review Letters* 2011 May 31; 106:226401. doi: [10.1103/PhysRevLetters106.226401](https://doi.org/10.1103/PhysRevLetters106.226401) (cited on pages 4, 5)
65. Manzeli S, Ovchinnikov D, Pasquier D, Yazyev OV, and Kis A. 2D transition metal dichalcogenides. *Nature Reviews Materials* 2017 Aug; 2:17033. doi: [10.1038/natrevmats.2017.33](https://doi.org/10.1038/natrevmats.2017.33) (cited on page 4)
66. Radisavljevic B, Radenovic A, Brivio J, Giacometti V, and Kis A. Single-layer MoS₂ transistors. *Nature Nanotechnology* 2011 Mar; 6:147–50. doi: [10.1038/nnano.2010.279](https://doi.org/10.1038/nnano.2010.279) (cited on page 4)
67. Koppens FHL, Mueller T, Avouris P, Ferrari AC, Vitiello MS, and Polini M. Photodetectors based on graphene, other two-dimensional materials and hybrid systems. *Nature Nanotechnology* 2014 Oct; 9:780–93. doi: [10.1038/nnano.2014.215](https://doi.org/10.1038/nnano.2014.215) (cited on page 4)
68. Mak KF and Shan J. Photonics and optoelectronics of 2D semiconductor transition metal dichalcogenides. *Nature Photonics* 2016 Apr; 10:216–26. doi: [10.1038/nphoton.2015.282](https://doi.org/10.1038/nphoton.2015.282) (cited on page 4)
69. Zhang Y, Tang TT, Girit C, Hao Z, Martin MC, Zettl A, Crommie MF, Shen YR, and Wang F. Direct observation of a widely tunable bandgap in bilayer graphene. *Nature* 2009 Jun; 459:820–3. doi: [10.1038/nature08105](https://doi.org/10.1038/nature08105) (cited on page 4)

70. Mak KF, Lee C, Hone J, Shan J, and Heinz TF. Atomically Thin MoS₂: A New Direct-Gap Semiconductor. *Physical Review Letters* 2010 Sep 24; 105:136805. doi: [10.1103/PhysRevLetters105.136805](https://doi.org/10.1103/PhysRevLetters105.136805) (cited on page 4)
71. Tian H, Chin ML, Najmaei S, Guo Q, Xia F, Wang H, and Dubey M. Optoelectronic devices based on two-dimensional transition metal dichalcogenides. *Nano Research* 2016 Jun 1; 9:1543–60. doi: [10.1007/s12274-016-1034-9](https://doi.org/10.1007/s12274-016-1034-9) (cited on page 4)
72. Khan M and Leuenberger MN. Optoelectronics with single layer group-VIB transition metal dichalcogenides. *Nanophotonics* 2018; 7:1589–600. doi: [10.1515/nanoph-2018-0041](https://doi.org/10.1515/nanoph-2018-0041) (cited on page 4)
73. Barthelmi K, Klein J, Hötger A, Sigl L, Sigger F, Mitterreiter E, Rey S, Gyger S, Lorke M, Florian M, Jahnke F, Taniguchi T, Watanabe K, Zwiller V, Jöns KD, Wurstbauer U, Kastl C, Weber-Bargioni A, Finley JJ, Müller K, and Holleitner AW. Atomistic defects as single-photon emitters in atomically thin MoS₂. *Applied Physics Letters* 2020; 117:070501. doi: [https://doi/10.1063/5.0018557](https://doi.org/10.1063/5.0018557) (cited on page 4)
74. Xiao D, Liu GB, Feng W, Xu X, and Yao W. Coupled Spin and Valley Physics in Monolayers of MoS₂ and Other Group-VI Dichalcogenides. *Physical Review Letters* 2012 May 7; 108:196802. doi: [10.1103/PhysRevLetters108.196802](https://doi.org/10.1103/PhysRevLetters108.196802) (cited on page 4)
75. Schaibley JR, Yu H, Clark G, Rivera P, Ross JS, Seyler KL, Yao W, and Xu X. Valleytronics in 2D materials. *Nature Review Materials* 2016 Nov; 1:16055. doi: [10.1038/natrevmats.2016.55](https://doi.org/10.1038/natrevmats.2016.55) (cited on page 4)
76. Enaldiev VV. Edge states and spin-valley edge photocurrent in transition metal dichalcogenide monolayers. *Physical Review B* 2017 Dec 21; 96:235429. doi: [10.1103/PhysRevB.96.235429](https://doi.org/10.1103/PhysRevB.96.235429) (cited on page 4)
77. Ciccario CJ, Christensen T, Sundararaman R, and Narang P. Dynamics and Spin-Valley Locking Effects in Monolayer Transition Metal Dichalcogenides. *Nano Letters* 2018 Sep 12; 18:5709–15. doi: [10.1021/acs.nanolett.8b02300](https://doi.org/10.1021/acs.nanolett.8b02300) (cited on page 4)
78. Zhou BT, Taguchi K, Kawaguchi Y, Tanaka Y, and Law KT. Spin-orbit coupling induced valley Hall effects in transition-metal dichalcogenides. *Communications Physics* 2019 Mar 1; 2:26. doi: [10.1038/s42005-019-0127-7](https://doi.org/10.1038/s42005-019-0127-7) (cited on page 4)
79. Molas MR, Slobodeniuk AO, Kazimierczuk T, Nogajewski K, Bartos M, Kapuściński P, Oreszczuk K, Watanabe K, Taniguchi T, Faugeras C, Kossacki P, Basko DM, and Potemski M. Probing and Manipulating Valley Coherence of Dark Excitons in Monolayer WSe₂. *Physical Review Letters* 2019; 123(9):096803. doi: [10.1103/PhysRevLetters123.096803](https://doi.org/10.1103/PhysRevLetters123.096803) (cited on page 4)
80. Wakabayashi K, Sigrist M, and Fujita M. Spin Wave Mode of Edge-Localized Magnetic States in Nanographite Zigzag Ribbons. *Journal of the Physical Society of Japan* 1998 Jun 15; 67:2089–93. doi: [10.1143/JPSJ.67.2089](https://doi.org/10.1143/JPSJ.67.2089) (cited on page 4)
81. Yamashiro A, Shimoi Y, Harigaya K, and Wakabayashi K. Spin- and charge-polarized states in nanographene ribbons with zigzag edges. *Physical Review B* 2003 Nov 20; 68:193410. doi: [10.1103/PhysRevB.68.193410](https://doi.org/10.1103/PhysRevB.68.193410) (cited on page 4)
82. Son YW, Cohen ML, and Louie SG. Half-metallic graphene nanoribbons. *Nature* 2006 Nov; 444:347. doi: [10.1038/nature05180](https://doi.org/10.1038/nature05180) (cited on page 4)
83. Son YW, Cohen ML, and Louie SG. Energy Gaps in Graphene Nanoribbons. *Physical Review Letters* 2006 Nov 22; 97:216803. doi: [10.1103/PhysRevLetters97.216803](https://doi.org/10.1103/PhysRevLetters97.216803) (cited on page 4)

84. Rudberg E, Sałek P, and Luo Y. Nonlocal Exchange Interaction Removes Half-Metallicity in Graphene Nanoribbons. *Nano Letters* 2007 Aug 8; 7:2211–3. doi: [10.1021/nl070593c](https://doi.org/10.1021/nl070593c) (cited on page 4)
85. Hod O, Barone V, Peralta JE, and Scuseria GE. Enhanced Half-Metallicity in Edge-Oxidized Zigzag Graphene Nanoribbons. *Nano Letters* 2007 Aug 8; 7:2295–9. doi: [10.1021/nl0708922](https://doi.org/10.1021/nl0708922) (cited on page 4)
86. Fernández-Rossier J. Prediction of hidden multiferroic order in graphene zigzag ribbons. *Physical Review B* 2008 Feb 27; 77:075430. doi: [10.1103/PhysRevB.77.075430](https://doi.org/10.1103/PhysRevB.77.075430) (cited on page 4)
87. Jia X, Hofmann M, Meunier V, Sumpter BG, Campos-Delgado J, Romo-Herrera JM, Son H, Hsieh YP, Reina A, Kong J, Terrones M, and Dresselhaus MS. Controlled formation of sharp zigzag and armchair edges in graphitic nanoribbons. *Science* 2009; 323:1701–5. doi: [10.1126/science.1166862](https://doi.org/10.1126/science.1166862) (cited on page 4)
88. Jiao L, Zhang L, Wang X, Diankov G, and Dai H. Narrow Graphene Nanoribbons from Carbon Nanotubes. *Nature* 2009; 458:877–80. doi: <https://doi.org/10.1038/nature07919> (cited on page 4)
89. Tao C, Jiao L, Yazyev OV, Chen YC, Feng J, Zhang X, Capaz RB, Tour JM, Zettl A, Louie SG, Dai H, and Crommie MF. Spatially Resolving Spin-Split Edge States of Chiral Graphene Nanoribbons. *Nature Physics* 2011; 7:616–20. doi: <https://doi.org/10.1038/nphys1991> (cited on page 4)
90. Nair RR, Sepioni M, Tsai IL, Lehtinen O, Keinonen J, Krasheninnikov AV, Thomson T, Geim AK, and Grigorieva IV. Spin-half paramagnetism in graphene induced by point defects. *Nature Physics* 2012; 8:199–202. doi: [10.1038/nphys2183](https://doi.org/10.1038/nphys2183) (cited on page 5)
91. Chen C, Lin Y, Zhou W, Gong M, He Z, Shi F, Li X, Wu JZ, Lam KT, Wang JN, Yang F, Zeng Q, Guo J, Gao W, Zuo JM, Liu J, Hong G, Antaris AL, Lin MC, Mao WL, and Dai H. Sub-10-nm graphene nanoribbons with atomically smooth edges from squashed carbon nanotubes. *Nature Electronics* 2021; 4:653–63. doi: [10.1038/s41928-021-00633-6](https://doi.org/10.1038/s41928-021-00633-6) (cited on page 5)
92. Pizzochero M and Kaxiras E. Imprinting Tunable π -Magnetism in Graphene Nanoribbons via Edge Extensions. *Journal of Physical Chemistry Letters* 2021; 12:1214–9. doi: [10.1021/acs.jpclett.0c03677](https://doi.org/10.1021/acs.jpclett.0c03677) (cited on page 5)
93. Chen Y, Cui P, Ren X, Zhang C, Jin C, Zhang Z, and Shih CK. Fabrication of MoSe₂ nanoribbons via an unusual morphological phase transition. *Nature Communications* 2017 May 4; 8:15135. doi: [10.1038/ncomms15135](https://doi.org/10.1038/ncomms15135) (cited on page 5)
94. Cheng F, Xu H, Xu W, Zhou P, Martin J, and Loh KP. Controlled Growth of 1D MoSe₂ Nanoribbons with Spatially Modulated Edge States. *Nano Letters* 2017; 17:1116–20. doi: [10.1021/acs.nanolett.6b04715](https://doi.org/10.1021/acs.nanolett.6b04715) (cited on page 5)
95. Li S, Lin YC, Zhao W, Wu J, Wang Z, Hu Z, Shen Y, Tang DM, Wang J, Zhang Q, Zhu H, Chu L, Zhao W, Liu C, Sun Z, Taniguchi T, Osada M, Chen W, Xu QH, Wee ATS, Suenaga K, Ding F, and Eda G. Vapour–liquid–solid growth of monolayer MoS₂ nanoribbons. *Nature Materials* 2018; 17:535–42. doi: [10.1038/s41563-018-0055-z](https://doi.org/10.1038/s41563-018-0055-z) (cited on page 5)
96. Wang Z, Zhang X, Hachtel JA, Apte A, Tiwary CS, Vajtai R, Idrobo JC, Ozturk R, and Ajayan P. Etching of transition metal dichalcogenide monolayers into nanoribbon arrays. *Nanoscale Horizons* 2019; 4(3):689–96. doi: [10.1039/C8NH00364E](https://doi.org/10.1039/C8NH00364E) (cited on page 5)

97. Yang C, Wang B, Xie Y, Zheng Y, and Jin C. Deriving MoS₂ nanoribbons from their flakes by chemical vapor deposition. *Nanotechnology* 2019; 30:255602. doi: [10.1088/1361-6528/ab0a1d](https://doi.org/10.1088/1361-6528/ab0a1d) (cited on page 5)
98. Munkhbat B, Yankovich AB, Baranov DG, Verre R, Olsson E, and Shegai TO. Transition metal dichalcogenide metamaterials with atomic precision. *Nature Communications* 2020; 11:4604. doi: [10.1038/s41467-020-18428-2](https://doi.org/10.1038/s41467-020-18428-2) (cited on page 5)
99. Mao X, Xu Y, Xue Q, Wang W, and Gao D. Ferromagnetism in exfoliated tungsten disulfide nanosheets. *Nanoscale Research Letters* 2013; 8:430. doi: [10.1186/1556-276X-8-430](https://doi.org/10.1186/1556-276X-8-430) (cited on page 5)
100. Gao D, Si M, Li J, Zhang J, Zhang Z, Yang Z, and Xue D. Ferromagnetism in freestanding MoS₂ nanosheets. *Nanoscale Research Letters* 2013; 8:129. doi: [10.1186/1556-276X-8-129](https://doi.org/10.1186/1556-276X-8-129) (cited on page 5)
101. Yang Z, Gao D, Zhang J, Xu Q, Shi S, Tao K, and Xue D. Realization of high Curie temperature ferromagnetism in atomically thin MoS₂ and WS₂ nanosheets with uniform and flower-like morphology. *Nanoscale* 2015; 7:650–8. doi: [10.1039/c4nr06141a](https://doi.org/10.1039/c4nr06141a) (cited on page 5)
102. Zhang R, Li Y, Qi J, and Gao D. Ferromagnetism in ultrathin MoS₂ nanosheets: from amorphous to crystalline. *Nanoscale Research Letters* 2014; 9:586. doi: <https://doi.org/10.1186/1556-276X-9-586> (cited on page 5)
103. Huo N, Li Y, Kang J, Li R, Xia Q, and Li J. Edge-states ferromagnetism of WS₂ nanosheets. *Applied Physics Letters* 2014; 104:202406. doi: <https://doi.org/10.1063/1.4875582> (cited on page 5)
104. Kondo G, Yokoyama N, Yamada S, Hashimoto Y, Ohata C, Katsumoto S, and Haruyama J. Edge-spin-derived magnetism in few-layer MoS₂ nanomeshes. *AIP Advances* 2017; 7:125019. doi: [10.1063/1.4989477](https://doi.org/10.1063/1.4989477) (cited on page 5)
105. Sarma S, Ghosh B, Ray SC, Wang HT, Mahule TS, and Pong WF. Electronic structure and magnetic behaviors of exfoliated MoS₂ nanosheets. *Journal of Physics: Condensed Matter* 2019; 31:135501. doi: [10.1088/1361-648X/aafc12](https://doi.org/10.1088/1361-648X/aafc12) (cited on page 5)
106. Gao G, Chen C, Xie X, Su Y, Kang S, Zhu G, Gao D, Trampert A, and Cai L. Toward edges-rich MoS₂ layers via chemical liquid exfoliation triggering distinctive magnetism. *Materials Research Letters* 2017; 5:267–75. doi: [10.1080/21663831.2016.1256915](https://doi.org/10.1080/21663831.2016.1256915) (cited on page 5)
107. Braz JEH, Amorim B, and Castro EV. Valley-polarized magnetic state in hole-doped monolayers of transition-metal dichalcogenides. *Physical Review B* 2018 Oct 18; 98:161406. doi: [10.1103/PhysRevB.98.161406](https://doi.org/10.1103/PhysRevB.98.161406) (cited on page 5)
108. Bollinger MV, Lauritsen JV, Jacobsen KW, Nørskov JK, Helveg S, and Besenbacher F. One-Dimensional Metallic Edge States in MoS₂. *Physical Review Letters* 2001 Oct 18; 87:196803. doi: [10.1103/PhysRevLetters87.196803](https://doi.org/10.1103/PhysRevLetters87.196803) (cited on page 5)
109. Bollinger MV, Jacobsen KW, and Nørskov JK. Atomic and electronic structure of MoS₂ nanoparticles. *Physical Review B* 2003 Feb 18; 67:085410. doi: [10.1103/PhysRevB.67.085410](https://doi.org/10.1103/PhysRevB.67.085410) (cited on page 5)
110. Li Y, Zhou Z, Zhang S, and Chen Z. MoS₂ Nanoribbons: High Stability and Unusual Electronic and Magnetic Properties. *Journal of the American Chemical Society* 2008; 130:16739. doi: [10.1021/ja805545x](https://doi.org/10.1021/ja805545x) (cited on page 5)

111. Vojvodic A, Hinnemann B, and Nørskov JK. Magnetic edge states in MoS₂ characterized using density-functional theory. *Physical Review B* 2009 Sep 18; 80:125416. doi: [10.1103/PhysRevB.80.125416](https://doi.org/10.1103/PhysRevB.80.125416) (cited on page 5)
112. Botello-Méndez AR, López-Urías F, Terrones M, and Terrones H. Metallic and ferromagnetic edges in molybdenum disulfide nanoribbons. *Nanotechnology* 2009 Jul; 20:325703. doi: [10.1088/0957-4484/20/32/325703](https://doi.org/10.1088/0957-4484/20/32/325703) (cited on page 5)
113. Pan H and Zhang YW. Edge-dependent structural, electronic and magnetic properties of MoS₂ nanoribbons. *Journal of Materials Chemistry* 2012; 22(15):7280–90. doi: [10.1039/C2JM15906F](https://doi.org/10.1039/C2JM15906F) (cited on page 5)
114. Kou L, Tang C, Zhang Y, Heine T, Chen C, and Frauenheim T. Tuning Magnetism and Electronic Phase Transitions by Strain and Electric Field in Zigzag MoS₂ Nanoribbons. *Journal of Physical Chemistry Letters* 2012 Oct 18; 3:2934–41. doi: [10.1021/jz301339e](https://doi.org/10.1021/jz301339e) (cited on page 5)
115. López-Urías F, Laura Elías A, Perea-López N, Gutiérrez HR, Terrones M, and Terrones H. Electronic, magnetic, optical, and edge-reactivity properties of semiconducting and metallic WS₂ nanoribbons. *2D Materials* 2015; 2:015002. doi: [10.1088/2053-1583/2/1/015002](https://doi.org/10.1088/2053-1583/2/1/015002) (cited on page 5)
116. Cui P, Choi JH, Chen W, Zeng J, Shih CK, Li Z, and Zhang Z. Contrasting Structural Reconstructions, Electronic Properties, and Magnetic Orderings along Different Edges of Zigzag Transition Metal Dichalcogenide Nanoribbons. *Nano Letters* 2017; 17:1097–101. doi: [10.1021/acs.nanolett.6b04638](https://doi.org/10.1021/acs.nanolett.6b04638) (cited on page 5)
117. Vancsó P, Hagymási I, Castenetto P, and Lambin P. Stability of edge magnetism against disorder in zigzag MoS₂ nanoribbons. *Physical Review Materials* 2019; 3:094003. doi: [10.1103/PhysRevMaterials.3.094003](https://doi.org/10.1103/PhysRevMaterials.3.094003) (cited on page 5)
118. Yang G, Xu S, Zhang W, Ma T, and Wu C. Room-temperature magnetism on the zigzag edges of phosphorene nanoribbons. *Physical Review B* 2016 Aug 3; 94:075106. doi: [10.1103/PhysRevB.94.075106](https://doi.org/10.1103/PhysRevB.94.075106) (cited on pages 5, 76)
119. Raczkowski M and Assaad FF. Interplay between the edge-state magnetism and long-range Coulomb interaction in zigzag graphene nanoribbons: Quantum Monte Carlo study. *Physical Review B* 2017 Sep 26; 96:115155. doi: [10.1103/PhysRevB.96.115155](https://doi.org/10.1103/PhysRevB.96.115155) (cited on pages 5, 76)
120. Yang G, Li B, Zhang W, Ye M, and Ma T. Strain-tuning of edge magnetism in zigzag graphene nanoribbons. *Journal of Physics: Condensed Matter* 2017 Aug; 29:365601. doi: [10.1088/1361-648X/aa7dc1](https://doi.org/10.1088/1361-648X/aa7dc1) (cited on pages 5, 76)
121. Shin D, Tancogne-Dejean N, Zhang J, Okyay MS, Rubio A, and Park N. Identification of the Mott Insulating Charge Density Wave State in 1 T-TaS₂. *Physical Review Letters* 2021; 126:196406. doi: [10.1103/PhysRevLetters126.196406](https://doi.org/10.1103/PhysRevLetters126.196406) (cited on page 5)
122. Liu GB, Shan WY, Yao Y, Yao W, and Xiao D. Three-band tight-binding model for monolayers of group-VIB transition metal dichalcogenides. *Physical Review B* 2013 Aug 26; 88:085433. doi: [10.1103/PhysRevB.88.085433](https://doi.org/10.1103/PhysRevB.88.085433) (cited on pages 6, 73, 74)
123. Dagotto E, Hotta T, and Moreo A. Colossal magnetoresistant materials: the key role of phase separation. *Physics Reports* 2001; 344:1–153. doi: [https://doi.org/10.1016/S0370-1573\(00\)00121-6](https://doi.org/10.1016/S0370-1573(00)00121-6) (cited on page 7)

124. Ribic T, Assmann E, Tóth A, and Held K. Cubic interaction parameters for t_{2g} Wannier orbitals. *Physical Review B* 2014; 90(16):165105. doi: [10.1103/PhysRevB.90.165105](https://doi.org/10.1103/PhysRevB.90.165105) (cited on page 7)
125. Nayak C, Simon SH, Stern A, Freedman M, and Das Sarma S. Non-Abelian anyons and topological quantum computation. *Reviews of Modern Physics* 2008 Sep; 80:1083–159. doi: [10.1103/RevModPhysics80.1083](https://doi.org/10.1103/RevModPhysics80.1083) (cited on page 7)
126. Andersen TI et al. Non-Abelian braiding of graph vertices in a superconducting processor. *Nature* 2023 Jun; 618:264–9. doi: [10.1038/s41586-023-05954-4](https://doi.org/10.1038/s41586-023-05954-4) (cited on page 7)
127. Jackeli G and Khaliullin G. Mott Insulators in the Strong Spin-Orbit Coupling Limit: From Heisenberg to a Quantum Compass and Kitaev Models. *Physical Review Letters* 2009 Jan; 102:017205. doi: [10.1103/PhysRevLetters102.017205](https://doi.org/10.1103/PhysRevLetters102.017205) (cited on pages 7, 10, 11)
128. Singh Y and Johnston DC. Singlet ground state in the spin- $\frac{1}{2}$ dimer compound $\text{Sr}_3\text{Cr}_2\text{O}_8$. *Physical Review B* 2007 Jul; 76:012407. doi: [10.1103/PhysRevB.76.012407](https://doi.org/10.1103/PhysRevB.76.012407) (cited on page 8)
129. Okamoto Y, Nohara M, Aruga-Katori H, and Takagi H. Spin-Liquid State in the $S = 1/2$ Hyperkagome Antiferromagnet $\text{Na}_4\text{Ir}_3\text{O}_8$. *Physical Review Letters* 2007 Sep; 99:137207. doi: [10.1103/PhysRevLetters99.137207](https://doi.org/10.1103/PhysRevLetters99.137207) (cited on page 8)
130. Singh Y, Manni S, Reuther J, Berlijn T, Thomale R, Ku W, Trebst S, and Gegenwart P. Relevance of the Heisenberg-Kitaev Model for the Honeycomb Lattice Iridates A_2IrO_3 . *Physical Review Letters* 2012 Mar; 108:127203. doi: [10.1103/PhysRevLetters108.127203](https://doi.org/10.1103/PhysRevLetters108.127203) (cited on page 8)
131. Modic KA, Smidt TE, Kimchi I, Breznay NP, Biffin A, Choi S, Johnson RD, Coldea R, Watkins-Curry P, McCandless GT, Chan JY, Gandara F, Islam Z, Vishwanath A, Shekhter A, McDonald RD, and Analytis JG. Realization of a three-dimensional spin–anisotropic harmonic honeycomb iridate. *Nature Communications* 2014 Jun; 5:4203. doi: [10.1038/ncomms5203](https://doi.org/10.1038/ncomms5203) (cited on page 8)
132. Plumb KW, Clancy JP, Sandilands LJ, Shankar VV, Hu YF, Burch KS, Kee HY, and Kim YJ. $\alpha - \text{RuCl}_3$: A spin-orbit assisted Mott insulator on a honeycomb lattice. *Physical Review B* 2014 Jul; 90:041112. doi: [10.1103/PhysRevB.90.041112](https://doi.org/10.1103/PhysRevB.90.041112) (cited on page 8)
133. Takayama T, Kato A, Dinnebier R, Nuss J, Kono H, Veiga LSI, Fabbris G, Haskel D, and Takagi H. Hyperhoneycomb Iridate $\beta - \text{Li}_2\text{IrO}_3$ as a Platform for Kitaev Magnetism. *Physical Review Letters* 2015 Feb; 114:077202. doi: [10.1103/PhysRevLetters114.077202](https://doi.org/10.1103/PhysRevLetters114.077202) (cited on page 8)
134. Norman MR. Colloquium: Herbertsmithite and the search for the quantum spin liquid. *Reviews of Modern Physics* 2016 Dec; 88:041002. doi: [10.1103/RevModPhysics88.041002](https://doi.org/10.1103/RevModPhysics88.041002) (cited on page 8)
135. Yamada MG, Fujita H, and Oshikawa M. Designing Kitaev Spin Liquids in Metal-Organic Frameworks. *Physical Review Letters* 2017 Aug; 119:057202. doi: [10.1103/PhysRevLetters119.057202](https://doi.org/10.1103/PhysRevLetters119.057202) (cited on page 8)
136. Zhou Y, Kanoda K, and Ng TK. Quantum spin liquid states. *Reviews of Modern Physics* 2017 Apr; 89:025003. doi: [10.1103/RevModPhysics89.025003](https://doi.org/10.1103/RevModPhysics89.025003) (cited on page 8)
137. Zare MH and Mosadeq H. Spin liquid in twisted homobilayers of group-VI dichalcogenides. *Physical Review B* 2021 Sep; 104:115154. doi: [10.1103/PhysRevB.104.115154](https://doi.org/10.1103/PhysRevB.104.115154) (cited on page 8)

138. Kiese D, He Y, Hickey C, Rubio A, and Kennes DM. TMDs as a platform for spin liquid physics: A strong coupling study of twisted bilayer WSe₂. *APL Materials* 2022 Mar; 10:031113. doi: [10.1063/5.0077901](https://doi.org/10.1063/5.0077901) (cited on page 8)
139. Hasan MZ and Kane CL. Colloquium: Topological insulators. *Reviews of Modern Physics* 2010 Nov; 82:3045–67. doi: [10.1103/RevModPhysics82.3045](https://doi.org/10.1103/RevModPhysics82.3045) (cited on page 9)
140. Qi XL and Zhang SC. Topological insulators and superconductors. *Reviews of Modern Physics* 2011 Oct; 83:1057–110. doi: [10.1103/RevModPhysics83.1057](https://doi.org/10.1103/RevModPhysics83.1057) (cited on page 9)
141. Yan B and Felser C. Topological Materials: Weyl Semimetals. *Annual Review of Condensed Matter Physics* 2017; 8:337–54. doi: [10.1146/annurev-conmatphys-031016-025458](https://doi.org/10.1146/annurev-conmatphys-031016-025458) (cited on page 9)
142. Winter SM, Li Y, Jeschke HO, and Valentí R. Challenges in design of Kitaev materials: Magnetic interactions from competing energy scales. *Physical Review B* 2016 Jun; 93:214431. doi: [10.1103/PhysRevB.93.214431](https://doi.org/10.1103/PhysRevB.93.214431) (cited on pages 11, 18)
143. Nasu J, Knolle J, Kovrizhin DL, Motome Y, and Moessner R. Fermionic response from fractionalization in an insulating two-dimensional magnet. *Nature Physics* 2016 Oct; 12:912–5. doi: [10.1038/nphys3809](https://doi.org/10.1038/nphys3809) (cited on page 12)
144. Anderson PW. Resonating valence bonds: A new kind of insulator? *Materials Research Bulletin* 1973 Feb; 8:153–60. doi: [10.1016/0025-5408\(73\)90167-0](https://doi.org/10.1016/0025-5408(73)90167-0) (cited on page 12)
145. White SR and Chernyshev AL. Néel Order in Square and Triangular Lattice Heisenberg Models. *Physical Review Letters* 2007 Sep; 99:127004. doi: [10.1103/PhysRevLetters99.127004](https://doi.org/10.1103/PhysRevLetters99.127004) (cited on page 12)
146. Ye F, Chi S, Cao H, Chakoumakos BC, Fernandez-Baca JA, Custelcean R, Qi TF, Korneta OB, and Cao G. Direct evidence of a zigzag spin-chain structure in the honeycomb lattice: A neutron and x-ray diffraction investigation of single-crystal NaIrO₃. *Physical Review B* 2012 May; 85:180403. doi: [10.1103/PhysRevB.85.180403](https://doi.org/10.1103/PhysRevB.85.180403) (cited on page 12)
147. Choi SK, Coldea R, Kolmogorov AN, Lancaster T, Mazin II, Blundell SJ, Radaelli PG, Singh Y, Gegenwart P, Choi KR, Cheong SW, Baker PJ, Stock C, and Taylor J. Spin Waves and Revised Crystal Structure of Honeycomb Iridate NaIrO₃. *Physical Review Letters* 2012 Mar; 108:127204. doi: [10.1103/PhysRevLetters108.127204](https://doi.org/10.1103/PhysRevLetters108.127204) (cited on page 12)
148. Banerjee A, Bridges CA, Yan JQ, Aczel AA, Li L, Stone MB, Granroth GE, Lumsden MD, Yiu Y, Knolle J, Bhattacharjee S, Kovrizhin DL, Moessner R, Tennant DA, Mandrus DG, and Nagler SE. Proximate Kitaev quantum spin liquid behaviour in a honeycomb magnet. *Nature Materials* 2016 Jul; 15:733–40. doi: [10.1038/nmat4604](https://doi.org/10.1038/nmat4604) (cited on page 12)
149. Banerjee A, Yan J, Knolle J, Bridges CA, Stone MB, Lumsden MD, Mandrus DG, Tennant DA, Moessner R, and Nagler SE. Neutron scattering in the proximate quantum spin liquid α -RuCl₃. *Science* 2017 Jun; 356:1055–9. doi: [10.1126/science.aah6015](https://doi.org/10.1126/science.aah6015) (cited on page 12)
150. Janša N, Zorko A, Gomilšek M, Pregelj M, Krämer KW, Biner D, Biffin A, Rüegg C, and Klanjšek M. Observation of two types of fractional excitation in the Kitaev honeycomb magnet. *Nature Physics* 2018 Aug; 14:786–90. doi: [10.1038/s41567-018-0129-5](https://doi.org/10.1038/s41567-018-0129-5) (cited on page 12)

151. Yamamoto J, Nagai Y, Jinno T, Shimizu Y, Matsushita T, Kobayashi Y, Itoh M, Nasu J, and Motome Y. NMR Evidence for Majorana Gap in the Kitaev Quantum Spin Liquid. *Proceedings of the 29th International Conference on Low Temperature Physics (LT29)*. Vol. 38. JPS Conference Proceedings 38. Journal of the Physical Society of Japan, 2023 May. doi: [10.7566/JPSCP.38.011130](https://doi.org/10.7566/JPSCP.38.011130) (cited on page 12)
152. Liu X, Berlijn T, Yin WG, Ku W, Tsvetik A, Kim YJ, Gretarsson H, Singh Y, Gegenwart P, and Hill JP. Long-range magnetic ordering in NaIrO₃. *Physical Review B* 2011 Jun; 83:220403. doi: [10.1103/PhysRevB.83.220403](https://doi.org/10.1103/PhysRevB.83.220403) (cited on page 12)
153. Hwan Chun S, Kim JW, Kim J, Zheng H, Stoumpos CC, Malliakas CD, Mitchell JF, Mehlawat K, Singh Y, Choi Y, Gog T, Al-Zein A, Sala MM, Krisch M, Chaloupka J, Jackeli G, Khaliullin G, and Kim BJ. Direct evidence for dominant bond-directional interactions in a honeycomb lattice iridate Na₂IrO₃. *Nature Physics* 2015 Jun; 11:462–6. doi: [10.1038/nphys3322](https://doi.org/10.1038/nphys3322) (cited on page 12)
154. Baskaran G, Sen D, and Shankar R. Spin-S Kitaev model: Classical ground states, order from disorder, and exact correlation functions. *Physical Review B* 2008 Sep; 78:115116. doi: [10.1103/PhysRevB.78.115116](https://doi.org/10.1103/PhysRevB.78.115116) (cited on page 13)
155. Henley CL. The “Coulomb Phase” in Frustrated Systems. *Annual Review of Condensed Matter Physics* 2010; 1:179–210. doi: [10.1146/annurev-conmatphys-070909-104138](https://doi.org/10.1146/annurev-conmatphys-070909-104138) (cited on page 13)
156. Pavarini E and Koch E. Orbital Physics in Correlated Matter. en. Tech. rep. FZJ-2023-03329. Forschungszentrum Jülich GmbH Zentralbibliothek, Verlag, 2023 (cited on page 14)
157. Nasu J and Motome Y. Thermodynamics of Chiral Spin Liquids with Abelian and Non-Abelian Anyons. *Physical Review Letters* 2015 Aug; 115:087203. doi: [10.1103/PhysRevLetters115.087203](https://doi.org/10.1103/PhysRevLetters115.087203) (cited on pages 16, 17)
158. Yamaji Y, Suzuki T, Yamada T, Suga Si, Kawashima N, and Imada M. Clues and criteria for designing a Kitaev spin liquid revealed by thermal and spin excitations of the honeycomb iridate Na₂IrO₃. *Physical Review B* 2016 May; 93:174425. doi: [10.1103/PhysRevB.93.174425](https://doi.org/10.1103/PhysRevB.93.174425) (cited on pages 18, 108)
159. Kimchi I and Vishwanath A. Kitaev-Heisenberg models for iridates on the triangular, hyperkagome, kagome, fcc, and pyrochlore lattices. *Physical Review B* 2014 Jan; 89:014414. doi: [10.1103/PhysRevB.89.014414](https://doi.org/10.1103/PhysRevB.89.014414) (cited on page 19)
160. Banerjee A, Lampen-Kelley P, Knolle J, Balz C, Aczel AA, Winn B, Liu Y, Pajerowski D, Yan J, Bridges CA, Savici AT, Chakoumakos BC, Lumsden MD, Tennant DA, Moessner R, Mandrus DG, and Nagler SE. Excitations in the field-induced quantum spin liquid state of α - RuCl₃. en. *npj Quantum Materials* 2018 Feb; 3:1–7. doi: [10.1038/s41535-018-0079-2](https://doi.org/10.1038/s41535-018-0079-2) (cited on page 20)
161. Lieb EH and Wu FY. Absence of Mott Transition in an Exact Solution of the Short-Range, One-Band Model in One Dimension. *Physical Review Letters* 1968 Jun; 20:1445–8. doi: [10.1103/PhysRevLetters20.1445](https://doi.org/10.1103/PhysRevLetters20.1445) (cited on page 21)
162. Baxter RJ. Exactly Solved Models in Statistical Mechanics. *Integrable Systems in Statistical Mechanics*. Vol. Volume 1. Series on Advances in Statistical Mechanics Volume 1. WORLD SCIENTIFIC, 1985. doi: [10.1142/9789814415255_0002](https://doi.org/10.1142/9789814415255_0002) (cited on page 21)

163. Mattis DC. The Many-Body Problem: An Encyclopedia of Exactly Solved Models in One Dimension(3rd Printing with Revisions and Corrections). World Scientific, 1993 Mar (cited on page 21)
164. Sriram Shastry B and Sutherland B. Exact ground state of a quantum mechanical antiferromagnet. *Physica B+C*. 1981 Aug 1; 108. doi: [10.1016/0378-4363\(81\)90838-X](https://doi.org/10.1016/0378-4363(81)90838-X) (cited on page 21)
165. Affleck I, Kennedy T, Lieb EH, and Tasaki H. Valence bond ground states in isotropic quantum antiferromagnets. *Communications in Mathematical Physics*. 1988 Sep 1; 115:477–528. doi: [10.1007/BF01218021](https://doi.org/10.1007/BF01218021) (cited on page 21)
166. Newman MEJ and Barkema GT. Monte Carlo Methods in Statistical Physics. en. Clarendon Press, 1999 Feb (cited on pages 22, 23)
167. Metropolis N and Ulam S. The Monte Carlo Method. *Journal of the American Statistical Association* 1949; 44:335–41. doi: [10.2307/2280232](https://doi.org/10.2307/2280232) (cited on pages 23, 24)
168. Brito FMO. Development of a QMC code to tackle interacting electronic systems in 2D with application to TMD nanoribbons. Instituto Superior Técnico, 2018 (cited on pages 25, 28)
169. Bai Z, Chen W, Scalettar R, and Yamazaki I. Numerical Methods for Quantum Monte Carlo Simulations of the Hubbard Model. *Multi-Scale Phenomena in Complex Fluids*. Vol. 12. Series in Contemporary Applied Mathematics. Co-published With Higher Education Press, 2009 Jun 1:1–110. doi: [10.1142/9789814273268_0001](https://doi.org/10.1142/9789814273268_0001) (cited on pages 27, 28, 76)
170. Hirsch JE. Discrete Hubbard-Stratonovich transformation for fermion lattice models. *Physical Review B* 1983 Oct 1; 28:4059–61. doi: [10.1103/PhysRevB.28.4059](https://doi.org/10.1103/PhysRevB.28.4059) (cited on pages 27, 73)
171. Held K and Vollhardt D. Microscopic conditions favoring itinerant ferromagnetism: Hund's rule coupling and orbital degeneracy. *European Physical Journal B* 1998; 5:473–8. doi: <https://doi.org/10.1007/s100510050468> (cited on page 27)
172. Hanke W, KopaeV YV, and John W. Electronic Phase Transitions. *Modern Problems in Condensed Matter Sciences Vol. 32*. North Holland: Amsterdam, London, New York, Tokio 1992; 336 Seiten, ISBN 0-444-88885-3. *Crystal Research and Technology* 1993; 28:28–8. doi: [10.1002/crat.2170280106](https://doi.org/10.1002/crat.2170280106) (cited on pages 28, 73)
173. Bai Z, Lee C, Li RC, and Xu S. Stable solutions of linear systems involving long chain of matrix multiplications. *Linear Algebra and its Applications*. Special Issue: Dedication to Pete Stewart on the occasion of his 70th birthday 2011 Aug 1; 435:659–73. doi: [10.1016/j.laa.2010.06.023](https://doi.org/10.1016/j.laa.2010.06.023) (cited on page 28)
174. Weisse A, Wellein G, Alvermann A, and Fehske H. The kernel polynomial method. *Reviews of Modern Physics*. 2006 Mar 24; 78:275–306. doi: [10.1103/RevModPhysics78.275](https://doi.org/10.1103/RevModPhysics78.275) (cited on pages 29, 30, 39, 43, 45, 66, 93, 104)
175. García JH, Covaci L, and Rappoport TG. Real-Space Calculation of the Conductivity Tensor for Disordered Topological Matter. *Physical Review Letters*. 2015 Mar 19; 114:116602. doi: [10.1103/PhysRevLetters114.116602](https://doi.org/10.1103/PhysRevLetters114.116602) (cited on page 29)
176. Cysne TP, Rappoport TG, Ferreira A, Lopes JMVP, and Peres NMR. Numerical calculation of the Casimir-Polder interaction between a graphene sheet with vacancies and an atom. *Physical Review B*. 2016; 94:235405. doi: [10.1103/PhysRevB.94.235405](https://doi.org/10.1103/PhysRevB.94.235405) (cited on page 29)
177. Mashkooi M, Björnson K, and Black-Schaffer AM. Impurity bound states in fully gapped d-wave superconductors with subdominant order parameters. en. *Scientific Reports* 2017 Mar; 7. doi: [10.1038/srep44107](https://doi.org/10.1038/srep44107) (cited on pages 29, 93)

178. Lado JL and Zilberberg O. Topological spin excitations in Harper-Heisenberg spin chains. *Physical Review Research*. 2019 Oct 4; 1:033009. doi: [10.1103/PhysRevResearch.1.033009](https://doi.org/10.1103/PhysRevResearch.1.033009) (cited on pages 29, 66)
179. Lado JL and Sigrist M. Solitonic in-gap modes in a superconductor-quantum antiferromagnet interface. *Physical Review Research*. 2020 Jun 16; 2:023347. doi: [10.1103/PhysRevResearch.2.023347](https://doi.org/10.1103/PhysRevResearch.2.023347) (cited on page 29)
180. Varjas D, Fruchart M, Akhmerov AR, and Perez-Piskunow PM. Computation of topological phase diagram of disordered $\text{Pb}_{1-x}\text{Sn}_x\text{Te}$ using the kernel polynomial method. *Physical Review Research*. 2020 Feb 28; 2:013229. doi: [10.1103/PhysRevResearch.2.013229](https://doi.org/10.1103/PhysRevResearch.2.013229) (cited on pages 29, 93)
181. João SM and Viana Parente Lopes JM. Basis-independent spectral methods for non-linear optical response in arbitrary tight-binding models. *Journal of Physics: Condensed Matter*. 2020 Mar 20; 32:125901. doi: [10.1088/1361-648X/ab59ec](https://doi.org/10.1088/1361-648X/ab59ec) (cited on pages 29, 93)
182. Kaskela V and Lado JL. Dynamical topological excitations in parafermion chains. *Physical Review Research*. 2021 Jan 29; 3:013095. doi: [10.1103/PhysRevResearch.3.013095](https://doi.org/10.1103/PhysRevResearch.3.013095) (cited on page 29)
183. Rösner M and Lado JL. Inducing a many-body topological state of matter through Coulomb-engineered local interactions. *Physical Review Research*. 2021 Mar 19; 3:013265. doi: [10.1103/PhysRevResearch.3.013265](https://doi.org/10.1103/PhysRevResearch.3.013265) (cited on page 29)
184. Pires JPS, Amorim B, Ferreira A, Adagideli İ, Mucciolo ER, and Lopes JMVP. Breakdown of universality in three-dimensional Dirac semimetals with random impurities. *Physical Review Research*. 2021 Feb 25; 3:013183. doi: [10.1103/PhysRevResearch.3.013183](https://doi.org/10.1103/PhysRevResearch.3.013183) (cited on pages 29, 93)
185. Löthman T, Triola C, Cayao J, and Black-Schaffer AM. Efficient numerical method for evaluating normal and anomalous time-domain equilibrium Green's functions in inhomogeneous systems. *Physical Review B*. 2021 Sep 2; 104:125405. doi: [10.1103/PhysRevB.104.125405](https://doi.org/10.1103/PhysRevB.104.125405) (cited on pages 29, 93)
186. Löthman T, Triola C, Cayao J, and Black-Schaffer AM. Disorder-robust p -wave pairing with odd-frequency dependence in normal metal-conventional superconductor junctions. *Physical Review B* 2021 Sep; 104:094503. doi: [10.1103/PhysRevB.104.094503](https://doi.org/10.1103/PhysRevB.104.094503) (cited on pages 29, 93)
187. Boyd JP. Chebyshev & Fourier Spectral Methods. en. *Lecture Notes in Engineering*. Berlin Heidelberg: Springer-Verlag, 1989 (cited on pages 29, 30, 54)
188. Braun A and Schmitteckert P. Numerical evaluation of Green's functions based on the Chebyshev expansion. *Physical Review B*. 2014 Oct 9; 90:165112. doi: [10.1103/PhysRevB.90.165112](https://doi.org/10.1103/PhysRevB.90.165112) (cited on pages 29, 30)
189. Ferreira A and Mucciolo ER. Critical Delocalization of Chiral Zero Energy Modes in Graphene. *Physical Review Letters*. 2015 Aug 31; 115:106601. doi: [10.1103/PhysRevLetters115.106601](https://doi.org/10.1103/PhysRevLetters115.106601) (cited on pages 29, 30, 32, 54, 61, 93, 105)
190. João SM, Anđelković M, Covaci L, Rappoport TG, Lopes JMVP, and Ferreira A. KITE: high-performance accurate modelling of electronic structure and response functions of large molecules, disordered crystals and heterostructures. *Royal Society Open Science* 2020; 7:191809. doi: [10.1098/rsos.191809](https://doi.org/10.1098/rsos.191809) (cited on pages 29, 56, 93, 105, 131)
191. Iitaka T and Ebisuzaki T. Random phase vector for calculating the trace of a large matrix. *Physical Review E* 2004; 69(5):057701. doi: [10.1103/PhysRevE.69.057701](https://doi.org/10.1103/PhysRevE.69.057701) (cited on page 29)

192. Sandvik AW. Computational Studies of Quantum Spin Systems. AIP Conference Proceedings. 2010 Nov 3; 1297:135–338. doi: [10.1063/1.3518900](https://doi.org/10.1063/1.3518900) (cited on pages 36, 50, 127)
193. Dhillon IS. A New $O(n^2)$ Algorithm for the Symmetric Tridiagonal Eigenvalue/Eigenvector Problem. EECS Department, University of California, Berkeley, 1997 (cited on pages 38, 51, 66)
194. Anderson E, Bai Z, Bischof C, Blackford S, Demmel J, Dongarra J, Du Croz J, Greenbaum A, Hammarling S, McKenney A, and Sorensen D. LAPACK Users' Guide. Third. Philadelphia, PA: Society for Industrial and Applied Mathematics, 1999 (cited on page 38)
195. Dhillon IS, Parlett BN, and Vömel C. The design and implementation of the MRRR algorithm. ACM Transactions on Mathematical Software. 2006 Dec 1; 32:533–60. doi: [10.1145/1186785.1186788](https://doi.org/10.1145/1186785.1186788) (cited on pages 38, 51, 66)
196. Demmel JW, Marques OA, Parlett BN, and Vömel C. Performance and Accuracy of LAPACK's Symmetric Tridiagonal Eigensolvers. SIAM Journal on Scientific Computing. 2008; 30:1508–26. doi: [10.1137/070688778](https://doi.org/10.1137/070688778) (cited on pages 38, 51, 66)
197. Long MW, Prelovšek P, El Shawish S, Karadamoglou J, and Zotos X. Finite-temperature dynamical correlations using the microcanonical ensemble and the Lanczos algorithm. Physical Review B. 2003 Dec 15; 68:235106. doi: [10.1103/PhysRevB.68.235106](https://doi.org/10.1103/PhysRevB.68.235106) (cited on page 51)
198. Ikeuchi H, De Raedt H, Bertaina S, and Miyashita S. Computation of ESR spectra from the time evolution of the magnetization: Comparison of autocorrelation and Wiener-Khinchin-relation-based methods. Physical Review B 2015 Dec; 92:214431. doi: [10.1103/PhysRevB.92.214431](https://doi.org/10.1103/PhysRevB.92.214431) (cited on page 62)
199. Endo H, Hotta C, and Shimizu A. From Linear to Nonlinear Responses of Thermal Pure Quantum States. Physical Review Letters 2018 Nov; 121:220601. doi: [10.1103/PhysRevLetters121.220601](https://doi.org/10.1103/PhysRevLetters121.220601) (cited on page 64)
200. Holzner A, Weichselbaum A, McCulloch IP, Schollwöck U, and Delft J von. Chebyshev matrix product state approach for spectral functions. Physical Review B 2011 May 10; 83:195115. doi: [10.1103/PhysRevB.83.195115](https://doi.org/10.1103/PhysRevB.83.195115) (cited on pages 66, 93)
201. Blankenbecler R, Scalapino DJ, and Sugar RL. Monte Carlo calculations of coupled boson-fermion systems. I. Physical Review D 1981 Oct 15; 24:2278–86. doi: [10.1103/PhysRevD.24.2278](https://doi.org/10.1103/PhysRevD.24.2278) (cited on page 73)
202. Chu RL, Liu GB, Yao W, Xu X, Xiao D, and Zhang C. Spin-orbit-coupled quantum wires and Majorana fermions on zigzag edges of monolayer transition-metal dichalcogenides. Physical Review B 2014 Apr 22; 89:155317. doi: [10.1103/PhysRevB.89.155317](https://doi.org/10.1103/PhysRevB.89.155317) (cited on pages 73, 74)
203. Mermin ND and Wagner H. Absence of Ferromagnetism or Antiferromagnetism in One- or Two-Dimensional Isotropic Heisenberg Models. Physical Review Letters 1966 Nov 28; 17:1133–6. doi: [10.1103/PhysRevLetters17.1133](https://doi.org/10.1103/PhysRevLetters17.1133) (cited on page 74)
204. Feynman RP. Statistical Mechanics: A Set Of Lectures. Boca Raton: CRC Press, 2019 Jun (cited on page 75)
205. Varney CN, Lee CR, Bai ZJ, Chiesa S, Jarrell M, and Scalettar RT. Quantum Monte Carlo study of the two-dimensional fermion Hubbard model. Physical Review B 2009 Aug 18; 80:075116. doi: [10.1103/PhysRevB.80.075116](https://doi.org/10.1103/PhysRevB.80.075116) (cited on page 76)

206. Golor M, Lang TC, and Wessel S. Quantum Monte Carlo studies of edge magnetism in chiral graphene nanoribbons. *Physical Review B* 2013 Apr 30; 87:155441. doi: [10.1103/PhysRevB.87.155441](https://doi.org/10.1103/PhysRevB.87.155441) (cited on page 76)
207. Johnston S, Nowadnick EA, Kung YF, Moritz B, Scalettar RT, and Devereaux TP. Determinant quantum Monte Carlo study of the two-dimensional single-band Hubbard-Holstein model. *Physical Review B* 2013 Jun 24; 87:235133. doi: [10.1103/PhysRevB.87.235133](https://doi.org/10.1103/PhysRevB.87.235133) (cited on page 76)
208. Cheng S, Yu J, Ma T, and Peres NMR. Strain-induced edge magnetism at the zigzag edge of a graphene quantum dot. *Physical Review B* 2015 Feb 11; 91:075410. doi: [10.1103/PhysRevB.91.075410](https://doi.org/10.1103/PhysRevB.91.075410) (cited on page 76)
209. Roldán R, Cappelluti E, and Guinea F. Interactions and superconductivity in heavily doped MoS₂. *Physical Review B* 2013; 88(5):054515. doi: [10.1103/PhysRevB.88.054515](https://doi.org/10.1103/PhysRevB.88.054515) (cited on page 80)
210. Cortés N, Ávalos-Ovando O, Rosales L, Orellana PA, and Ulloa SE. Tunable Spin-Polarized Edge Currents in Proximitized Transition Metal Dichalcogenides. *Physical Review Letters* 2019 Feb 25; 122:086401. doi: [10.1103/PhysRevLetters122.086401](https://doi.org/10.1103/PhysRevLetters122.086401) (cited on pages 89, 90)
211. Correa JH, Dias AC, Villegas-Lelovsky L, Fu J, Chico L, and Qu F. Anisotropy of the spin-polarized edge current in monolayer transition metal dichalcogenide zigzag nanoribbons. *Physical Review B* 2020; 101(19):195422. doi: [10.1103/PhysRevB.101.195422](https://doi.org/10.1103/PhysRevB.101.195422) (cited on pages 89, 90)
212. Cortés N, Ávalos-Ovando O, and Ulloa SE. Reversible edge spin currents in antiferromagnetically proximitized dichalcogenides. *Physical Review B* 2020; 101:201108R. doi: [10.1103/PhysRevB.101.201108](https://doi.org/10.1103/PhysRevB.101.201108) (cited on pages 89, 90)
213. Čadež T, Li L, Castro EV, and Carmelo JMP. Robust one dimensionality at twin grain boundaries in MoSe₂. *Physical Review B* 2019; 99:155109. doi: [10.1103/PhysRevB.99.155109](https://doi.org/10.1103/PhysRevB.99.155109) (cited on page 90)
214. Ávalos-Ovando O, Mastrogiuseppe D, and Ulloa SE. Lateral heterostructures and one-dimensional interfaces in 2D transition metal dichalcogenides. *Journal of Physics: Condensed Matter* 2019; 31:213001. doi: [10.1088/1361-648X/ab0970](https://doi.org/10.1088/1361-648X/ab0970) (cited on page 90)
215. Okamoto S, Alvarez G, Dagotto E, and Tohyama T. Accuracy of the microcanonical Lanczos method to compute real-frequency dynamical spectral functions of quantum models at finite temperatures. *Physical Review E*. 2018 Apr 20; 97:043308. doi: [10.1103/PhysRevE.97.043308](https://doi.org/10.1103/PhysRevE.97.043308) (cited on page 93)
216. Schnack J, Richter J, and Steinigeweg R. Accuracy of the finite-temperature Lanczos method compared to simple typicality-based estimates. *Physical Review Research*. 2020 Feb 21; 2:013186. doi: [10.1103/PhysRevResearch.2.013186](https://doi.org/10.1103/PhysRevResearch.2.013186) (cited on page 93)
217. Wannier GH. Antiferromagnetism. The Triangular Ising Net. *Physical Review*. 1950 Jul 15; 79:357–64. doi: [10.1103/PhysReview79.357](https://doi.org/10.1103/PhysReview79.357) (cited on page 93)
218. Pesin D and Balents L. Mott physics and band topology in materials with strong spin-orbit interaction. *Nature Physics* 2010 May; 6:376–81. doi: [10.1038/nphys1606](https://doi.org/10.1038/nphys1606) (cited on page 93)
219. Balents L. Spin liquids in frustrated magnets. *Nature* 2010 Mar; 464:199–208. doi: [10.1038/nature08917](https://doi.org/10.1038/nature08917) (cited on page 93)
220. Maksimov PA and Chernyshev AL. Rethinking α -RuCl₃. *Physical Review Research*. 2020 Jul 2; 2:033011. doi: [10.1103/PhysRevResearch.2.033011](https://doi.org/10.1103/PhysRevResearch.2.033011) (cited on page 93)

221. Nasu J and Motome Y. Thermodynamic and transport properties in disordered Kitaev models. *Physical Review B*. 2020 Aug 25; 102:054437. doi: [10.1103/PhysRevB.102.054437](https://doi.org/10.1103/PhysRevB.102.054437) (cited on page 94)
222. Widmann S, Tsurkan V, Prishchenko DA, Mazurenko VG, Tsirlin AA, and Loidl A. Thermodynamic evidence of fractionalized excitations in α -RuCl₃. *Physical Review B*. 2019 Mar 14; 99:094415. doi: [10.1103/PhysRevB.99.094415](https://doi.org/10.1103/PhysRevB.99.094415) (cited on page 101)
223. Catuneanu A, Yamaji Y, Wachtel G, Kim YB, and Kee HY. Path to stable quantum spin liquids in spin-orbit coupled correlated materials. *npj Quantum Materials*. 2018 Apr 24; 3:1–6. doi: [10.1038/s41535-018-0095-2](https://doi.org/10.1038/s41535-018-0095-2) (cited on page 101)
224. Kimchi I, Coldea R, and Vishwanath A. Unified theory of spiral magnetism in the harmonic-honeycomb iridates Li₂IrO₃. *Physical Review B* 2015 Jun; 91:245134. doi: [10.1103/PhysRevB.91.245134](https://doi.org/10.1103/PhysRevB.91.245134) (cited on page 115)
225. Rademaker L. Quenching the Kitaev honeycomb model. en. *SciPost Physics* 2019 Nov; 7:071. doi: [10.21468/SciPostPhysics7.5.071](https://doi.org/10.21468/SciPostPhysics7.5.071) (cited on pages 115, 121–123, 125)
226. Polkovnikov A, Sengupta K, Silva A, and Vengalattore M. Colloquium: Nonequilibrium dynamics of closed interacting quantum systems. *Reviews of Modern Physics* 2011 Aug; 83:863–83. doi: [10.1103/RevModPhysics83.863](https://doi.org/10.1103/RevModPhysics83.863) (cited on page 121)
227. Heyl M. Dynamical quantum phase transitions: a review. en. *Reports on Progress in Physics* 2018 Apr; 81:054001. doi: [10.1088/1361-6633/aaaf9a](https://doi.org/10.1088/1361-6633/aaaf9a) (cited on page 121)
228. Heyl M, Polkovnikov A, and Kehrein S. Dynamical Quantum Phase Transitions in the Transverse-Field Ising Model. *Physical Review Letters* 2013 Mar; 110:135704. doi: [10.1103/PhysRevLetters110.135704](https://doi.org/10.1103/PhysRevLetters110.135704) (cited on page 121)
229. Bertini B, Essler FHL, Groha S, and Robinson NJ. Prethermalization and Thermalization in Models with Weak Integrability Breaking. *Physical Review Letters* 2015 Oct; 115:180601. doi: [10.1103/PhysRevLetters115.180601](https://doi.org/10.1103/PhysRevLetters115.180601) (cited on page 122)
230. Abanin D, De Roeck W, Ho WW, and Huveneers F. A Rigorous Theory of Many-Body Prethermalization for Periodically Driven and Closed Quantum Systems. en. *Communications in Mathematical Physics* 2017 Sep; 354:809–27. doi: [10.1007/s00220-017-2930-x](https://doi.org/10.1007/s00220-017-2930-x) (cited on page 123)
231. Reimann P. Typicality for Generalized Microcanonical Ensembles. *Physical Review Letters* 2007 Oct; 99:160404. doi: [10.1103/PhysRevLetters99.160404](https://doi.org/10.1103/PhysRevLetters99.160404) (cited on page 143)

Alphabetical Index

Abstract, iii	Edge magnetism in	Kitaev-Heisenberg model,
Acknowledgements, xv	transition metal	114
Appendix, 151	dichalcogenide	Kitaev-Ising model, 123
Concluding remarks, 127	nanoribbons, 90	Methods, 69
Conclusion, 136	Future work, 134	
Declaration, xvii	Introduction, 20	